Multiwavelength Probes of Physical Conditions in the Blazar Zone of AGN jets

Dissertation zur Erlangung des naturwissenschaftlichen Doktorgrades der Julius-Maximilians-Universität Würzburg

Vorgelegt von

Paul Ray Burd

aus Münchberg

Würzburg, 2021

Eingereicht am:
bei der Fakultät für Physik und Astronomie

1. Gutachter: Prof. Dr. Matthias Kadler
2. Gutachter: Prof. Dr. Eduardo Ros Ibarra
3. Gutachter:
der Dissertation.

Vorsitzende(r):

1. Prüfer: Prof. Dr. Matthias Kadler
2. Prüfer: Prof. Dr. Eduardo Ros Ibarra
3. Prüfer:
im Promotionskolloquium.

Tag des Promotionskolloquiums:
Doktorurkunde ausgehändigt am:

Contents

Zusammenfassung **1**

Abstract **4**

1 Active galactic nuclei **7**
1.1 AGN unification scheme . . . 8
1.2 Blazars . . . 10
1.3 Blazar variability in the GeV and TeV regime . . . 13
1.3.1 The stochastic nature of high-energy blazar variability . . . 15
1.3.2 The Ornstein-Uhlenbeck parameters and their impact on time series 17
1.3.3 The location of the γ-ray emitting region . . . 18
1.4 Synchrotron radiation - the curse and blessing of beamed emission . . . 20
1.5 Apparent super-luminal motion . . . 23
1.6 The Blandford & Königl (1979) jet model and extensions . . . 26
1.7 Geometry transitions in blazar jets and the acceleration zone . . . 29
1.8 So what is my plan? . . . 30

2 Analyzing blazar jets on parsec scales **33**
2.1 Radio interferometry . . . 34
2.2 Model fitting a jet with circular Gaussian components . . . 37
2.3 15 GHz and 43 GHz sample . . . 41
2.4 Measuring the brightness temperature and the diameter gradients . . . 41
2.5 Finding and fitting geometry breaks . . . 43
2.6 Magnetic field strength gradients . . . 44
2.7 The Magnetic field of the radio core in blazar jets . . . 46
2.7.1 Concerning the intrinsic bulk speed, the bulk Lorentz factor and the maximum apparent jet speed . . . 47
2.7.2 The procecdure to actually calculate the magnetic fields in the radio core . . . 48
2.8 Scaling the magnetic field down to the SMBH . . . 48

3 Statistical analysis of blazar light curves in the γ-ray regime **51**
3.1 Fermi Large Area Telescope . . . 51
3.2 Samples of gamma-ray light curves of blazars . . . 52
3.2.1 Monthly-binned light curves . . . 52
3.2.2 Weekly-binned light curves from the 20 radio sources . . . 54
3.3 Statistical analysis of light curves . . . 55

3.3.1 Ornstein-Uhlenbeck parameter extraction . . . 55
3.3.1.1 Extraction of σ - approximating the non-deterministic part 55
3.3.1.2 Extraction of θ - approximating the deterministic part . . 56
3.3.1.3 The calibration of the ϵ environment . . . 57
3.3.2 Further light curve analysis - asymmetry measure of flares and power spectral densities . . . 57

4 The brightness temperature, geometry and magnetic field structure of parsec-scale blazar jets 63
4.1 Sample results of single power law fits . . . 64
4.1.1 Results of the diameter gradients . . . 64
4.1.2 Results of the brightness temperature gradients . . . 64
4.1.3 Brightness temperature and diameter gradients in context . . . 66
4.1.4 Gradients of the magnetic field strength . . . 72
4.1.5 Magnetic fields in the radio cores . . . 72
4.2 Discussion . . . 73
4.2.1 Single power law fits . . . 73
4.2.2 Differences between the modelfit method and the stacked-image analysis . . . 76
4.2.3 The effect of cosmological distances and projection . . . 76
4.2.4 Scaling the magnetic fields to the ergosphere . . . 77
4.2.5 Geometry breaks . . . 78
4.3 Remarks on single sources . . . 81
0219+428 (B) . . . 83
0336-019 (Q) . . . 83
0415+379 (G) . . . 86
0430+052 (G) . . . 86
0528+134 (Q) . . . 86
0716+714 (B) . . . 91
0735+178 (B) . . . 91
0827+243 (Q) . . . 91
0829+046 (B) . . . 95
0836+710 (Q) . . . 95
0851+202 (B) . . . 100
0954+658 (B) . . . 100
1101+384 (B) . . . 100
1127-145 (Q) . . . 100
1156+295 (Q) . . . 105
1219+285 (B) . . . 105
1222+216 (Q) . . . 105
1253-055 (Q) . . . 105
1308+326 (Q) . . . 111
1633+382 (Q) . . . 111
1652+398 (B) . . . 111
1730-130 (Q) . . . 111
1749+096 (B) . . . 111
2200+420 (B) . . . 111

2223-052 (B) . . . 118
2230+114 (B) . . . 118
2251+158 (B) . . . 118

5 Results from the γ-ray light curve analysis 123
5.1 1 GeV sample . . . 124
5.2 100 MeV sample . . . 125
5.2.1 OU parameters and PSD slopes . . . 125
The TS1 filter . . . 125
The TS4 filter . . . 126
The TS9 filter . . . 126
5.2.2 Asymmetry of flare shapes . . . 127
5.3 Results from the jet gradient sample . . . 127
5.4 Discussion . . . 128
5.4.1 General comments . . . 128
5.4.2 The effect of the TS filter in the 100 MeV sample . . . 130
5.4.3 The σ distributions . . . 131

6 Summary and future perspectives 133
6.1 Radio and gamma results in context . . . 133
6.2 What about my plan? . . . 135
6.3 Work that needs to be done . . . 137
6.4 Used software . . . 138

List of figures 139

List of tables 145

Bibliography 147

Acknowledgements 158

A Significant contributions to Co-Authored papers 161
Wagner et al. (2021): Statistical properties of flux variations in blazar light curves at GeV and TeV energies . . . 161
Baczko et al. 2021 submitted and revised: Ambilateral collimation study of the twin-jets in NGC 1052 . 161
Kappes 2021 submitted and revised : The sub-arcsecond view on the high-redshift blazar GB 1508+5714 by the International LOFAR Telescope . . . 162
Kappes et al. (2019): LOFAR measures the hotspot advance speed of the high-redshift blazar S5 0836+710 162
Müller et al. (2016): The MHz-peaked radio spectrum of the unusual γ-ray source PMN J1603-4904 . . . 162

Zusammenfassung

Einordnung. Durch Akkretion von Materie auf supermassive schwarze Löcher (engl.: super massive black holes, SMBH) in den Zentren von aktiven Galaxien (engl.: active galactic nuclei, AGN) wird auf einer Skala von der Größe unseres Sonnensystems eine Energie freigesetzt, die den Rest der Galaxie dieser AGN überstrahlt. In einigen dieser AGN werden, parallel zur Rotationsachse des SMBHs, hochrelativistische Teilchenströme (Jets) erzeugt. Einige dieser AGN werden unter einem kleinen Winkel zwischen der Jetachse und der Beobachtungssichtlinie erfasst. Ist dies der Fall, führt der kleine Sichtwinkel bei gleichzeitigem Bestehen hochrelativistischer Geschwindigkeiten der Teilchen im Jet dazu, dass die Strahlung der Teilchen den sogenannten Beaming-Effekten unterliegt. Diese AGN nennt man Blazare, welche anhand der Leuchtkraft unterschieden werden können in Radioquasare, die ein flaches Radiospektrum aufweisen (engl.: flat spectrum radio quasars, FSRQs), mit einer hohen Leuchtkraft und BL Lacertae Ojekte (BL Lacs) mit einer niedrigen Leuchtkraft. Blazare sind Breitbandemitter und daher mit den längsten Wellenlängen im Radiobereich bis zu den kleinsten Wellenlängen im γ-Bereich beobachtbar. In dieser Arbeit werde ich Eigenschaften dieser Blazare auf Parsecskalen durch Radiobeobachtungen und die Zeitentwicklung der Helligkeit dieser im γ-Bereich analysieren.

Methoden. Im Radioregime wird die Technik der sehr langen Basislinieninterferometrie (engl. very long baseline interferometry, VLBI) genutzt, um die Synchrotronstrahlung von Blazaren auf sub-Parsecskalen räumlich aufzulösen. Große Monitoringprogramme wie 'MOJAVE' (Beobachtungen bei 15 GHz) und das 'Boston University blazar monitoring program' (Beobachtungen bei 43 GHz) beobachten diese Quellen mit einer circa monatlichen Kadenz. Bei jeder Beobachtung spricht man von einer Epoche. Für diese Arbeit werde ich Daten von 28 Quellen dieser Programme aus einem Zeitraum von zehn Jahren (2003 bis 2013) nutzen. Das ergibt mehr als 1800 Epochen. Anhand dieser Daten sollen die Helligkeitstemperaturen und Geometrien der Jets analysiert werden. Des Weiteren werde ich nach systematischen Geometrieübergängen in den Jets der Blazare suchen und die Synchrotronkühlzeit nutzen, um die Magnetfeldstärken in den Radiokernen der Jets zu berechnen. Diese Kernmagnetfeldstärken können genutzt werden, um die Abstände der Radiokerne von den Ergosphären der SMBHs zu berechnen. Im γ-Bereich können diese Quellen nicht räumlich aufgelöst werden. Daher ist es schwierig auszumachen, woher genau in einer solchen Quelle die γ-Strahlung stammt. In diesem Energiebereich sind Blazare sehr variabel. Variabilitätszeitskalen können in den hellsten Quellen bis zur Minutenskala aufgelöst werden. Die Eigenschaft dieser Variabilität kann Hinweise auf die Teilchenbeschleunigungsprozesse, die Region, aus der diese Strahlung stammt, und die Größe der Emissionsregion geben. Blazare können im Energiebereich zwischen $0.1 \leq E/\mathrm{GeV} \leq 1$ zum Beispiel mit dem Teilchenpaarumwandlungsteleskop auf

dem Fermisatelliten beobachtet werden. In dieser Arbeit werden ca. 10 Jahre an *Fermi*-LAT-Beobachtungen verwendet (LAT: engl. large area telescope), um die Variabilität einer großen Zahl an Blazaren ca. 300-800 je nach Signifikanzfiltern) zu untersuchen. Dabei werden Ornstein-Uhlenbeck-Parameter (OU-Parameter), sowie die spektrale Leistungsdichte genutzt, um die Variabilität dieser Quellen zu untersuchen. Dies wird auch auf die γ-Lichtkurven von 20 der 28 Radioquellen angewandt.

Ergebnisse. Die Entwicklung des Jetdurchmessers entlang der Jetachse legt nahe, dass FSRQs, weiter außen im Jet, flachere Gradienten zeigen als BL Lacs. Eine einfache Potenzgesetzanpassung dieser Gradienten zeigt, dass FSRQs systematisch schlechter durch ein solches Potenzgesetz beschrieben werden als BL Lacs, sowohl in der Durchmesserentwicklung entlang der Jetachse, als auch in der Helligkeitstemperaturentwicklung. In neun der 28 Quellen, $0219+421$, $0336-019$, $0415+379$, $0528+134$, $0836+710$, $1101+384$, $1156+295$, $1253-055$ und $2200+420$, ist es möglich einen systematischen Geometrieübergang im Jet zu finden. In jedem dieser Fälle ist die Position des Geometrieübergangs entlang der Jetachse außerhalb der Bondisphäre. BL Lac-Objekte zeigen systematisch größere Magnetfeldstärken in den Radiokernen als FSRQs. Skaliert man diese in die Ergosphäre des SMBHs, kann man zeigen, dass die Radiokerne der BL Lacs näher an den schwarzen Löchern liegen als die Radiokerne der FSRQs. Die Variabilitätsanalyse der γ-Lichtkurven zeigt, dass FSRQs systematisch steilere spektrale Leistungsdichten aufweisen als BL Lacs und sich auch in den OU-Parametern von BL Lacs unterscheiden. Des Weiteren gibt es eine messbare Antikorrelation zwischen der Steigung der spektralen Leistungsdichten und der OU Parameter der γ-Lichtkurven und der Komplexität der Radiojets.

Schlussfolgerung. Flachere Jetdurchmessergradienten weisen darauf hin, dass FSRQs, weiter außen im Jet kollimierter sind als BL Lacs. Die Tatsache, dass FSRQs durch einfache Potenzgesetze in der Anpassung der Helligkeitstemperatur und der Jetgeometrie systematisch schlechter beschrieben sind als BL Lacs, zeigt, dass FSRQs komplexere Jetstrukturen aufweisen. Dies gilt sowohl für die Jetgeometrie, welche in einigen Quellen auch Regionen der Rekollimation aufweisen, als auch für die Oberflächenhelligkeitsverteilungen, die in FSRQs oft ausgeprägte Knoten aufweisen. In Quellen, in welchen ein Geometrieübergang festgestellt werden kann, ist es aufgrund der Position der Geometrieübergänge entlang der Jetachse, die systematisch außerhalb der Bondisphäre zu sehen sind, unwahrscheinlich, dass diese Übergänge allein durch sich ändernde äußere Druckgradienten erklärt werden können. Sich ändernde Druckgradienten können in manchen Quellen eine systematische Erhellung einer Region außerhalb der Bondisphäre und des Geoemtrieübergangs, einhergehend mit einer Rekollimation des Durchmessers, erklären. Die unterschiedlichen Abstände der Radiokerne von BL Lacs und FSRQs können vermutlich durch eine Kombination aus verschiedenen SMBH-Massen und Jetleistungen erklärt werden. Die Variabilität in den γ-Lichtkurven bei

Energien von mehr als 100 MeV und über 1 GeV legt nahe, dass BL Lac-Objekte mehr weißes Rauschen aufweisen als FSRQs, während die Steigung der spektralen Leistungsdichte und die OU-Parameter zeigen, dass FSRQs systematisch mehr Variabilität auf längeren Zeitskalen respektive des Zeitbinnings aufweisen als BL Lacs. Eine Antikorrelation zwischen den Steigungen der spektralen Leistungsdichten und der OU-Parameter aus den γ-Lichtkurven mit den Komplexitäten der Radiojets ist messbar. Diese Antikorrelation zeigt, dass komplexere Jets eher variablere γ-Lichtkurven aufweisen. Daraus lässt sich aber nicht die Region der γ-Strahlung im Radiojet ableiten. Es ist nicht klar, ob diese Korrelation auf Kausalität beruht. Wenn diese Korrelation auf kausalen Zusammenhängen beruht, ist nicht klar, ob ein komplexer Jet stärkere γ-Variabilität bedingt oder ob starke γ-Variabilität komplexere Jets bedingen. Aus den verwendeten Korrelationstests geht jedoch hervor, dass die Art der Korrelation nicht auf einen einfachen linearen Zusammenhang zurückzuführen ist, was darauf hindeutet, dass beide Aspekte sich vermutlich gegenseitig bedingen.

Abstract

Context. In active galaxies, matter is accreted onto super massive black holes (SMBH). This accretion process causes a region roughly the size of our solar system to outshine the entire host galaxy, forming an active galactic nucleus (AGN). In some of these active galaxies, highly relativistic particle jets are formed parallel to the rotation axis of the super massive black hole. A fraction of these sources is observed under a small inclination angle between the pointing direction of the jet and the observing line of sight. These sources are called blazars. Due to the small inclination angle and the highly relativistic speeds of the particles in the jet, beaming effects occur in the radiation of these particles. Blazars can be subdivided into the high luminosity flat spectrum radio quasars (FSRQs) and the low luminosity BL Lacertae objects (BL Lacs). As all AGN, blazars are broadband emitters and therefore observable from the longest wavelengths in the radio regime to the shortest wavelengths in the γ-ray regime. In this thesis I will analyze blazars at these two extremes with respect to their parsec-scale properties in the radio and their time evolution properties in γ-ray flux.

Method. In the radio regime the technique of very long baseline interferometry (VLBI) can be used in order to spatially resolve the synchrotron radiation coming from those objects down to sub-parsec scales. This information can be used to observe the time evolution of the structure of such sources. This is done in large monitoring programs such as the MOJAVE (15 GHz) and the Boston University blazar monitoring program (43 GHz). In this thesis I utilize data of 28 sources from these monitoring programs spanning 10 years of observation from 2003 to 2013, resulting in over 1800 observed epochs, to study the brightness temperature and diameter gradients of these jets. I conduct a search for systematic geometry transitions in the radio jets. The synchrotron cooling time in the radio core of the jets is used to determine the magnetic field strength in the radio core. Considering the jet geometry, these magnetic field strengths are scaled to the ergosphere of the SMBH in order to obtain the distance of the radio core to the SMBH. In the γ-regime these blazars cannot be spatially resolved. Due to this, it is hard to put strong constrains onto where the γ-ray emitting region is. Blazars have shown to be variable at high energies on time scales down to minutes. The nature of this variability can be studied in order to put constrains on the particle acceleration mechanism and possibly the region and size of the γ-ray emitting region. The variability of blazars in the energy range $0.1 \leq E/\mathrm{GeV} \leq 1$ can for example be observed with the pair-conversion telescope on board the *Fermi* satellite. I use 10 years of data from the *Fermi*-LAT (LAT: Large Area Telescope) satellite in order to study the variability of a large sample of blazars (300-800, depending on the used significance filters for data points). I quantify this variability with the Ornstein-Uhlenbeck (OU) parameters and the power spectral density (PSD) slopes. The same procedure is applied to 20 light

curves available for the radio sample.

Results. The diameter evolution along the jet axis of the radio sources suggests, that FSRQs feature flatter gradients than BL Lacs. Fitting these gradients, it is revealed that BL Lacs are systematically better described by a simple single power law than FSRQs. I found 9 sources with a strongly constrained geometry transition. The sources are $0219+421$, $0336-019$, $0415+379$, $0528+134$, $0836+710$, $1101+384$, $1156+295$, $1253-055$ and $2200+420$. In all of these sources, the geometry transition regions are further out in the jet than the Bondi sphere. The magnetic field strengths of BL Lacs is systematically larger than that of FSRQs. However the scaling of these fields suggest that the radio cores of BL Lac objects are closer to the SMBHs than the radio cores of FSRQs. Analyzing the variability of *Fermi*-LAT light curves yields consistent results for all samples. FSRQs show systematically steeper PSD slopes and feature OU parameters more favorable to strong variability than BL Lacs. The *Fermi*-LAT light curves of the sub-sample of radio jets, suggest an anticorrelation between the jet complexity from the radio observations and the OU-parameters as well as the PSD slopes from the γ-ray observations.

Conclusion. The flatter diameter gradients of FSRQs suggest that these sources are more collimated further down the jet than BL Lacs. The systematically better description of the diameter and brightness temperature gradient by a single power law of BL Lacs, suggest that FSRQs are more complex with respect to the diameter evolution along the jet and the surface brightness distribution than BL Lac objects. FSRQs often feature regions where recollimation can occur in distinct knots within the jets. For the sources where a geometry transition could be constrained, the Bondi radius, being systematically smaller than the position of the transition region along the jet axis, suggest that changing pressure gradients are not the sole cause for these systematic geometry transitions. Nevertheless they may be responsible for recollimation regions, found typically downstream the jet, beyond the Bondi radius and the transition zone. The difference in the distance of the radio cores between FSRQs and BL Lacs is most likely due to the combination of differences in SMBH masses and systematically smaller jet powers in BL Lacs. The variability in energy ranges above 100 MeV and above 1 GeV-regime suggest that many light curves of BL Lac objects are more likely to be white noise while the PSD slopes and the OU parameters of FSRQ γ-ray light curves favor stronger variability on larger time scales with respect to the time binning of the analyzed light curve. Although the anticorrelation of the jet complexity acquired from the radio observations and the PSD slopes and OU parameters from the γ-observations suggest that more complex sources favor OU parameters and PSD slopes resulting in more variability (not white noise) it is beyond the scope of this thesis to pinpoint whether this correlation results from causation. The question whether a complex jet causes more γ-ray variability or

more γ-ray variability causes more complex jets cannot be answered at this point. Nevertheless the computed correlation measures suggest that this dependence is most likely not linear and therefore an indication that these effects might even interact.

Chapter 1

Active galactic nuclei

> It means, you're a baboon and I'm not
>
> Rafiki

Active galactic nuclei (AGN) are broad band emitters (e.g. Arbet-Engels et al. 2021; MAGIC Collaboration et al. 2020; Potter & Cotter 2015), which are also likely to emit neutrinos (e.g. Mannheim et al. 2000; Kadler et al. 2016; IceCube Collaboration et al. 2018a,b; Keivani et al. 2018; Ansoldi et al. 2018). Typical observed luminosities range between $42 \leq \log\left(L/\frac{\mathrm{erg}}{s}\right) \leq 47$ while the masses of super massive black holes (SMBH) in the center of these galaxies, associated with the AGN range between $7 \leq \log(M/M_{\odot}) \leq 10$ (Peterson et al. 2004a; Vestergaard & Peterson 2006). Such luminosities can be reached by accretion onto the SMBH (Shakura & Sunyaev 1973). On the high energy (GeV/TeV) end of the electromagnetic (EM) spectrum, these sources show variability in their observed flux which can be measured and characterized from monthly time scales (Peñil et al. 2020; Burd et al. 2021), down to hours (Meyer et al. 2019; Gokus et al. 2021), and even minutes (Shukla et al. 2018; Shukla & Mannheim 2020). On the lower end of the EM spectrum, the radio regime (cm/mm-wavelengths), the technique of radio interferometry can for example be used to spatially resolve those sources to acquire information on their morphology, luminosity and radio spectrum on kpc-scales (Cooper et al. 2007; Kharb et al. 2010; Kappes et al. 2019), down to pc to sub-pc-scales (e.g. Lister et al. 2009; Jorstad et al. 2017; Müller et al. 2018; Angioni et al. 2019). There is a whole zoo of source classes with different spectral, morphological and luminosity properties, which are condensed into the class of AGN (e.g. Antonucci 1993; Urry & Padovani 1995; Antonucci 2013, 2015). One broad distinction between the AGN sub-classes is the so-called radio loudness, introduced by Kellermann et al. (1969).

The radio loudness categorizes sources according to the ratio of the radio and optical flux density ($R_{R,O} = F_R/F_O$). In this work, the main focus lies on the examination of the jet geometry and brightness temperature, as well as the γ-ray variability of radio loud ($R_{R,O} > 10$) AGN. Radio loud AGN are known to feature jets which are highly relativistic outflows that emit synchrotron radiation (Antonucci 1993, 2015). In recent years, also radio quiet AGN have been found to feature jets, albeit the main emission component here is not synchrotron radiation but molecular radiation. These radio-quiet jets are thought to play a role in AGN feedback to the host galaxy (Aalto et al. 2016, 2020). The focus for this thesis will be on radio-loud, synchrotron-jetted AGN, especially the sub-group of blazars. Following sections build the foundation which is necessary to understand the concepts, discussed in this work.

1.1 AGN unification scheme

The unification scheme of AGN (Antonucci 1993; Urry & Padovani 1995; Antonucci 2013) aims to explain observed properties of the different AGN types under one class of objects. According to this unification scheme of AGN, all AGN have three common features, I) a SMBH in the center of the host galaxy onto which the matter is accreted, forming an II) accretion disk and III) a dust torus structure. Although known to be non-continuous (clumpy) with respect to the mass density (Krolik & Begelman 1988), early models approximated to the dust torus to be of continuous mass density (Pier & Krolik 1992, 1993). In more recent years simulations were done using a clumpy cloud structure Hönig et al. (2010); Hönig & Kishimoto (2010); Esparza-Arredondo et al. (2021). In case of radio loud AGN, the radio jets are a fourth feature of the structure. To further elaborate how AGN are divided into sub-classes, it is worth to take a look at some scales. When discussing accretion onto a SMBH the immediate question that arises is, how close can matter ($m > 0$) or photons ($m = 0$) come to a SMBH before falling onto it. This depends on whether the SMBH has a spin $a_* = a/M,\ 0 \leq a \leq M$ (Kerr 1963; Misner et al. 1973). For a more in depth treatment I refer to Abramowicz & Fragile (2013). According to Abramowicz & Fragile (2013) different characteristic radii in a black hole/accretion disk system can be parametrized in terms of the gravitational radius $r_g = M$[1], the radius of the photon sphere

$$r_{ph} = 2r_g \left[1 + \cos\left(\frac{2}{3}\arccos(a_*)\right)\right] \ , \tag{1.1a}$$

the radius of the horizon

$$r_h = r_g \left(1 + \sqrt{1 - a_*^2}\right) \ , \tag{1.1b}$$

[1] natural units: $c = G = 1$

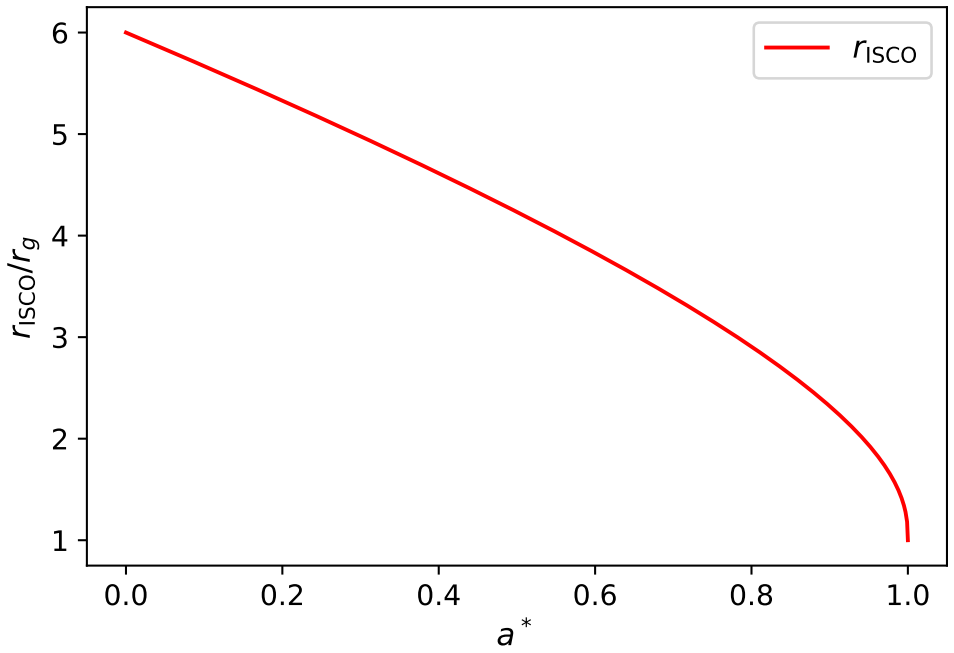

FIGURE 1.1: The radius of the ISCO is plotted versus a_*. In the case of a Schwarzschild black hole, where $a_* = 0$, $r_{\mathrm{ISCO}} = 6r_g$. The more energy of the black hole is stored within the rotation of the black hole ($a_* \to 1$), the smaller r_{ISCO} can be with respect to the gravitational radius.

and the radius of the innermost stable (circular) orbit (ISCO)

$$r_{\mathrm{ISCO}} = r_g \left[3 + Z_2 - \sqrt{(3 - Z_1)(3 + Z_1 + 2Z_2)}\right] , \tag{1.1c}$$

where $Z_1 = 1 + (1 - a_*^2)^{1/3}\left[(1 + a_*)^{1/3} + (1 - a_*)^{1/3}\right]$ and $Z_2 = \sqrt{3a_*^2 + Z_1^2}$. Figure 1.1 shows the radius of the ISCO depending on the spin of the black hole. For a Schwarzschild (1916) black hole, $r_{\mathrm{ISCO}} = 6r_g$. The more energy of the black hole is stored within the spin of the black hole ($a_* \to 1$), the closer r_{ISCO} will approach the gravitational radius r_g. This means that the more a SMBH in an AGN spins, the closer the accretion disk can come to the SMBH without falling onto it. Considering an AGN with a SMBH of mass $M(= r_g)$, the accretion disk would form at distances between $r_g < d \leq 30r_g$, the dust torus forms on scales of $\sim 10^4 r_g$, spanning up to $(10^5 - 10^7)r_g$ (Holt et al. 1992; Urry & Padovani 1995). The accretion disk shows extreme tangential (to the circular motion) velocities that are responsible for broad observable emission lines which show full widths at half maxima (FWHM) on the order of $(10^3 - 10^4)\frac{\mathrm{km}}{s}$ (Wandel et al. 1999; Peterson et al. 2004b). It is possible that the dusty torus obscures the inner part of an AGN, effectively blocking the broad emission lines from the accretion disk. Typical observed emission lines in this case are much more narrow, in the order of $\sim 10^2 \frac{\mathrm{km}}{s}$ (Bennert et al. 2006). From an optical astronomer's point of view, AGN

can be subdivided into two classes, type 1 sources, where broad and narrow emission lines are visible in the spectrum and type 2 sources where only narrow lines are visible. Another way to categorize AGN is whether they show a low or a high luminosity which is linked to the accretion rate of the SMBH ($L \sim \dot{M}$) (Cooper et al. 2007; Ghisellini & Tavecchio 2008; Kharb et al. 2010).
All in all the following parameters/features are used when classifying AGN:

- Radio loudness
- Luminosity
- Inclination angle to the line of sight θ ($\theta = 0° \rightarrow$ pole on view onto the SMBH, $\theta = 90° \rightarrow$ edge on view onto the SMBH)

The sub-class of radio-quiet AGN consists of Seyfert galaxies (low luminosity) and QSOs (quasi stellar objects, high luminosity). These sources both have sub-classes, Seyfert 1/2, QSO 1/2, depending on whether broad and narrow or only narrow emission lines can be seen which is explained by the angle to the line of sight θ. If θ is small, the dust torus does not block the broad emission line from the accretion disk, if θ is large the torus blocks the broad emission lines and only narrow lines are visible.
The sub-class of radio-loud AGN consists of Blazars (small inclination angle) and Radio galaxies (RGs) (large inclination angle). Blazars can be subdivided into two classes, the high luminosity flat-spectrum radio quasars (FSRQs) and the low luminosity BL Lacertae objects (BL Lacs). FSRQs feature broad and narrow emission lines while BL Lacs typically feature no emission lines due to the jet continuum outshining the line emission region. In the case of the radio galaxies, sources can be subdivided into the classes of broad line radio galaxies (BLRG) and narrow line radio galaxies (NLRG). Both BLRGs and NLRGs have a high and low luminosity version. These low (FR1) and high luminosity (FR2) Radio galaxies have first been classified by Fanaroff & Riley (1974)[2], each class showing a distinct radio morphology on large (kpc) scales. Table 1.1 summarizes the unification scheme for AGN with the above discussed parameters.

1.2 Blazars

Blazars represent AGN featuring relativistic plasma jets observed under inclination angles θ of a few degrees to the line of sight. The radiation pattern of isotropic emission in the frame comoving with the relativistic jet is boosted mainly into a cone of opening angle $\sim 1/\Gamma$ (Rybicki & Lightman 1979, chapter 4.1) where Γ denotes the

[2] hence FR1/2

TABLE 1.1: Summary of the unification model; Credit: Matthias Kadler, edited by Paul Ray Burd

Type	Radio Loudness	Emission Lines	Luminosity	Jet	Radio Morphology
Seyfert 1	quiet	broad+narrow	low	none	none
Seyfert 2	quiet	narrow	low	none	none
QSO	quiet	broad+narrow	high	none	none
QSO	quiet	narrow	high	none	none
BLRG	loud	broad+narrow	low	yes	FR1
BLRG	loud	broad+narrow	high	yes	FR2
NLRG	loud	narrow	low	yes	FR1
NLRG	loud	narrow	high	yes	FR2
BL Lac	loud	none	low	yes	compact or rotated FR1
FSQR	loud	broad+narrow	high	yes	compact or rotated FR2

bulk Lorentz factor of the jet plasma. The flux is amplified by a factor $\delta^{3+\alpha}$ where $\delta = [\Gamma(1 - \beta\cos\theta)]^{-1} \sim \Gamma$ is the relativistic Doppler factor for citical observation angles $\theta \sim 1/\Gamma$ to the jet axis and α denotes the spectral index of the power-law spectrum characteristic for the non-thermal emission from blazars (Blandford & Königl 1979). Also anisotropic radiation in the comoving frame of the jet could be possible. In this case there would be no frame where the radiation is isotrope. For blazar jets, typical values are $\delta =\sim 10$ (Cohen et al. 2007; Hovatta et al. 2009) implying large variations of the apparent flux for small variations of the angle θ. The spectral energy distribution (SED) of blazars (across the EM spectrum) features a so-called double-hump structure (Ghisellini et al. 1998; Albert et al. 2007b; Ghisellini & Tavecchio 2008; Abdo et al. 2011). Figure 1.2 shows such a double-hump structure of the SED of the blazars Mrk 421. The multi-wavelength SEDs of blazars can be explained with synchrotron emission (low-energy hump) and synchrotron-self-Compton emission, external Compton or lepto-hadronic electromagnetic cascade emission models (e.g. Finke 2016), for the high energy hump, which depend on physical parameters characterizing the plasma density, magnetic field strength and size of the emission region. In many cases, a single emission zone is sufficient to adequately describe the SED (e.g. Albert et al. 2007a; Aleksić et al. 2011), in some cases two-emission zones are required (MAGIC Collaboration et al. 2018, 2020). Based on the observation of large optical polarization swings associated with γ-ray flares, this emission component seems to be associated with stationary components in the jet, such as the unresolved radio core or a recollimation shock in the radio jet (e.g. Nishikawa et al. 2020; MAGIC Collaboration et al. 2018; Casadio et al. 2019). In the past there have been efforts to map the peak luminosity of the synchrotron hump in the SEDs according to the position, where high luminosity sources have their synchrotron peaks at lower frequencies (Fossati et al. 1998; Ghisellini et al. 1998), which is known

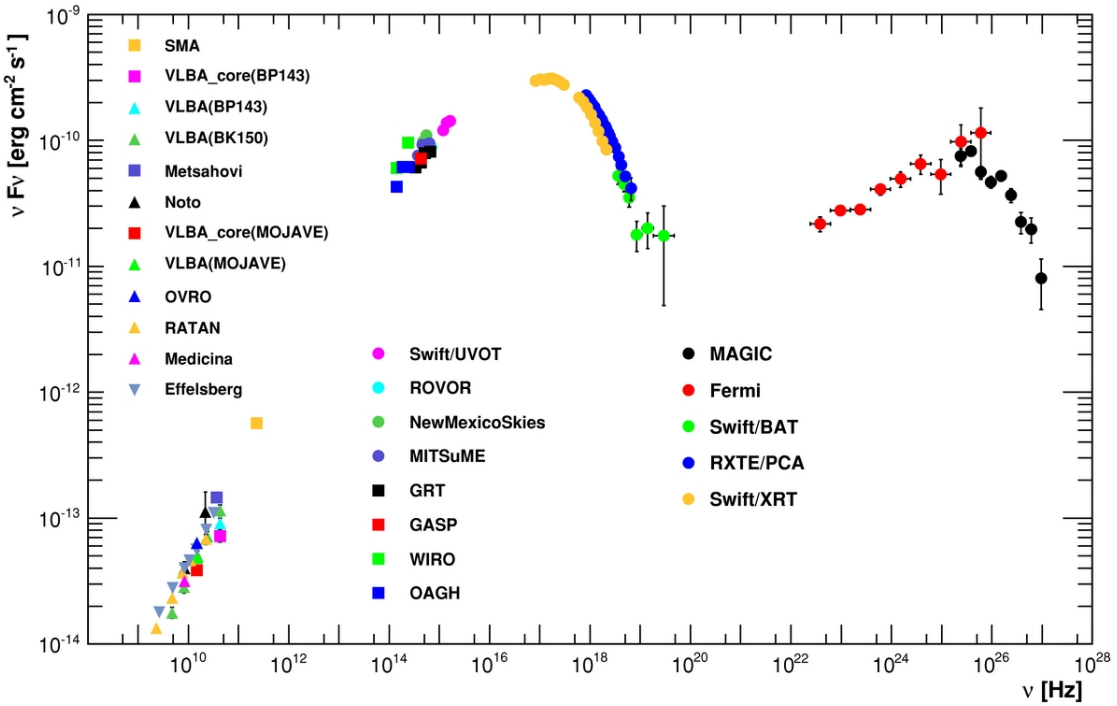

FIGURE 1.2: The spectral energy distribution of Mrk 421, measured across the EM spectrum. The low energy peak is typically explained by synchrotron radiation, while the high energy peak in this particular case is well described by two-zone leptonic model (model not shown in plot). Plot taken from: Abdo et al. (2011).

as the blazar sequence. The consequence of the blazar sequence would be that different types of blazars (with higher and lower synchrotron peak position) would have distinct SED properties, only determined by the jet power. In recent years however this has been refined, as more and more sources were found with high peak-luminosity at larger synchrotron peaks (Meyer et al. 2011). A very recent study by Keenan et al. (2021) shows, that it is not possible to categorize blazars with a single parameter. In particular they found that there are sources with a high synchrotron peak position and a high luminosity, namely BL Lac objects with a low accretion rate, which the blazar sequence would rule out. From the perspective of a radio astronomer (analyzing images of the objects), Blazars can be sub-devided into two categories. The high luminosity FSRQs and the low-luminosity BL Lacs. Applying the unification scheme of AGN, on large scales, FSRQs should resemble the rotated counter part of FR2 radio galaxies. FR2 radio galaxies typically show a bright radio core and strongly collimated jets terminating in so-called radio-lobes usually featuring hot spots. On the other hand, FR1 radio galaxies also show a bright core and less collimated jets, terminating in so called plumes. Figure 1.3 features blazars observed with the Giant Metre Wave Radio Telescope (GMRT), observed at 610 MHz. On the left hand side, the BL Lac object $1807+698$ is shown. The morphology resemples a rotated FR1 radio galaxy, with the bright core, the jet extending into the western direction and the diffuse emission from the radio plumes.

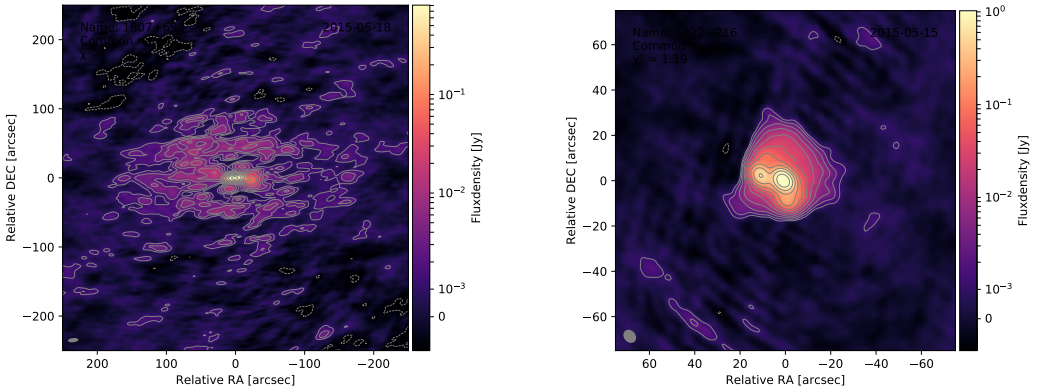

FIGURE 1.3: Images from GMRT observations at 610 MHz from the BL Lac object $1807+698$ (left) and the FSRQ $1222+216$ (right). The BL Lac object resembles the morphology of a rotated FR1 radio galaxy and the FSRQ resembles the morphology of a rotated FR2 radio galaxy.

The FSRQs $1222+216$ (on the right hand side) resembles the morphology of a rotated FR2 radio galaxy. Besides the radio core in the image's center, a bright component, a hot spot in the eastern direction can be seen. The resolution does not allow to resolve the jet, however, the sensitivity of the telescope is sufficient to detect the radio lobe surrounding the hot spot and the radio core. The morphology of blazars on kpc-scales has systematically been studied by Cooper et al. (2007) and Kharb et al. (2010). They found that there are BL Lac objects that also resemble FR2 radio galaxies and that the power of the extended emission can in principal be used to classify FSRQs and BL Lacs. However the difference between these source classes is not clear and discrete but rather continuous, indicating sources of a mixed form between FSRQs and BL Lacs. The possible dichotomy of these source classes will be one of the core aspects of this work, with a focus on the pc scales.

1.3 Blazar variability in the GeV and TeV regime

As briefly mentioned above, the high-energy variability of blazars can be studied on various time scales (Ulrich et al. 1997; Peñil et al. 2020; Burd et al. 2021; Meyer et al. 2019; Shukla et al. 2018; Shukla & Mannheim 2020). Different processes can be found in different sources to provide a reasonable understanding of the observed SEDs (Albert et al. 2007a; Aleksić et al. 2011; MAGIC Collaboration et al. 2018, 2020; Arbet-Engels et al. 2021). Physical models of blazars indicate that their variability could be associated with the dynamical evolution of the jet (e.g. Finke 2016; Albert et al. 2007a; Aleksić et al. 2011). One option is that shocks in the jet are responsible for the variability at γ-rays by accelerating particles to relativistic energies (e.g. Nishikawa et al. 2020; MAGIC Collaboration et al. 2018; Casadio et al. 2019) in which case the flux variations

might track fluctuations of the jet velocity or the mass loading. Another option to explain the variability of blazars is the magnetic reconnection resulting in plasmoids (plasma blobs of a certain polarization) (Giannios et al. 2009; Petropoulou et al. 2019; Christie et al. 2019). These plasmoids travel through the jet (see e.g. the 'jet in jet model of' Giannios et al. 2009), some of them are of opposite polarity. When these plasmoids interact, magnetic reconnection can occur, accelerating particles to energies causing them to create high energy radiation. This loss of energy through reconnection is probably caused by current-driven instabilities, like kink-instabilities (Eichler 1993). However Giannios et al. (2009) argue that also a change in the polarization sorrounding the SMBH could lead to magnetic reconnection within the jet. Analyzing the light curves (flux variation in time) of blazars in the GeV and TeV regime, in some cases it was possible to constrain a physical mechanism, driving the variability of a blazar. In the case of 3C 279 Shukla & Mannheim (2020) showed that the variability on minute time-scales is driven by reconnection events. In the case of IC 310 another exotic mechanism explains short term variability by so called 'black hole lightning' by particle acceleration due to electric fields in the vacuum gaps, randomly occuring in the magnetosphere of SMBHs (Aleksić et al. 2014). The cases where it is possible to constrain the physical process without a certain degree of ambiguity, that allows multiple explanations or even a combination of those, have either a very well constrained SED or, due to the high flux density of the emission of the source, it is possible to acquire light curves that resolve the flux variability on very small time scales (minutes/hours). As Scargle (2020) points out, inferring physical information of a 3+1 dimensional object just from a time series of flux densities, which is a one dimensional curve is inherently difficult. Often characteristics of a light curve, such as the flux-density distribution is analyzed, where a histogram for the flux-density values in the light curve is created. The question that is typically asked is, whether the distribution is best described with a Gaussian (normal) or a log-normal distribution (Uttley et al. 2005; Chakraborty & Cologna 2015; Deka et al. 2021). In the case of a log-normal distribution it is often posed that log-normalcy is a signature for multiplicative processes which goes back to a theoretical work of variability in accretion disks from Lyubarskii (1997). While this inference might hold in single cases, it is generally not correct, since additive processes are also able to produce light-curves, where the flux-density distribution is best described by a log-normal function, see (Scargle 2020). A multiplicative/additive process is a process, where the total flux density is composed of the multiplication/summation of the fluxes from different sub-processes. Scargle (2020) points out that several other relations like the rms[3]-flux relation, linearity or stationarity, can generically be realized by random processes. This immediately causes the question how meaningful said characterizations of light curves and their physical interpretation in certain cases truly are.

[3] root-mean square

1.3.1 The stochastic nature of high-energy blazar variability

The power spectral density (PSD), also called periodogram is often used to analyze the frequency spectrum of time series (light curves) $X(t)$. It is calculated by the squared, absolute value (modulus) of the Fourier transform of $X(t)$ (Timmer & König 1995):

$$\mathrm{Per}(X(\omega)) = |\mathrm{FT}\,(X(t), \omega)\,|^2 \ . \tag{1.2a}$$

If the signal is composed of a periodic, single frequency signal without noise the PSD will show a curve with one prominent peak, as seen in Fig. 1.4 (top). If a periodic signal without noise is composed of a superposition of several signals of different frequencies, the PSD can be used to obtain these frequencies, see Fig. 1.4 (mid). In the case of random time series $x(t)$, the PSD becomes a power law of the form $\mathrm{PSD}[x(t)] \propto f^{\xi}$ (Timmer & König 1995). The slope of the PSD, the ξ-value, is determined by the nature of the variability within the time series $x(t)$. The larger the time-scale on which the variation occurs with respect to the time-sampling, the steeper (more negative) the PSD-slope becomes as shown in Fig. 1.4 (bottom). Different cases of ξ are traditionally referred to with different names. In the case of $\xi = 0$, the time series, is called white noise. In a white noise time series, the values of different time steps are completely un-correlated and independent from each other. In the cases, where $\xi < 0$, the noise becomes correlated. In every time step a certain memory from previous time steps is present, meaning that the value at a given time step is dependent on previous ones[4]. The case of $\xi = -1$ is called pink (flicker) noise, whereas the case of $\xi = -2$ is called red (shot) noise. Abdo et al. (2010b) studied the variation of *Fermi*-LAT blazars (GeV-regime) with periodograms and found that the ξ-value distribution ranges from pink to red noise, explicitly mentioning the stochastic nature of *Fermi*-LAT light curves. Sobolewska et al. (2014) showed on a sample of 13 blazars, that it is possible to fit *Fermi*-LAT light curves with Ornstein-Uhlenbeck (OU) processes (Uhlenbeck & Ornstein 1930), using each a single OU-process or a linear-combination of several OU processes. Also in the optical regime the OU-process and alterations have been deployed to study and describe AGN light curves (Kelly et al. 2009, 2011; Kelly et al. 2014; Takata et al. 2018). On a larger sample (236 blazars), in Burd et al. (2021) we have shown that it is possible to describe a plethora of different monthly-binned *Fermi*-LAT light curves with simple OU-processes. It was shown that it is possible to extract the parameters, defining the OU process from a given light curve. With this set of parameters it is possible to simulate light curves, that are un-distinguishable from the astrophysical ones with respect to the ξ distribution and the temporal behavior of the flux variation. This will be discussed in more detail in the following.

[4] the number of time step conserving the memory depends on the order of the process

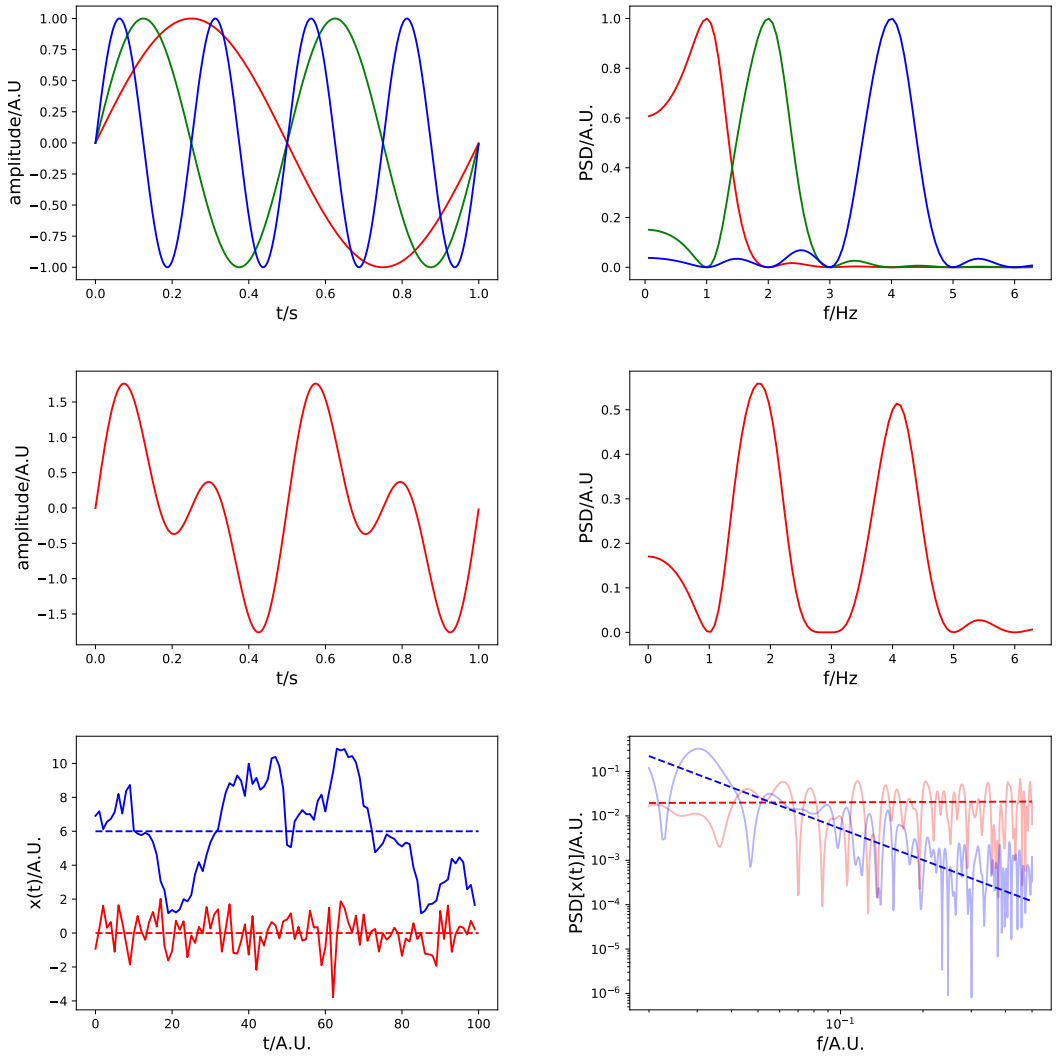

FIGURE 1.4: *Top:* Sine waves (left) of frequencies $(1, 2, 4)$ Hz (red, green, blue) yield PSDs, showing prominent peaks at given frequencies (right). *Mid:* A function (red line), composed of sine-waves can be analyzed with the PSD to find the composing frequencies, with prominent peaks at 2 Hz and 4 Hz. *Bottom, left:* Random time series showing variations on long time scales with respect to the time sampling (blue line) around $x(t) = 6$ and a random time series showing variations on small time scales with respect to the time sampling (red line), around $x(t) = 0$. The shift is used for clear illustration. Random time series show PSDs of different power law behavior (PSD $\propto f^{\xi}$). For time series, where the variation occurs on large time scales with respect to the time sampling, the PSD-slope becomes steep (blue), whereas for time series where the variation occurs on shorter time scales, the PSD-slope flattens (here: $\xi \sim 0$).

1.3.2 The Ornstein-Uhlenbeck parameters and their impact on time series

In Burd et al. (2021) my dear co-authors and I have developed a framework, which allows to extract OU-parameters from given light curves. This paper contains an extensive formula apparatus combined with mathematical proofs when needed. In the following I will discuss the most important steps, which should help to understand the basic principles about what an OU-analysis can do in order to understand light curves and their stochastic nature. I will explicitly cite certain formulae with the exact number/name, given in Burd et al. (2021) to pinpoint where to look for a more rigorous mathematical context if desired. This will be done by the phrase ' Eq. X in B21'. In this work the focus will be more on the consequences on parameters, obtained from the light curve and showing some examples to clarify certain aspects, giving an intuitive understanding on this issue. Brownian motion is one of the first well understood stochastic processes. Uhlenbeck & Ornstein (1930) described this motion of particles with velocities $u(t)$ and an average velocity μ in an ambient medium in terms of a stochastic differential equation (SDE), the famously known Ornstein-Uhlenbeck equation (Eq. 1 in B21).

$$\frac{\mathrm{d}u(t)}{\mathrm{d}t} = \theta(\mu - u(t)) + W(t) \tag{1.3a}$$

In the context of Brownian motion, θ is the friction parameter of the ambient medium[5]. Abstracting this from the original meaning in the context of Brownian motion, θ (friction) and μ (mean velocity), the parameter θ can be understood as a mean reversion rate, driving the time evolution of $u(t)$ back to mean reversion level μ. The term $W(t)$ resembles white noise and can be realized in different ways. A time series for a set of θ and μ can be generated by drawing identically and independently distributed (IID) values from the white noise term, which in turn can be understood as causally disconnected realizations of an observable in the time dependent process, describing its physical state. This white noise term (the IID variables) has to satisfy certain conditions, in order to realize the OU process (given in Eqs. 2a-2d ni B21). I) The expectation value of $W(t)$ has to be zero, II) at any given two time steps $W(t)$ has to be uncorrelated, III) W(t) has to be a martingal, which means that the expectation value of a given time step τ, $W(\tau)$, given all prior time-steps, only depends on the time-step τ itself and IV) two samples W_1 and W_2 are statistically independent, which means that the joint probability distribution is exactly the product of the individual probability distributions. Gillespie (1996) showed that this is realized for example by a normal distribution of the form $\mathcal{N}(m = 0, \sigma^2 = 1, t)$. The white noise term can then be re-written in terms of $\mathcal{N}$ as (Eq.

[5] in cases, where the friction is depended of the location in the medium and the direction of the motion, θ has to be described by a tensor, reflecting the dimension of the ambient medium

4 in B21)

$$W(t)\mathrm{d}t = \sigma\mathcal{N}(t)\sqrt{\mathrm{d}t}\ . \tag{1.3b}$$

The discrete OU process can be written in terms of the three OU parameters (μ, σ, θ) and T, which is a positive integer, describing the current time step ($u_T = u(t = \Delta tT)$), in the form of (Eq. 5e in B21)

$$u_{T+1} = u_T + \theta\Delta(\mu - u_T) + \sigma\sqrt{\Delta t}\mathcal{N}_T \tag{1.3c}$$

This discrete OU process can only be a good approximation in the case where the sampling of the data is smaller than the relevant time scales. The Ornstein-Uhlenbeck process describes a stationary process. As Scargle (2020) points out, stationarity is a concept, that heavily depends on the light curve itself, whether it is analyzed over the entire observed time or only sections of a given light curve are analyzed. For a time series to be stationary, certain conditions have to be met. These are discussed and proven to hold in the OU-case in Burd et al. (2021) and will not be discussed in detail here. In this context, the OU process is used to study the flux variations of blazars, where u_{T+1} is the logarithmic flux at a given time step depending only, with respect to all flux values coming before, on the (logarithmic) flux density directly before u_T. The parameters μ, σ and θ can also be interpreted in this context, where μ is a reversion level around which the light curve evolves. There are several ways to define this reversion level. Meyer et al. (2019) suggest a 'quiescent state' that can be defined by excluding the parts of a light curve with high activity. Burd et al. (2021) adopted the expectation value of a given logarithmic light curve. All of those methods in the choice of μ are to a certain degree arbitrary. However once set, they should be used consistently. The σ-parameter influences the maximum amplitude of the random process. In the context of auto-regressive processes (Scargle 1981, 2020), the term $\sigma\sqrt{\Delta t}\mathcal{N}_T$ is referred to as the innovation. Figure 1.5 (left) illustrates the impact of the innovation on the OU time series. Larger σ-parameters yield larger random amplitudes. Figure 1.5 (right) illustrates the impact of the mean reversion rate on a OU time series. Smaller θ-values yield time series that deviate for longer times (with respect to the time sampling) from the mean reversion level μ. The parameters σ and θ influence the shape of the time series/light curve, and therefore the PSD-slope ξ. This will be discussed in Sect. 6.

1.3.3 The location of the γ-ray emitting region

As discussed above, when studying the variability of blazars, the exact nature of the flux variation is not easily assessed as different processes are capable explaining observed time signatures. In certain special cases, where time-scales in the minute regime can

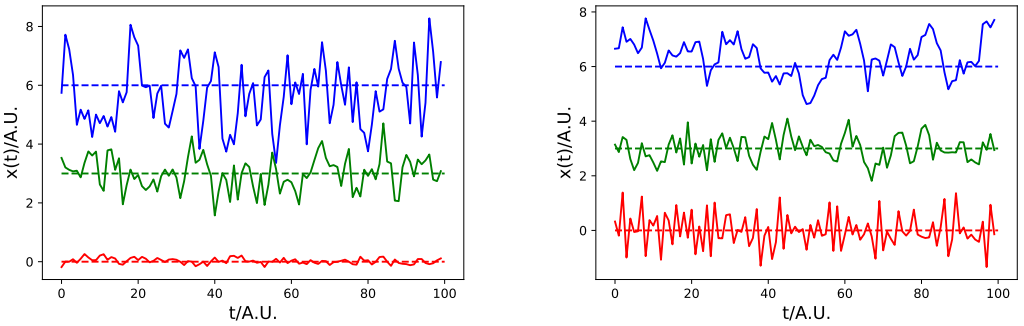

FIGURE 1.5: The different cases of OU time series (red,green,blue) are shown shifted from each other for clearness $(\mu_r.\mu_g, \mu_b) = (0, 3, 6)$. *Left:* The different OU time series (red,green,blue) are generated using $\sigma_r, \sigma_g, \sigma b = (0.1, 0.5, 1)$ and a fixed $\theta_{r,g,b} = 0.5$. The σ parameter impacts the maximum random amplitude of a given time series, where larger σ-values indicate larger random amplitudes. *Right*: The different OU time series are generated using $(\theta_r, \theta_g, \theta_b) = (1.5, 0.7, 0.1)$, while $\sigma_{r,g,b} = 0.5$ is fixed in this case. The larger θ, the more a time series is drawn back to the mean reversion level μ.

be resolved in the light curve due to the large signal to noise ratio (SNR) of the event, it was possible to constrain the mechanism of the variability as well as the location of the emission (e.g. Aleksić et al. 2014; Shukla & Mannheim 2020). The question however when analyzing the γ-ray emission of any blazar is, where in the blazar does the high energy emission come from. The following discussion is based on Finke (2016). In this paper, the question, where the high energy emission may originate from by studying the inverse Compton (IC) scattering with different seed photons, is addressed. The discussion within the paper is extensive and many approximations and numerical methods are discussed. In this context I will focus on the basic idea and reasoning behind possible γ-emitting regions. According to Finke (2016), the emissivity from Compton radiation can be written in terms of the number density of the seed photon field $n_ph(\epsilon, \Omega)$ and the number density of the incoming electrons $n_e(\gamma, \Omega_e)$:

$$\epsilon_s j(\epsilon_s, \Omega_s) = m_e c^3 \epsilon_s^3 \int \mathrm{d}\Omega \int \mathrm{d}\epsilon \; n_{ph}(\epsilon, \Omega) \times \int \mathrm{d}\Omega \int \mathrm{d}\gamma \; n_e(\gamma, \Omega_e) \times (1 - \cos(\Psi)) \frac{\mathrm{d}\sigma}{\mathrm{d}\epsilon_s \mathrm{d}\Omega_s}, \tag{1.4a}$$

where the energy of the seed photons ranges between ϵ and $\epsilon + \mathrm{d}\epsilon$ in a solid angle between Ω and $\Omega + \mathrm{d}\Omega$. The Lorentz factor of the incoming electrons ranges between γ and $\gamma + \mathrm{d}\gamma$ in solid angles between Ω_e and $\Omega_e + \mathrm{d}\Omega_e$. The possible different directions for the incoming electrons and photons are accounted for with the angle Ψ and the differential cross section per scattered photon energy and solid angle is accounted for with the term $\frac{\mathrm{d}\sigma}{\mathrm{d}\epsilon_s \mathrm{d}\Omega_s}$. The energy of the scattered photon is denoted ϵ_s and is given in units of the electron mass $m_e\ c^2$. Depending on where the seed photons come from, and also correcting for synchrotron self absorption Finke (2016) calculates different scenarios: the accretion disk, the broad line region and the dust torus, each with its own photon (energy) density. These photon fields can cause another effect, pair production, where

the produced photons ($E > 2 \times 512$ MeV) can create an electron-positron pair. Taking this into account, the spectrum of high energy radiation is attenuated by the optical depth ($\tau_{\gamma\gamma}$), caused by this kind of photon absorption with a factor of $e^{-\tau_{\gamma\gamma}(\epsilon_1)}$. With these considerations, Finke (2016) shows that photons of $E \sim 20$ GeV (source frame of reference) escape un-absorbed. For higher energies, the escape depends on several factors. Simulating an emission region (blob), moving through a jet, Finke (2016) uses the ratio of Compton-scattered and synchrotron flux density and the duration of excesses (flares) in this quotient to find clues of where the emission originates. For timescales which are longer than about a day, the emission region is well beyond the broad line region. He further shows, that a torus ~ 10 pc from the SMBH would not be able to cool photons fast enough to explain the short time variability, seen in blazars (hour, minutes). Alternatively within the (structured) jet of the blazar, the interaction between possible shear layers[6] and the particle acceleration at the boundary of the layers is also a plausible source for high energy photons (Marscher et al. 2010; Tavecchio & Ghisellini 2008; Ghisellini et al. 2007). As discussed above, reconnetion events within the jet (Giannios et al. 2009; Shukla & Mannheim 2020) and shocks propagating within the jet (Blandford & Königl 1979; Königl 1981) can also explain the high-energy emission of blazars. This shows even when completely neglecting hadronic models it is not trivial to constrain the spatial origin of the gamma radiation. Different energetic electrons undergo inverse Compton scattering with different sources of seed photons, while different seed photon fields cool emitted photons more or less efficiently, which rules out regions from within the broad line region, considering the time-scale of variability in blazars.

1.4 Synchrotron radiation - the curse and blessing of beamed emission

The following explanations are closely related to the much more extensive and thorough discussions, given in Rybicki & Lightman (1979). Here only the most important concepts necessary for this work will be elaborated. The low energy hump of blazar SEDs, as elaborated above, is well understood and can be explained by synchrotron emission. Contrary to thermal emission (Planck spectrum), synchrotron emission naturally explains polarization, found in radio observations (e.g. Hodge et al. 2018; Lister et al. 2018; Pushkarev et al. 2017a). According to Rybicki & Lightman (1979, chapter 6.1), the emitted power of an electron with a random pitch angle distribution is given by

$$P = \frac{4}{3}\,\sigma_T\,c\,\beta_e^2\,\gamma^2\,u_B \tag{1.5a}$$

[6] layers of different Lorentz factors γ

Where c is the speed of light, $u_B = \frac{B^2}{8\pi}$ is the magnetic field density, $\sigma_T = \frac{8\pi e^2}{3m^2c^4}$ is the Thomson cross section, defined by the electron charge e and the electron mass m. β_e is the electron speed and γ the Lorenz factor. When comparing two particles at the same energy with different masses, the radiation of lower-mass particles dominate over the radiation of particles with higher masses, as $\sigma_T \propto m^{-2}$. Due to this, early jet models were purely leptonic (Blandford & Königl 1979; Königl 1981). Higher-mass particles (protons) can be accelerated to much higher energies than electrons in the acceleration zone of the jet. Therefore protons radiate into the X-ray and γ-ray (also neutrinos) regime (Mannheim 1993; Mücke & Protheroe 2001; Mücke et al. 2003). The emitted power of an electron distribution can be constructed by weighting Eq. 1.5a with the electron energy density $n(\gamma)$, which scales with γ with a power law $n(\gamma)\mathrm{d}\gamma = n_0\gamma^{-p}\mathrm{d}\gamma$ as follows:

$$P_\nu = -\frac{\mathrm{d}E}{\mathrm{d}t} = \int_1^\infty P_\nu(\gamma)n(\gamma)\,\mathrm{d}\gamma. \tag{1.5b}$$

Furthermore, assuming that the electrons emit only at a frequency $\omega_c = \frac{eB}{mc}\left(\frac{E}{mc^2}\right)^2 = \gamma^2\nu_L$ (ν_L is the Larmor frequency), a spectral shape of the form $\Phi_n \propto \delta(\omega - \omega_c)$ can be introduced. For highly relativistic electrons ($\beta \to 1$), Eq. 1.5b reads

$$P_\nu = \frac{4}{3}\sigma_\mathrm{T} c u_B n_0 \int_1^\infty \gamma^2\delta(\nu - \gamma^2\nu_L)\gamma^{-p}\mathrm{d}\gamma\,, \tag{1.5c}$$

which simplifies to

$$P_\nu = \frac{2}{3}\frac{1}{\nu_L}\sigma_\mathrm{T} c u_B n_0 \left(\frac{\tilde{\nu}}{\nu_L}\right)^{\frac{1-p}{2}}. \tag{1.5d}$$

The power law behavior of the electron energy density also dictates the behavior of synchrotron radiation spectrum of this bulk of energies, namely falling with a power law $P \propto \nu^{\frac{1-p}{2}}$. This only holds in the case of optically thin (transparent) matter, where it is unlikely for synchrotron emitted photons to be re-absorbed by the electrons which moving in the magnetic fields, giving their energy $h\nu$ back to the electrons again. The optical depth here is

$$\tau_\nu(z) = \int_{z_0}^{z} \alpha_\nu(z')\mathrm{d}z' < 1\,. \tag{1.5e}$$

α_ν is the absorption coefficient and z is the path (of the emitted photon) travelled in the medium. In the case of $\tau > 1$, re-absorption, stimulated emission/negative absorption[7], becomes more and more likely. A detailed description of this requires the interrelation of these processes via the Einstein coefficients. This will not be discussed in detail here but is again discussed in detail in Rybicki & Lightman (1979, chapter 6.8). The bottom line, when accounting for all possible states, an electron can have, while travelling in a magnetic field, in opaque matter, is that in the regime where $\tau > 1$ the power-spectrum follows $P \propto \nu^{5/2}$. In blazars, bulks (blob) of electrons which themselves show highly

[7] particles are induced to emit preferably at an energy where already photons of $h\nu$ are present

relativistic speeds, travel with a small inclination angle towards the direction of the observer. This has some implications on the observed power spectrum of the synchrotron radiation. I) If in the rest frame of the emitting electron blob the radiation pattern (antenna pattern) is isotrope, the radiation pattern (antenna pattern) for the observer has a preferred direction into a cone, directed at the observer with an semi-opening angle ϑ related to the bulk Lorentz Factor Γ as $\vartheta \propto 1/\Gamma$. This is not a special feature of synchrotron radiation but a consequence of the Lorentz transformation (boost) between the bulk's rest frame and the observer's frame (Rybicki & Lightman 1979, chapter 4.1). II) As the electron approaches the observer, the observed radiation frequency is blue-shifted with respect to the intrinsic emission frequency and III) the observed power (luminosity L) of the radiation is augmented as illustrated in Fig. 1.6. Cohen et al. (2007) points out that the beamed (augmented) luminosity L relates to the intrinsic luminosity L_0 via the Doppler factor $\delta = \Gamma^{-1}\ (1 - \beta\cos(\theta))$[8] as

$$L = L_0\delta^n,\ n = \alpha + p\,. \tag{1.5f}$$

α is the spectral index, and the value of p depends on the jet geometry and the optical depth (Lind & Blandford 1985). In sources, where only one synchrotron emitting region is seen, the peak position of the spectrum (see Fig. 1.6) has been shown to be anti-correlated to the size of the source (O'Dea 1998). In sources, dominated by beamed emission, where more than one emission region is present, as typical for blazars, the spectrum of the single emission regions smear out to an overall flat radio spectrum as the power at higher energies get enhanced with a power law, counter acting the falling of the spectrum with a power law of the single emission region in the optically thin part of the spectrum as illustrated in Fig 1.7. Considering the discussed points in this section, why is beamed emission a curse? As indicated by Eq. 1.5f, the measured luminosity of a source is never the intrinsic luminosity as it gets augmented (beamed) by a power of the Doppler factor, which depends on the speed of the emission region. The measured speed of these emission regions, however is also not the intrinsic speed. Due to the high relativistic internal speed and the small inclination angle, the measured speed can reach apparent super-luminal values due to projection, which will be discussed in the following section. This means, that in order to get intrinsic information on observed sources that are influenced by beaming effects, at least the inclination angle has to be known. There are several approaches to determine the inclination angles, that will be discussed later when analyzing the sources of interest in this work. On the other hand, beaming is the reason, that blazars can be observed at large distances in the universe.

[8] β is the intrinsic speed of the radiation blob

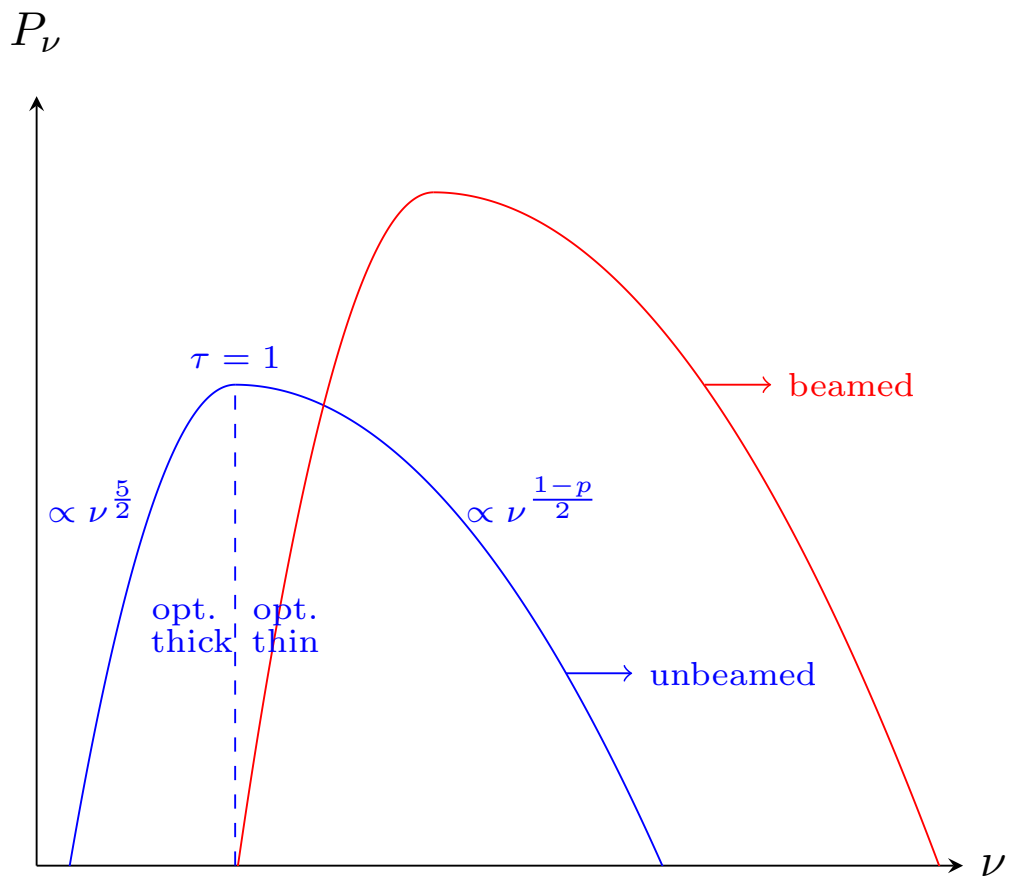

FIGURE 1.6: Synchrotron spectrum of a single emitting region. In the optically thick region ($\tau > 1$), the power of the synchrotron emission of one electron bulk (blob) depends on the frequency as $\propto \nu^{5/2}$. At $\tau = 1$ the spectrum has a maximum. In sources where only one synchrotron emission region was found, an anti-correlation between the peak position of the synchrotron spectrum and the size of the emission region was found (O'Dea 1998). In the optically thin region, the spectrum falls with ν^{α}. If the emitting region is boosted towards an observer, the frequency is blue shifted (blue line shifted to the right with respect to the red line) and the emitted power is augmented. Adapted from Burd (2017)

1.5 Apparent super-luminal motion

As discussed above, when observing the jets of blazars, a common feature is the apparent super-luminal motion of synchrotron emission regions (blobs) (Kellermann et al. 2004, 2007; Lister et al. 2009, 2016, 2019). This of course is not a violation of special relativity (Einstein 1905) but a projection effect when a blob with relativistic speed, observed at a small inclination angle, emits photons into the observer's direction. Following formulae are derived with the quantities shown in Fig. 1.8. The intrinsic travelled distance Δx_{app} of the blob relates to the observed (projected) distance Δx_{app} through the Pythagorean

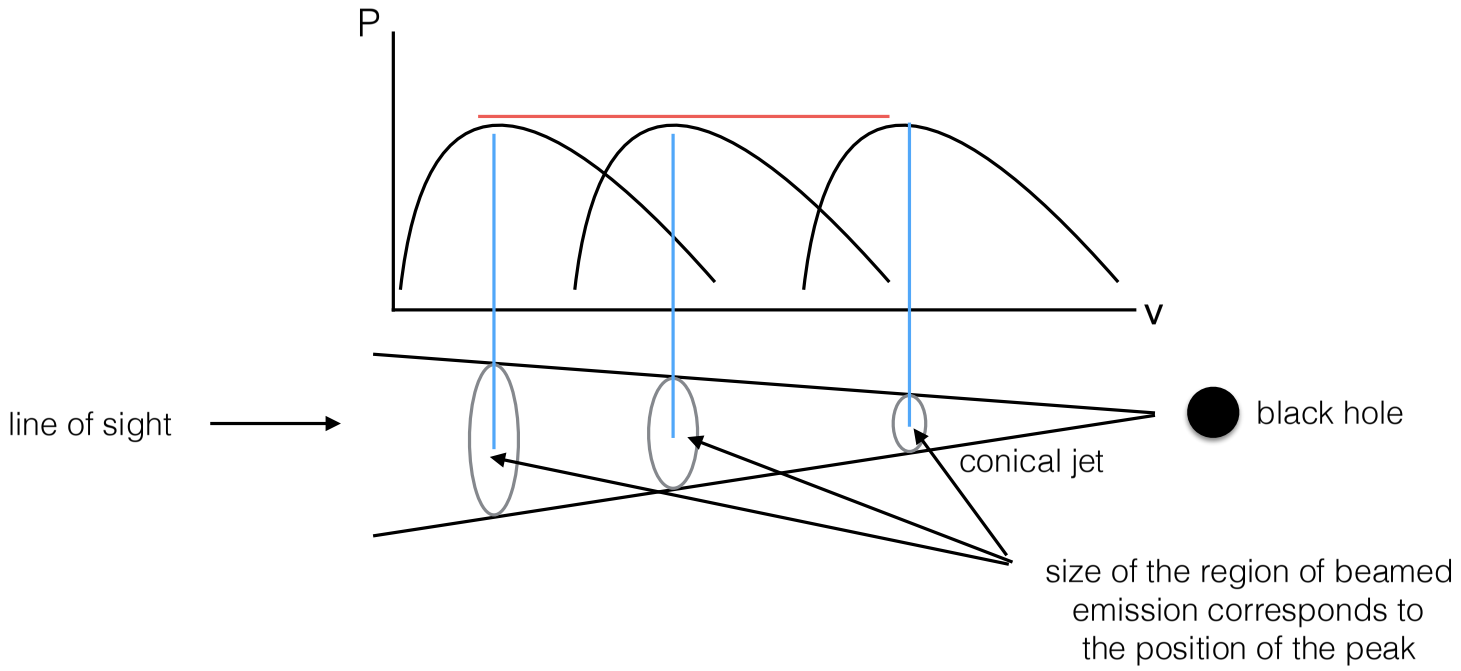

FIGURE 1.7: In sources that are dominated by beamed emission, where not only one synchrotron emission region is observed, typically in blazar jets, the power spectrum smears out to a flat spectrum, as higher energetic powers get enhanced by a power law, cancelling out the falling of the spectrum as a power law in the optically thin region of a single emission region. At higher observing frequencies, the part of the source, where the emission becomes optically thin, comes closer and closer to the physical jet base which is known as core shift (Sokolovsky et al. 2011; Kudryavtseva et al. 2011) which depends on the geometry of the jet (a conical jet is illustrated here). Illustration taken from Burd (2017).

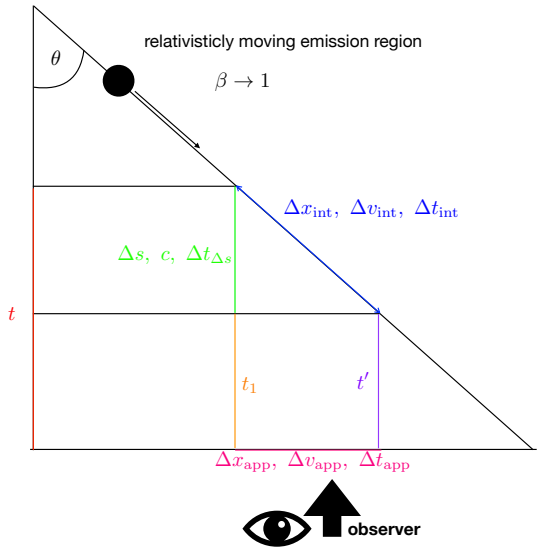

FIGURE 1.8: If a fast moving emitting region ($\beta \to 1$) travels towards an observer with a small inclination angle ϑ, the apparent motion becomes super luminal. Adapted from Burd (2017)

triangle:

$$\Delta x_{\mathrm{app}} = \Delta x_{\mathrm{int}} \sin(\vartheta) \ , \tag{1.6a}$$

and therefore the apparent (measured) speed reads:

$$\beta_{\mathrm{app}} = \frac{\Delta x_{\mathrm{int}} \sin(\vartheta)}{c \Delta t_{\mathrm{app}}} \tag{1.6b}$$

With $t_{\Delta s} = \frac{\Delta s}{c} = \frac{\Delta x_{\mathrm{int}} \cos(\vartheta)}{c} = \beta_{\mathrm{int}}\, t_{\mathrm{int}} \cos(\vartheta)$, the light-travel time between the positions defined by Δx_{int} and the observer is given by

$$\left.\begin{aligned} t &= t_{\Delta s} + t_1 \\ t' &= t_{\mathrm{int}} + t_1 \end{aligned}\right\} \to \Delta t_{\mathrm{app}} = t' - t = t_{\mathrm{int}} - t_{\Delta s} = t_{\mathrm{int}} \left(1 - \beta_{\mathrm{int}} \cos(\vartheta)\right) \tag{1.6c}$$

The expression for the intrinsic time, found in Eq. 1.6c can be used to find an expression for the apparent speed in Eq. 1.6b, dependent on the internal speed and the inclination angle.

$$\beta_{\mathrm{app}} = \frac{\beta_{\mathrm{int}} \sin(\vartheta)}{1 - \beta_{\mathrm{int}} \cos(\vartheta)} \tag{1.6d}$$

Figure 1.9 illustrates the apparent speed according to Eq. 1.6d.

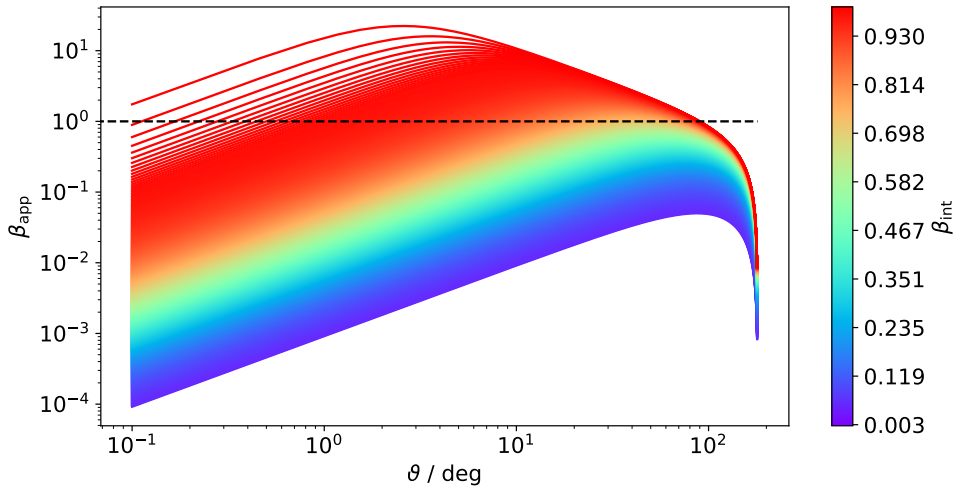

FIGURE 1.9: The apparent speed is plotted vs. the observation angle ϑ, according to Eq. 1.6d. Dependent on the internal velocity (color coded). The dashed line marks the region where $\beta_{app} = 1$. Generally it can be seen, that for small inclination angles and large β_{int} values, an apparent super-luminal motion can be observed.

1.6 The Blandford & Königl (1979) jet model and extensions

In this thesis one core aspect is the study of blazar jets on pc-scales. It is worth taking a look at the radio-jet model of Blandford & Königl (1979). In the following I will list the assumptions of the model and how it can be used in order to build a framework which allows to analyze pc-scale radio jets.

1. The constantly accelerated electron plasma forms a conical jet, where the diameter of the jet d_j scales along the jet axis r as $d_j \propto r^1$. This can be extended by allowing all sorts of jet-geometries by letting $d_j \propto r^l$. If $l = 1$, the Blandford & Königl (1979)-case occurs and the jet becomes conical. This is the case when the jet expands freely and an electron gas, that does not undergo any form of continuous acceleration expands and cools adiabatically. A cylindrical jet is described in the case of $l = 0$, a parabolic jet is described in the case of $l = 0.5$. In these cases the jet plasma likely is accelerated. In the case of $l > 1$ the jet shape becomes hyperbolic and decelerates. The different cases are schematically shown in Fig. 1.10.

2. The magnetic field of a Blandford & Königl (1979) jet scales along the jet axis as $B(r) \propto r^{-1}$. This is the scaling behavior of a torodial magnetic field component in the case of conical jet geometry. This of course can also be generalized, by also allowing polodial magnetic field components, a mix of torodial and polodial components and by also taking the effect of the jet geometry into account. If the

magnetic flux is frozen into the plasma $\dot{\Phi} = \int \vec{B} \mathrm{d}\vec{A} = 0$ (Alfvén 1942), the strength of the torodial magnetic field component scales in a cone along with the growing radius R, $B_{\mathrm{tor}}(R) \propto R^{-1}$. As discussed above the diameter, and thus the radius of the jet, scales as $d_j \propto r^l$. Therefore the strength of a torodial component of the magnetic field scales along the jet axis as $B_{\mathrm{tor}}(r) \propto r^{-l}$. The strength of a polodial magnetic field component frozen into the expanding plasma scales with the cross-section area of the jet as $B_{\mathrm{pol}}(A(R)) \propto A^{-1} \propto R^{-2}$. Along the jet axis the strength of a polodial magnetic field component scales as $B_{\mathrm{pol}}(r) \propto r^{-2l}$.

3. In a Blandford & Königl (1979) jet, the electron number density scales with the Lorentz factor as $N(\gamma) = N_0 \gamma^{-2}$ and the electron energy density u_e is in equipartition with the magnetic field density $n_e \propto B^2/8\pi$. In principle it is also possible to assume particle conservation. In this case the electron energy density would scale with the area of the cross section as $n_e \propto A^{-1}$ and therefore n_e^{-2l}. In the following, the scaling parameter of the electron energy density n will not be constrained and $n_e \propto r^n$ will be adapted.

In radio observations of pc-scale jets these parameters are relevant for the observed flux density. The flux density in the co-moving frame of the source $F_{\nu,co}$ can be connected to the radius of the emission region $R = (d_j/2)\ (D_L/(1+z)^2)$ via the synchrotron emissivity j_ν of this region (Kino et al. 2014)

$$\frac{4\pi}{3} R^3 j_\nu = 4\pi F_{\nu,co} R^2 \ \rightarrow \ F_{\nu,co} = \frac{R j_\nu}{3}. \tag{1.7a}$$

The observed flux density depends on the redshift and the Doppler factor of the region:

$$F_\nu = \left(\frac{\delta}{1+z}\right)^3 \underbrace{F_{\nu,co}}_{\propto d_j j_\nu} \underbrace{\left(\frac{d_j}{2}\right)^2}_{\propto A}. \tag{1.7b}$$

The observed flux density F_ν of a circular radiating area A, can be written in terms of the synchrotron emissivity $j_\nu \propto n_e B \left(\frac{\nu}{\nu_B}\right)^\alpha$ ($\nu_B \propto B$)(section 9.2.1 in Krolik 1999) as follows:

$$F_\nu = A\ d_j\ j_\nu\,. \tag{1.7c}$$

Applying the scaling of the geometry (I), magnetic field strength (II) and electron energy density (III), the scaling of the flux desity along the jet axis can be re-written as

$$F_\nu \propto r^{3l+n+b(1-\alpha)}\ . \tag{1.7d}$$

For a circular emission region with radius R, which here is interpreted as the radius of the jet at a given position along the jet-axis r, the flux density relates to the brightness

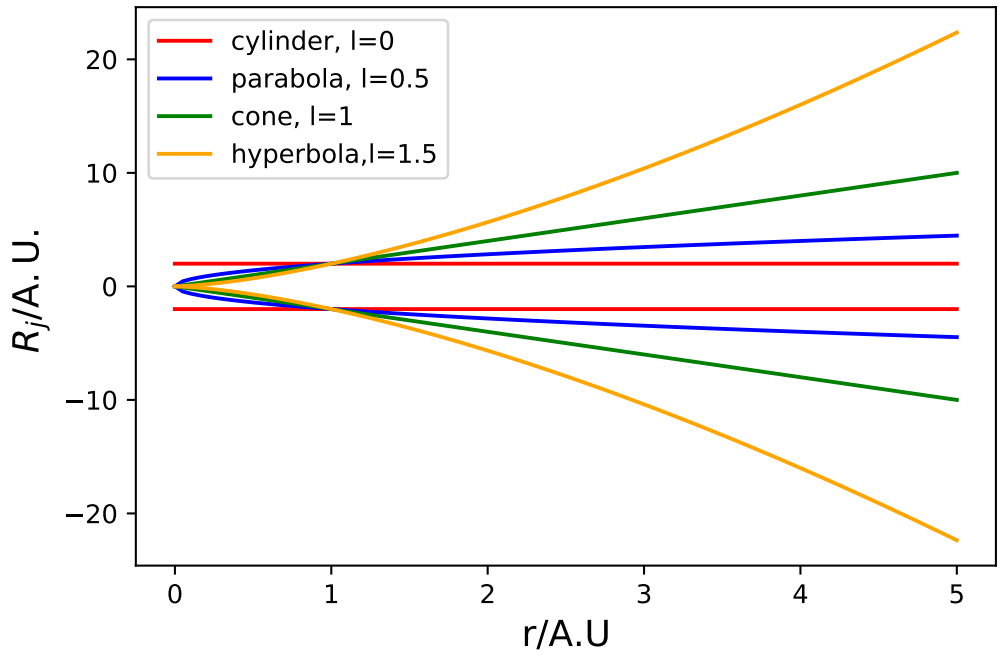

FIGURE 1.10: The different types of jet geometries are shown for comparison. The scales of the jet axis r and the diameter d_j are shown in arbitrary units. For $l > 0$ the apex of the jet lies at $r = 0$. For the cylindrical case $l = 0$ not artificial apex is shown. In reality of course also a cylindrical jet would start somewhere and probably open up at some point.

temperature T_b as $T_b \propto R^{-2} \propto r^{-2l}$ (Kovalev et al. 2005)[9]. Therefore, the brightness temperature can be re-written in terms of the jet-parameters, l, b, n, α (Kadler et al. 2004) as

$$T_b \propto r^s, \;\; s = l + n + b\,(1 - \alpha)\,. \tag{1.7e}$$

The brightness temperature measures the radiated power at a given frequency per frequency band width and solid angle (observed surface area). For thermal radiation (black-/gray body spectrum) the 'true' physical temperature can in principal be determined by dividing T_b with the emissivity of the observed surface. For non-thermal (synchrotron) radiation this conversion is not possible, since the physical temperature here is not well defined (Condon & Ransom 2016) as the expectation value of a power law distribution is not defined.

[9] see Sect-2.4

1.7 Geometry transitions in blazar jets and the acceleration zone

Since the early jet models (Blandford & Königl 1979; Königl 1981), more refined jet models were established[10]. Where the early models required electrons to be accelerated in a uniform geometry somewhere, the focus over time has shifted to build a more complete picture of radio jets that also is general enough to possibly explain the variability of blazars seen in all wavelengths. Potter & Cotter (2015) used their jet model, based on magnetohydrodynamical (MHD) simulations they developed and refined over the years (Potter & Cotter 2012, 2013a,b,c), to extract physical parameters from 42 simultaneuosly observed blazar SEDs, like the maximum/minimum/accretion Lorentz factor, inclination angle, jet power, magnetic field, etc. . While in the earlier works Potter & Cotter (2012) adopted a purely conical jet model, the measured geometry transition of M 87 (Asada & Nakamura 2012) inspired them to invoke jet geometries, that can show transitions, where the jet accelerates in the parabolic section $l \sim 0.5$. The jet model of Potter & Cotter (2015) is based on simulations and observations. It is a one-dimensional time-independent flow of a relativistic fluid where Γ (bulk Lorentz factor) and the geometry can vary. They argue that the total relativistic energy of the plasma is conserved

$$\nabla_\mu T^{\mu\nu} = 0,\ T^{\mu\nu} = T^{\mu\nu}_{\text{magnetic}} + T^{\mu\nu}_{\text{particles}} + T^{\mu\nu}_{\text{losses}}, \tag{1.8a}$$

where $T^{\mu\nu}$ is the energy-momentum tensor of the plasma in the observer's frame, composed of the magnetic energy density, particle (electron) energy density and losses. They consider synchrotron, inverse compton and adiabatic losses, which are calculated in Potter & Cotter (2012, 2013a). In the acceleration zone, where the jet geometry is parabolic (and the jet starts), $T^{\mu\nu}_{\text{magnetic}}$ dominates over the other terms in Eq. 1.8a and the jet is said to be magnetically dominated. While the plasma accelerates, the magnetic energy converts to kinetic energy via Poynting flux. In this model, the point, where $T^{\mu\nu}_{\text{particles}}$ starts to dominate over $T^{\mu\nu}_{\text{magnetic}}$, is the point, where the jet geometry switches from parabolic to conical, see Fig. 1.11. These geometry transitions have been found in several single-source studies in recent years (as mentioned above, M87 by Asada & Nakamura (2012), but also NGC 6251 (Tseng et al. 2016), NGC 4261 (Nakahara et al. 2018), NGC 1052 (Nakahara et al. 2020; Baczko et al. 2022), NGC 315 (Boccardi et al. 2021; Park et al. 2021) and 1H0323+342 (Hada et al. 2018)). In the parabolic region of M87 (Mertens et al. 2016; Hada et al. 2018; Park et al. 2019), NGC 315 (Park et al. 2021) and 1H0323+342 (Hada et al. 2018) also jet acceleration could be measured. Pushkarev & Kovalev (2012) found first hints for this behavior (geometry transition) in a sample of 370 AGN, observed at 2 GHz and 8 GHz over a time-period of 5 years (1998-2003),

[10] and computing power has drastically grown to address recently upcoming question

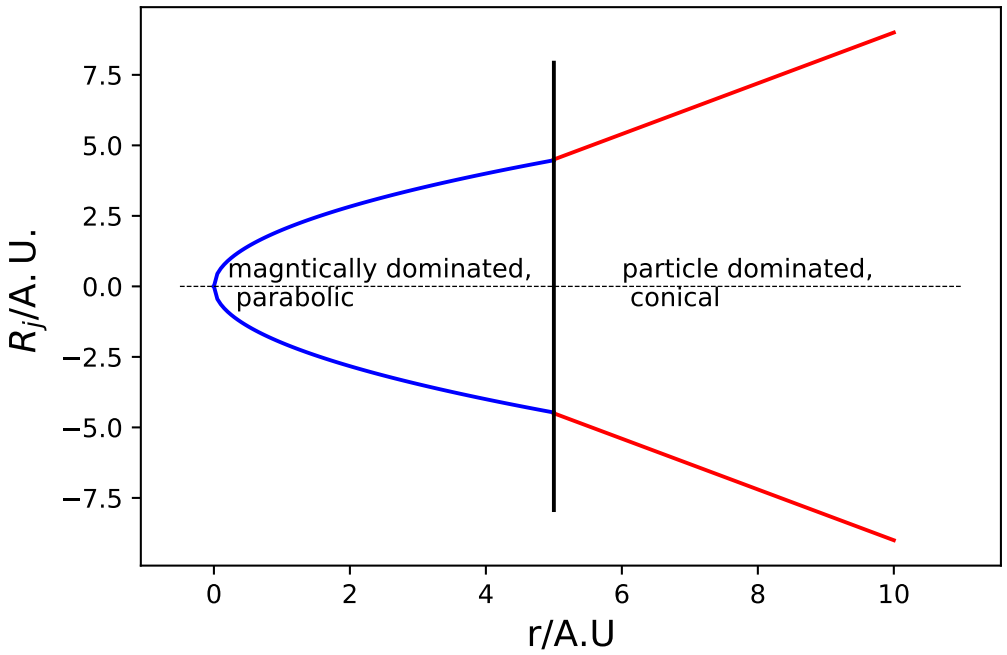

FIGURE 1.11: Schematic illustration of a jet, showing a parabolic shape (blue lines) where the flow is magnetically dominated and accelerated. The jet shows a geometry transition from parabolic to conical

where the 8 GHz-jets were more collimated than the 2 GHz jets. Kovalev et al. (2020) showed that these transitions are a common feature for AGN and are likely explained by the switching of the jet from magnetically to particle dominated. Overall the number of objects where these geometry transitions have been systematically studied is small. Independent studies by different groups showed that different results can be obtained, applying different methods. For the source NGC315, Boccardi et al. (2021) used a modelfit[11] analysis in the visibility domain. For this they utilize multi-wavelength data from different observation epochs. They find a transition of the jet geometry at a distance of about half a pc. Park et al. (2021) used also single epoch multi-frequency data and studied the jet geometry in the image plane. They found the geometry transition at a distance of $\sim$ 5 pc. This shows that it is important to systematically study larger samples with consistent methodology.

1.8 So what is my plan?

Considering the different points discussed above about the stochastic nature of γ-ray light curves and the difficulty to pinpoint the origin of this radiation on the one hand

[11] see Sect. 2.2

and the pc-scale jets in the GHz-regime of radio observations which are in some cases known to switch their geometry from a collimated state to a freely expanding state, probably marking the point where a jet, dominated by the magnetic flux density, accelerating the charged particles within the plasma of the jet, switching to particle/kinetically dominated jet on the other hand I want to try to explore following questions:

1. Considering the jet model discussed in this chapter, what is the behavior of blazars regarding the parameters s, l, n, b? This will include a detailed investigation of especially the behavior of the jet geometry and the magnetic field strength gradient.
2. Is it possible to find these geometry breaks within pc-scale jets in a high frequency sample (15GHz, 43GHz)?
3. If found, do these breaks occur due to external (of the jet) influences like altering pressure profile due to Bondi accretion, or is it plausible that these breaks happen due to inner mechanism in the jet?
4. Can the magnetic field in the radio jet be scaled to the region of the central engine, the SMBH? If so, how strong is the magnetic field in these regions?
5. Knowing the stochastic nature of γ-ray light curves, is it possible to quantify details regarding the flux density variations in such light curves, in particular with regard to the Ornstein-Uhlenbeck parameters μ, σ, θ and the power spectral density?
6. Do the jet parameters s, l, n, b play a role in the nature of the γ-ray variability?
7. Is there a systematic difference of any kind regarding the source classes of BL Lacs and FSRQs?

In the following chapters I will try to address these questions. First I will discuss the data acquisition and data reduction. Since for this work I use archival data, the calibration and imaging process in the radio data has already been done. Therefore I will discuss the observation/calibration techniques involved in this process only briefly and focus on both cases, the radio and γ-regime data on the methods I used to analyze the data. Following this, I will present the results of the analysis and finally discuss them with respect to each other.

Chapter 2

Analyzing blazar jets on parsec scales

> Niemand hat die Absicht eine Mauer zu errichten
>
> Walter Ulbricht

In order to analyze the jet structure of blazars on parsec-scales I use data from the Very Long Baseline Array[1] (VLBA) at 15GHz and 43GHz. The VLBA is a telescope array, consisting of ten antennas, each with a diameter of 25 m, scattered across the USA, with a maximum baseline (length of the airline between two antennas) of $\sim 8000\,\mathrm{km}$ between the stations Mauna Kea on Hawaii and St. Croix on the Virgin islands. The VLBA receivers allow to observe frequencies in the range of $1.2 \leq \nu/\mathrm{GHz} \leq 96$. A collage of the VLBA can be seen in Fig. 2.1. There are two monitoring programs utilizing the VLBA, from which I use archival data in this work. 'Monitoring Of Jets in Active galactic nuclei with VLBA Experiments'[2] (MOJAVE) is an experiment monitoring AGN roughly once every one to three months since $\sim$ 1994 at 15 GHz. With the MOJAVE program, jet kinematics (Lister et al. 2009, 2016, 2019), opening angles of jets (Pushkarev et al. 2017b), the spectral distribution (Hovatta et al. 2014), the collimation and acceleration zone (Homan et al. 2015) and the polarization (Lister et al. 2018; Pushkarev et al. 2017a) of AGN jets have been studied. The Boston University blazar monitoring program[3] (BU) monitors 34 blazars and 3 radio galaxies with a cadence of $\sim$ one per month since $\sim$ 2007 at 43GHz and recently (since 2020) also some sources at 86 GHz with the VLBA (Jorstad & Marscher 2016).

[1] https://science.nrao.edu/facilities/vlba
[2] https://www.physics.purdue.edu/MOJAVE/
[3] https://www.bu.edu/blazars/VLBAproject.html

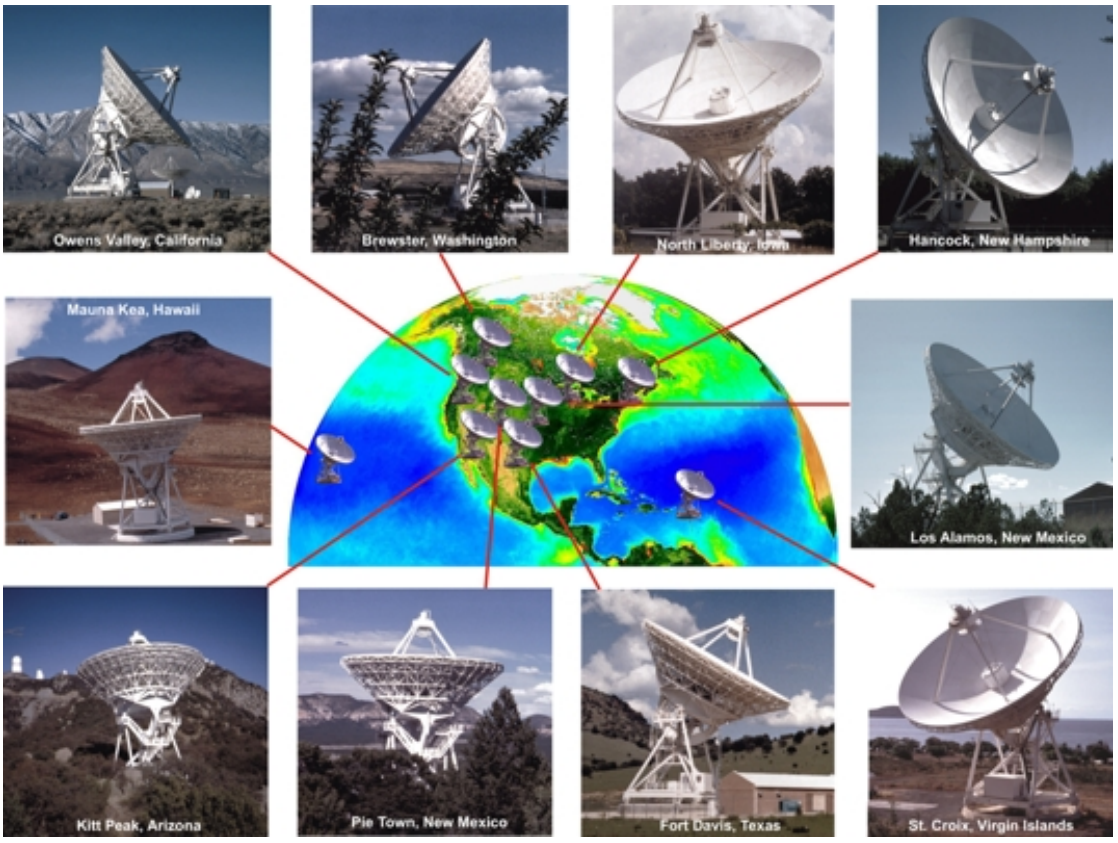

FIGURE 2.1: Locations of the VLBA antennas across the USA; credit: Image courtesy of NRAO/AUI and Earth image courtesy of the SeaWiFS Project NASA/GSFC and ORBIMAGE

2.1 Radio interferometry

Depending on the observing frequency ν, the largest single-dish radio telescopes reach spatial resolutions of $\sim$ arcmin which, when studying blazar jets on parsec scales, requiring mas resolutions lacks $4-5$ orders of magnitude. The smallest spatial resolution which can be reached by a telescope with diameter D is limited by the Rayleigh criterion (Rayleigh 1879):

$$\theta/\mathrm{rad} \sim c/D\nu \ . \tag{2.1a}$$

In order to reach mas-resolutions one could build a telescope with a diameter of thousands of kilometers which for obvious reasons will not happen, or several, smaller sized telescopes can be placed at different locations across the globe, where the diameter in Eq. 2.1a is replaced by the length of the largest baseline. These telescopes then observe the same object at the same time and the signals are then correlated, meaning Fourier transformed (FT) and multiplied (x), see FT-x correlators (Romney 1999). The concepts of radio interferometry are written down in several books (e.g. Burke & Graham-Smith 2009; Thompson et al. 1986; Taylor et al. 1999). Each emphasize different aspects. If one intends to build a radio interferometer Thompson et al. (1986) goes into technical

detail that will help in this case. From the perspective of an astronomer, wanting to understand the general issue, Burke & Graham-Smith (2009) gives a thorough introduction to radio interferometry, while Taylor et al. (1999) is a solid basis when trying to get into the deeper foundations of radio interferometry, leading to a good understanding of the calibration and imaging process.
According to Clark (1999), the coherence function of an event, emitting an electromagnetic wave which can be measured at two positions $\vec{r_1}$ and $\vec{r_2}$ is dependent on the observed intensity I_ν in an solid angle $\mathrm{d}\Omega$

$$V_\nu(\vec{r}_1, \vec{r}_2) = \int \mathrm{d}\Omega \, I_\nu(\vec{s}) \mathrm{e}^{-2\pi i \nu \vec{s}(\vec{r}_1 - \vec{r}_2)/c} \,, \tag{2.1b}$$

where ν is the observing frequency[4] and $\vec{s}$ is a unit vector describing the path between observer and event. An interferometer is a machine, measuring this coherence function and the intensity of an object in the sky[5] is accessible through Fourier inversion. In reality, the coherence function is measured at certain points and therefore not continuous. The root of artefacts in radio images is often the sampling of the coherence function. Furthermore antennas have a geometry and therefore a beam pattern, causing an angle-dependent sensititiviity of each antenna. However, before discussing the effect of beam pattern and discrete sampling, two coordinate systems, the (u, v, w) system for the antennas and (l, m, n) for the intensity distribution must be introduced.

$$\begin{aligned} \vec{b}_\lambda \vec{s} &= ul + vm + wn \\ \vec{b}_\lambda \vec{s}_0 &= w \\ \mathrm{d}\Omega = \frac{\mathrm{d}l \, \mathrm{d}m}{n} &= \frac{\mathrm{d}l \, \mathrm{d}m}{\sqrt{1 - l^2 - m^2}} \,, \end{aligned} \tag{2.1c}$$

where $\vec{b}_\lambda = \vec{r}_1 - \vec{r}_2$ describes the baseline between two telescopes in units of the observing wavelength. This coordinate system is schematically illustrated in Fig. 2.2.

In the case that all telescopes, forming the array, populate a single plane (telescopes are co-planar), a baseline vector in units of the observing wavelength $\vec{b}_\lambda = \vec{r}_1 - \vec{r}_2 = \lambda(u, v, 0)^\mathrm{T}$ and the unit vector $\vec{s} = \left(l, m, \sqrt{1 - l^2 - m^2}\right)^\mathrm{T}$ can be defined. Let the sources of interest occupy only a small fraction of the sky and let $\vec{s}_0$ and $\vec{s} = \vec{s}_0 + \vec{\sigma}$ be unit vectors, such that $\vec{s}_0^2 = \vec{s}^2 = 1 = \vec{s}_0^2 + 2\vec{s}_0\vec{\sigma} + \vec{\sigma}^2 \approx 1 + 2\vec{s}_0\sigma \rightarrow \vec{s}_0\vec{\sigma} = 0 \rightarrow \vec{s}_0 \perp \vec{\sigma}$, see

[4] in reality observations are not done at a single peak frequency but in a frequency band, which can cause bandwidth smearing, which will not be discussed in this thesis. For details, see Bridle & Schwab (1999).

[5] blazars are far away, therefore, only the 2D-intensity distribution is accessible. The complete 3D structure of a source can only be deciphered combining different observations on different scales (e.g. Seeg 2017)

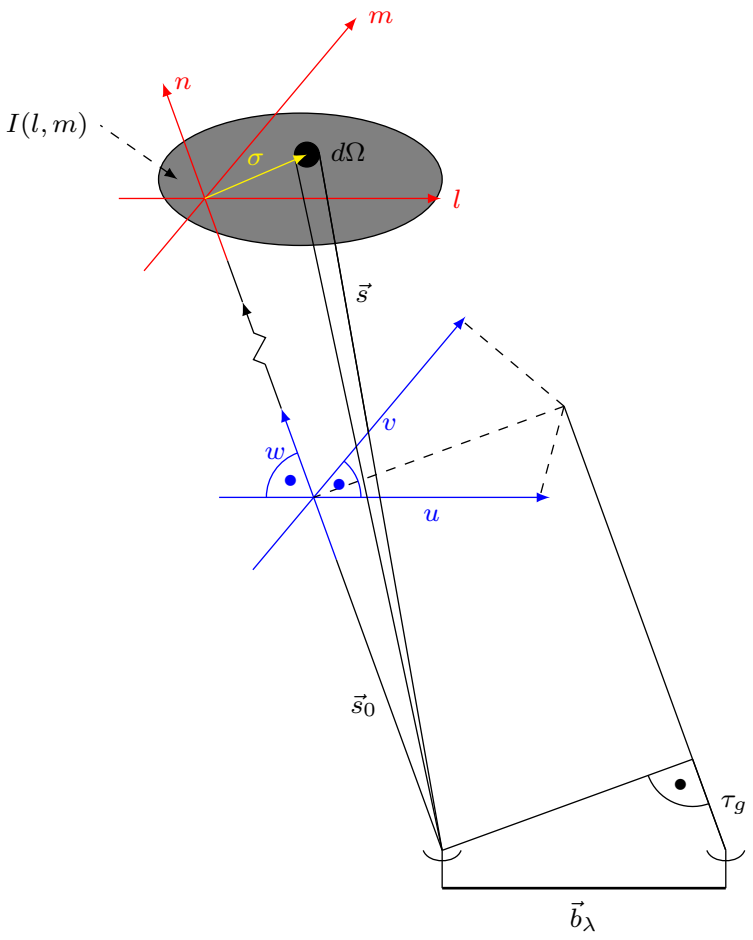

FIGURE 2.2: The intensity distribution of a source (grey area) is described in the (l, m, n)-system (red). The antennas, connected by a basesline $\vec{b}_\lambda$ are described in the (v, w, w)-system (blue). A coherent wave arrives at a reference (left) antenna and also at the right antenna with a geometric delay τ_g. From: Burd (2017)

Fig. 2.2. In this case, the coherence function simplifies to

$$V_\nu(u, v) = \int \mathrm{d}l \int \mathrm{d}m \, I_\nu(l, m) \, \mathrm{e}^{-2\pi i(ul+vm)} \, . \tag{2.1d}$$

The intensity in the sky can be obtained by Fourier inversion.

$$I_\nu(l, m) = \int \mathrm{d}u \int \mathrm{d}v \, V_\nu(u, v) \, \mathrm{e}^{2\pi i(ul+vm)} \, . \tag{2.1e}$$

The effect of a discretely sampled coherence function can be accounted for by introducing a sampling function $S(u, v)$, which defines the synthesized beam, also called dirty beam,

which can be undertstood as the point spread function by

$$B^D(l,m) = \int \mathrm{d}u \int \mathrm{d}v\, S(u,v)\, \mathrm{e}^{2\pi i(ul+vm)}\,. \tag{2.1f}$$

A dirty image ($I^D_\nu(l,m)$) can be obtained by convolution of the intensity distribution and the dirty beam

$$I^D_\nu(l,m) = I_\nu(l,m) \star B^D(l,m) = \int \mathrm{d}u \int \mathrm{d}v\, V_\nu(u,v)\, S(u,v)\, \mathrm{e}^{2\pi i(ul+vm)}\,. \tag{2.1g}$$

The antenna reception pattern can be taken into account with the so-called primary beam B^P, which contains the antenna geometry:

$$B^P(u,v) = \int \mathrm{d}l \int \mathrm{d}m\, A_\nu(l,m)\, \mathrm{e}^{-2\pi i(ul+vm)} \tag{2.1h}$$

$A_\nu(l,m)$ takes values between zero and one, quickly declining to zero for signals that are off the pointing direction. The complex visibility function is the convolution of the primary beam B^P and the coherence function

$$V(u,v) = B^P(u,v) \star V_\nu(u,v) = \int \mathrm{d}l \int \mathrm{d}m\, A_\nu(l,m)\, I_\nu(l,m)\, \mathrm{e}^{-2\pi i(ul+vm)}\,. \tag{2.1i}$$

Due to the dicrete sampling of the visibility, to obtain an image, an iterative approach has to be used, containing the CLEAN algorithm (Högbom 1974; Clark 1980; Cornwell & Braun 1989) and the use of self-calibration (Jennison 1958; Cornwell 1989; Cornwell & Fomalont 1989). Modern imaging algorithms, for example, based on information field theory (Arras et al. 2018, 2022) have shown to be promising candidates, replacing the CLEAN and self-calibration procedure. The exact procedure in any way will not be discussed in this context, since archival data are used, which are already calibrated and imaged.

2.2 Model fitting a jet with circular Gaussian components

The following dicsussion is based on Fomalont (1999). First I will make some general remarks about model fitting in DIFMAP, which is a software package that allows the imaging, self-calibration and model fitting of (u,v) data from radio interferometric data (Shepherd 1997). Examples from the selected sample are shown. When analyzing radio images, the content of the image has to be quantified. If an image for example contains a set of isolated bright features (often called components), which might be a collection of point sources or even extended bright features belonging to the same source, some properties of these components can be extracted by estimating statistical moments of

the brightness distribution $I(x_i)$ (in this case one-dimensional), where x_i is the position at a grid point i:

The integrated intensity of a component

$$F = \sum_i I(x_i), \tag{2.2a}$$

the mean position of the component

$$X = F^{-1} \sum_i x_i I(x_i) \tag{2.2b}$$

and the width of the component

$$W = \sqrt{F^{-1} \sum_i (x_i - X)^2 I(x_i)}\,. \tag{2.2c}$$

Fomalont (1999) explains, that in order to obtain parameters from an image or regions within an image, it is often easier to model a certain region (or the entire image) with well-defined functions, due to the fact that above mentioned components often do show a certain geometry or brightness distribution. For un-resolved components, it is possible to use the point spread function of the dirty image B^P or the typically Gaussian shaped, synthesized beam of the clean image. Complex objects, such as jets, that are resolved along the jet axis require a more complex model $M(p_j, i)$ with a set of free parameters p_j, which in many cases consists of a number of Gaussian components (Lister et al. 2009, 2016, 2019). Typical free parameters in such a Gaussian model are the flux density, the full width at half maximum (FWHM). The exact parameters, relevant for this work, are discussed later in this section. The parameters p_j and their errors are determined by minimizing the variance

$$\sigma^2 = \sum_i (M(p_j, i) - I(x_i))^2\,. \tag{2.2d}$$

Minimizing this variance requires non-linear fitting methods, since even in this one-dimensional example, the free parameters involved are not necessarily orthogonal (Likelihood of $L(p1, p2) \neq L(p1)L(p2)$), which in DIFMAP often converge on a solution, by setting good initial conditions. This typically is achieved by examining the dirty image by eye, identifying bright regions and estimating shape and position. In general, DIFMAP allows to modelfit elliptical and circular Gaussian components. Elongated features, e.g. bright features in jets can often be described by elliptical components, however, elliptical Gaussians, in the context of a jet with several components tend to show diverging axis-ratios, which make them an unstable fit. In these cases it is often more reliable to 'split' this elongated region into two regions and fit a circular Gaussian

component with less relevant free parameters (axis ratio, position angle). Fig. 2.3 shows an example of a jet model, built with 2D circular Gaussian components. The source shown is $0219+428$, observed at 15 GHz with the VLBA in 2008. The image features a bright radio core, from which the jet extends ~ 15 mas into the southern direction. The data for this image are taken from the MOJAVE website[6]. The jet is fit with circular Gaussian components (red circles) with the DIFMAP command MODELFIT. The parameters that can be obtained from this fit are shown in Table 2.1, as given by DIFMAP. This particular epoch of $0219+428$ is fit with nine circular Gaussian components, each containing a flux density F. The distances $\Delta x, \Delta y$ are measured from the origin of the map see Fig. 2.3 which is the phase center of the observation, often the position of the radio core at a given frequency. The MAJORAX and MINORAX would be the major and minor axis of an elliptical Gaussian. Since there are only circular components, each of those parameters, is equivalent to the diameter of a circular Gaussian component. In this context, the diameter of a circular Gausssian component is equivalent to the diameter of the pc-scale jet. The position angle (POSANGLE), for an elliptical component would give additional information on where an elongated component is aligned. For circular components, the parameter does not contain information. MODELFIT is an iterative procedure. As mentioned above, in order to make the fit converge quickly, initial parameters for each component are given. In the case of a circular Gaussian fit, the initial conditions are given by the position and diameter of a component. MODELFIT will then vary the parameters flux density, position and diameter according to the data in the considered region. The procedure is started in the brightest region, and subsequently extended further for less bright regions. The final fit, containing all components that can be identified by separate bright regions in the map, again varies all parameters from all components in order to minimize Eq. 2.2d. Only when all bright regions in the map are found and the fit properly converges, the fit itself is considered satisfactory in this work. According to Fomalont (1999) the error of the parameters of each component can be estimated with the post-fit map rms[7] σ_{rms}. The error of the flux density of each component is the sum of the post-fit map rms, the information on the SNR of each component and a systematic error

$$\sigma_F = \sqrt{\underbrace{\sigma^2_{\mathrm{rms}}}_{\text{post-fit map RMS}} + \underbrace{\sigma^2_{\mathrm{rms}}\mathrm{SNR}}_{\text{SNR of each component}} + \underbrace{(5\%\ F)^2}_{\text{estimated systematic error}}} \,. \tag{2.2e}$$

The flux density in a component also determines the error of the diameter of a component σ_d

$$\sigma_d = d\frac{\sigma_F}{F} \,. \tag{2.2f}$$

[6] http://www.physics.purdue.edu/astro/MOJAVE/sourcepages/0219+428.shtml
[7] root mean square of flux density, or noise

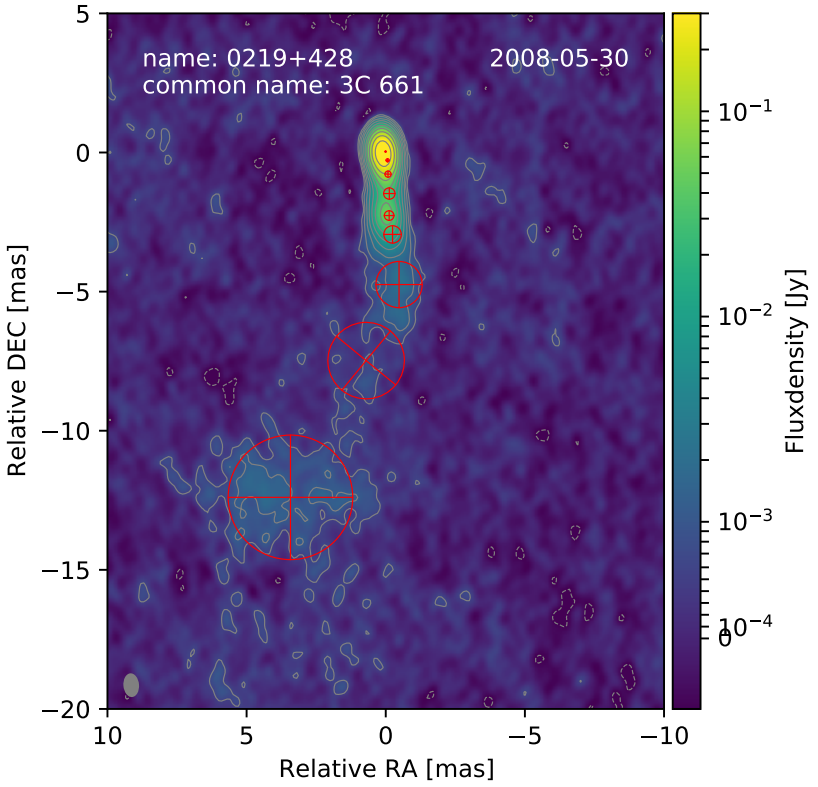

FIGURE 2.3: Radio image of $0219 + 428$ observed at 15 GHz with the VLBA in 2008. The data for this image is taken from the MOJAVE website. The jet of this source extends up to ~ 15 mas from the radio core. The jet is model fit with circular Gaussian components, see parameters in Tab. 2.1.

TABLE 2.1: MODELFIT parameters from the example, shown in Fig. 2.3, exported from DIFMAP; Col. 1: flux density in Jy, col. 2: x-position from the map center in deg, col. 3: y-position from the map center in deg, col. 4: major axis in deg, col. 5: minor axis in deg, col. 6: position angle in deg

F/Jy	$\Delta x/$ deg	$\Delta y/$ deg	MAJORAX/ deg	MINORAX/ deg	POSANGLE/ deg
0.5077251	1.7991778e-09	9.372175e-09	1.2035814e-08	1.2035814e-08	0.0
0.12401577	-1.837136e-08	-7.7517456e-08	3.1742378e-08	3.1742378e-08	0.0
0.05829134	-3.406297e-08	-6.294992e-07	9.6420784e-08	9.6420784e-08	0.0
0.05656678	-2.257689e-08	-2.1596452e-07	6.1841284e-08	6.1841284e-08	0.0
0.054632064	9.5114257e-07	-3.442827e-06	1.2432414e-06	1.2432414e-06	0.0
0.026190141	-3.5488615e-08	-4.0979523e-07	1.136324e-07	1.136324e-07	0.0
0.0133994995	-1.3276852e-07	-1.318494e-06	4.61215e-07	4.61215e-07	0.0
0.015026881	-6.80512e-08	-8.1787886e-07	1.7426528e-07	1.7426528e-07	0.0
0.009123064	1.9590607e-07	-2.0776354e-06	7.6359777e-07	7.6359777e-07	0.0

2.3 15 GHz and 43 GHz sample

The sample of sources from which the pc-scale radio jets are studied consists of the overlap of sources between the MOJAVE data archive (Lister et al. 2018) and the BU (Jorstad & Marscher 2016) sample, observed between 2003 and 2013. A source is considered, when the jet can be fit with at least three 2D Gaussians (except the radio core) in at least five epochs. The peculiar, complex-structured radio galaxy 0316+413 (3C84) is excluded from this sample. The resulting sample is listed in Table 2.2. It consists of 28 sources: 15 FSRQs, 11 BL Lacs and 2 radio galaxies. For each source all available epochs in the mentioned time span are fit, resulting in a total of 1850 epochs.

2.4 Measuring the brightness temperature and the diameter gradients

From the MODELFIT components, described in Sect. 2.2, the diameter of each component which in this context is interpreted as the local diameter of the jet d_j, the distance of each component from the radio core $d_c = \sqrt{\Delta x^2 + \Delta y^2}$ and the flux density of each component can be measured. The radio jet and the radio core can be separated by applying a resolution filter. According to Kovalev et al. (2005), the limit of the smallest MODELFIT components that can be resolved, depends on the beam b_Ψ and the signal to noise ratio (SNR)

$$r_{\mathrm{lim}} = b_\Psi \sqrt{\frac{4\ln(2)}{\pi} \ln\left(\frac{\mathrm{SNR}}{\mathrm{SNR}-1}\right)}. \tag{2.3a}$$

In this analysis, unresolved MODELFIT components in the phase center of the observation are interpreted as the radio core, resolved MODELFIT components, describing the jet are interpreted as the jet components, each describing the diameter of the jet at the components location in the jet. These core components are filtered in order to properly study the jet properties. With the information of the flux density and the diameter in each component, a brightness temperature T_b for each component can be calculated, see Kovalev et al. (2005):

$$T_b = \frac{2\ln(2)}{\pi k} \frac{F_{\mathrm{comp}} \lambda^2 (1+z)}{(d_j/2)^2}, \tag{2.3b}$$

where k is the Boltzman constant and z is the red shift of the observed source. The extraction of the diameter, flux density and brightness temperature and the respective errors from the .fits-files obtained from DIFMAP after fitting each epoch is realized in

TABLE 2.2: Source properties of the pc-scale radio jet study

Name	Alt. name	Class.	z	$\log_{10}(M_{\rm BH}/M_\odot)$	Epochs (15GHz/43GHz)	$\frac{\rm pc}{\rm mas}$
0219+428	3C 66A	B	0.34[a]	$(8.47-8.65)^{\rm I}$	19/38	4.8
0336-019	CTA 26	Q	0.852[b]	$(7.55-7.73)^{\rm I}$	20/15	7.7
0415+379	3C 111	G	0.0491[c]	$(8.18-8.38)^{\rm II}$	59/20	0.95
0430+052	3C 120	G	0.033[d]	$(7.08-7.58)^{\rm III}$	59/24	0.65
0528+134	PKS 0528 + 134	Q	2.07[e]	$(8.35-8.52)^{\rm I}$	18/79	8.5
0716+714	TXS 0716 + 714	B	0.803[f]	$(7.51-7.68)^{\rm I}$	59/75	7.5
0735+178	OI 158	B	0.45[g]	$(8.35-8.51)^{\rm I}$	14/63	5.8
0827+243	OJ 248	Q	0.94[h]	$(6.94-7.12)^{\rm I}$	14/14	7.9
0829+046	OJ 049	B	0.174[i]	$(8.55-8.71)^{\rm I}$	14/68	2.9
0836+710	4C +71.07	Q	2.218[j]	$(7.8-7.97)^{\rm I}$	14/14	8.4
0851+202	OJ 287	B	0.306[k]	$(7.12-7.31)^{\rm I}$	26/68	4.5
0954+658	S4 0954 + 65	B	0.45[l]	$(8.6-8.77)^{\rm I}$	21/61	5.7
1101+384	Mrk 421	B	0.0308[m]	$(7.28-7.49)^{\rm I}$	27/40	0.61
1127-145	PKS 1127−14	Q	1.184[n]	$(7.77-7.94)^{\rm I}$	15/48	8.3
1156+295	4C +29.45	Q	0.725[i]	$(8.2-8.38)^{\rm I}$	20/14	7.3
1219+285	W Comae	B	0.102[o]	$(7.17-7.37)^{\rm I}$	11/49	1.9
1222+216	4C +21.35	Q	0.433[i]	$(8.38-8.55)^{\rm I}$	23/18	5.6
1226+023	3C 273	Q	0.1583[p]	$(8.13-8.3)^{\rm I}$	32/13	2.7
1253-055	3C 279	Q	0.6[q]	$(8.65-8.83)^{\rm I}$	24/70	6.7
1308+326	OP 313	Q	0.997[i]	$(7.64-8.56)^{\rm IV}$	19/28	8.0
1633+382	4C +38.41	Q	1.814[h]	$(8.36-8.54)^{\rm I}$	28/79	8.5
1652+398	Mrk 501	B	0.0337[r]	$(8.02-8.22)^{\rm I}$	12/7	0.65
1730-130	NRAO 530	Q	0.902[s]	$(8.35-8.52)^{\rm I}$	24/72	7.8
1749+096	OT 081	B	0.322[t]	$(8.66-8.66)^{\rm V}$	27/49	4.6
2200+420	BL Lac	B	0.0686[u]	$(8.02-8.17)^{\rm I}$	64/80	1.3
2223-052	3C 446	Q	1.404[v]	–	15/14	8.5
2230+114	CTA 102	Q	1.037[w]	$(8.4-8.57)^{\rm I}$	18/13	8.1
2251+158	3C 454.3	Q	0.859[x]	$(7.21-7.4)^{\rm I}$	22/14	7.7

Columns: (1) IAU B 1950 name, (2) Alternative (common) name, (3) Classification, (4) Redshift, (5) Black-hole mass, (6) Number of fit epochs, (7) parsec per milliarcsec. a) Torres-Zafra et al. (2018), b) Wills & Lynds (1978), c) Eracleous & Halpern (2004), d) Michel & Huchra (1988), e) Hunter et al. (1993), f) Stadnik & Romani (2014), g) Nilsson et al. (2012), h) Pâris et al. (2017), i) Schneider et al. (2010), j) Stickel & Kuehr (1993), k) Stickel et al. (1989), l) Wills et al. (1992), m) Ulrich et al. (1975), n) Wilkes (1986), o) Paiano et al. (2017), p) Strauss et al. (1992), q) Marziani et al. (1996), r) Stickel et al. (1993), s) Junkkarinen (1984), t) Stickel et al. (1988), u) Vermeulen et al. (1995), v) Wright et al. (1983), w) Falomo et al. (1994), x) Jackson & Browne (1991), I) Fan et al. (2008), II) Chatterjee et al. (2011), III) Kaspi et al. (2000) IV) Gupta et al. (2012), V), Falomo et al. (2003)

python code[8]. The brightness temperature T_b and diameter d_j from each component in all epochs is then plotted against the distance to the radio core d_c and fit with a power law[9] along the entire jet length and the overlap region of the 15 GHz and 43 GHz jet. In order to claim such an overlap region, the core shift has to be taken into account (Pushkarev et al. 2012; Sokolovsky et al. 2011; Kudryavtseva et al. 2011). The phenomenon of core shift states, that the region where the synchrotron emission becomes optically thin, shifts closer to the physical jet apex (closer to the SMBH) for higher frequencies. O'Sullivan & Gabuzda (2009) showed in a sample of three sources that the core shift between 15 GHz and 43 GHz is between 0.04 mas and 0.1 mas. The beam size of the frequencies is typically ~ 0.5 mas and ~ 0.3 mas, respectively, which is an order of magnitude larger than the effect of the core shift. This means that the images of both frequencies can be treated as if the same regions along the jet axis are observed. Although the core shift cannot be measured, the jets at 15 GHz typically extend farther out than the jets of the 43 GHz data, due to the 43 GHz emission cooling quicker along the jet axis and the radio antennas themselves having a smaller effective area at higher frequencies, resulting in less sensitivity. Thus the flux densities fall below the SNR at shorter distances from the radio core at 43 GHz. Therefore the overlap region of both frequencies for each source is defined as the distance between the minimum resolvable core distance in the 15 GHz jet and the maximum core distance in the 43 GHz jet. This can schematically be seen in Fig. 2.4. For each of the 28 sources, following parameters are obtained for both frequencies and saved for further analysis: The brightness temperature gradient slope s and the diameter gradient slope l, both resulting from a single power law fit applied to the $T_b - d_c$ and $d_j - d_c$ plots, with their respective errors.

2.5 Finding and fitting geometry breaks

In order to find geometry breaks within the 28 sources, following procedure is applied[10]:

- Both frequencies are analyzed in context and at the same time for each jet.
- With these new, combined data sets, the $d_j - d_c$ are considered. The entire jet length along the jet axis r now is also defined by both frequencies.
- Along the entire jet length, 10^4 random geometry break points r_b are drawn.
- For each r_b, an inner/outer single power law fit is applied in order to obtain the diameter gradient slope $l_{\mathrm{in/out}}$.

[8] The code can be accessed via https://github.com/PRBurd/tb/blob/main/extract_data.py.
[9] Python code: https://github.com/PRBurd/tb/blob/main/plot_fit.py
[10] python code: https://github.com/PRBurd/tb/blob/main/MC_find_breaks_filter.py

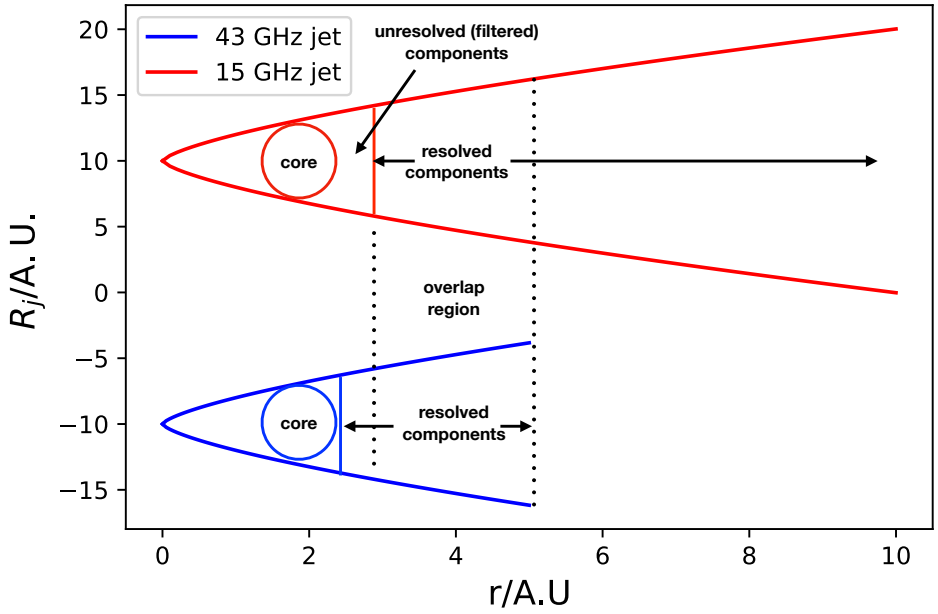

FIGURE 2.4: The location difference between the 15 GHz jet (red) and the 43 GHz jet (blue) cannot be resolved with the VLBA. The overlap region is defined as the distance between the smallest resolved core distance at 15 GHz and the largest core distance at 43 GHz.

- The obtained parameters $l_{\mathrm{in/out}}$ and r_b are used as initial values for a smoothly broken power law fit in the form of

$$f(x) = A\ 2^{(l_{in}-l_{out})/\Delta}\ \left(\frac{r}{r_b}\right)^{l_{in}}\ \left[1+\left(\frac{r}{r_b}\right)^{\Delta}\right]^{(l_{out}-l_{in})\Delta} \tag{2.4}$$

(Nakahara et al. 2020; Astropy Collaboration et al. 2013; Price-Whelan et al. 2018), where $A = d_j(x_b)$ is the jet diameter at the break point x_b. Δ regulates the smoothness of the transitions between l_{in} and l_{out}.

2.6 Magnetic field strength gradients

Equation 1.7e defines the slope of the brightness temperature gradient as $s = l+n+b\,(1-\alpha)$. In this equation s and l are measured independently. To obtain the spectral index α the flux of the components along the jet axis is fitted with a power law at both frequencies where the slope is set to -1. The offset between the two fits is then used to calculate the spectral index according to $\alpha = \frac{\log(F_{15}/F_{43})}{\log(\nu_{15}/\nu_{43})}$. The relative error of the spectral indices, determined by this method is estimated to be in the same region as the scattering of the fluxes along the jet axis, to be about 15%. Three of the five parameters are decoupled and measured independently while the electron energy distribution $n_e \propto r^n$

and the magnetic field strength gradient $B \propto r^b$ are still coupled. At this point it is not possible to proceed without making assumptions, because from the data itself it is not possible to decouple those. There are two ways to proceed further: First one can assume equipartition between the electron energy density and the magnetic field density, meaning

$$\int_{\gamma_{\min}}^{\gamma_{\max}} n_e(\gamma)\, m_e c^2 \,\mathrm{d}\gamma = \frac{B^2}{8\,\pi}$$

Let $\gamma_{\min}$ and $\gamma_{\max}$ be constant and the spectrum of the electron energy density be a power law like $n_e = n_0 \gamma^{-p}$, p =const.

$$\begin{aligned} n_e \int_{\gamma_{\min}}^{\gamma_{\max}} m_e c^2 \,\mathrm{d}\gamma &= \frac{B^2}{8\,\pi} \\ \rightarrow n_e &\propto \frac{B^2}{8\,\pi}; \\ \rightarrow r^n &\propto r^{2b}; \\ \rightarrow n &= 2b; \\ s = l + 2b + b(1-\alpha) &= l + b(3-\alpha); \\ \rightarrow b_{\mathrm{equip}} &= \frac{s-l}{3-\alpha}\,. \end{aligned} \tag{2.5}$$

Another way to decouple n and b would be to asume particle number conservation

$$\begin{aligned} n_e \propto A^{-1} &\propto r^{-2l}; \\ \rightarrow n &= -2l; \\ s = l - 2l + b(1-\alpha) &= -l + b(1-\alpha); \\ \rightarrow b_{\mathrm{pcons}} &= \frac{s+l}{1-\alpha}\,. \end{aligned} \tag{2.6}$$

Both scenarios from Eqs. 2.5 and 2.6 are calculated for s_{ol} and l_{ol}. The subindex 'ol' denoted the overlap region of the jet between both frequencies. Let R be the transversal jet radius, then a torodial magnetic field component would show following scaling behavior

$$B_{\mathrm{tor}} \propto R^{-1} \propto r^{-l} \rightarrow \frac{b}{l} = -1\,. \tag{2.7}$$

A polodial magnetic field would scale like

$$B_{\mathrm{pol}} \propto R^{-2} \propto r^{-2l} \rightarrow \frac{b}{l} = -2\,. \tag{2.8}$$

2.7 The Magnetic field of the radio core in blazar jets

Following Baczko et al. (2016) the magnetic field in the core region of the jets can be calculated via synchrotron cooling, since this is the region where the emission transitions from optically thick to optically thin. However in this case, due to relativistic bulk velocities, beaming effects and small inclination angles, I have to take certain adjustments into account. As discussed in Sect. 1.4, the emitted power of an electron with a random pitch angle distribution is given by

$$P = \frac{4}{3}\,\sigma_T\,c\,\beta_e^2\,\gamma^2\,u_B\,, \tag{2.9}$$

where c is the speed of light, $u_B = \frac{B^2}{8\pi}$ is the magnetic field density, $\sigma_T = \frac{8\pi\,r_0^2}{3}$ is the Thomson cross section, defined by the classical electron radius r_0 and β_e is the electron velocity. To obtain the cooling time of the electron, the energy loss has to be calculated

$$\dot{E}_{\rm loss} = -P \;\rightarrow\; \frac{\mathrm{d}\gamma}{\mathrm{d}t} = -\frac{P}{m_e\,c^2} = -\frac{4}{3}\,\frac{\sigma_T}{m_e\,c}\,\beta_e^2\,\gamma^2\,u_B\,. \tag{2.10a}$$

Separating the variables leads to

$$\frac{\mathrm{d}\gamma}{\gamma^2} = -\frac{4}{3}\,\frac{\sigma_T}{m_e\,c}\,\beta_e^2\,u_B\,\mathrm{d}t\,, \tag{2.10b}$$

integration yields

$$-\frac{1}{\gamma} = -\frac{4}{3}\,\frac{\sigma_T}{m_e\,c}\,\beta_e^2\,u_B t_c\,. \tag{2.10c}$$

The cooling time of the electron t_c then reads

$$t_c = \frac{3}{4}\,\frac{m_e\,c}{\sigma_T\,\beta_e^2\,u_B\,\gamma} \tag{2.10d}$$

Inserting the magnetic field density and expressing the Lorentz factor γ via the critical frequency, where the optical depth $\tau = 1$,

$$\nu_c = \frac{3}{4\pi}\,\frac{e\,B}{m_e\,c}\,\gamma^2 \;\rightarrow\; \gamma = \sqrt{\frac{4\pi\,m_e\,c\,\nu_c}{3\,e\,B}}\,, \tag{2.10e}$$

the cooling time then reads

$$t_c = \frac{3}{4}\,\frac{m_e\,c}{\sigma_T\,\beta_e^2\,\frac{B^2}{8\pi}}\,\sqrt{\frac{3\,e\,B}{4\pi\,m_e\,c\,\nu_c}} = 3\sqrt{3\pi}\,\sqrt{\frac{m_e\,c\,e}{\nu_c}}\,\frac{B^{-\frac{3}{2}}}{\sigma_T\,\beta_e^2}\,. \tag{2.10f}$$

Since the electron moves in a bulk which itself moves at highly relativistic speeds with a bulk Lorentz factor of Γ, the cooling time becomes larger due to time dilatation. Furthermore, due to relativistic beaming, the critical frequency has to be corrected with the Doppler factor $\delta = \frac{1}{\Gamma(1-\beta_{b,\rm int}\cos(\theta))}$, where θ is the inclination angle, under which the

emission of the moving bulk is observed and $\beta_{b,\mathrm{int}}$ is the intrinsic velocity of the bulk.

$$\begin{gathered} t_c \to t_c' = \Gamma\, t_c;\; \nu_c \to \nu_c' = \frac{\nu_c}{\Gamma} \\ t_c = \Gamma\, 3\sqrt{3\pi}\, \sqrt{\frac{m_e\, c\, e\, \delta}{\nu_c}}\, \frac{B^{-\frac{3}{2}}}{\sigma_T\, \beta_e^2} \text{ (observables in observer's frame)} \end{gathered} \tag{2.10g}$$

The projected distance over which the electrons pass while cooling at an optical depth of unity should then equal the size of the core region in the VLBI images $t_c = \frac{d_{CR}}{\beta_e}$. This in turn has to be de-projected, since blazars have small angles to the line of sight. One can assume that the electrons travel nearly at the speed of light, meaning $\beta_e \to 1$. Therefore Eq. 2.10g can be reorganized, expressing the magnetic field as

$$\begin{gathered} t_c = \frac{d_{CR}}{c}\,(\beta_e \to 1),\; d_{CR} \to d_{CR}' = \frac{d_{CR}}{\sin(\theta)}\,(\textit{deprojected}) \\ B = \left(\frac{d_{CR}\, \sigma_T}{3\sqrt{3\pi}\, \Gamma \sin(\theta)}\, \sqrt{\frac{\nu_c}{m_e\, c\, \delta}}\right)^{-\frac{2}{3}};\; [B] = \mathrm{G},\; [d_{CR}] = \mathrm{cm}\,. \end{gathered} \tag{2.10h}$$

2.7.1 Concerning the intrinsic bulk speed, the bulk Lorentz factor and the maximum apparent jet speed

In Eq. 2.10h the bulk Lorentz factor Γ itself and the Doppler factor δ with the Lorentz factor within, and the intrinsic bulk speed, appear. If the maximum apparent speed in a jet is sufficiently large, the bulk Lorentz factor can be estimated by this speed. the error occurring at this point is smaller, the larger the intrinsic speed of the jet is. At $\sim 90\%$ of the speed of light, the error, done by this method is $\sim 10\%$. One also has to take into account that this statement is done under the assumption of a critical inclination angle, where the apparent speed of the jet peaks. When taking a sample of radio loud AGN, and drawing a random source, the chance, finding a blazar under the critical angle is about 50%, see Cohen et al. (2007). For the purposes of the B-field calculation it is assumed that the approximation $\Gamma \sim \beta_{\mathrm{b,max,app}}$ to be valid. Eq. 2.10h then reads.

$$\begin{gathered} \Gamma \to \beta_{\mathrm{b,max,app}} \\ B = \left(\frac{d_{CR}\, \sigma_T}{3\sqrt{3\pi}\, \beta_{\mathrm{b,max,app}} \sin(\theta)}\, \sqrt{\frac{\nu_c}{m_e\, c\, \delta}}\right)^{-\frac{2}{3}} \\ [B] = \mathrm{G},\; [d_{CR}] = \mathrm{cm},\; [\beta_{\mathrm{b,max,app}}] = \mathrm{cm/s}\,. \end{gathered} \tag{2.10i}$$

This of course is also applied for the Doppler factor δ. For sources where no luminosity distance is given, the magnetic field in the radio core cannot be calculated, since the size of the region where the electrons pass through has to be available in cm and the

apparent maximum jet speed in cm/s. Furthermore, for sources, where the maximum apparent speed is very low ($\beta_{\mathrm{app,max}} < 1$), this method cannot be applied.

2.7.2 The procecdure to actually calculate the magnetic fields in the radio core

In order to actually calculate the magnetic fields in the respective radio core, following steps are performed for each source and each frequency:

- Under the assumption, that the blazar is seen under a critical angle, the Lorentz factor can be approximated to be the maximum measured apparent jet speed $\gamma \rightarrow \beta_{\mathrm{app,max}}$, therefore the intrinsic speed can be calculated by Eq. 1.6d in order to find the position of the maximum which yields the estimated critical angle.
- With this angle the intrinsic speed, corresponding to the apparent maximum speed can be calculated by inverting Eq. 1.6d.
- In all epochs for each source, the core component is identified by searching the closest component to the (0,0)-position in the (u,v)-plane
- The diameter of this component is identified as the minimum distance the electrons have to travel in order to pass the radio core, which corresponds to d_{CR} in Eq. 2.10i.
- the estimated inclination angle, the maximum apparent jet speed and diameter of the core component are applied to Eq. 2.10i in order to get an estimate for the magnetic field strength in the radio core.

2.8 Scaling the magnetic field down to the SMBH

The absolute position of the radio cores with respect to the jet engine is not known due to the use of the closure relations in the imaging process which destroys the absolute phase information, (Jennison 1958). Also it is not clear where - with respect to the position of host galaxies' SMBH, which is also often not known - the position of the radio core ($\tau \sim 1$) is located. Therefore the scaling of the calculated core magnetic field is arbitrary. However utilizing different ideas of magnetic fields in the SMBH's ergospheres, estimates of the scales of distances between the magnetic fields in the supposed ergosphere and the magnetic field in the radio cores can be calculated. The scaling of the magnetic field

from the ergosphere to the radio core is assumed to follow a power law like:

$$\begin{aligned} B_{c,\nu} &= B_{\text{ergosphere}}\, r_\nu^{-b} \\ r_\nu &= \left(\frac{B_{\text{ergosphere}}}{B_\nu}\right)^{\frac{1}{b}} . \end{aligned} \tag{2.11a}$$

In the following, two different cases, describing $B_{\text{ergosphere}}$ are studied. The first case assumes that the magnetic field strength in the ergosphere nears the Eddington field (Daly 2009, 2011; Daly & Sprinkle 2014):

$$\frac{B_{\text{Eddington}}}{10^4}\, G = 6 \times \left(\frac{M}{10^8 M_\odot}\right)^{-\frac{1}{2}} \tag{2.11b}$$

Secondly it is assumed that the jet is driven by the Blandford & Znajek (1977) process. In this case a polodial magnetic field component, driven by the spin of the black hole supports a jet with a certain luminosity. Daly & Sprinkle (2014) show the formula for the polodial magnetic field component

$$\frac{B_{\text{Blandford-Znajek}}}{10^4\, G} = \left(\frac{P_j}{10^{44}}\right)^{0.5} \left(\frac{M}{10^8}\right)^{-1} \frac{\sqrt{5}}{j} \tag{2.11c}$$

In both cases the black hole masses need to be known. The black hole masses are listed with references in Table 2.2. For sources in the sample, where no mass is given, no scaling will be done. In the second case, the spin parameter is set to $j = 0.5$ which of course will not yield absolute positions, however possible relative distances within the source classes will still be measurable. This is a reasonable guess, since in radio galaxies spin parameters rangeing between $0.1 \lesssim j \lesssim 0.99$ are found, see Daly & Sprinkle (2014). The jet powers P_j are obtained by estimating the power budget of the extended, un-beamed emission in the manner of Godfrey & Shabala (2013). For this the luminosities of the extended emission is obtained for each of the sources from Kharb et al. (2010). The jet powers, under the assumption, FSRQs can be associated with rotated FR2 galaxies and BL Lacs with FR1 galaxies, can be estimated according to

$$\begin{aligned} P_{j,\text{FSRQs}} &= 3 \times 10^{44} \left(\frac{L_{151}}{10^{25}}\right)^{0.67} W \\ P_{j,\text{BLLacs}} &= 5 \times 10^{44} \left(\frac{L_{151}}{10^{25}}\right)^{0.64} W . \end{aligned} \tag{2.11d}$$

In Kharb et al. (2010), the luminosities are measured at 1.4 GHz, the method from Godfrey & Shabala (2013) measures at 0.151 GHz, therefore the Flux is scaled to the needed frequency with a power law of $\alpha \sim -0.75$ due to the steepened spectrum of the

extended, un-beamed emission of blazars at these frequencies.

Chapter 3

Statistical analysis of blazar light curves in the γ-ray regime

Beilzeit, Schwertzeit, zerschmetterte
Schilde, Windzeit, Wolfszeit, bis
einstürzt die Welt

Völuspa, v. 45/46

The atmosphere is opaque from energies of several electronvolts up to the highest measured energies of cosmic particles $E \sim 10^{20}\,\mathrm{eV}$. In order to collect data in the $\mathrm{MeV} - \mathrm{GeV}$ range several satellites have been placed in orbit around Earth in the past, like the second Small Astronomy Satellite (SAS-2), observing at energies $E > 35$ MeV (Fichtel et al. 1975), the COS-B satellite ($E_{\mathrm{obs}} > 20$ MeV) (e.g. Bignami et al. 1975; Bignami & Hermsen 1983) and CGRO with the EGRET-detector ($E_{\mathrm{obs}} > 50$ MeV) (e.g., Thompson et al. 1993b, 1995). Building on the success of these early instruments which already detected the high-energy emission from several AGN (Thompson et al. 1993a, e.g.,), NASA launched the *Fermi* satellite on June 8, 2008. Onboard the satellite the pairconversion Large Area Telescope (LAT) is mounted. In the following this instrument is referred to as *Fermi*-LAT. The following basic technical explanation concerning the *Fermi*-LAT is based on Atwood et al. (2009).

3.1 Fermi Large Area Telescope

Fermi-LAT consists of four main components, a precision-converter tracker, the calorimeter, an anti-coincidence detector and a data acquisition system. The converter tracker

is composed of 16 towers. Each tracker tower includes 16 layers of planes of material with high order atomic number (in this case tungsten) in order to maximize the probability of electron-positron pair production by an incoming photon. The converter planes track the charged particles on their way through the detector which allows to reconstruct the direction of the photon with a precision (angular resolution), depending on the photon energy, between 0.15° at the highest energies and 3.5° at the lowest energies. The calorimeter consists of 96 scintillator crystals arranged in 8 horizontal layers. The calorimeter measures the energy deposition due to electromagnetic particle showers resulting from the electron-positron pair. The development of the shower profile can be tracked in time which can be used to distinguish the signal from the background noise. The energy resolution which is also largely determined by the calorimeter, depends on the energy but also on the inclination angle of the incoming photon and ranges between 6% and 15%. A schematic representation is shown in Fig. 3.1. The anti-coincidence detector provides a charged-particle background rejection (cosmic ray filter) to ensure that the measured electron-positron pair originates from an incident photon. The data acquisition system collects the data from the sub-systems and provides a first, on-board science analysis platform in order to quickly react to transient phenomena. *Fermi*-LAT is sensitive in the energy range from 20 MeV up to 2 TeV. Its field of view is $\sim 2.4\,\mathrm{sr}$ at an energy of ~ 1 GeV. The *Fermi* satellite orbits earth in a distance of ~ 565 km above the surface at an inclination of $\sim 25.5°$. One orbit around earth takes $\sim 3\,\mathrm{h}$ and the sky exposure is nearly uniform within two orbits, where any single region is observed about $\sim 30\,\mathrm{min}$. This means that each day ~ 24 all-sky exposures can be obtained. This has been going on for the last 13 years, providing an excellent data basis for γ-ray blazar light curves.

3.2 Samples of gamma-ray light curves of blazars

3.2.1 Monthly-binned light curves

Due to continuous all-sky monitoring of *Fermi*-LAT since 2008, it is possible to acquire light curves for a large number of γ-ray sources for the time span of over a decade. For the purpose of illustrating the power of the OU-process the same sources as used in IceCube Collaboration et al. (2018a), Peñil et al. (2020) and Burd et al. (2021), are analyzed in this context. This data set was originally used in a chance coincidence study for the neutrino event $IC170922A$ (IceCube Collaboration et al. 2018a). The data set contains light curves of 2278 extra-galactic *Fermi*-LAT sources, with a time binning of 28-days and were computed for energies above 1 GeV. The light curves were kindly provided by Prof. Sara Buson, who has produced the light curves in accordance to the *Fermi*-LAT

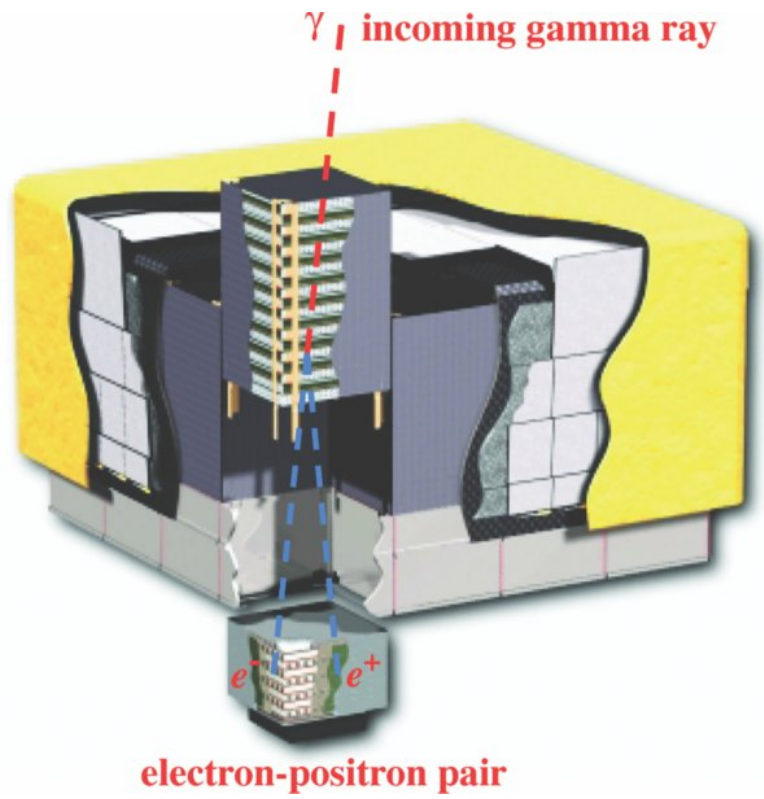

FIGURE 3.1: Schematic illustration of the *Fermi* LAT. An incident photon, passing through the converter tracker and the calorimeter, producing an electron/positron pair. From: Atwood et al. (2009).

collaboration recommendations for point-source analysis[1]. In the following I will list the parameters used in the analysis, which are also listed in IceCube Collaboration et al. (2018a) and Burd et al. (2021):

- In a time interval between August 2008 and October 2017, *Fermi*-LAT data were analyzed with the *Fermi*-LAT ScienceTools package[2] (v11r05p3). The version of the instrument response functions was P8R2_SOURCE_V6 and the fermipy software package (Wood et al. 2018).
- A zenith angle filter of $\theta < 90\,\mathrm{deg}$ was applied in order to reduce the contamination of atmospheric γ photons.
- Standard quality cuts were applied. $(DATA\_QUAL > 0)\&\&(LAT\_CONFIG == 1)$
- Time periods, coinciding with bright solar flares and γ-ray bursts where excluded.
- For each source a $10\,\mathrm{deg} \times 10\,\mathrm{deg}$ region of interest around the source is considered in the analysis.

[1] http://fermi.gsfc.nasa.gov/ssc/data/analysis/documentation/Pass8_usage.html
[2] http://fermi.gsfc.nasa.gov/ssc/data/analysis/

- The flux of each time bin was derived by modelling the source itself and its surrounding 15 deg $\times$15 deg region was considered via a spatially and energetically binned likelihood analysis. Included in the model is also the diffuse isotropic and the galactic background.

For the analysis in Burd et al. (2021), only flux bins above the significance level, defined by a so-called test statistics (TS) are considered. The test statistic is a measure of the significance of the detection of an astrophysical signal (Mattox et al. 1996). The null hypothesis is that no source is there, the alternative hypothesis is that a source is present. The significance is estimated through a likelihood ratio test. This is possible due to Wilks' theorem (Wilks 1938) which states that the likelihood ratio (i.e. the TS) follows a χ^2 distribution with N degrees of freedom, where N is the number of additional parameters in the alternative model. Let $\mathcal{L}_1$ be the maximum likelihood for the hypothesis that the photon origins from a certain source and $\mathcal{L}_2$ be the maximum likelihood that an additional photon source is present. The TS-parameter can be calculated as $\mathrm{TS} = -2\ln(\mathcal{L}_2/\mathcal{L}_1)$, (Wilks 1938; Mattox et al. 1996). For all light curves Burd et al. (2021) used a TS ≥ 9 filter (henceforth called TS9 filter) on each time bin which corresponds to a $\sim 3\sigma$ (Mattox et al. 1996). Light curves with more than 62% of the data points being flagged flagged according to this criterion, are not considered in this study due to the too poor sampling. Applying this filter, 253 of the original 2278 light curves remain. Those 253 source are composed of 144 BL Lac objects, 88 FSRQs, 4 unclassified blazars, 4 Pulsars, 4 radio galaxies, 7 unclassified sources, one AGN of unknown class, and one narrow-line Seyfert 1 Galaxy (Abdollahi et al. 2020; Ajello et al. 2020). In the context of this work and Burd et al. (2021), only blazars are of interest, which account for 236 of the 2278 sources in the entire sample.

3.2.2 Weekly-binned light curves from the 20 radio sources

With a similar procedure as described above, Andrea Gokus kindly provided me with weekly binned *Fermi*-LAT light curves for the 20 sources from the radio sample, described in Sect. 2.3. Of the 28 sources, light curves from 20 sources could be obtained 0219+428, 0415+379, 0430+052, 0528+134, 0735+178, 0829+046, 0836+710, 0851+202, 0954+658, 1127-145, 1219+285, 1222+216, 1226+023, 1253-055, 1308+326, 1633+382, 1730-130, 1749+096, 2200+420 and 2223-052.

3.3 Statistical analysis of light curves

This section is the culmination of an effort I started with several students, where we studied to understand whether light curves can be explained in the context of simple stochastic processes. Each student worked with me on different aspects, written down in their respective Bachelor and Master theses. Niklas Richter (Richter 2019) simulated light curves by applying a random number of Gaussian shots with random amplitude into a constant flux stream. Max Knopf (Knopf 2020) studied the behavior of rise and decay times with an algorithm inspired by the topographic prominence in geography. Luca Kohlhepp (Kohlhepp 2020) intensively worked with me on the Ornstein-Uhlenbeck process and Sarah Wagner refined the methods used in Meyer et al. (2019) which allow to identify outbreaks in light curves and determine the rise and decay times of these (Wagner 2020; Wagner et al. 2021). In Burd et al. (2021) and Wagner et al. (2021) we presented many aspects of this about a year and a half lasting endeavor.

3.3.1 Ornstein-Uhlenbeck parameter extraction

According to the Wold-theorem (Wold 1939), any stationary process can be de-composed into a deterministic and a non-deterministic part. This is the basis of a procedure, presented in Burd et al. (2021), which allows to extract the OU parameters of a given light curve, more specifically the time series of the light curve. For the OU-process to reproduce authentic synthetic light curves, two main properties have to be mimicked: I) The flux is non-negative. II) Large outbreaks in flux, with respect to a certain flux-base level, are sparse. The time series X of a light curve in this context is defined as the logarithm of the flux values $X = \log_{10}(F)$. The synthetic OU light curve Y_{OU} is defined as the power of the OU time series (base 10) $Y_{OU} = 10^{X_{OU}}$. The extraction algorithm of the OU parameters are all applied to all time series. Following what was presented in Burd et al. (2021), the extraction of μ simply is the expectation value (mean) of the time series. Following the Wold-theorem, any time series can be decomposed into a white noise part (non-deterministic), and a correlated colored noise part (deterministic).

3.3.1.1 Extraction of σ - approximating the non-deterministic part

In order to extract σ, the following ansatz is applied to Eq. 1.3c: Let u_T be the sum of the mean reversion level μ and a small derivation ϵ from μ such that

$$u_T = \mu + \epsilon, \tag{3.1a}$$

thus Eq. 1.3c reads

$$u_{T+1} = u_T + \theta\Delta t(\mu - (\mu + \epsilon)) + \sigma\sqrt{\Delta t}\mathcal{N}(t). \tag{3.1b}$$

Therefore the difference between two subsequent time steps reads

$$u_{T+1} - u_T = -\theta\Delta t\ \epsilon + \sigma\sqrt{\Delta t}\mathcal{N}(t). \tag{3.1c}$$

In cases where $\epsilon \ll \frac{\sigma\sqrt{\Delta t}}{\theta\Delta t}$, the θ-terms become negligible, and therefore

$$u_{T+1} - u_T = \mathcal{N}(0, \sigma^2\Delta t, t) \tag{3.1d}$$

The variance on both sides of the equation can be calculated

$$\mathrm{Var}(u_{T+1} - u_T) = \mathrm{Var}(\mathcal{N}(0, \sigma^2\Delta t, t)) = \sigma^2\Delta t, \tag{3.1e}$$

and thus

$$\sigma\sqrt{\Delta t} = \sqrt{\mathrm{Var}\left(\left\{u_{T+1} - u_T \middle| u_T < \epsilon \ll \frac{\sigma\sqrt{\Delta t}}{\theta\Delta t}\right\}\right)}. \tag{3.1f}$$

3.3.1.2 Extraction of θ - approximating the deterministic part

We used the proof of stationarity of the OU process to obtain an expression for the variance of the OU process (see appendix A2, Eq. A.3d in Burd et al. 2021).

$$\mathrm{Var}(u(t)) = \frac{\sigma^2\Delta t}{1 - (1 - \theta\Delta t)^2} \tag{3.2a}$$

Let $\alpha = 1 - \theta\Delta t$. Solving Eq. 3.2a for α yields

$$\alpha = \pm\sqrt{1 - \frac{\sigma^2\Delta t}{\mathrm{Var}(u_T)}}, \tag{3.2b}$$

which is insensitive to the sign of the deviation from μ.

$$|\alpha| = \sqrt{1 - \frac{\sigma^2\Delta t}{\mathrm{Var}(u_T)}} \tag{3.2c}$$

To obtain information on the sign of α, one can proceed with a similar ansatz as before when extracting $\sigma\Delta t$. In this case Eq. 1.3c is considered for cases where the impact of the white noise term is small with respect to the θ-terms, $\mathcal{N}(t) \ll \frac{\alpha u_T + \theta\Delta t\mu}{\sigma\sqrt{\Delta t}}$ and for large deviations from μ.

$$u_{T+1} = u_T + \theta\Delta t(\mu - u_T) \tag{3.2d}$$

This method to extract θ is less precise than the method using the variance, because data points with large deviations from the mean are sparse. However it is precise enough to extract the sign and use it in combination with the variance method. Solving Eq. 3.2d for α, yields

$$\alpha_{\pm} = \left\langle \left\{ \frac{u_{T+1} - \mu}{u_T - \mu} \middle| \mathcal{N}(t) \ll \frac{\alpha u_T + \theta \Delta t \mu}{\sigma \sqrt{\Delta t}} \right\} \right\rangle \tag{3.2e}$$

The absolute value of α from the variance (Eq. 3.2c) and the sign obtained by approximating the colored noise part of a time series (Eq. 3.2e) can now be combined to obtain

$$\alpha = \text{sign}(\alpha_{\pm}) \ |\alpha| \tag{3.2f}$$

and thus the mean reversion rate is

$$\theta \Delta t = 1 - \text{sign}(\alpha_{\pm}) \ |\alpha| \,. \tag{3.2g}$$

3.3.1.3 The calibration of the ϵ environment

We calibrated the best ϵ environment in both cases, the $\sigma\sqrt{\Delta t}$ and $\theta \Delta t$ with a data set of 10^5 OU light curves[3], where we extracted the parameters and compared them to the parameters, set in the simulation (Burd et al. 2021). In Kohlhepp (2020) we considered many different methods fo the calibration of the ϵ environments, like fractions of the maximum values in the time series, or a fraction of the expectation value. The best way to do this turned out to be by applying a factor onto the standard deviation of the flux variation. The resulting parameters are $\epsilon_\sigma = [\pm(0.343 \pm 0.004) \ \text{std}(X)]$ and $\epsilon_\theta = [\pm(1.48 \pm 0.34) \ \text{std}(X)]$ (see Sect. 4.4 in Burd et al. 2021). The concept of the ϵ parameters is illustrated in Fig. 3.2.

3.3.2 Further light curve analysis - asymmetry measure of flares and power spectral densities

In order to measure the asymmetry between the rise and decay time (t_r, t_d) of a flare

$$A = \frac{t_r - t_d}{t_r + t_d}, \tag{3.3a}$$

it is necessary to define what a flare in this context is supposed to be. The term flare, loosely spoken, defines a sudden bright event. In solar physics, the term flare is used in the context of magnetic reconnection events, ejecting mass from the sun (Kopp & Pneuman 1976). In the analysis of AGN light curves, however, the term is often used

[3] OU light curves are generated with a given set of OU parameters which are not necessarily obtained from measured light curves.

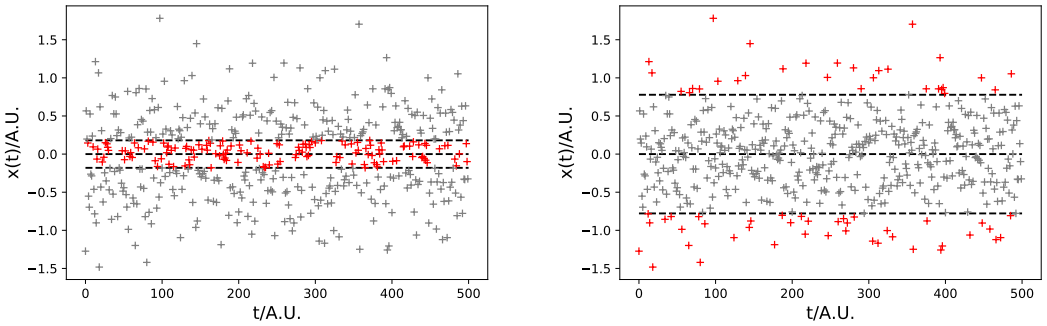

FIGURE 3.2: OU time series with 500 simulated time steps and $(\mu, \sigma, \theta) = (0, 0.5, 0.5)$. *Left:* the red colored data points are used to extract the σ parameter in a region $[\pm(0.343 \pm 0.004)$ std] around the mean. With this procedure, the bins fluctuating very close to the mean - representing stochastic fluctuations (σ) - are factored in. *Right:* the red colored data points are used to extract the θ parameter in a region $[\pm(1.48 \pm 0.34)$ std] around the mean. The bins determined with this procedure represent fluctuations that deviate largely form the mean which are assumed to be due to the deterministic drift of the stochastic process (θ).

very loosely to describe (often subjectively) interesting flux variations, without knowing the physical cause for such events in many cases. Due to the fact that a physical cause cannot be directly observed or even properly determined in many cases, there are some important questions that have to be answered and applied consistently in order to analyze flares in the context of blazar light curves and a non-physical parametrization:

- What is a flare? This question addresses the issue of what a flux variation has to fulfill in order to be significant enough to count as flare.
- When does a flare start and when does a flare end?

In order to address the first point, it is necessary to suppress statistical fluctuations in a light curve in order to find significant variations in the flux. This can be achieved by the Bayesian Block algorithm (Scargle et al. 2013a,b) and has been applied on *Fermi*-LAT light curves by Krauß et al. (2016), Meyer et al. (2019), Burd et al. (2021), Gokus et al. (2021) and Wagner et al. (2021). According to Scargle et al. (2013a) the Bayesian block algorithm segments the data in a way that imposes a number if blocks N_B which is smaller than the number of given data points in the light curve N with a geometric prior and a free parameter f.

$$P(N_b) = \begin{cases} P_0 f^{N_b} \text{ if } 0 \leq N_b \leq N \\ 0 \text{ else} \end{cases} \tag{3.3b}$$

P_0 is given by

$$P(N_b) = \frac{1-f}{1-f^{N_b+1}} f^{N_b} \tag{3.3c}$$

The expectation value of the number of Bayesian blocks is then given by

$$\langle N_b \rangle = \sum_{N_b=0}^{N} N_b f^{N_b} = \frac{N f^{N+1}}{f^{N+1} - 1} + \frac{1}{1-f} \tag{3.3d}$$

The choice of the prior function influences the number of Bayesian blocks that are assigned in a light curve, which basically is controlled by free parameter f. For $f \to 0$ fewer blocks are found to represent a given light curve if $f \to 1$ each time step is assigned one block which is basically over-fitting. In this thesis I adapt $f = 0.01$ which yields a good balance between suppressing the statistical fluctuation while finding potential interesting flux segments in a light curve while not over-fitting the data. In order to identify a flare, different methods can be considered. Meyer et al. (2019) used a baseline (mean value of flux distribution) to identify blocks which are above and below this baseline. Blocks, above the baseline are defined as a flare. The time period of a flare is defined by the first block above the baseline and the length of the subsequent block up to the first one that descends below the baselines, as seen in Fig. 3.3 (top). This idea is based on the so-called HOP algorithm (Eisenstein & Hut 1998) to identify HOP groups in the Bayesian block representation of the light curve, which define a flare. In Wagner (2020) and Knopf (2020) we developed several different methods to define a flare which are independent of the choice of a baseline. Most of these methods were summarized by Sarah Wagner in a python class for easy use[4]. The problem of the somewhat arbitrary choice of a baseline can at least be resolved to a certain degree by analyzing local maxima and minima in the Bayesian block representation of a light curve, for instance in the methods shown in Fig. 3.3 (second from top - bottom). The 'half'-method (second from top in Fig 3.3) splits the valley blocks between two subsequent groups in half in order to define the start end the end of one HOP group. The 'flip' method also is independent of a baseline (second from top in Fig 3.3). The slope of a HOP group is extrapolated by flipping the length of the adjacent block onto the valley block. The start then sits at the right side of the bordering edge of the valley block plus the length of the adjacent block. The 'sharp'-method , cuts the HOP group right at the edges (Fig 3.3, bottom). In the following I will use the 'half' method, because it allows to use as many blocks as possible while not extending the rise or decay time of a flare too much. The 'half' method, however could prolong a flare unnaturally, when a valley block becomes very long in cases of a source not showing activity in a long period of time. On the other hand, the 'sharp'-method does not take a possible slope of the rise or decaying time of a flare into account in any case. The 'half' method has proven to be a good trade-off between an arbitrary choice of how to define a flare with start and end points, while allowing to analyze as many data as possible. In all methods, in order to obtain the

[4] https://github.com/swagner-astro/lightcurves

rise and decay time of a flare $t_{r/d}$, the highest value block in a HOP group is split in half which marks the peak of a flare. The rise time is the time span between the start time and that peak, the decay time is the time span between peak and the end point of the HOP group. In order to properly study the flare shape asymmetry, certain artefacts have to be accounted for. Flares, that are described by a single Bayesian block for example will by definition have an asymmetry of $A = 0$. These are filtered out in every case. It is also possible, due to the binning of the light curve itself that flares built of more blocks have to be excluded because they might contain too few data points and unnaturally accumulate at certain values which would lead to sharp peaks in the Bayesian binned histogram of the asymmetry measure, see Burd et al. (2021) and Wagner et al. (2021). This has to be assessed for each sample and each TS filter separately. These artifacts have to be taken into account when analyzing a possible trend in the asymmetry measures. Another aspect which will be studied for each light curve, is the slope of the PSD, ξ. The periodogram for each light curve is calculated with the Lomb-Scargle algorithm. (Lomb 1976; Scargle 1982; Townsend 2010).

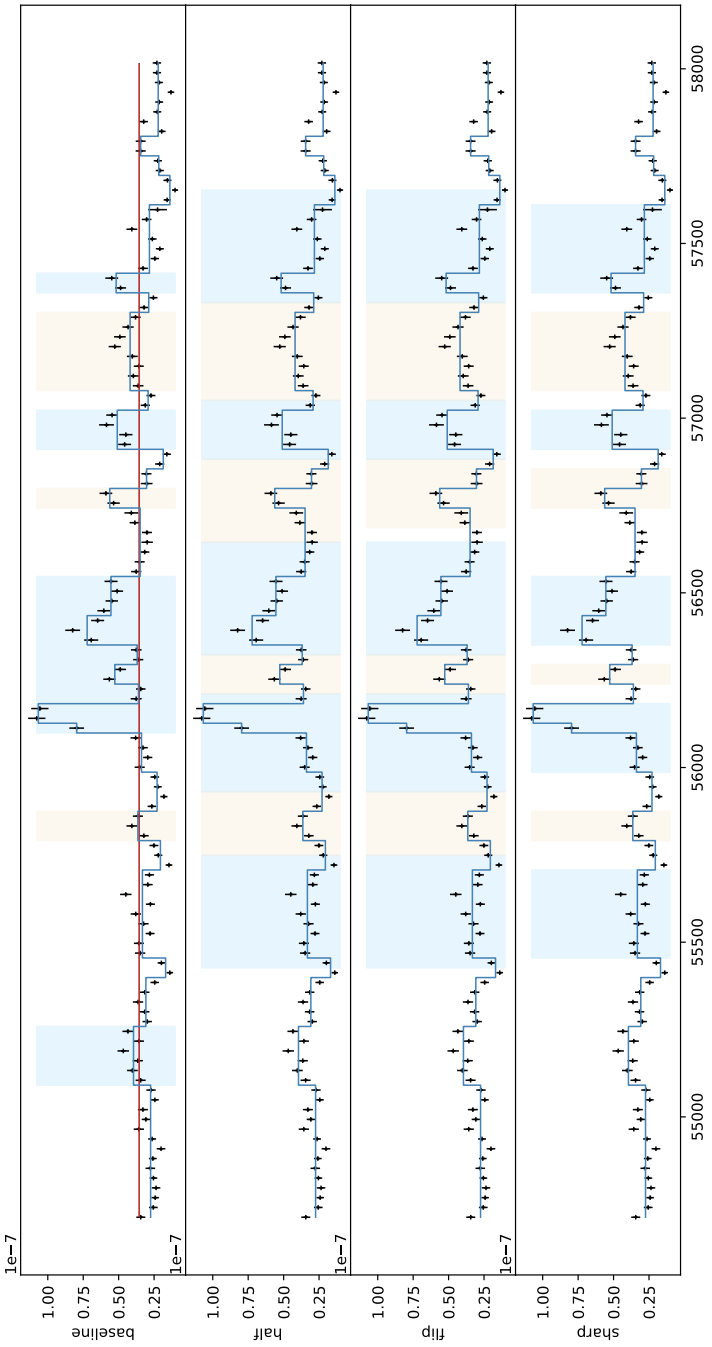

FIGURE 3.3: Bayesian block representation of the monthly binned light curve of Mrk 421. The x-axes represent the time in MJD and the y-axes represent the flux in erg cm^{-2} s^{-1}. *Top*: Definition of a flare as given in Meyer et al. (2019), where all Bayesian blocks above a certain base line are defined as a flare. All subsequent blocks belong to the flare, until a block again is below the baseline. *Second from top:* The 'half'-method abandons the necessity of a baseline (of any kind). The valley between two subsequent groups is split in half in order to define the start end the end of one HOP group. *Third from top:* The 'flip' method also is independent of a baseline. The slope of a HOP group is extrapolated by flipping the length of the adjacent block onto the valley block. The start then sits at the left side of the bordering edge of the valley block minus the length of the adjacent block. *Bottom:* The 'sharp'-method , cuts the HOP group right at the edges.

Chapter 4

The brightness temperature, geometry and magnetic field structure of parsec-scale blazar jets

In die Wiege gelegt der Verfall

Verborgene Wege, P. R. Burd, A. Kieckhöfel

In this chapter I will show and discuss the results from the analysis, based on the MODELFIT components of each of the 28 sources (Sect. 2.3). I will show the sample results from the single power law fits regarding the jet diameter, brightness temperature and the scaling of the magnetic field strength, as well as the estimation of the magnetic field strength in the respective radio core and the estimation of the jet power of each source. After this, the study of possible geometry breaks is presented and analyzed, followed by a detailed section for each source where possible peculiarities will be addressed on a source by source base. All histograms in the following are shown in Bayesian binning[1] and are normalized in a way that the bin width multiplied with the bin height yields unity, equal to a probability density plot.

[1]Implemented in AstroPy (Astropy Collaboration et al. 2013; Price-Whelan et al. 2018), `https://docs.astropy.org/en/stable/api/astropy.visualization.hist.html`

4.1 Sample results of single power law fits

The results of the single power law fits for each source in the diameter vs. core distance and brightness temperature vs. core distance are listed in table 4.1. The distributions of the l-values for both frequencies are compared in Fig. 4.1. The distributions of the s-values for both frequencies are compared in Fig. 4.3. Each frequency is analyzed with respect to possible differences between the source classes. The corresponding plots are shown in Fig. 4.2 and Fig. 4.4. For each analyzed pair a two sided Kolmogorov-Smirnov (KS) test is performed with the H_0-hypothesis, that the two test distributions are drawn from the same overall distribution[2]. The results of this analysis are listed in table 4.2 and 4.3 for the l and s-values respectively.

4.1.1 Results of the diameter gradients

The comparison of both frequencies along the entire jet length, see Fig 4.1, yields a tentative difference between the two frequencies (KS: $p \sim 2.6\%$) which is not measurable when analyzing the jets in the overlap region between the two frequencies (KS: $p \sim 94\%$). In the overlap region and along the entire jet length, the l-values at both frequencies are weakly correlated at most $[R_{\mathrm{spearman}}, R_{\mathrm{pearson}}, \tau_{\mathrm{kendall}}]_{l_{15,43}} = [0.37, 0.42, 0.27]$,$[R_{\mathrm{spearman}}, R_{\mathrm{pearson}}, \tau_{\mathrm{kendall}}]_{l_{15,43,ol}} = [0.25, 0.43, 0.15]$. The results of the analysis of both frequencies with respect to the different source classes are illustrated in Fig. 4.2 and listed in table 4.2. In the following I will only discuss compared pairs that show a p-value of less than 5% from the KS test. Comparing the l-values with respect to the source classes FSRQs (Q) and BL Lacs (B) yields that FSRQs are more collimated than BL Lacs at 15 GHz along the entire jet length (KS: $p \sim 0.24\%$) however in the overlap region between the frequencies, this difference vanishes (KS: $p \sim 62\%$). Both, along the entire jet length and the overlap region, the χ^2_{red}-values are systematically larger for FSRQs than for BL Lacs (KS full jet length: $p \sim 0.24$ %; KS overlap region: $p \sim 3.2$ %). At 43 GHz a difference between the FSRQs and BL Lacs cannot be measured along the entire jet length (KS: $p \sim 12$ %). However, a hint for more collimated FSRQs can be seen in the overlap region (KS: $p \sim 2.7$ %).

4.1.2 Results of the brightness temperature gradients

The comparison of both frequencies along the entire jet length, see Fig 4.3 yields no difference between the two frequencies (KS: $p \sim 55\%$) which is also not measurable when

[2]Implemented in SciPy (Virtanen et al. 2020), https://docs.scipy.org/doc/scipy/reference/generated/scipy.stats.ks_2samp.html

TABLE 4.1: Fitting results of jet geometry and brightness-temperature gradients. For each source, the top row refers to the full jet length probed and the bottom row refers to the overlap region probed at both frequencies; Columns: (1) IAU B 1950 name, (2) Fit parameter of jet-geometry at 15 GHz l (reduced χ^2), (3) Fit parameter of jet-geometry at 43 GHz l (reduced χ^2), (4) Fit parameter of brightness-temperature gradient at 15 GHz l (reduced χ^2), (3) Fit parameter of brightness-temperature gradient at 43 GHz l (reduced χ^2). From: Burd et al. (2022)

Name	l_{15}	l_{43}	s_{15}	s_{43}
0219+428	1.02 ± 0.17 (1.0)	0.57 ± 0.16 (0.9)	-2.05 ± 0.43 (2.1)	-1.6 ± 0.35 (1.1)
	0.63 ± 0.12 (0.4)	0.56 ± 0.17 (1.1)	-2.08 ± 0.38 (1.1)	-1.45 ± 0.36 (1.2)
0336-019	0.7 ± 0.17 (3.5)	0.81 ± 0.25 (2.7)	-1.12 ± 0.38 (3.8)	-1.87 ± 0.48 (3.1)
	0.68 ± 0.18 (3.9)	0.84 ± 0.26 (3.0)	-1.18 ± 0.36 (3.1)	-1.7 ± 0.51 (3.6)
0415+379	0.62 ± 0.19 (2.5)	0.53 ± 0.2 (1.2)	-1.83 ± 0.59 (5.3)	-1.51 ± 0.55 (2.5)
	0.58 ± 0.2 (2.8)	0.6 ± 0.18 (1.3)	-1.57 ± 0.63 (6.0)	-1.56 ± 0.53 (2.7)
0430+052	0.56 ± 0.23 (5.6)	0.46 ± 0.17 (1.0)	-1.54 ± 0.54 (6.5)	-1.67 ± 0.48 (2.3)
	0.56 ± 0.19 (3.0)	0.43 ± 0.18 (1.2)	-1.42 ± 0.54 (5.0)	-1.44 ± 0.51 (2.5)
0528+134	0.79 ± 0.21 (1.8)	0.45 ± 0.19 (1.5)	-2.65 ± 0.46 (2.5)	-1.23 ± 0.43 (2.4)
	0.6 ± 0.18 (1.8)	0.51 ± 0.19 (1.5)	-2.34 ± 0.59 (4.5)	-1.94 ± 0.43 (2.4)
0716+714	0.84 ± 0.16 (0.6)	0.78 ± 0.21 (1.8)	-3.0 ± 0.35 (0.3)	-2.6 ± 0.52 (1.0)
	0.79 ± 0.14 (0.6)	0.78 ± 0.19 (1.5)	-2.84 ± 0.35 (0.3)	-2.56 ± 0.46 (0.7)
0735+178	0.85 ± 0.08 (0.6)	0.77 ± 0.21 (1.2)	-2.46 ± 0.37 (2.3)	-1.75 ± 0.36 (1.0)
	0.83 ± 0.08 (0.7)	0.75 ± 0.21 (1.2)	-1.85 ± 0.33 (1.6)	-1.77 ± 0.29 (0.8)
0827+243	0.82 ± 0.19 (1.2)	0.56 ± 0.17 (0.7)	-2.61 ± 0.47 (1.6)	-2.55 ± 0.48 (1.6)
	0.83 ± 0.17 (1.0)	0.54 ± 0.14 (0.6)	-3.11 ± 0.5 (2.2)	-2.74 ± 0.44 (1.4)
0829+046	0.98 ± 0.13 (1.0)	0.7 ± 0.23 (1.7)	-2.56 ± 0.3 (0.9)	-1.87 ± 0.54 (1.8)
	0.7 ± 0.12 (0.6)	0.79 ± 0.24 (1.8)	-2.0 ± 0.33 (0.9)	-1.89 ± 0.56 (2.0)
0836+710	0.77 ± 0.18 (2.7)	0.37 ± 0.22 (3.9)	-1.96 ± 0.49 (14.2)	-1.97 ± 0.7 (15.8)
	0.46 ± 0.18 (1.2)	0.3 ± 0.22 (4.7)	-1.98 ± 0.52 (14.1)	-1.63 ± 0.66 (15.9)
0851+202	0.88 ± 0.19 (1.5)	0.82 ± 0.34 (5.1)	-2.87 ± 0.46 (2.9)	-2.79 ± 0.81 (8.3)
	0.69 ± 0.17 (1.3)	0.94 ± 0.33 (5.7)	-2.1 ± 0.49 (3.0)	-3.05 ± 0.77 (8.7)
0954+658	1.2 ± 0.21 (1.2)	1.09 ± 0.25 (2.8)	-3.39 ± 0.47 (1.3)	-2.97 ± 0.52 (2.4)
	1.37 ± 0.21 (1.2)	1.17 ± 0.26 (3.1)	-3.98 ± 0.5 (1.6)	-3.32 ± 0.52 (2.7)
1101+384	0.89 ± 0.19 (1.8)	0.61 ± 0.26 (1.9)	-2.19 ± 0.26 (0.9)	-1.57 ± 0.46 (1.5)
	0.75 ± 0.15 (1.9)	0.65 ± 0.27 (2.0)	-2.2 ± 0.2 (1.1)	-1.57 ± 0.45 (1.5)
1127-145	0.48 ± 0.24 (6.3)	0.35 ± 0.26 (7.1)	-1.14 ± 0.66 (10.7)	-1.52 ± 0.62 (6.1)
	0.41 ± 0.27 (7.5)	0.71 ± 0.25 (5.8)	-1.03 ± 0.61 (9.2)	-2.18 ± 0.6 (6.1)
1156+295	0.76 ± 0.16 (3.6)	0.73 ± 0.18 (1.6)	-2.47 ± 0.39 (1.1)	-2.24 ± 0.49 (2.5)
	0.55 ± 0.14 (0.5)	0.73 ± 0.18 (1.6)	-2.21 ± 0.47 (1.4)	-2.44 ± 0.49 (2.7)
1219+285	0.77 ± 0.2 (2.1)	0.73 ± 0.23 (1.3)	-1.78 ± 0.38 (1.3)	-1.76 ± 0.5 (1.9)
	0.98 ± 0.18 (0.8)	0.74 ± 0.26 (1.7)	-2.58 ± 0.32 (0.5)	-1.56 ± 0.52 (2.2)
1222+216	0.85 ± 0.19 (2.2)	0.55 ± 0.17 (0.7)	-2.17 ± 0.58 (3.5)	-2.5 ± 0.58 (2.3)
	0.93 ± 0.14 (0.4)	0.53 ± 0.18 (0.8)	-3.47 ± 0.52 (2.1)	-2.89 ± 0.61 (2.7)
1226+023	0.68 ± 0.21 (12.9)	0.5 ± 0.23 (4.7)	-1.86 ± 0.47 (9.1)	-1.65 ± 0.47 (3.6)
	0.81 ± 0.24 (9.1)	0.48 ± 0.23 (5.2)	-1.93 ± 0.5 (6.8)	-1.63 ± 0.46 (3.8)
1253-055	0.85 ± 0.3 (10.1)	0.44 ± 0.24 (3.7)	-2.33 ± 0.63 (9.2)	-1.95 ± 0.69 (4.6)
	0.92 ± 0.22 (4.0)	0.6 ± 0.24 (3.6)	-2.96 ± 0.5 (4.2)	-2.53 ± 0.69 (4.3)
1308+326	0.9 ± 0.25 (2.8)	0.87 ± 0.25 (2.6)	-2.58 ± 0.61 (3.6)	-2.81 ± 0.66 (3.7)
	0.69 ± 0.21 (1.9)	0.87 ± 0.25 (2.6)	-2.88 ± 0.56 (3.1)	-2.81 ± 0.66 (3.7)
1633+382	0.74 ± 0.22 (4.8)	0.71 ± 0.22 (2.9)	-2.16 ± 0.47 (5.3)	-1.9 ± 0.45 (4.2)
	0.75 ± 0.23 (5.2)	0.72 ± 0.22 (3.0)	-1.84 ± 0.49 (7.1)	-1.92 ± 0.44 (4.6)
1652+398	0.64 ± 0.14 (6.5)	0.51 ± 0.22 (1.4)	-1.72 ± 0.18 (1.2)	-1.33 ± 0.39 (2.0)
	0.53 ± 0.15 (0.6)	0.81 ± 0.16 (0.8)	-1.37 ± 0.17 (0.3)	-1.51 ± 0.16 (0.4)
1730-130	0.68 ± 0.2 (9.4)	1.04 ± 0.26 (2.8)	-1.63 ± 0.46 (6.5)	-2.78 ± 0.48 (2.9)
	0.85 ± 0.21 (5.8)	1.05 ± 0.26 (2.9)	-2.64 ± 0.39 (3.7)	-2.79 ± 0.44 (2.8)
1749+096	0.98 ± 0.16 (0.9)	0.79 ± 0.26 (2.5)	-3.1 ± 0.34 (1.0)	-3.19 ± 0.64 (3.7)
	0.99 ± 0.17 (1.0)	0.95 ± 0.27 (2.5)	-3.34 ± 0.38 (1.2)	-3.47 ± 0.54 (2.6)
2200+420	1.59 ± 0.3 (5.1)	0.84 ± 0.18 (3.4)	-2.98 ± 0.46 (6.0)	-2.4 ± 0.49 (3.6)
	0.91 ± 0.17 (3.6)	0.96 ± 0.17 (3.2)	-2.45 ± 0.4 (3.5)	-2.58 ± 0.46 (3.5)
2223-052	0.61 ± 0.24 (2.8)	0.89 ± 0.24 (2.5)	-2.49 ± 0.42 (2.5)	-2.45 ± 0.45 (3.7)
	0.63 ± 0.25 (3.7)	0.96 ± 0.23 (2.3)	-2.75 ± 0.48 (3.8)	-2.44 ± 0.41 (3.2)
2230+114	0.76 ± 0.23 (6.8)	0.58 ± 0.26 (2.3)	-1.91 ± 0.41 (4.3)	-1.7 ± 0.53 (2.5)
	0.71 ± 0.13 (1.2)	0.69 ± 0.27 (2.8)	-2.48 ± 0.35 (2.1)	-1.83 ± 0.54 (2.8)
2251+158	0.77 ± 0.2 (13.6)	0.48 ± 0.26 (3.6)	-1.94 ± 0.39 (8.3)	-1.96 ± 0.63 (5.5)
	0.88 ± 0.2 (9.7)	0.48 ± 0.28 (4.0)	-2.46 ± 0.4 (6.4)	-1.75 ± 0.67 (5.9)

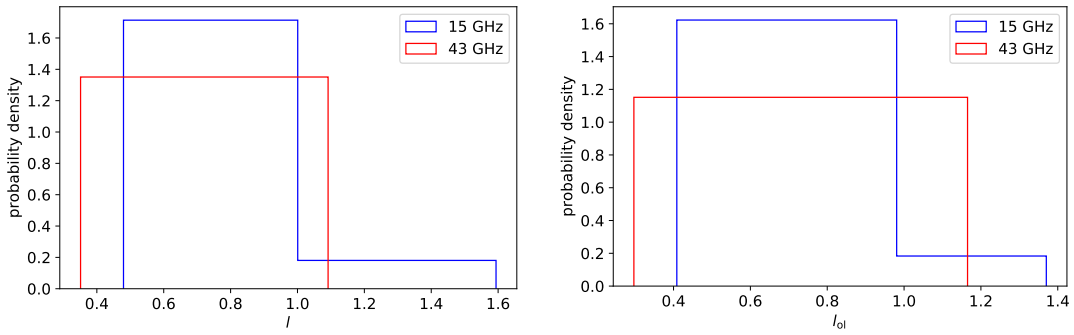

FIGURE 4.1: Values at 15 GHz are shown in blue and 43 GHz in red. Distribution of l-values along the entire jet (left panel) and along the overlap-region (right).

analyzing the jets in the overlap region between the two frequencies (KS: $p \sim 0.35\%$). Both in the overlap region and along the entire jet length, the s-values at both frequencies show a correlation

$$(R_{\text{spearman}}, R_{\text{pearson}}, \tau_{\text{kendall}})_{s_{15,43}} = (0.59, 0.61, 0.45)$$
$$(R_{\text{spearman}}, R_{\text{pearson}}, \tau_{\text{kendall}})_{s_{15,43,ol}} = (0.70, 0.73, 0.51)$$

The results of the analysis of both frequencies with respect to the different source classes are illustrated in Fig. 4.4 and listed in table 4.3. In the following I will also only discuss compared pairs that show a p-value of less than 5% from the KS test. At both frequencies there is no hint for a difference between the source classes regarding the s-value distribution along the entire jet length and the overlap region. Regarding the χ^2_{red} distributions, a difference between FSRQs and BL Lacs can be constituted along the entire jet length and the overlap region at both frequencies (KS: $p([\chi^2_{\text{red,s15}}, \chi^2_{\text{red,s15,ol}}, \chi^2_{\text{red,s43}}, \chi^2_{\text{red,s43,ol}}]_{\text{Q,B}}) \sim (0.2\ \%, 0.1\ \%, 1.4\ \%, 1.4\ \%)$, where, consistently with the χ^2_{red}-values for the diameter gradients, the brightness temperature gradient of FSRQs are systematically worse described by a single power law than for BL Lacs.

4.1.3 Brightness temperature and diameter gradients in context

The s and l-values for all sources at both frequencies show an anti-correlation along the entire jet length, see Fig. 4.5 (left) ($R_{\text{spearman}} \sim -0.73$, $R_{\text{pearson}} \sim -0.69$). This holds for both frequencies

$$(R_{\text{spear,15}}, R_{\text{pear,15}}, R_{\text{spear,43}}, R_{\text{pear,43}}) \sim (-0.73, -0.69, -0.64, -0.69)\ ,$$

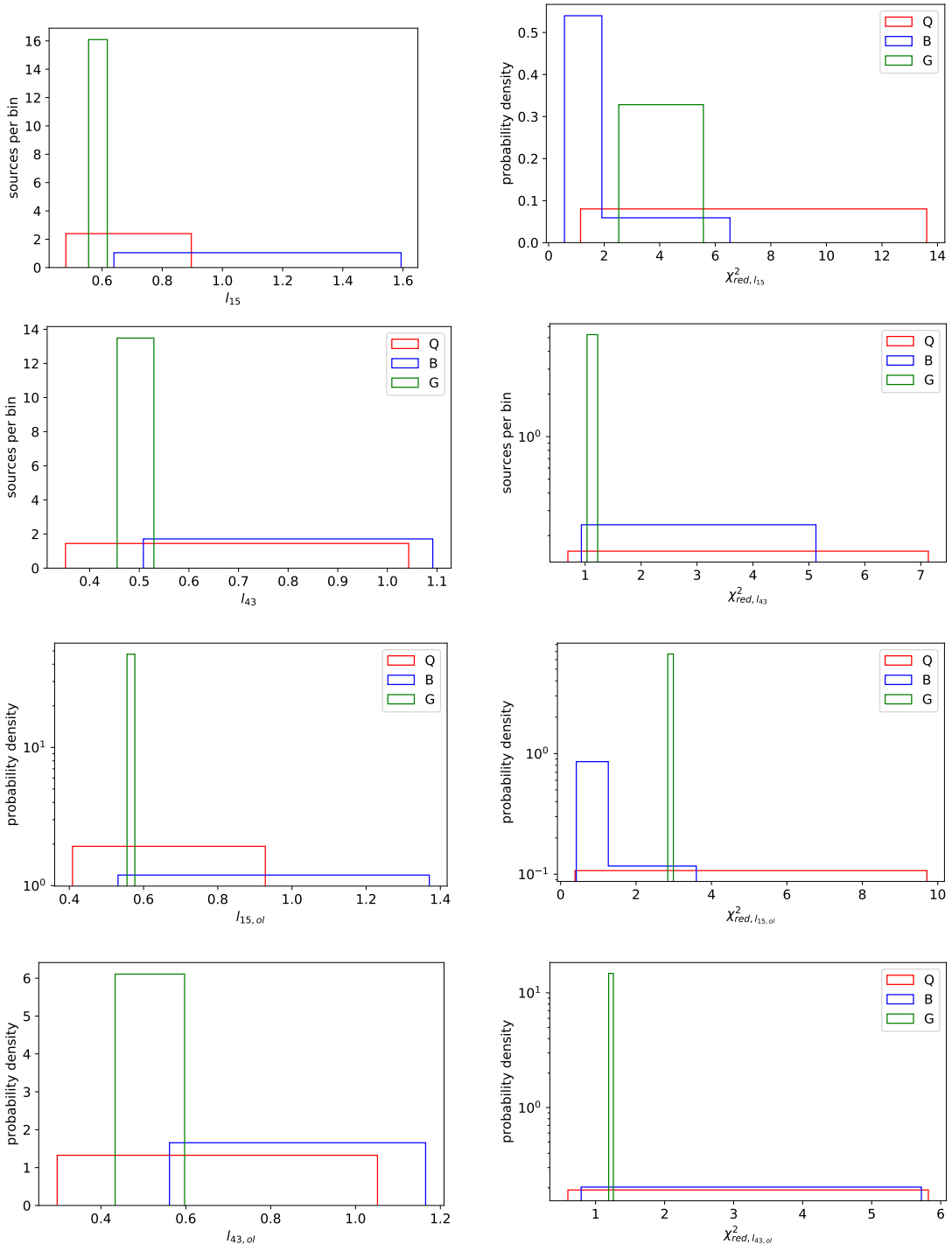

FIGURE 4.2: Colors indicate source classes (red: FSRQs, blue: BL Lacs, green: RGs). *Top two lines*: Distributions along the entire jet for both frequencies; *Bottom two lines*: Distributions constrained to the overlap-region of both frequencies. *Left column:* Distribution of l-values. *Right column* χ^2_{red} value distribution for the l-fits.

TABLE 4.2: Different correlation tests are performed on obtained parameters; col. 1: tested pair, col.2: test, col. 3: p-value, Values From: Burd et al. (2022)

tested pair	test	correlation coefficient	p-value
diameter gradients			
$l_{15} - l_{43}$	KS		0.026
	pearson	0.42	0.027
	spearman	0.37	0.056
	τ_{kendall}	0.27	0.044
$l_{15,\text{overlap}} - l_{43,\text{overlap}}$	KS		0.94
	pearson	0.43	0.021
	spearman	0.25	0.20
	τ_{kendall}	0.15	0.27
$l_{15,Q} - l_{15,B}$	KS		0.0037
$l_{15,Q} - l_{15,G}$	KS		0.088
$l_{15,B} - l_{15,G}$	KS		0.026
$\chi^2_{\text{red},l_{15},Q} - \chi^2_{\text{red},l_{15},B}$	KS		0.0024
$\chi^2_{\text{red},l_{15},Q} - \chi^2_{\text{red},l_{15},G}$	KS		0.88
$\chi^2_{\text{red},l_{15},B} - \chi^2_{\text{red},l_{15},G}$	KS		0.154
$l_{15,Q,\text{overlap}} - l_{15,B,\text{overlap}}$	KS		0.62
$l_{15,Q,\text{overlap}} - l_{15,G,\text{overlap}}$	KS		0.15
$l_{15,B,\text{overlap}} - l_{15,G,\text{overlap}}$	KS		0.077
$\chi^2_{\text{red},l_{15,\text{ol}},Q} - \chi^2_{\text{red},l_{15_\text{ol}},B}$	KS		0.032
$\chi^2_{\text{red},l_{15,\text{ol}},Q} - \chi^2_{\text{red},l_{15_\text{ol}},G}$	KS		0.53
$\chi^2_{\text{red},l_{15,\text{ol}},B} - \chi^2_{\text{red},l_{15_\text{ol}},G}$	KS		0.077
$l_{43,Q} - l_{43,B}$	KS		0.12
$l_{43,Q} - l_{43,G}$	KS		0.41
$l_{43,B} - l_{43,G}$	KS		0.077
$\chi^2_{\text{red},l_{43},Q} - \chi^2_{\text{red},l_{43},B}$	KS		0.21
$\chi^2_{\text{red},l_{43},Q} - \chi^2_{\text{red},l_{43},G}$	KS		0.088
$\chi^2_{\text{red},l_{43},B} - \chi^2_{\text{red},l_{43},G}$	KS		0.077
$l_{43,Q,\text{overlap}} - l_{43,B,\text{overlap}}$	KS		0.027
$l_{43,Q,\text{overlap}} - l_{43,G,\text{overlap}}$	KS		0.41
$l_{43,B,\text{overlap}} - l_{43,G,\text{overlap}}$	KS		0.077
$\chi^2_{\text{red},l_{43,\text{ol}},Q} - \chi^2_{\text{red},l_{43,\text{ol}},B}$	KS		0.21
$\chi^2_{\text{red},l_{43,\text{ol}},Q} - \chi^2_{\text{red},l_{43,\text{ol}},G}$	KS		0.088
$\chi^2_{\text{red},l_{43,\text{ol}},B} - \chi^2_{\text{red},l_{43,\text{ol}},G}$	KS		0.26

TABLE 4.3: Different correlation tests are performed on obtained parameters; col. 1: tested pair, col.2: test, col. 3: p-value, Values From: Burd et al. (2022)

tested pair	test	correlation coefficient	p-value
brightness temperature gradients			
$s_{15} - s_{43}$	KS		0.55
	pearson	0.61	5.3×10^{-4}
	spearman	0.59	0.0011
	τ_{kendall}	0.45	7.8×10^{-4}
$s_{15,\mathrm{overlap}} - s_{43,\mathrm{overlap}}$	KS		0.35
	pearson	0.73	1.0×10^{-5}
	spearman	0.70	4.0×10^{-5}
	τ_{kendall}	0.51	1.5×10^{-4}
$s_{15,Q} - s_{15,B}$	KS		0.10
$s_{15,Q} - s_{15,G}$	KS		0.15
$s_{15,B} - s_{15,G}$	KS		0.15
$\chi^2_{\mathrm{red},s_{15},Q} - \chi^2_{\mathrm{red},s_{15},B}$	KS		0.002
$\chi^2_{\mathrm{red},s_{15},Q} - \chi^2_{\mathrm{red},s_{15},G}$	KS		0.41
$\chi^2_{\mathrm{red},s_{15},B} - \chi^2_{\mathrm{red},s_{15},G}$	KS		0.077
$s_{15,Q,\mathrm{overlap}} - s_{15,B,\mathrm{overlap}}$	KS		0.86
$s_{15,Q,\mathrm{overlap}} - s_{15,G,\mathrm{overlap}}$	KS		0.088
$s_{15,B,\mathrm{overlap}} - s_{15,G,\mathrm{overlap}}$	KS		0.077
$\chi^2_{\mathrm{red},s_{15,\mathrm{ol}},Q} - \chi^2_{\mathrm{red},s_{15_{\mathrm{o}}\mathrm{l}},B}$	KS		0.001
$\chi^2_{\mathrm{red},s_{15,\mathrm{ol}},Q} - \chi^2_{\mathrm{red},s_{15_{\mathrm{o}}\mathrm{l}},G}$	KS		0.31
$\chi^2_{\mathrm{red},s_{15,\mathrm{ol}},B} - \chi^2_{\mathrm{red},s_{15_{\mathrm{o}}\mathrm{l}},G}$	KS		0.026
$s_{43,Q} - s_{43,B}$	KS		0.81
$s_{43,Q} - s_{43,G}$	KS		0.15
$s_{43,B} - s_{43,G}$	KS		0.26
$\chi^2_{\mathrm{red},s_{43},Q} - \chi^2_{\mathrm{red},s_{43},B}$	KS		0.014
$\chi^2_{\mathrm{red},s_{43},Q} - \chi^2_{\mathrm{red},s_{43},G}$	KS		0.22
$\chi^2_{\mathrm{red},s_{43},B} - \chi^2_{\mathrm{red},s_{43},G}$	KS		0.39
$s_{43,Q,\mathrm{overlap}} - s_{43,B,\mathrm{overlap}}$	KS		0.29
$s_{43,Q,\mathrm{overlap}} - s_{43,G,\mathrm{overlap}}$	KS		0.015
$s_{43,B,\mathrm{overlap}} - s_{43,G,\mathrm{overlap}}$	KS		0.26
$\chi^2_{\mathrm{red},s_{43,\mathrm{ol}},Q} - \chi^2_{\mathrm{red},s_{43,\mathrm{ol}},B}$	KS		0.014
$\chi^2_{\mathrm{red},s_{43,\mathrm{ol}},Q} - \chi^2_{\mathrm{red},s_{43,\mathrm{ol}},G}$	KS		0.15
$\chi^2_{\mathrm{red},s_{43,\mathrm{ol}},B} - \chi^2_{\mathrm{red},s_{43,\mathrm{ol}},G}$	KS		0.39

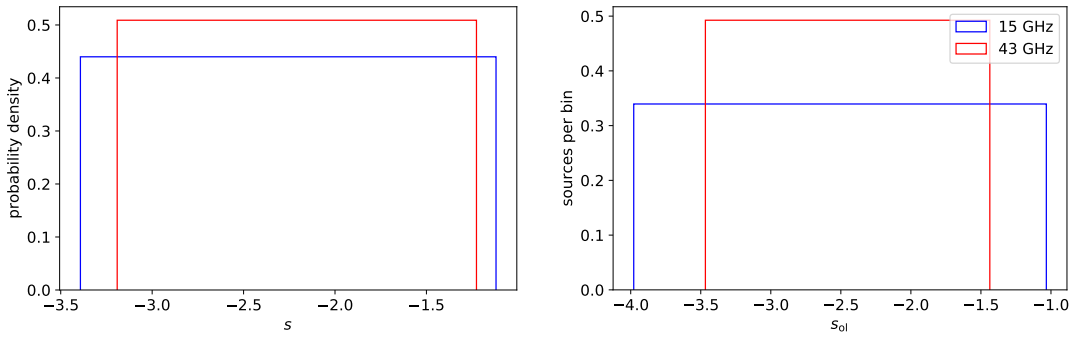

FIGURE 4.3: Distribution of s-values along the entire jet (top panel) and along the overlap-region (bottom). Values at 15 GHz are shown in blue and 43 GHz in red.

and also for the source classes,

$$(R_{\mathrm{spear,15,Q}}, R_{\mathrm{pear,15,Q}}, R_{\mathrm{spear,43,Q}}, R_{\mathrm{pear,43,Q}}) \sim (-0.60, -0.62, -0.56, -0.66)$$

and

$$(R_{\mathrm{spear,15,B}}, R_{\mathrm{pear,15,B}}, R_{\mathrm{spear,43,B}}, R_{\mathrm{pear,43,B}}) \sim (-0.56, -0.58, -0.86, -0.79) \ .$$

This anti–correlation can also be fit with a linear function of the form $f(x) = ax + b$. The values of the slope and the intersection are $(a, b) = (-3.42 \pm 0.46, 0.38 \pm 0.35)$. The same can be studied in the overlap region with similar results, see Fig. 4.5 (right),

$$R_{\mathrm{spearman}} \sim -0.61, R_{\mathrm{pearson}} \sim -0.69 \ .$$

Splitting into the frequencies yields

$$(R_{\mathrm{spear,15}}, R_{\mathrm{pear,15}}, R_{\mathrm{spear,43}}, R_{\mathrm{pear,43}}) \sim (-0.68, -0.77, -0.52, -0.60) \ ,$$

furthermore splitting the frequencies into the source classes (Q,B)[3] yields

$$(R_{\mathrm{spear,15,Q}}, R_{\mathrm{pear,15,Q}}, R_{\mathrm{spear,43,Q}}, R_{\mathrm{pear,43,Q}}) \sim (-0.61, -0.63, -0.47, -0.43)$$

and

$$(R_{\mathrm{spear,15,B}}, R_{\mathrm{pear,15,B}}, R_{\mathrm{spear,43,B}}, R_{\mathrm{pear,43,B}}) \sim (-0.79, -0.90, -0.80, -0.85) \ .$$

Also in this case the anti-correlation can be fit $(a, b)_{ol} = (-4.57 \pm 0.63, 1.11 \pm 0.47)$.

[3]RGs are not tested, due to there only being two in the sample

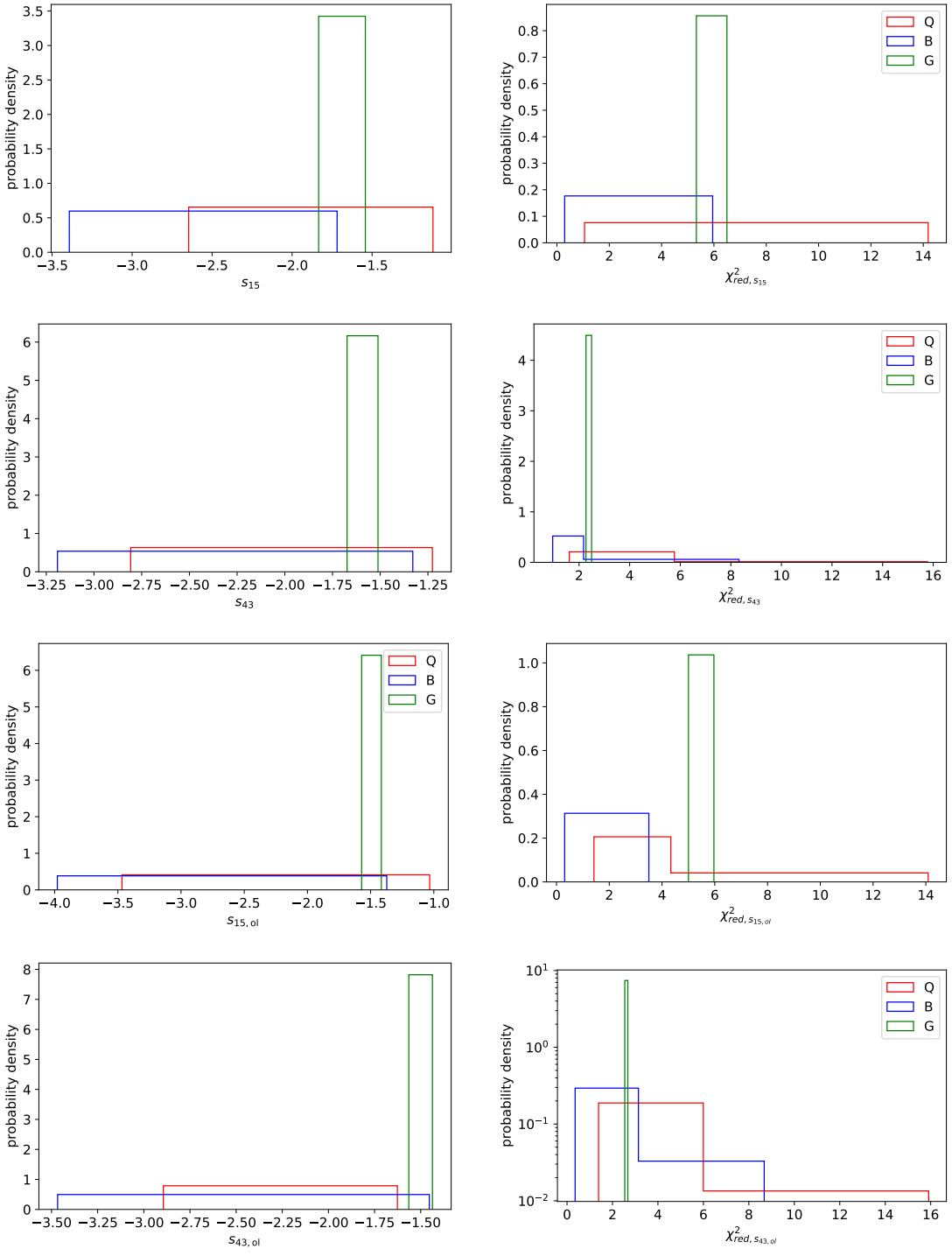

FIGURE 4.4: For all cases, the Bayesian histogram binning (solid lines) and the classical uniform binning (dashed lines) is shown. The colors indicate the source classes (red: FSRQs, blue: BL Lacs, green: RGs). *Top two lines*: Distributions along the entire jet for both frequencies; *Bottom two lines*: Distributions along the overlap-region of both frequencies. *Left column:* Distribution of s-values.

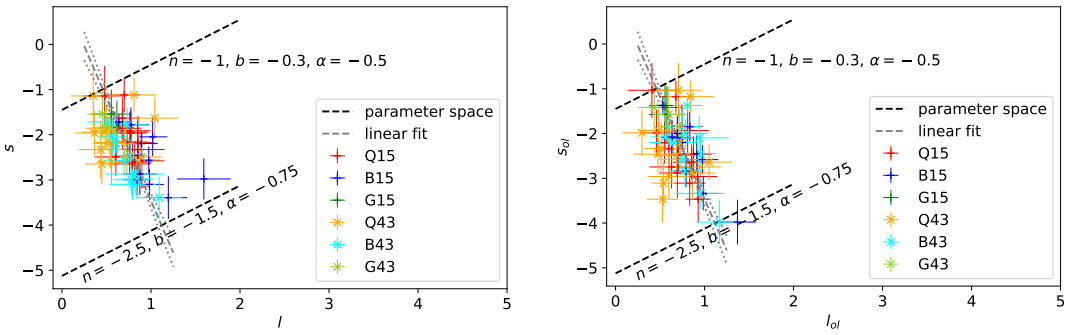

FIGURE 4.5: The colores (red,blue,green) indicate the source classes (Q,B,G) at 15 GHz, the colors (orange,cyan,yellowgreen), indicate the source classes (Q,B,G) at 43 GHz. The parameter space spanned by the direct measurement of the s and l values can be constrained with the additional information of the b-value distributions (see sections below) in order to constrain the parameter range of n and α. *Left:* respective entire jet length. *Right:* respective overlap region

4.1.4 Gradients of the magnetic field strength

In order to obtain the gradient slope of the magnetic field strength b, n and b in Eq. 1.7e have to be de-coupled which can be done by invoking equipartition between the electron energy density and the magnetic field energy density (Eq. 2.5) or by assuming overall particle conservation within the jet (Eq. 2.6). With $\alpha = -0.75$[4], the b-parameters, for equipartition and particle conservation is calculated for each source at both frequencies with the parameters of the overlap region between both frequencies. The results are listed in table 4.4 and shown in Fig. 4.6 (top three panels). The distributions themselves show that the source classes show a similar behavior in any case[5]. In order to assess whether there is a trend of possible preferred torodial/polodial or helical magnetic fields within the jets, also the respective jet geometry has to be taken into account, which is shown in Fig. 4.6 (third row). It turns out that in both cases, equipartition (left) and particle conservation (rigth), the b-values are consistent with helical magnetic fields. However in the case of equipartition, the distribution of the b-values tends to be more aligned with torodial fields than in the particle conservation case, where the data points scatter evenly down to the polodial field case. Overall the b-values scatter between $-1.5 \lesssim b \lesssim -0.3$ (see histograms in Fig. 4.6), which was used to constrain the parameter space in Fig. 4.5.

4.1.5 Magnetic fields in the radio cores

The magnetic fields in the radio core are calculated with the procedure, described in Sect. 2.7-2.7.2. The resulting B-values are listed in table 4.4. The distributions are

[4] $S(\nu) \propto \nu^{\alpha}$

[5] differences can also not be measured with the KS-test

shown in Fig. 4.6 (bottom row). In the radio core BL Lacs show systematically larger magnetic fields than BL Lac objects. For the sample, relevant in this work, this holds for both frequencies (KS at 15 GHz: $p \sim 3.7\ 10^{-3}\%$; KS at 43 GHz: $p \sim 3.7\ 10^{-3}\%$).

4.2 Discussion

4.2.1 Single power law fits

The main results from the single-power law study of the whole sample can be summarized as follow. FSRQs show systematically larger $\chi^2_{\rm red}$ values for both, the brightness temperature and diameter gradients. This means that FSRQs are systematically less well described by a single power law fit than BL Lac object. In the context of the brightness temperature this can be interpreted as regions along the jet axis where the jet locally shows a higher brightness temperature which can be seen as T_b-excesses in the gradient. Regarding the diameter gradient, these regions often show a local re-collimation of the jet and re-widening. Overall the jets of FSRQs show more structure than BL Lacs, which was already noted by Jorstad et al. (2017). FSRQs show smaller l-values than BL Lacs further down the jet. This means that FSRQs are able to collimate the jet farther down from the jet base than BL Lac object. The s and l values for both frequencies and the FSRQs/BL Lacs are anti-correlated. Sources where l is smaller tend to show flatter brightness temperature gradients. This means that more collimated sources are able to more effectively transport energy further out along the jet axis due to flatter brightness temperature gradients. A flat brightness temperature gradient indicates that the flux density of components further out in the jet are larger than the flux density of sources with steeper brightness temperature gradients. Equation 1.7e suggests that the slope of this anti-correlation between s and l should be ~ -1, if n, b and α were completely independent from the jet geometry. The fact that along the entire jet length and in the overlap region, the slopes are steeper, indicates that this is not the case. As discussed in Sect. 1.6, at least the scaling of the magnetic field strength is dependent on the jet geometry. Depending on whether equipartition or particle conservation is used in order to de-couple n and b, see Sect. 2.6, n is indirectly (through b) or directly dependent on l. Regarding the s-value distribution, there is no difference measureable between the FSRQs and the BL Lacs. However when looking at the histograms in Fig. 4.4, FSRQs at least show a trend for flatter T_b-gradients. Keeping in mind that FSRQs are more collimated further down the jet than BL Lacs, the hypothesis, that FSRQs feature larger extended luminosities than BL Lacs (e.g. Cooper et al. 2007; Kharb et al. 2010; Burd 2017) becomes plausible in the sense that this luminosity on kpc scales is ultimately fed

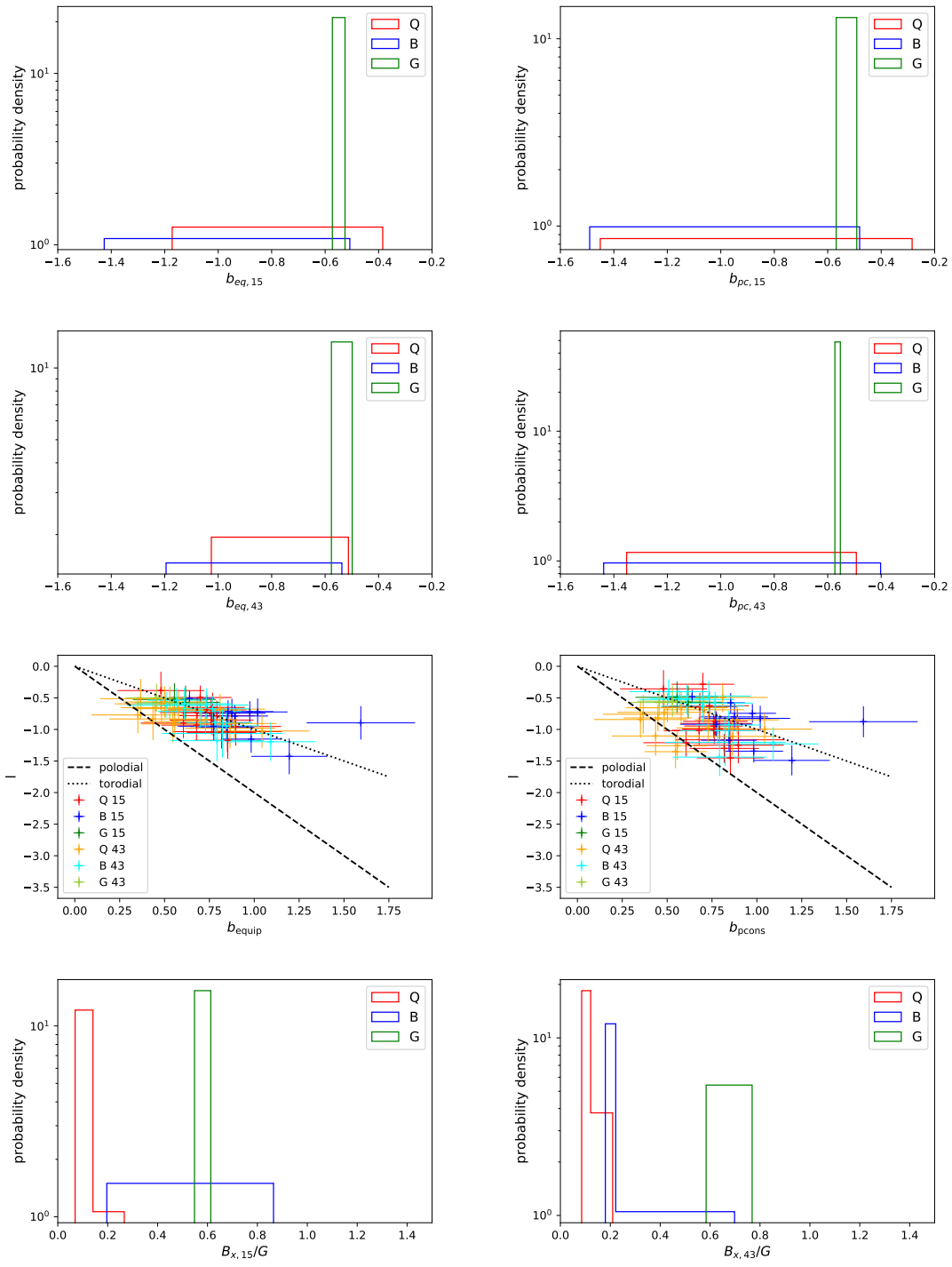

FIGURE 4.6: *Top two rows:* Distribution of the b-values at both frequencies (top 15GHz, bottom 43GHz) for the case equipartition (left) and particle conservation (right). *Third row:* $b - l$ scatter plots help to find out whether torodial, polodial or helical magnetic fields are preferred in the case of equipartition (left) and particle conservation (right). *Bottom row:* Distribution of the magnetic field strength in the radio core at 15 GHz (left) and 43 GHz (right).

TABLE 4.4: Col.1: Source (class); Col.2: $b_{\rm eq}$; Col.3: $b_{\rm pc}$; Col.4: magnetic field strength in the radio core; Col.5: jet power; Col.6: magnetic field in the ergosphere (Blandford & Znajek (1977)); Col.7: magnetic field in the ergosphere (Eddington); Col.8: distance of the radio core from the SMBH in the Blandford & Znajek (1977) case; Col.9: distance of the radio core from the SMBH in the Eddington case.

Source	$b_{\rm eq}$	$b_{\rm pc}$	B_c/G	$\log_{10}(P_j/10^{46}\frac{\rm erg}{s})$	$B_{BZ}/10^2G$	$B_{\rm Eddington}/10^4G$	$d_{cB,BZ}/10^2r_g$	$d_{cB,edd}/10^2r_g$
0219+428 (B)	-0.72 ± 0.21	-0.82 ± 0.2	0.38	-	-	11.4	-	2.0×10^2
	-0.54 ± 0.19	-0.51 ± 0.17	0.22				-	1.2×10^3
0336-019 (Q)	-0.49 ± 0.19	-0.28 ± 0.18	0.08	47.4	5.0	4.0	6.3	1.6×10^2
	-0.68 ± 0.24	-0.49 ± 0.23	0.1				1.6	21.3
0415+379 (G)	-0.57 ± 0.27	-0.57 ± 0.26	0.61	47.1	0.8	8.3	0.7	2.8×10^2
	-0.58 ± 0.25	-0.55 ± 0.25	0.58				0.6	2.1×10^2
0430+052 (G)	-0.53 ± 0.26	-0.49 ± 0.25	0.55	46.0	2.1	2.8	2.2	1.7×10^2
	-0.5 ± 0.22	-0.57 ± 0.21	0.77				6.6	1.8×10^3
0528+134 (Q)	-0.78 ± 0.24	-0.99 ± 0.22	0.1	47.6	1.0	9.9	3.2	9.8×10^2
	-0.65 ± 0.22	-0.82 ± 0.21	0.14				6.2	5.1×10^3
0716+714 (B)	-0.97 ± 0.2	-1.17 ± 0.18	0.27	47.1	4.1	3.8	1.0	17.5
	-0.89 ± 0.27	-1.02 ± 0.25	0.18				1.4	25.8
0735+178 (B)	-0.71 ± 0.18	-0.58 ± 0.16	-	46.9	0.5	9.8	-	-
	-0.67 ± 0.2	-0.58 ± 0.19	-				-	-
0827+243 (Q)	-1.05 ± 0.25	-1.3 ± 0.23	0.13	47.4	20.6	2.0	3.3	12.8
	-0.87 ± 0.25	-1.26 ± 0.23	0.11				87.7	7.1×10^2
0829+046 (B)	-0.72 ± 0.17	-0.74 ± 0.15	0.2	47.0	0.3	12.4	0.4	1.5×10^2
	-0.72 ± 0.26	-0.63 ± 0.25	0.21				0.2	45.3
0836+710 (Q)	-0.65 ± 0.23	-0.87 ± 0.22	0.1	47.7	3.9	5.3	79.9	1.6×10^3
	-0.51 ± 0.31	-0.76 ± 0.31	0.1				$1.1\ 10^4$	4.0×10^7
0851+202 (B)	-0.74 ± 0.23	-0.8 ± 0.21	0.27	46.6	5.2	2.4	2.3	36.9
	-1.06 ± 0.38	-1.2 ± 0.37	0.22				0.6	4.8
0954+658 (B)	-1.43 ± 0.28	-1.49 ± 0.24	0.27	-	-	13.2	-	1.2
	-1.19 ± 0.31	-1.23 ± 0.26	0.2				-	3.1
1101+384 (B)	-0.79 ± 0.17	-0.83 ± 0.15	-	-	-	3.0	-	-
	-0.59 ± 0.25	-0.52 ± 0.24	-				-	-
1127-145 (Q)	-0.38 ± 0.3	-0.36 ± 0.3	0.07	47.4	3.3	5.1	$3.1\ 10^2$	$1.5\ 10^5$
	-0.77 ± 0.29	-0.84 ± 0.29	0.09				3.3	1.2×10^2
1156+295 (Q)	-0.74 ± 0.2	-0.95 ± 0.19	0.14	47.6	1.5	8.4	5.7	1.8×10^3
	-0.84 ± 0.24	-0.98 ± 0.23	0.17				1.1	81.9
1219+285 (B)	-0.95 ± 0.22	-0.92 ± 0.19	0.48	-	-	2.6	-	2.7
	-0.61 ± 0.26	-0.47 ± 0.24	0.31				-	21.8
1222+216 (Q)	-1.17 ± 0.29	-1.45 ± 0.27	0.27	47.9	1.3	10.2	0.3	10.2
	-0.91 ± 0.29	-1.35 ± 0.26	0.18				5.2	2.8×10^3
1226+023 (Q)	-0.73 ± 0.24	-0.64 ± 0.22	0.13	48.2	3.6	7.7	1.3	36.3
	-0.56 ± 0.24	-0.66 ± 0.23	0.21				21.5	5.5×10^3
1253-055 (Q)	-1.04 ± 0.33	-1.16 ± 0.31	0.13	48.3	1.1	14.1	0.4	18.6
	-0.83 ± 0.33	-1.1 ± 0.31	0.11				3.2	1.3×10^3
1308+326 (Q)	-0.95 ± 0.3	-1.25 ± 0.29	0.12	47.4	1.8	6.7	1.9	134.6
	-0.98 ± 0.32	-1.11 ± 0.31	0.09				0.8	24.3
1633+382 (Q)	-0.69 ± 0.24	-0.63 ± 0.23	0.14	47.4	0.8	10.1	0.7	81.9
	-0.7 ± 0.23	-0.69 ± 0.22	0.12				0.9	1.4×10^2
1652+398 (B)	-0.51 ± 0.12	-0.48 ± 0.11	-	-	-	6.9	-	-
	-0.62 ± 0.21	-0.4 ± 0.2	-				-	-
1730-130 (Q)	-0.93 ± 0.24	-1.02 ± 0.22	0.13	48.0	1.6	9.9	0.6	28.0
	-1.03 ± 0.27	-1.0 ± 0.25	0.1				0.3	6.9
1749+096 (B)	-1.15 ± 0.22	-1.34 ± 0.18	0.4	46.4	0.1	12.8	0.1	6.2
	-1.18 ± 0.32	-1.44 ± 0.3	0.3				0.1	9.2
2200+420 (B)	-0.9 ± 0.26	-0.88 ± 0.25	0.86	45.9	0.3	6.7	0.1	4.8
	-0.94 ± 0.25	-0.93 ± 0.23	0.7				0.1	4.0
2223-052 (Q)	-0.9 ± 0.24	-1.21 ± 0.22	0.09	47.6	-	-	-	-
	-0.91 ± 0.25	-0.85 ± 0.23	0.09				-	-
2230+114 (Q)	-0.85 ± 0.23	-1.01 ± 0.21	0.1	47.7	1.0	10.5	1.3	$1.8\ 10^2$
	-0.67 ± 0.28	-0.66 ± 0.26	0.1				1.5	2.4×10^2
2251+158 (Q)	-0.89 ± 0.22	-0.91 ± 0.2	0.08	48.1	24.5	2.7	3.6	14.2
	-0.59 ± 0.31	-0.73 ± 0.29	0.12				3.3×10^2	4.2×10^3

by the VLBI jet. If the VLBI jet transports energy down the jet effectively without dissipating it in some way, the luminosity on larger scales is accordingly large.

4.2.2 Differences between the modelfit method and the stacked-image analysis

In this section the image stacking and ridgeline fitting method of determining the diameter gradient of a jet (Pushkarev et al. 2017b; Kovalev et al. 2020) is compared to the modelfit method, deployed for this work and in Burd et al. (2022). Stacked image maps map a broad jet profile while single components in single epochs typically do not fill an entire stacked jet profile (Pushkarev et al. 2017b; Lister et al. 2021). The apparent jet geometry in stacked images can be biased for example if a varying jet nozzle is resolved at higher frequencies, broadening the jet. Another difference can arise for wide, laterally resolved jet regions far from the core, that resemble more diffuse emission. Such emission regions are typically fit with a single, large Gaussian component in each epoch. If the inner jet itself is fit with much more components, the diameter gradient fit will have a much stronger weight on the inner jet with the many components than on the outer jet, which may result in more collimated (parabolic) jets. The image stacking and ridgeline fitting method on the other hand puts equal weight along the entire jet length, meaning, that regions with a large pixel area that might arise from stacked diffuse emission overall have a larger weight on the diameter gradient fit than the compact jet, typically resulting steeper diameter gradients (hyperbolic jet shapes).

4.2.3 The effect of cosmological distances and projection

In order to assess projection effects and redshift effects, each jet is de-projected with the inclination angle given in Pushkarev et al. (2009) and correct the scales for the redshift. This is necessary in order to avoid statements that might arise simply because of the effect that certain sources are farther away from us than others. For sources where no inclination angle in this paper is given, either different literature or a critical θ argument is used in order to obtain an inclination angle. This will be discussed on a source-by-source basis below. Each de-projected jet is then transformed from the angular to the parsec scale with following cosmology $H_0 = 0.71, \Omega_\Lambda = 0.73$, $\Omega_M = 0.27$. The conversion follows the calculations, shown in Hogg (1999) and is realized in python[6]. When trying to estimate the overlap region, the absolute scale is key - where is the true jet apex or the central engine. In order to have any kind of comparability, it is necessary to assume that the distance from the respective radio core of each source is much smaller

[6] https://github.com/PRBurd/useful_stuff/blob/master/cosmo.py

than the scales of the jet with respect to the radio core. Applying this assumption, the most common overlap region between these sources is between $5 \lesssim d_c/\mathrm{pc} \lesssim 100$. For the de-projected and redshift corrected diameter and brightness temperature gradients, I reapplied the single power law fit along the entire jet length and the overlap region at 15 GHz and compared the quantities, where I found differences in the source classes. The results are widely consistent. Measured difference are not as significant as before. FSRQs are more collimated along the entire jet length than BL Lacs (KS: $p \sim 1.7\%$), which does not hold in the overlap region (KS: $p \sim 28.7\%$). Regarding the diameter gradients FSRQs show a more complex structure than BL Lacs, which again is measured with the χ^2_{red}-distribution, along the entire jet length (KS: $p \sim 0.44\%$) which also does not hold in the overlap region (KS: $p \sim 25.9\%$). Regarding the brightness temperature gradients, FSRQs consistently show a larger complexities along the entire jet length (KS: $p \sim 2.4\%$) and the overlap region (KS: $p \sim 0.04\%$). These findings can be interpreted in the following way: FSRQs and BL Lacs show similar jet geometries in the overlap region. FSRQs tend to hold the collimation further down the jet, while BL Lacs widen up earlier along the jet axis. The surface brightness distribution in general is more complex for FSRQs than for BL Lacs, which tend to show more steady streams. The overall results and discussions for de-projected and redshift corrected sources is consistent with the projected sources on an angular scale.

4.2.4 Scaling the magnetic fields to the ergosphere

The results of all parameters, discussed in the following are listed in table 4.4. The magnetic fields, derived with the synchrotron cooling method are systematically larger than those derived with the core-shift method. This indicates systematically underestimated core region sizes. This effect, however, is small and the overall values are not too far from the core-shift method. It is not easy to properly estimate an error due to approximations that go into both methods, however certain trends are consistently seen in both methods for the sources in both these studies (mine and Pushkarev et al. (2012)). Both methods are consistent in the statement that BL Lacs show systematically larger magnetic fields in the radio cores than FSRQs. For each source, the Blandford & Znajek (1977) magnetic field B_{BZ} is calculated for a moderate spin parameter ($j = 0.5$) as discussed in Sect. 2.8. This of course can only be done for sources where a jet power can be extracted with the method of Godfrey & Shabala (2013). This relies on the extraction of extended luminosities from these sources on kpc scales (Cooper et al. 2007; Kharb et al. 2010). For sources where no extended luminosity can be acquired due to the source showing no extended features on kpc scales, no jet power can be estimated.

The calculation of an Eddington magnetic $B_{\mathrm{Eddington}}$-field does not depend on an extracted jet power. The Eddington magnetic field can be calculated for any source with a given mass. For both, $B_{\mathrm{Eddington}}$ and B_{BZ}, I chose to use the center of the range of possible SMBH masses, given in table 2.2. From well-studied sources, where a redshift and the angle to the line of sight is known, like M87 (Mertens et al. 2016; Hada et al. 2018; Park et al. 2019), NGC 315 (Park et al. 2021), 1H0323+342 (Hada et al. 2018), CTA120 (Fromm et al. 2015), BL Lacertae (Marscher et al. 2008), to name a few, it can be estimated that plausible distances of radio cores from the ergospheres of SMBHs (d_{cB}) range between $10^2 \lesssim d_{cB}/r_g \lesssim 10^6$. This of course depends on the frequencies of observation. Figure 4.7 shows the distance of the radio cores from the SMBHs, obtained from scaling the magnetic field in the respective radio core to the magnetic field in the ergospheres with the polodial magnetic field component ($b = -2\ l_{ol}$) in the Blandford & Znajek (1977) case (top) and the Eddington case (bottom) and are listed in table 4.4. From the consideration of plausible core distances, it becomes clear that $0836+710$ and $1127-145$ either do not reach an Eddiongton magnetic field in the ergosphere. For $0836+710$ this holds for both frequencies, for $1127-145$, it is the 15 GHz data that produces implausible core distances. In the Blandford & Znajek (1977) scenario, FSRQs do not only show systematically smaller magnetic fields within the radio cores but also farther away from the SMBH than BL Lacs (KS: $p \sim 3 \times 10^{-6}$) which is consistent with the findings of Pushkarev et al. (2012). This difference between the source classes cannot be measured in the Eddington-case (KS: $p \sim 0.3$).

4.2.5 Geometry breaks

With the methods, described in Sect. 2.5 I am able to find breaks in the geometry gradient in 9 sources, $0219+421$, $0336-019$, $0415+379$, $0528+134$, $0836+710$, $1101+384$, $1156+295$, $1253-055$ and $2200+420$. In order to assess, whether the Bondi radius, especially the change of the ambient pressure gradient, inside and outside the Bondi sphere, can be the cause for systematical geometry transitions the estimated Bondi radius is compared with the found position of the geometry break point. To calculate the Bondi radius for each source, the temperature of the matter close to the SMBH and its mass have to be known (Bondi 1952; Russell et al. 2015)

$$\frac{r_b}{\mathrm{pc}} = 31 \times \left(\frac{k_b T}{\mathrm{keV}}\right)^{-1} \times \left(\frac{M}{10^9 M_\odot}\right) \tag{4.1}$$

The well studied source M87 proves to be a suitable source to study such things. Gebhardt et al. (2011) and the Event Horizon Telescope Collaboration et al. (2019) calculated the mass independently to be $M \sim 6.5\,10^9 M_\odot$ while Russell et al. (2015) was

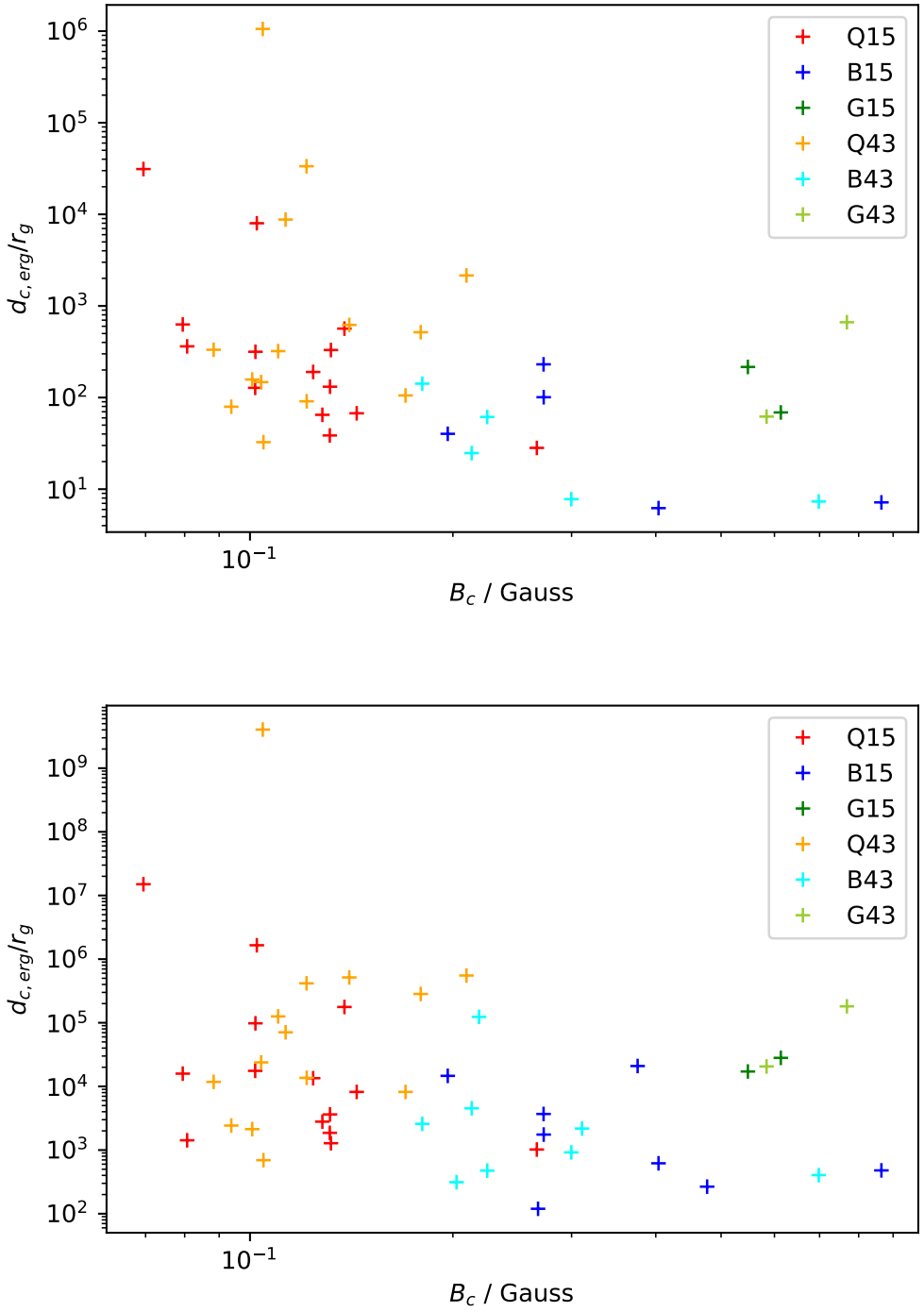

FIGURE 4.7: Distance between the radio core and the SMBH's ergosphere in the case of a Blandford & Znajek (1977) magnetic field (top) and an Eddinggton magnetic field (bottom).

able to determine the gas temperature ($T \sim 0.9\,\mathrm{keV}$) in the center of M87 with X-ray observations. These measurements yield a Bondi radius r_b of $r_b \sim 224\,\mathrm{pc}$. The observed X-ray emission in blazars is dominated by the non-thermal emission form the jet. It is therefore not strait forward to determine the gas temperature needed in order to calculate the Bondi radius. Balmaverde et al. (2008) measured a gas temperature between $0.4 \lesssim E/\mathrm{keV} \lesssim 1.7$ in a sample of low-power AGN. For high-power AGN typical gas temperatures near the SMBH can reach up to $\sim 7\,\mathrm{keV}$, (Yaji et al. 2010; Gaspari et al. 2013, e.g.). In Burd et al. (2022) we did not measure the gas temperature for the sample of blazars. Therefore the respective Bondi radius is calculated in the range $0.4 \lesssim E/\mathrm{keV} \lesssim 7$ for each source. The considered sources are blazars. Therefore projection due to small inclination angle has to be taken into account. The acquired, scaled Bondi radii are also de-projected with inclination angles taken from Pushkarev et al. (2009). In cases, where Pushkarev et al. (2009) does not provide an inclination angle, different literature and methods are consulted, which will be discusses in Sect. 4.3. For each source a minimum/maximum value of the Bondi radius is given. These values correspond to the minimum/maximum black hole masses from Table 2.2. If a range of inclination angles is given, the maximum/minimum Bondi radius also corresponds to the maximum/minimum θ. In the following I discuss the findings of all 10 sources in context. In Sect. 4.3 I discuss the detailed findings on a source by source basis. For the sources 3C 66A (0219+428), CTA 26 (0336-019), PKS 0528+134 (0528+134), 4C +71.07 (0836+710), Mrk 421 (1101+384), 4C +29.45 (1156+295), 3C 279 (1255-055) and BL Lac (2200+420), plausible Bondi radius ranges are smaller than the distance of the transition zone from the radio core. Kovalev et al. (2020) argue that in such cases the geometry transition could mark the transition of a magnetically dominated to a particle-dominated jet. The transition zone of 3C 111 (0415+379) lies within the plausible Bondi radius ranges. However the smallest plausible gas temperatures have to be assumed in order for the Bondi sphere to extend beyond the transition zone. Additionally $0336-019$ and $0836+710$ feature bright components which do not change position within the 10-year period of observation in this sample. Potter & Cotter (2015) predicted a dichotomy in the distribution of FSRQs and BL Lacs regarding the radius of the jet at the point where the jet switches from magnetically to particle dominated which in this context is interpreted as the position where the geometry break from collimated to less collimated (parabolic to conical) happens. To study this, the distribution of the break point position (Fig. 4.8 (top)) and the jet radius at the break point (same figure, bottom) can be studied. A two-sample KS test finds a difference between the x_b-values of BL Lacs and FSRQs ($p \sim 3.7\%$). The jet radius distributions of BL Lacs and FSRQs are likely drawn from the same overall distribution (KS: $p \sim 14.3\%$). The alternative $H0$-hypothesis $H_0 : R_j(x_{b,Q}) < R_j(x_{b,B})$ yields $p \sim 7\%$. This means that

although the jet radii at the break points for both source classes are likely drawn from the same distribution, however FSRQs show a tendency for larger jet radii.

TABLE 4.5: Geometry transition properties of individual sources. From: Burd et al. (2022)

Name	Class	x_b/mas (x_b/pc)	$R_j(x_b)$/mas	$l_{\rm in}$	$l_{\rm out}$	θ/deg	$\chi^2_{\rm red,broken}$	$\chi^2_{\rm red,single}$	$r_B/(mas)\,(r_B/(pc))$
3C 66A	B	2.31 ± 0.32 (65)	0.42 ± 0.14	0.56 ± 0.13	1.33 ± 0.11	9.8[a]	4.0 (326)	8.1(328)	$0.046 - 1.255$ $(1.31 - 35.51)$
CTA 26	Q	2.12 ± 0.26 (293)	0.68 ± 0.15	0.62 ± 0.12	1.78 ± 0.27	3.2[b]	16.8 (119)	21.3 (121)	$0.0011 - 0.0310$ $(0.16 - 4.27)$
3C 111	G	5.42 ± 0.29 (16)	0.56 ± 0.09	0.60 ± 0.08	1.69 ± 0.24	19.0[c]	12.1 (662)	12.8 (664)	$0.23 - 6.55$ $(0.67 - 19.07)$
PKS 0528+134	Q	2.10 ± 0.38 (596)	0.56 ± 0.16	0.54 ± 0.11	1.24 ± 0.25	1.7[b]	10.0 (336)	10.9 (338)	$0.0035 - 0.0925$ $(0.99 - 26.32)$
4C +71.04	Q	2.75 ± 0.41 (413)	0.35 ± 0.13	0.48 ± 0.14	1.15 ± 0.15	3.2[b]	15.7 (139)	19.0 (141)	$0.0018 - 0.0495$ $(0.28 - 7.42)$
Mrk 421	B	1.93 ± 0.38 $(13 - 34)$	0.63 ± 0.19	0.54 ± 0.13	1.02 ± 0.13	$(2 - 5)$[d]	10.1 (253)	11.5 (255)	$0.0048 - 0.3522$ $(0.084 - 2.456)$
4C +29.45	Q	2.52 ± 0.60 (522)	0.91 ± 0.37	0.73 ± 0.17	1.23 ± 0.21	2.0[b]	8.5 (84)	9.3 (86)	$0.0034 - 0.0918$ $(0.084 - 2.456)$
3C 279	Q	0.61 ± 0.22 (97)	0.15 ± 0.09	0.49 ± 0.15	0.78 ± 0.09	2.4[b]	33.1 (390)	33.8 (392)	$0.012 - 0.337$ $(1.98 - 53.74)$
BL Lac	B	1.97 ± 0.13 (20)	0.37 ± 0.07	0.78 ± 0.09	1.97 ± 0.08	7.5[b]	9.6 (1058)	17.0 1060	$0.046 - 1.184$ $(0.46 - 11.76)$

Columns: (1) Common name, (2) Classification, (3) geometry break point in angular scale (geometry break point in linear scale deprojected), (4) Jet radius at the break point, (5) $l_{\rm in}$, (5) $l_{\rm out}$, (6) inclination angle, (7) $\chi^2_{\rm red}$ for the broken power law fit, (8) $\chi^2_{\rm red}$ for the single power law fit. (9) range of plausible Bondi radii in angular scale (range of plausible Bondi radii in linear scale deprojected) a) Hovatta et al. (2009), b) Pushkarev et al. (2009), c) Kadler et al. (2008), d) Lico et al. (2012),

4.3 Remarks on single sources

For each source, I will discuss the diameter and brightness temperature gradient. If possible I will discuss geometry transitions in a source. The brightness temperature will be interpreted with respect to the canonical value of $s = -2.5$ which holds for a classical Blandford & Königl (1979) jet (conical jet, torodial magnetic fields and equipartition between the electron energy density and magnetic field energy density). Larger s-values indicating a flatter T_b-gradient, imply jets that are able to transport energy more efficiently outside along the jet axis and are often accompanied by a more collimated jet. If interesting features are seen in a jet, such as brightness temperature excesses, dips in the diameter trend of a jet or even geometry transitions, I will try to put these into context and give a possible interpretation based on the data. Figures 4.9-4.40 show the diameter and brightness temperature gradient for each source along the entire jet length and the overlap region at both frequencies. Each frequency is given a color bar, blueish colors for 43 GHz and redish colors for the 15 GHz data. The color trends for each source indicate the epoch. This is done in order to identify, whether potentially interesting regions in a plot (like T_b-excesses) are due to a systematic error in one single epoch or whether these features are consistently seen across the epochs. To explore this, it is worth, discussing a few cases, in order to put different possible s-values into context:

- conical jet:
  - torodial magnetic field ($b = -1$), equipartition ($n = -2$), $\alpha = -0.5$ (canonical case) $\rightarrow$ $s = -2.5$
  - polodial magnetic field ($b = -2$), equipartition ($n = -4$), $\alpha = -0.5 \rightarrow s = -6$

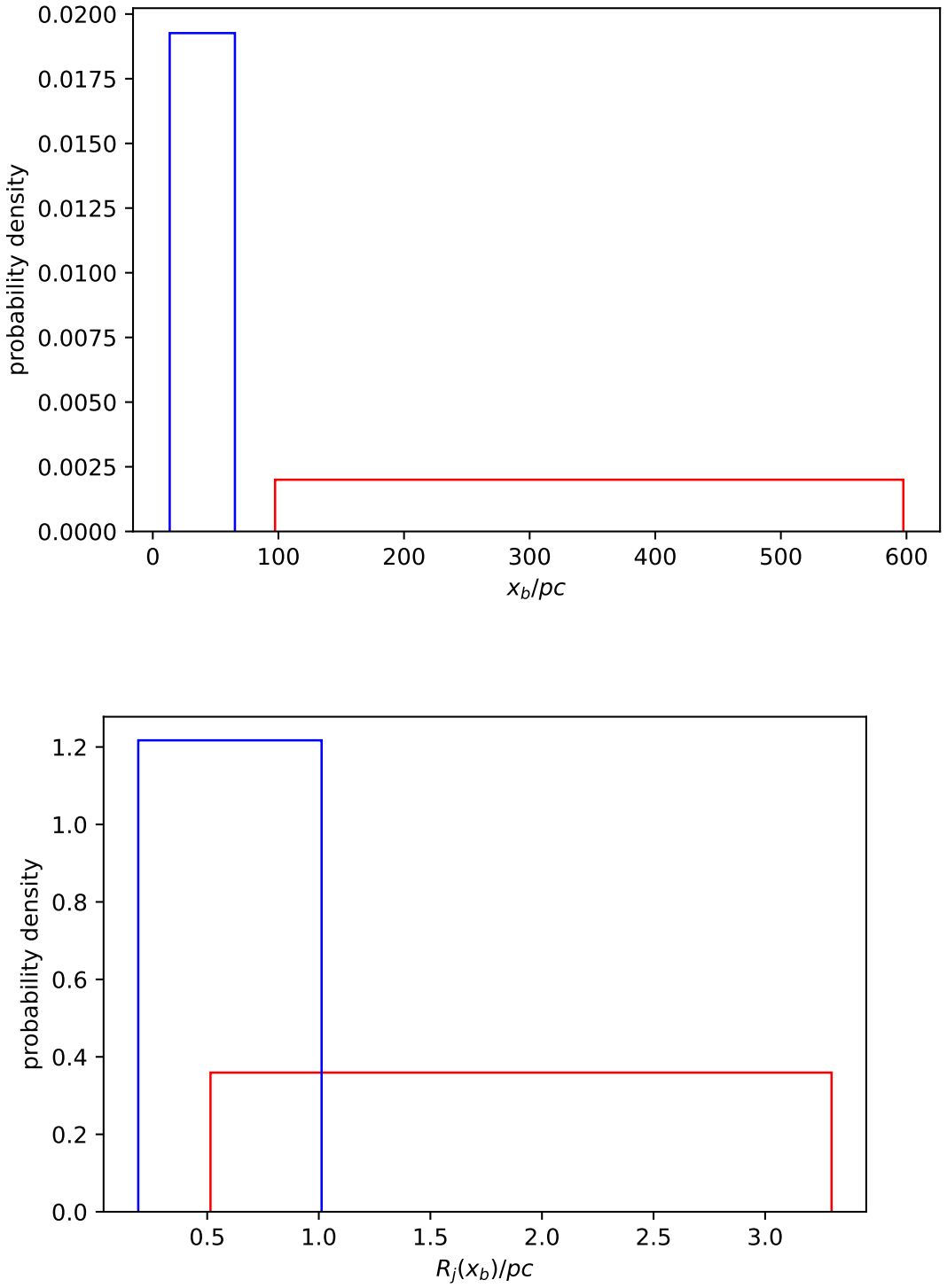

FIGURE 4.8: FSRQs are shown in red, BL Lacs in blue. *Top:* Distribution of the break points. *Bottom:* The distribution of the jet radii at the respective geometry break point.

  - In the case of a conical jet, equipartition, and a reasonable spectral index of $\alpha = -0.5$ the s-values have a domain of reasonable values of $-6 \leq s \leq -2.5$

- parabolic jet:
  - torodial magnetic field ($b = -0.5$), equipartition ($n = -1$), $\alpha = -0.5$ (canonical case) $\rightarrow s = -1.25$
  - polodial magnetic field ($b = -1$), equipartition ($n = -2$), $\alpha = -0.5 \rightarrow s = -3$
  - In the case of a parabolic jet, equipartition, and a reasonable spectral index of $\alpha = -0.5$ the s-values have a domain of reasonable values of $-3 \leq s \leq -1.25$

The l and s values that are referred to in the following comments can be found in tables 4.2 and 4.3 and also in the legend of each corresponding plot.

0219+428 (B) shows a dip in the diameter gradient between $2 \lesssim d_{\mathrm{core}}/\mathrm{mas} \lesssim 3$ which is prominent in both frequencies, which indicates a local recollimation of the jet at this position along the jet axis, see Fig. 4.9. At the same position, the brightness temperature gradient shows an excess, which means that a bright feature is present in the jet at the position of recollimation. The l-vales at both frequencies indicate two different jet geometries along the respective entire jet length, however are indistinguishable in the overlap region, which hints at a possible geometry break in this source. Indeed, when sytematically searching for a transition of the jet geometry, a break point can be found at ~ 2.3 mas at which the jet transitions from a parabolic ($l_{in} \sim 0.6$) to a conical geometry further down the jet ($l \sim 1.3$), see Fig. 4.10 (top). For this source, the variability Doppler factor $D_{\mathrm{var}} \sim 1.6$ (Hovatta et al. 2009) can be used in combination with the maximum apparent speed $\beta_{\mathrm{app}} \sim 11.5$ (Lister et al. 2019) to estimate the inclination angle $\theta = \arctan\left(\frac{2\beta_{\mathrm{app}}}{\beta_{\mathrm{app}}^2 + D_{\mathrm{var}}^2}\right) \sim 9.8\,\mathrm{deg}$. The s-values are indistinguishable from each other at both frequencies.

0336-019 (Q) shows a collimated jet at both frequencies $l < 1$, both along the entire jet length and the overlap region, as well as consistent s-values see Fig. 4.11. Combining the information of both frequencies makes it possible to constrain a break point of the geometry at $x_b \sim 2.1$ mas. This break point coincides with a bright feature seen in the T_b-gradient at this position, which is consistently seen across the epochs. The inner geometry resembles a parabola $l_{in} \sim 0.6$, while the outer geometry is hyperbolic $l_{out} \sim 1.8$, see Fig. 4.10 (bottom). The sudden geometry break from parabolic to hyperbolic indicates that this transitions might be due to the jet abruptly opening up after the steady bright feature, seen in the T_b-gradient. The location of the Bondi-radius is smaller than the location of the geometry break along the jet axis. Kovalev

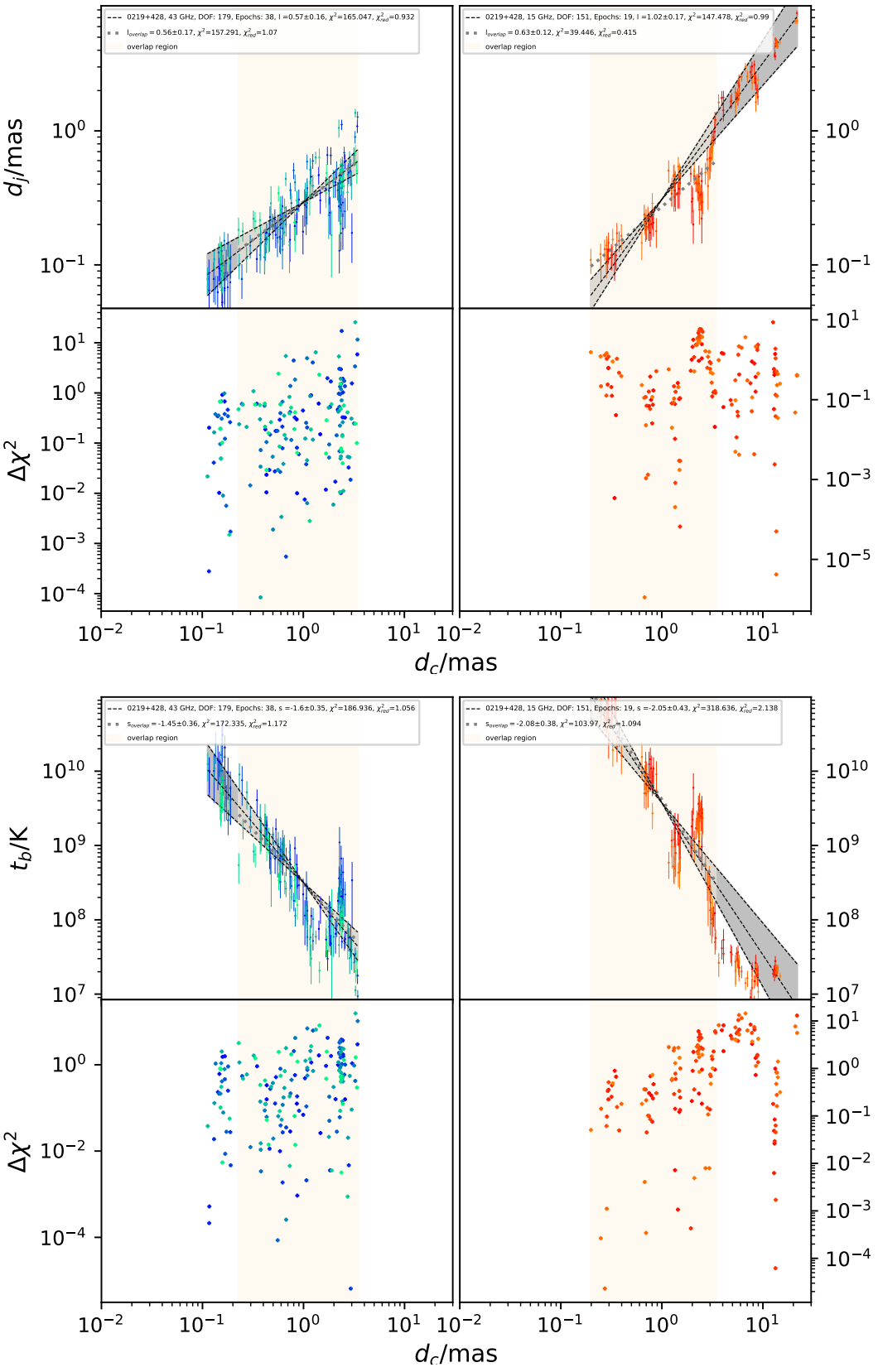

FIGURE 4.9: 0219+428; *Left columns:* 43 GHz data; *Right columns:* 15 GHz data; *Top* diameter gradient fit; *bottom* brightness temperature gradient fit.

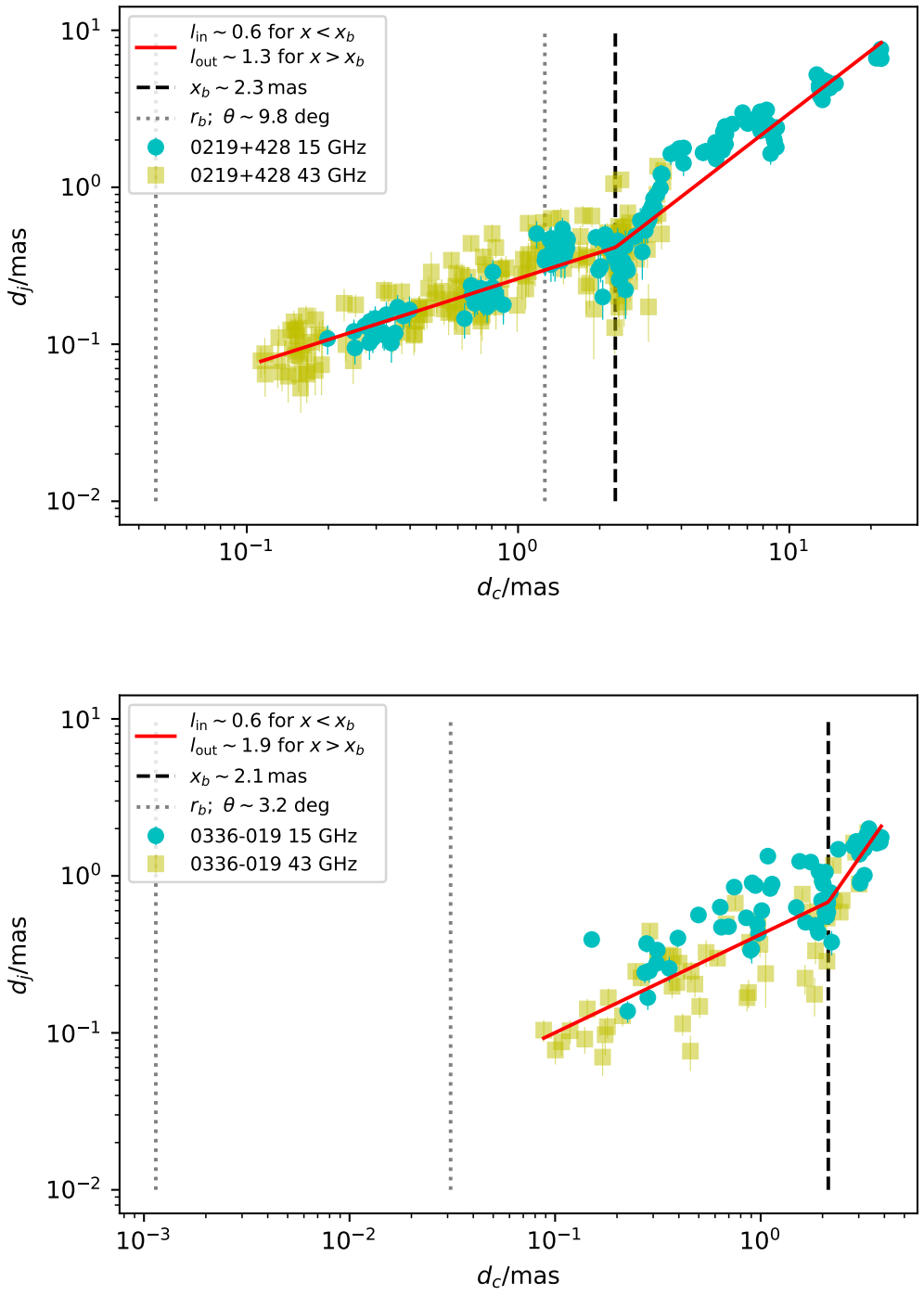

FIGURE 4.10: *Top:* 0219+428; *Bottom:* 0336-019 ; Both frequencies are fit together in order to constrain a break point as well as an outer and inner l-value.

et al. (2020) argue that the jet pressure is in equilibrium with the ambient pressure up to the Bondi radius. A standing shock can be expected if the ambient pressure shows a smaller pressure gradient than the jet, which might be an explanation for the bright, steady feature seen at the same region where the jet abruptly opens up.

0415+379 (G) is a complex structured jet. Kadler et al. (2008) studied the evolution of components extensively and found different physical effects influencing the brightness temperature and speed of certain components. However, over many epochs the jet can be described by a single power law in the diameter and brightness temperature gradient. At both frequencies the jet is collimated ($l < 1$) along the entire jet length and the overlap region, see Fig. 4.12 (top). The relatively flat brightness temperature gradients which again are indistinguishable in any case, also indicate, that the jet is able to transport the energy along the jet axis more effectively than a freely expanding jet, see Fig. 4.12 (bottom). Combining both frequencies, a geometry break can be found in this source at $x_b \sim 5.4$ mas, where the jet transitions from a parabolic ($l \sim 0.6$) to a hyperbolic shape ($l \sim 1.7$).

0430+052 (G) features a parabolic jet shape along the entire jet length and the overlap region at both frequencies. Corresponding to the collimated jet, the brightness temperature gradient is relatively flat. Analyzing the same source at 1.4 GHz and 15 GHz, Kovalev et al. (2020) are able to constrain a break point and a transition from a parabolic to a conical jet further down the physical jet axis. The findings from the data used in this work are consistent with the findings from Kovalev et al. (2020) in the sense, that closer to the physical jet base, this source features a parabolic jet.

0528+134 (Q) features a collimated jet at both frequencies along the entire jet length and the overlap region and are indistinguishable between the two frequencies, see Fig. 4.15 (top). The s-values at 15 GHz are indistinguishable along the entire jet length and the overlap region, however are steeper than the s-values at 43 GHz along the entire jet length. Interestingly, although the 43 GHz jet is also indistinguishable with respect to the s-values along the entire jet length and the overlap region, the overlap region shows a steeper s-value which is consistent with the steeper T_b-gradient of the 15 GHz jet, see Fig. 4.15 (bottom). This can be understood with the jet showing a zone of recollimation between $0.3 \lesssim d_{\mathrm{core}}/\mathrm{mas} \lesssim 1$, accompanied by an increase in brightness temperature in the same region, that steepens the fit in the overlap region. Above $\nu \sim 30$ GHz the radio core is not necessarily the region where the optical depth of synchrotron self absorption is $\tau \sim 1$ (Marscher 2016), but rather a standing recollimation shock which can be backed by polarization measurements in the 43 GHz radio core as has been done by Cawthorne et al.

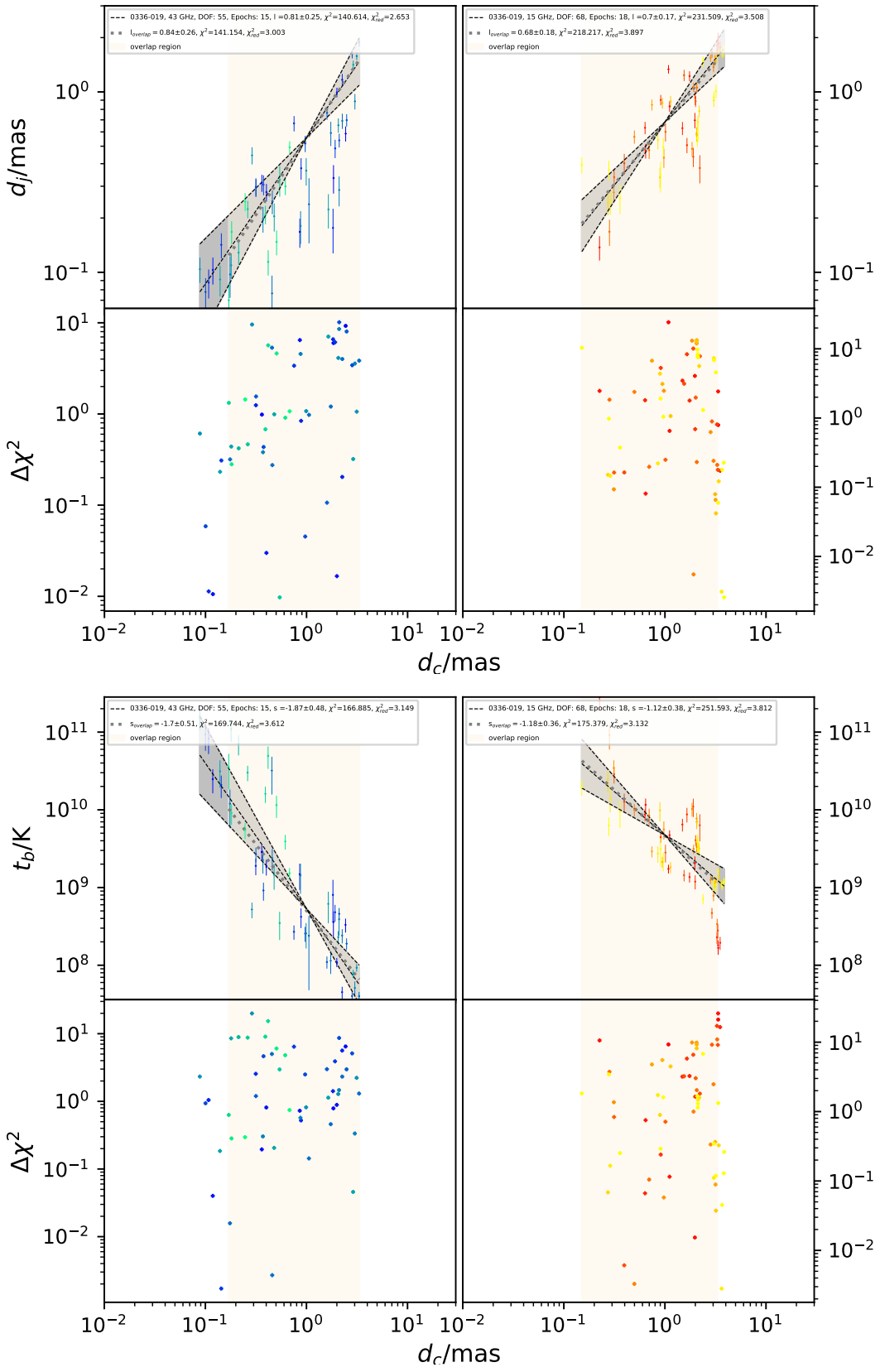

FIGURE 4.11: 0336-019; *Left columns:* 43 GHz data; *Right columns:* 15 GHz data; *Top* diameter gradient fit; *bottom* brightness temperature gradient fit.

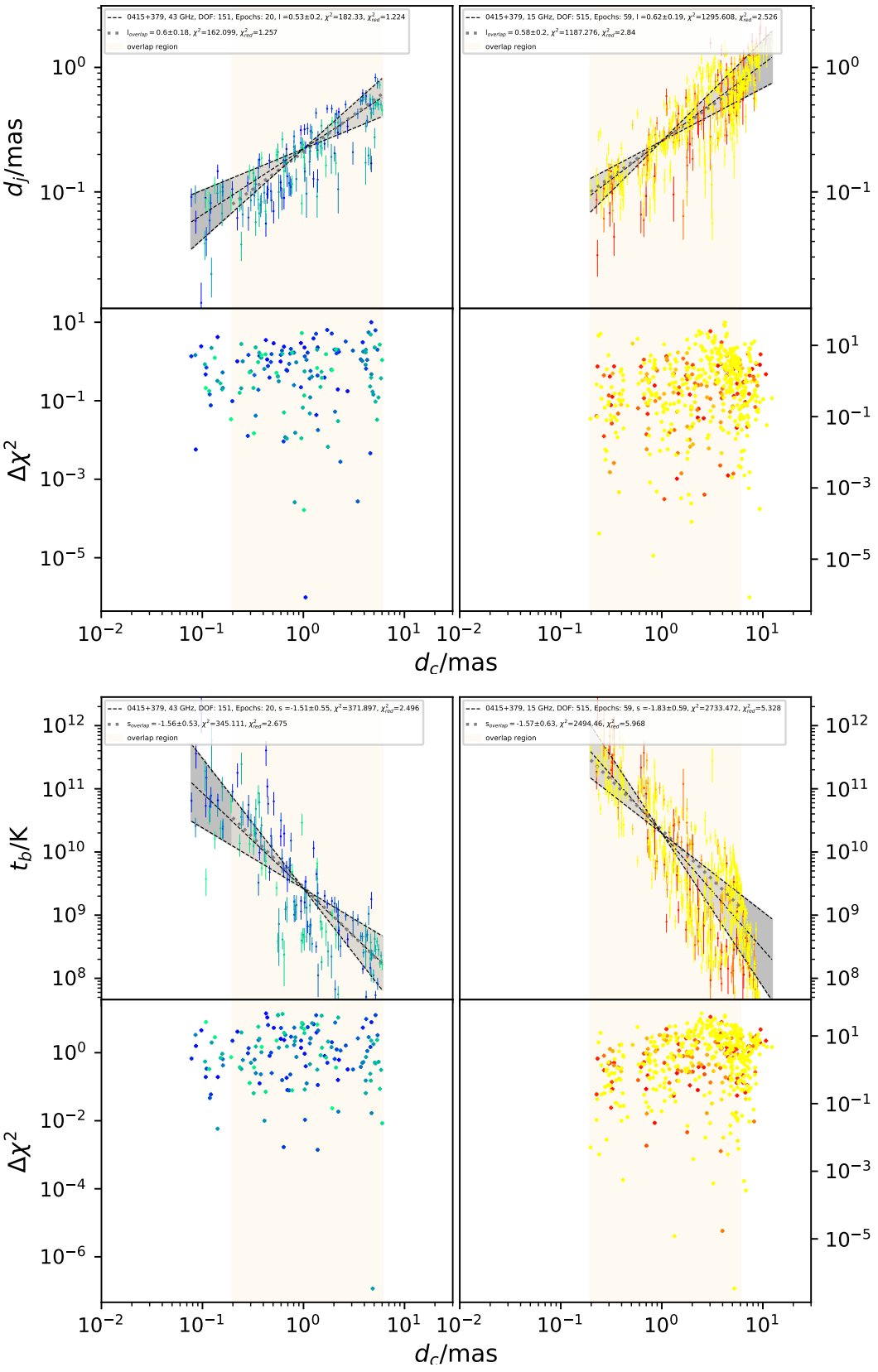

FIGURE 4.12: 0415+379; *Left columns:* 43 GHz data; *Right columns:* 15 GHz data; *Top* diameter gradient fit; *bottom* brightness temperature gradient fit.

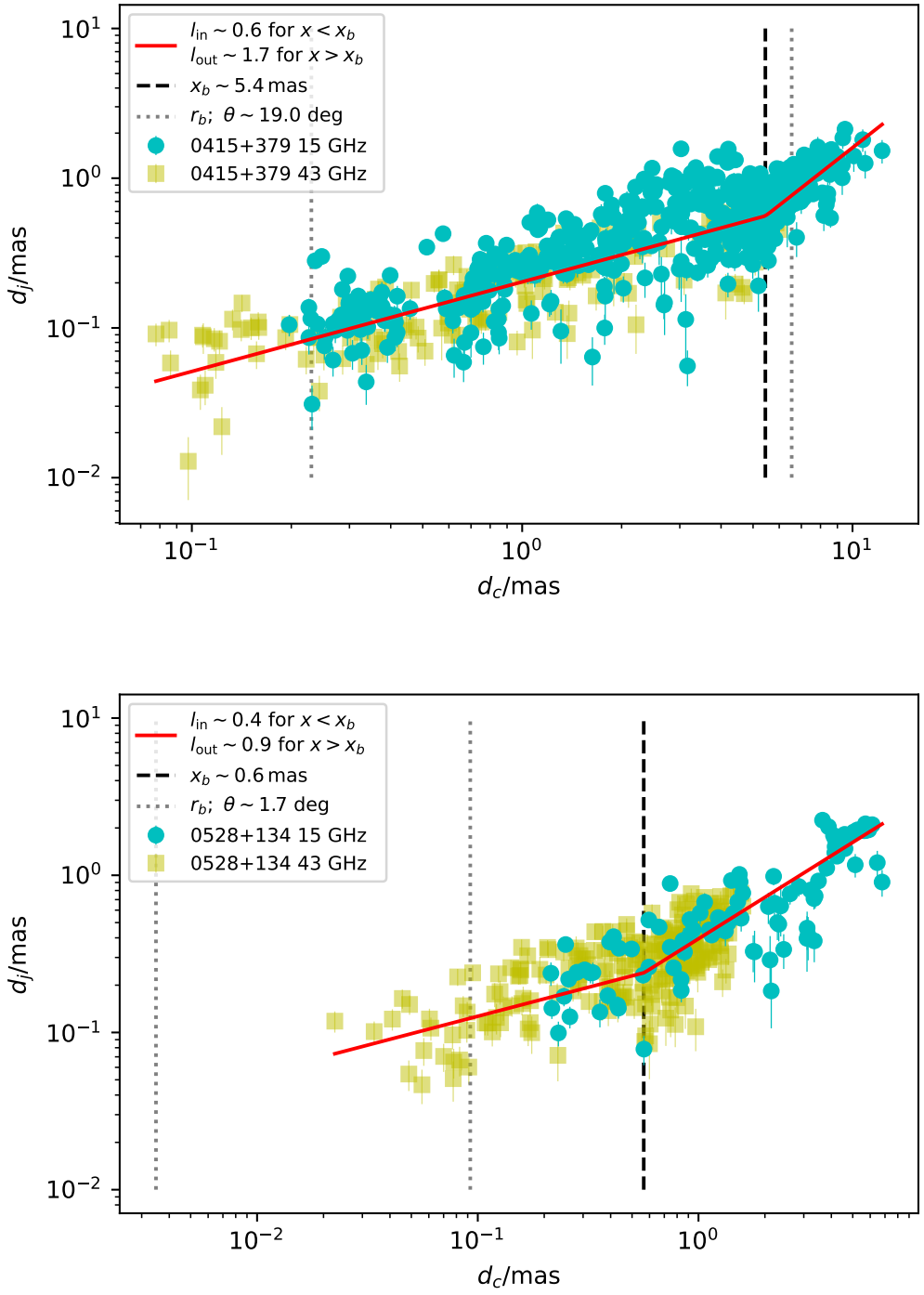

FIGURE 4.13: *Top:* 0415+379; *Bottom:* 0528+134; Both frequencies are fit together in order to constrain a break point as well as an outer and inner l-value.

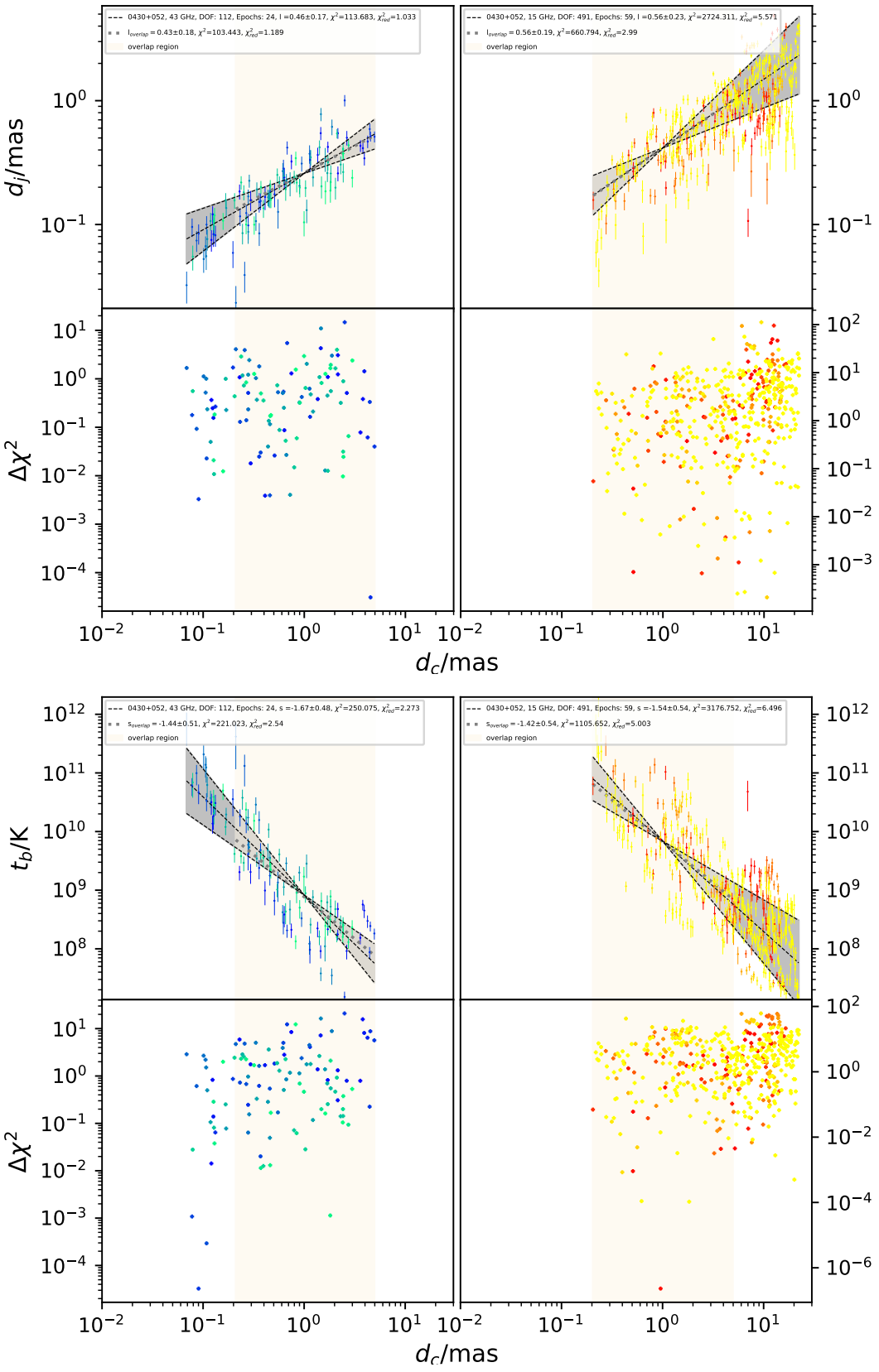

FIGURE 4.14: 0430+052; *Left columns:* 43 GHz data; *Right columns:* 15 GHz data; *Top* diameter gradient fit; *bottom* brightness temperature gradient fit.

(2013) in the case of 1803+784. This polarization is often linked to conical recollimation shocks (Daly & Marscher 1988; Cawthorne & Cobb 1990; Cawthorne 2006). In a sample of 43 γ-ray detected blazars, observed at 22 GHz and 43 GHz, Jorstad et al. (2001) found 27 sources that show a sum of 45 steady (non-moving) components in the jet (beside the core) which they also link to recollimation shocks. These studies, also performed at 43 GHz make it plausible, that between $0.3 \lesssim d_{\mathrm{core}}/\mathrm{mas} \lesssim 1$ a recollimation shock can be seen in this source. Combining both frequencies, also for this source, a transition from a parabolic ($l_{in} \sim 0.5$) to a conical jet ($l_{out} \sim 1.2$) can be found at $x_b \sim 2.1$ mas from the radio core. Also in this source, the recollimation shock would be outside the Bondi-radius (Kovalev et al. 2020) and the steepening of the diameter gradient happens after this recollimation shock. The overall interpretation could be as follows: The jet leaves the Bondi-sphere, the pressure gradient of the ambient medium is flatter than in the jet. The jet then forms a recollimation shock. After this shock, the jet becomes particle dominated which already might be indicated by the different brightness temperature gradients in the jets at the respective full length, indicating a possible variation of the electron energy density n and the magnetic field strength gradient b while featuring similar diameter gradients. By becoming particle dominated the jet does not convert the magnetic field energy into kinetic energy, stops accelerating and opens up to a cone.

0716+714 (B) shows hints for a slightly collimated jet at both frequencies, however the obtained l-values are consistent with a conical jet, both along the entire jet and the overlap region. Also the s-values indicate a canonical behavior of the jet, indicating a classical, freely expanding Blandford & Königl (1979) jet, as seen in Fig. 4.16.

0735+178 (B) shows hints for a slight collimation (Fig. 4.17), since, within the errors, the obtained l-values are slightly < 1. At 43 GHz the jet shows s-values indicating a flatter T_b-gradient than would be expected from a canonical jet. This is also seen in the 15 GHz jet in the overlap region, however the fit steepens along the entire jet length. Since no geometry transition is found in this source, this might indicate a variation of the n and b values along the jet axis. This however cannot be distinguished, since n and b are coupled.

0827+243 (Q) shows a 43 GHz jet with a parabolic geometry, see Fig. 4.18. The 15 GHz jet on the other hand shows a tendency for steeper diameter gradients, consistent with a conical jet, however, the error bars overlap in a way, that the two slopes between the two frequencies are still consistent with each other. Combining the two frequencies also does not make it possible to constrain a geometry break because the data points

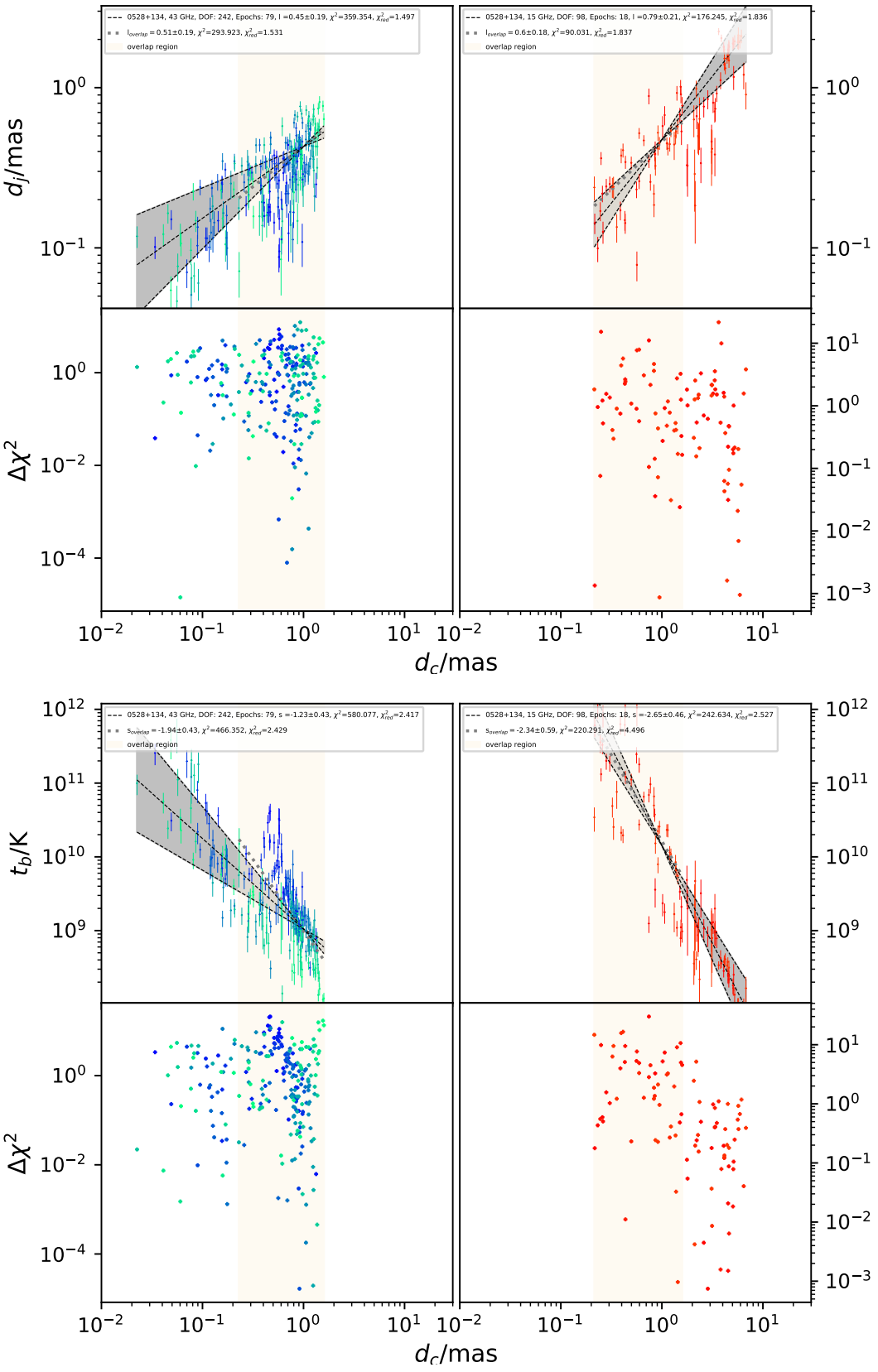

FIGURE 4.15: 0528+134; *Left columns:* 43 GHz data; *Right columns:* 15 GHz data; *Top* diameter gradient fit; *bottom* brightness temperature gradient fit

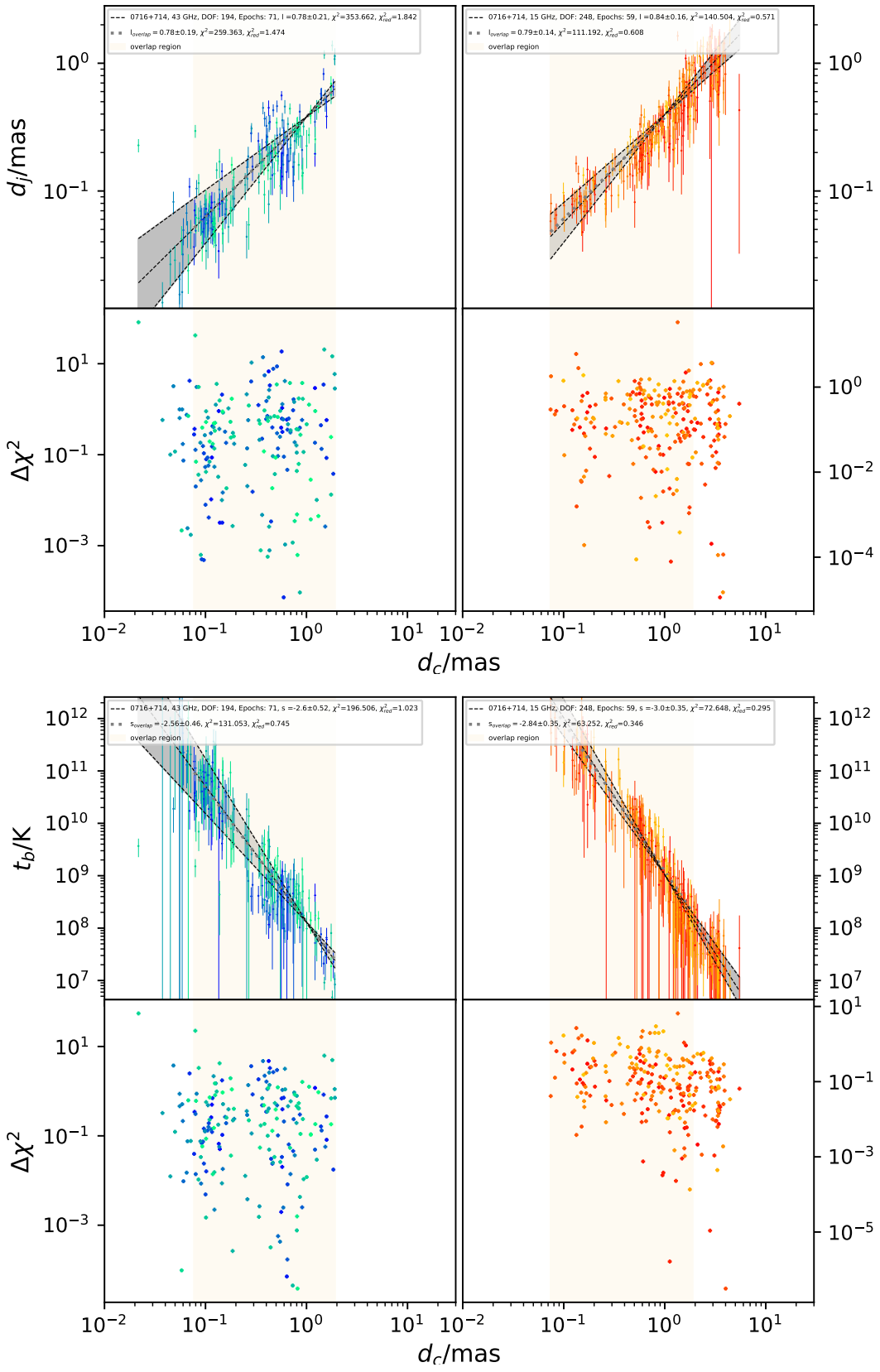

FIGURE 4.16: 0716+714; *Left columns:* 43 GHz data; *Right columns:* 15 GHz data; *Top* diameter gradient fit; *bottom* brightness temperature gradient fit

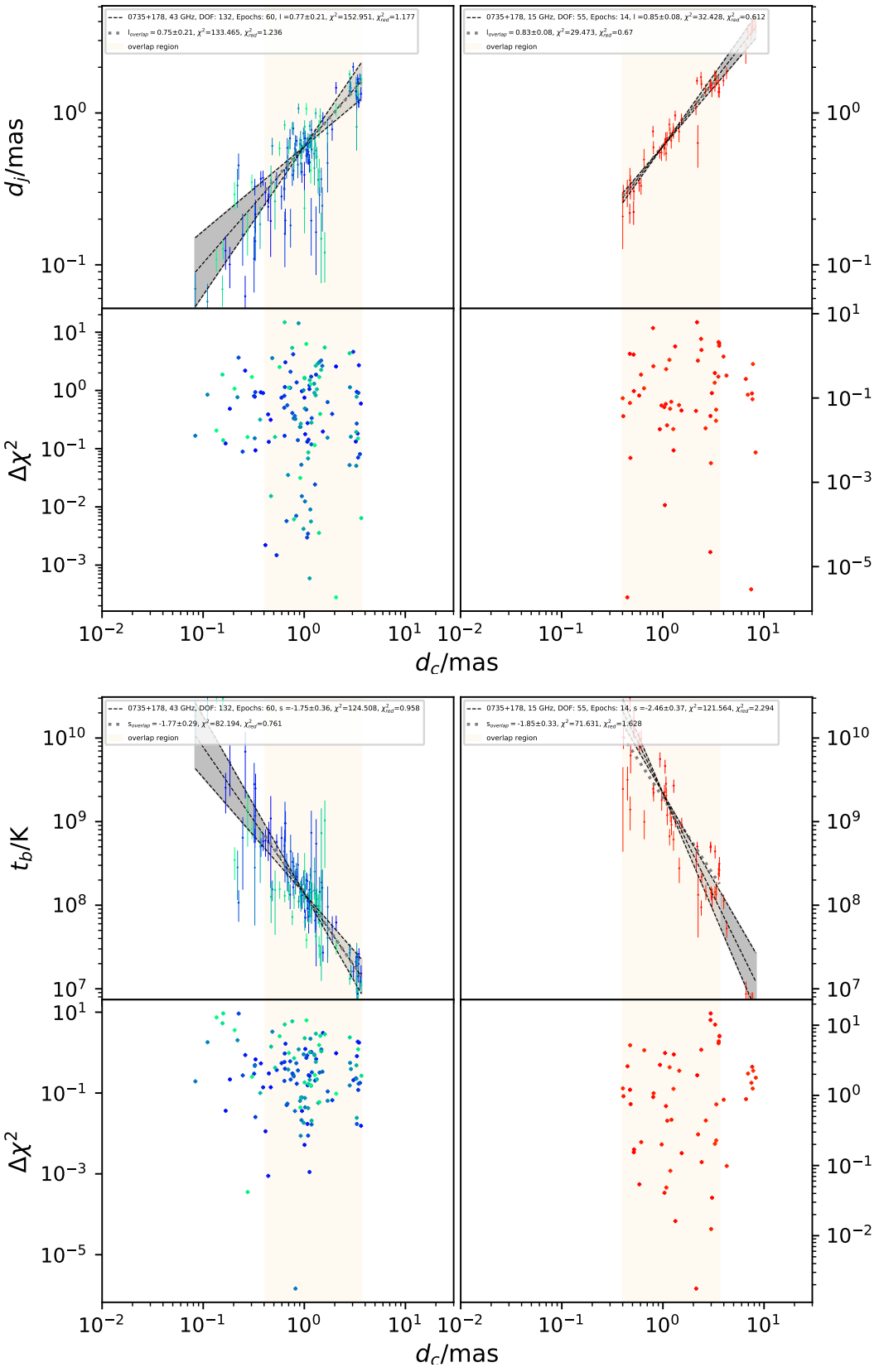

FIGURE 4.17: 0735+178; *Left columns:* 43 GHz data; *Right columns:* 15 GHz data; *Top* diameter gradient fit; *bottom* brightness temperature gradient fit

in both frequencies in the area $1 \lesssim d_c/\mathrm{mas} \lesssim 3$ scatter strongly with large error bars. Therefore this source is not in the sample of jets showing a geometry transition. The s-values are consistent with the canonical value.

0829+046 (B) features a collimated jet at 43 GHz, see Fig. 4.19, from which the l-values are consistent with the overlap region of the 15 GHz jet. The jet along the entire jet length is conical at 15 GHz, however a systematic geometry break cannot be properly constrained considering both frequencies due to the large scatter of the data at 43 GHz. However some kind of transition must happen within this jet, because the T_b-gradient at 43 GHz is systematically flatter than at 15 GHz. Furthermore, a recollimation region, accompanied by an excess in the brightness temperature can be seen at 43 GHz between $0.2 \lesssim d_c/\mathrm{mas} \lesssim 1$, which cannot be seen in the 15 GHz jet. This can be interpreted in a similar manner as the case of 0528+134 with a recollimation shock, however the geometry transition cannot be constrained properly in this source.

0836+710 (Q) is a complex and well studied source. On pc-scales this source is well understood in terms of Kelvin-Helmholtz instabilities propagating through the jet (Perucho et al. 2012; Vega-García et al. 2019, 2020). On kpc-scales the hot spot advance speed was measured with LOFAR-VLBI (Kappes et al. 2019). The diameter gradient at both frequencies suggest a collimated jet, however the jet at 43 GHz is more collimated than at 15 GHz while the overlap region at 15 GHz is consistent with the diameter gradient at 43 GHz, suggesting a transition in the geometry, see Fig. 4.20. Within the errors, the s-values are consistent with the canonical value. Only in the overlap region at 43 GHz the s-value indicates a flatter T_b gradient which can be understood with the scatter of the data between $0.1 \lesssim d_c/\mathrm{mas} \lesssim 0.3$. The systematic search for geometry transitions reveals a geometry break at $x_b \sim 2.7$ mas from parabolic to conical, see Fig. 4.21 (top). At both frequencies an excess in T_b and dip in d_j can be seen between $2 \lesssim d_c/\mathrm{mas} \lesssim 4$. The break lies in the inner (with respect to the jet axis) edge of this feature. This feature can be understood as standing recollimation shock. Polarized flux is observed in this sources up to ~ 1 mas which is not seen further down the jet (Orienti et al. 2020). This might indicate a transition in the magnetic field strength gradient. Vega-García et al. (2019) find the jet to be particle dominated over ~ 100 mas in jet length. The transition of geometry, found in this study, the limb-brightened polarization found by (Orienti et al. 2020) and the stability study by (Vega-García et al. 2019) make is plausible that the jet switches from magnetically to particle domination at the position of the steady recollimation shock.

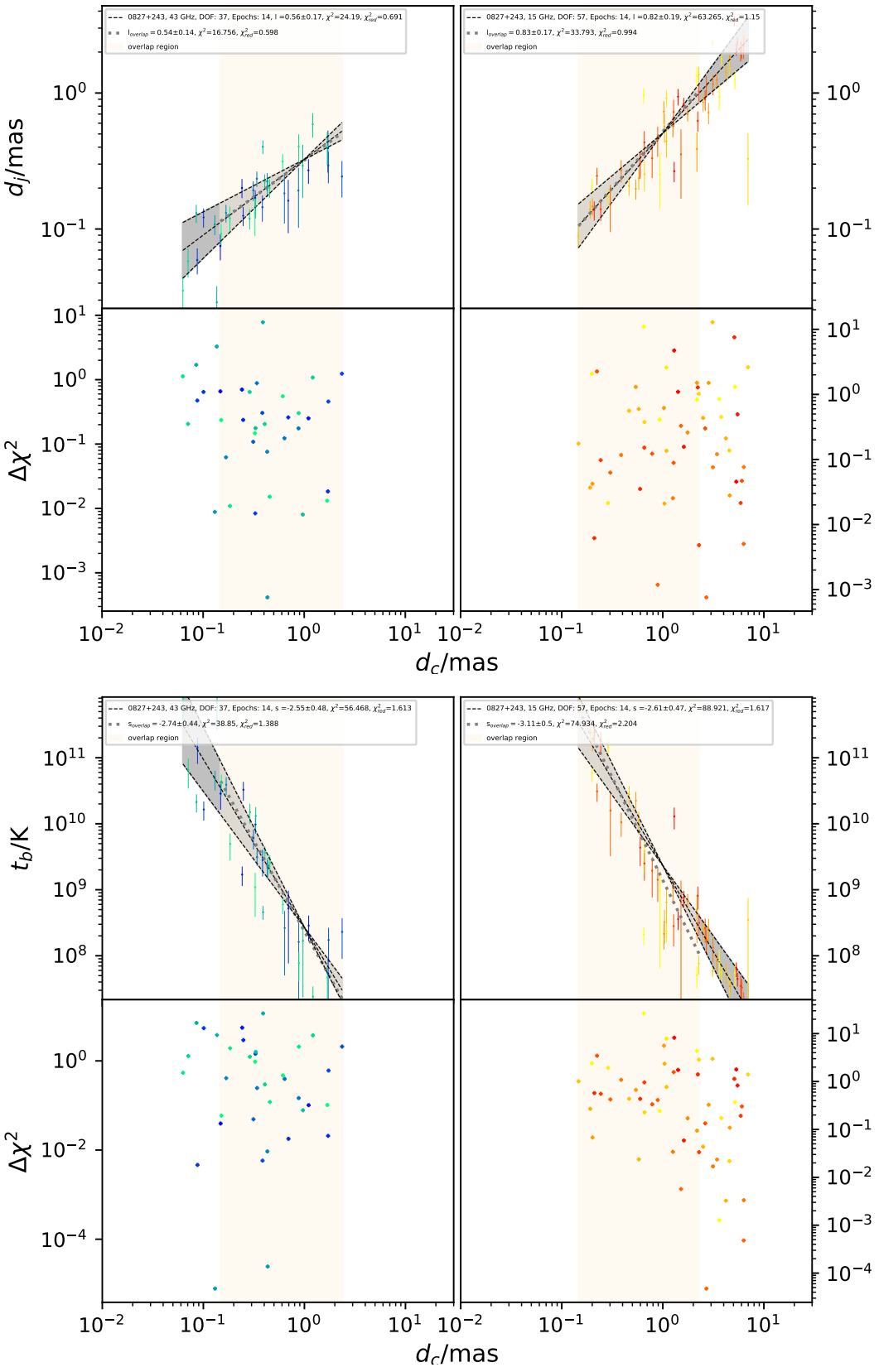

FIGURE 4.18: 0827+243; *Left columns:* 43 GHz data; *Right columns:* 15 GHz data; *Top* diameter gradient fit; *bottom* brightness temperature gradient fit

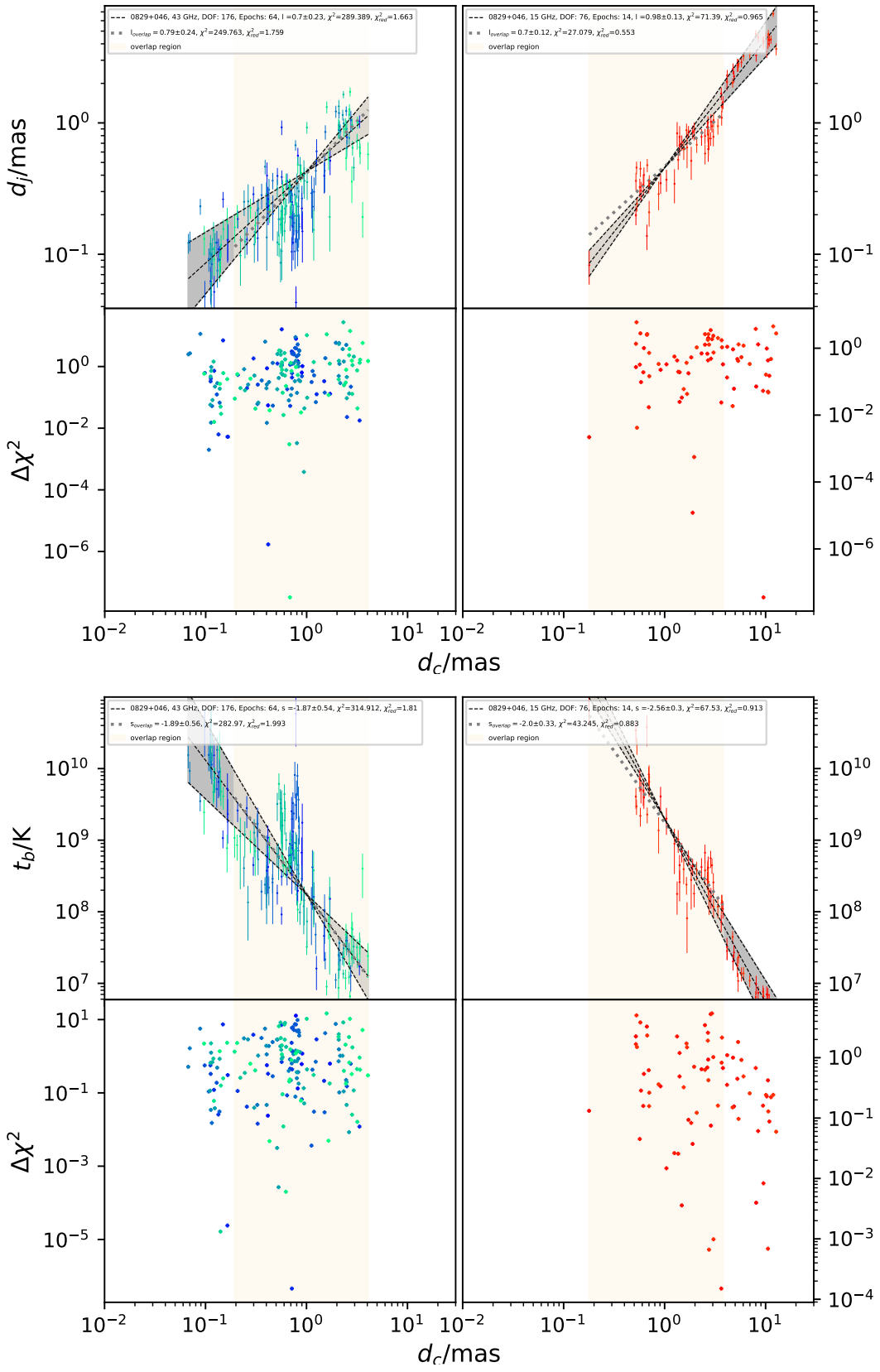

FIGURE 4.19: 0829+046; *Left columns:* 43 GHz data; *Right columns:* 15 GHz data; *Top* diameter gradient fit; *bottom* brightness temperature gradient fit

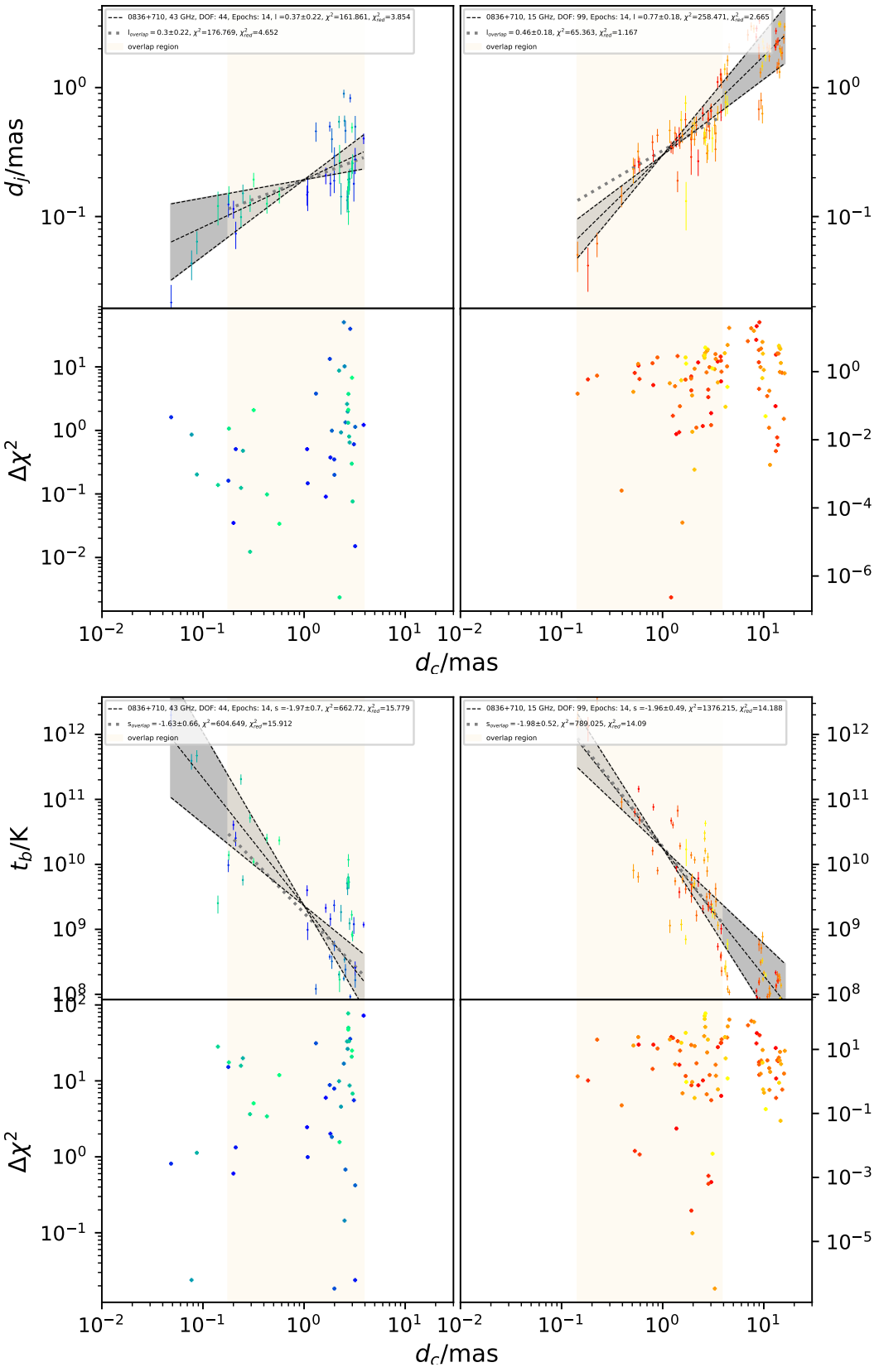

FIGURE 4.20: 0836+710; *Left columns:* 43 GHz data; *Right columns:* 15 GHz data; *Top* diameter gradient fit; *bottom* brightness temperature gradient fit

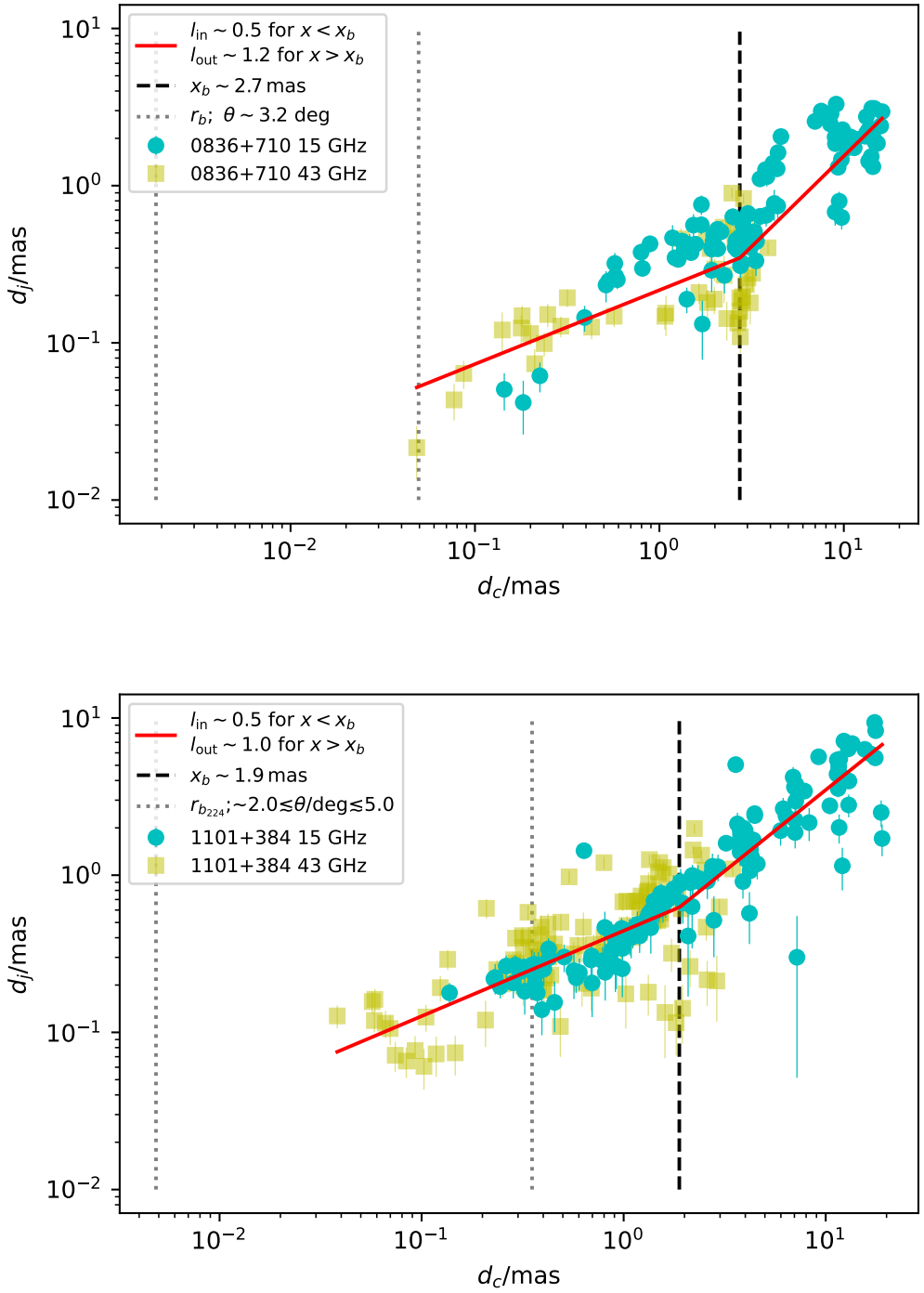

FIGURE 4.21: *Top:* 0836+710; *Bottom:* 1101+384; Both frequencies are fit together in order to constrain a break point as well as an outer and inner l-value.

0851+202 (B) is shown in Fig. 4.22. The l-values are consistent with a conical jet shape and the s-values are consistent with the canonical value. This jet is consistent with a classical Blandford & Königl (1979) jet.

0954+658 (B) features a conical jet shape at both frequencies, see Fig. 4.23. The s-value in the overlap region at 43 GHz is consistent with the canonical value, however the brightness temperature gradient along the entire jet length at both frequencies and the overlap region at 15 GHz is even steeper than the canonical value which can be cause by either electron energy density or the magnetic field strength density. In the case of a polodial magnetic field and equipartition, the s-values can theoretically become as steep as $s = -6$, with a reasonable spectral index of $\alpha = -0.5$. This means that in this source it is plausible to have a mix of torodial and polodial magnetic field gradients, thus a helical field, influencing the steepening of the s-values.

1101+384 (B) features a parabolic jet at 43 GHz (both cases). In the overlap region of the 15 GHz data the jet is less collimates, though not yet consistent with a cone, see Fig. 4.24. Along the entire jet length, the 15 GHz jet is consistent with a cone. A similar picture is seen with respect to the s-values. The parabolic jet shape causes a flattening of the brightness temperature gradient at 43 GHz. The s-values at 15 GHz are consistent with a conical jet. In this source it is possible to constrain a geometry break point (Fig. 4.21) at $x_b \sim 1.9$ mas where the geometry transitions from parabolic to conical. An inclination angle for this source is not easily obtained. (Giroletti et al. 2006) constrained $\theta \sim 19$ deg by analyzing the jet to counter-jet flux density ratio from observations on kpc scales. Based on Doppler factor and variability analysis Hovatta et al. (2015) estimated the inclination angle to be $0.5 \lesssim \theta/\mathrm{deg} \lesssim 4$. Lico et al. (2012) argue that the maximum apparent speed measured for this source, $\beta_{\mathrm{app,max}} = 0.218 \pm 0.026$, (Lister et al. 2019) is most likely not the speed of the physical jet's flow because the beaming properties, which would result from the jet to counter jet flux density ratio would be close to zero in this case. Based on the jet showing limb brightening (Piner et al. 2010), which is an indication for a transverse velocity structure across the jet, Lico et al. (2012) estimate an inclination angle in the range of $2 \lesssim \theta/\mathrm{deg} \lesssim 5$ which is adopted in this analysis.

1127-145 (Q) features l values which are consistent with a parabolic jet in both frequencies. Consistently with the strongly confined jets, the s-values indicate flat s-values in both frequencies. Both the s and l values are indistinguishable between the frequencies. Overall the jet shows a very complex structure which is resembled by the large χ^2_{red} values.

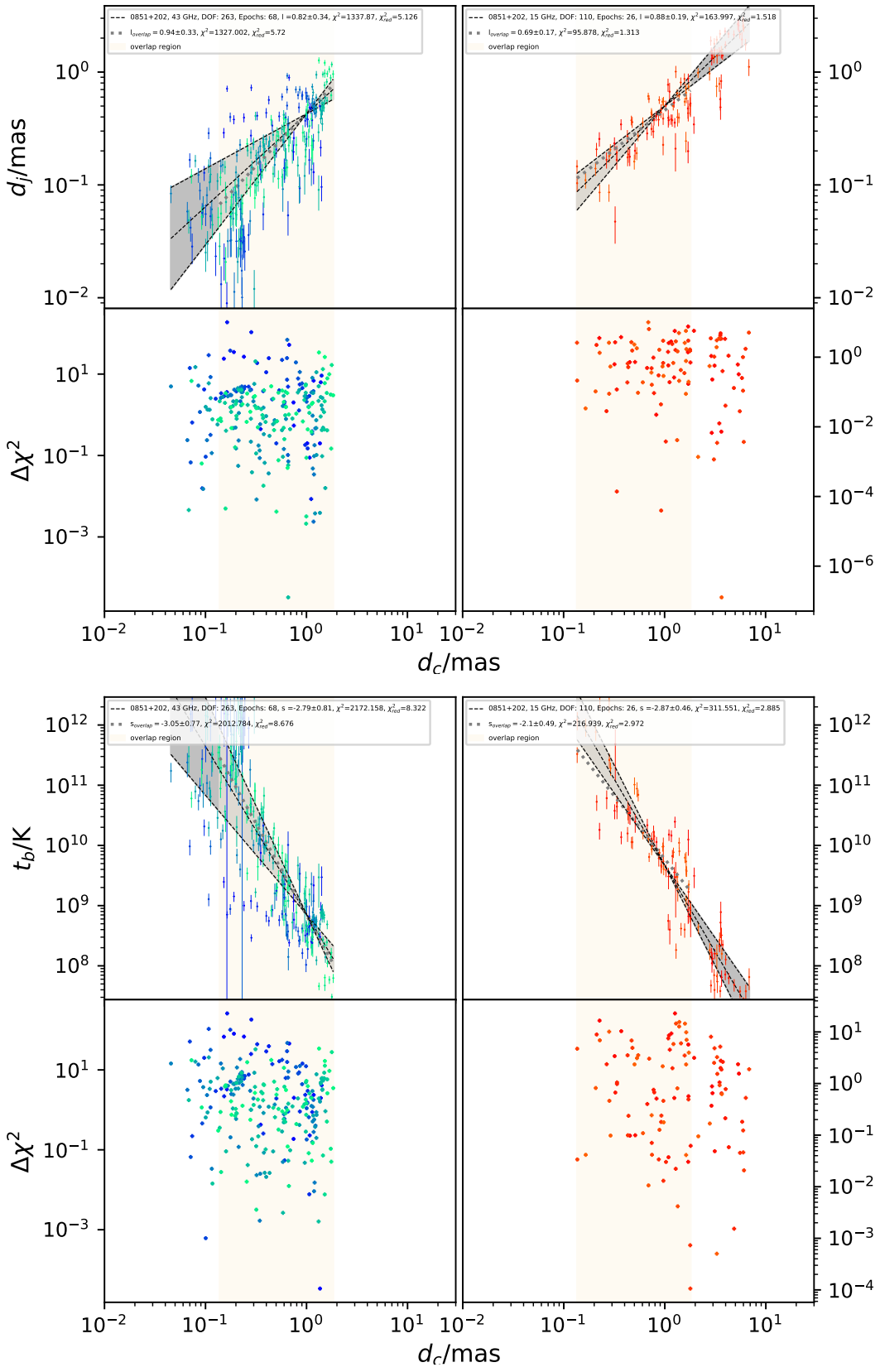

FIGURE 4.22: 0851+202; *Left columns:* 43 GHz data; *Right columns:* 15 GHz data; *Top* diameter gradient fit; *bottom* brightness temperature gradient fit

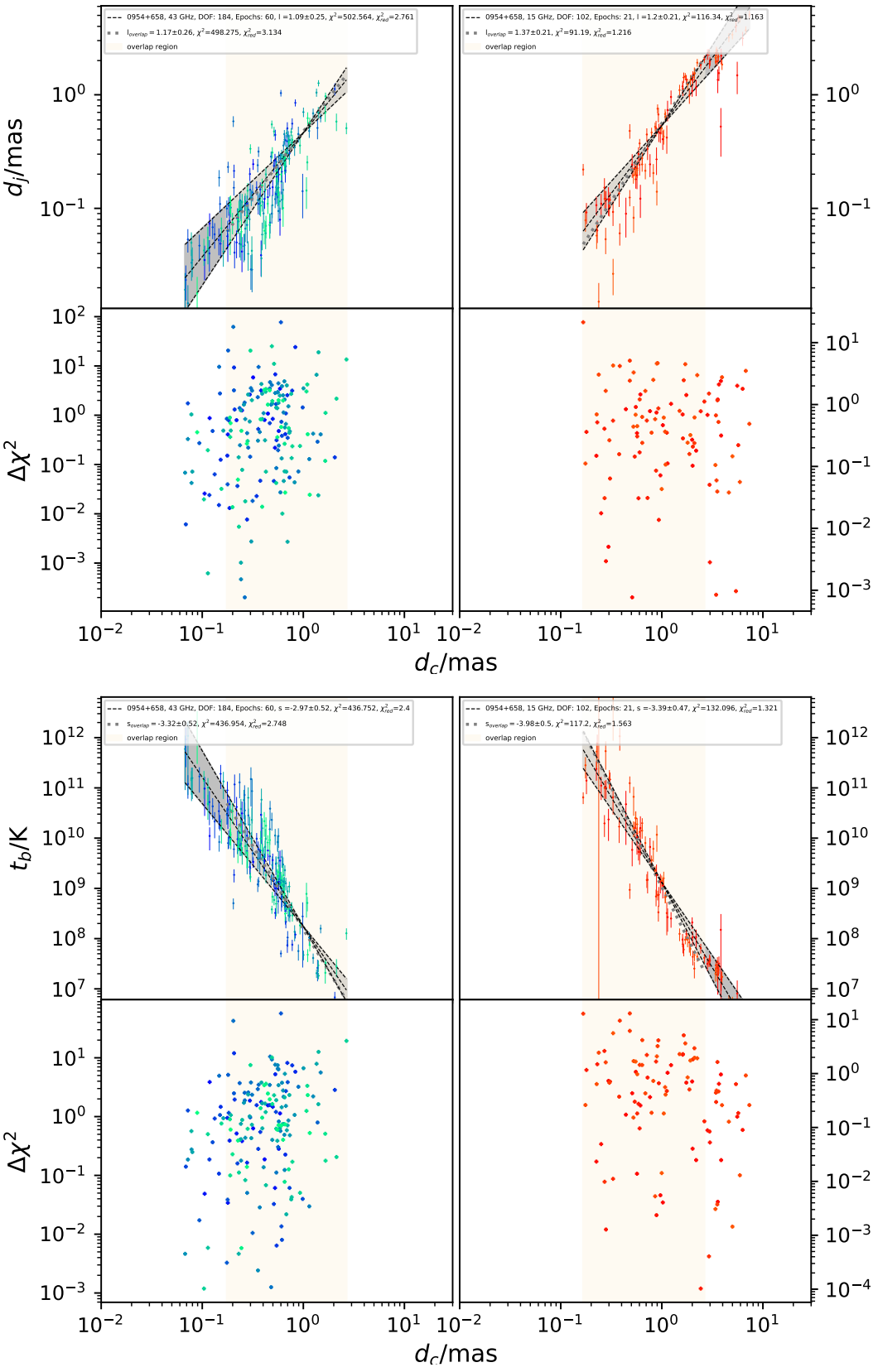

FIGURE 4.23: 0954+658; *Left columns:* 43 GHz data; *Right columns:* 15 GHz data; *Top* diameter gradient fit; *bottom* brightness temperature gradient fit

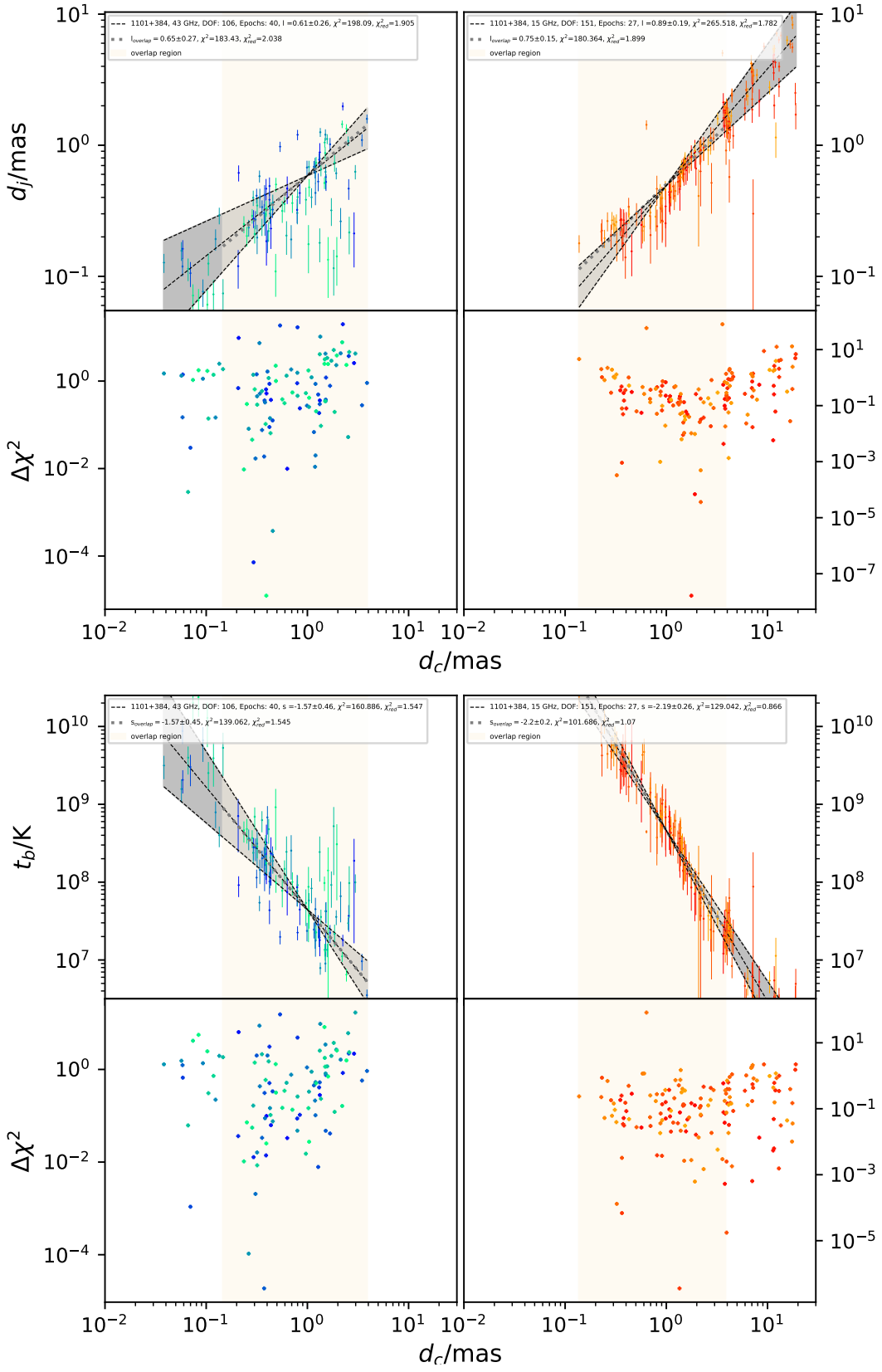

FIGURE 4.24: 1101+384; *Left columns:* 43 GHz data; *Right columns:* 15 GHz data; *Top* diameter gradient fit; *bottom* brightness temperature gradient fit

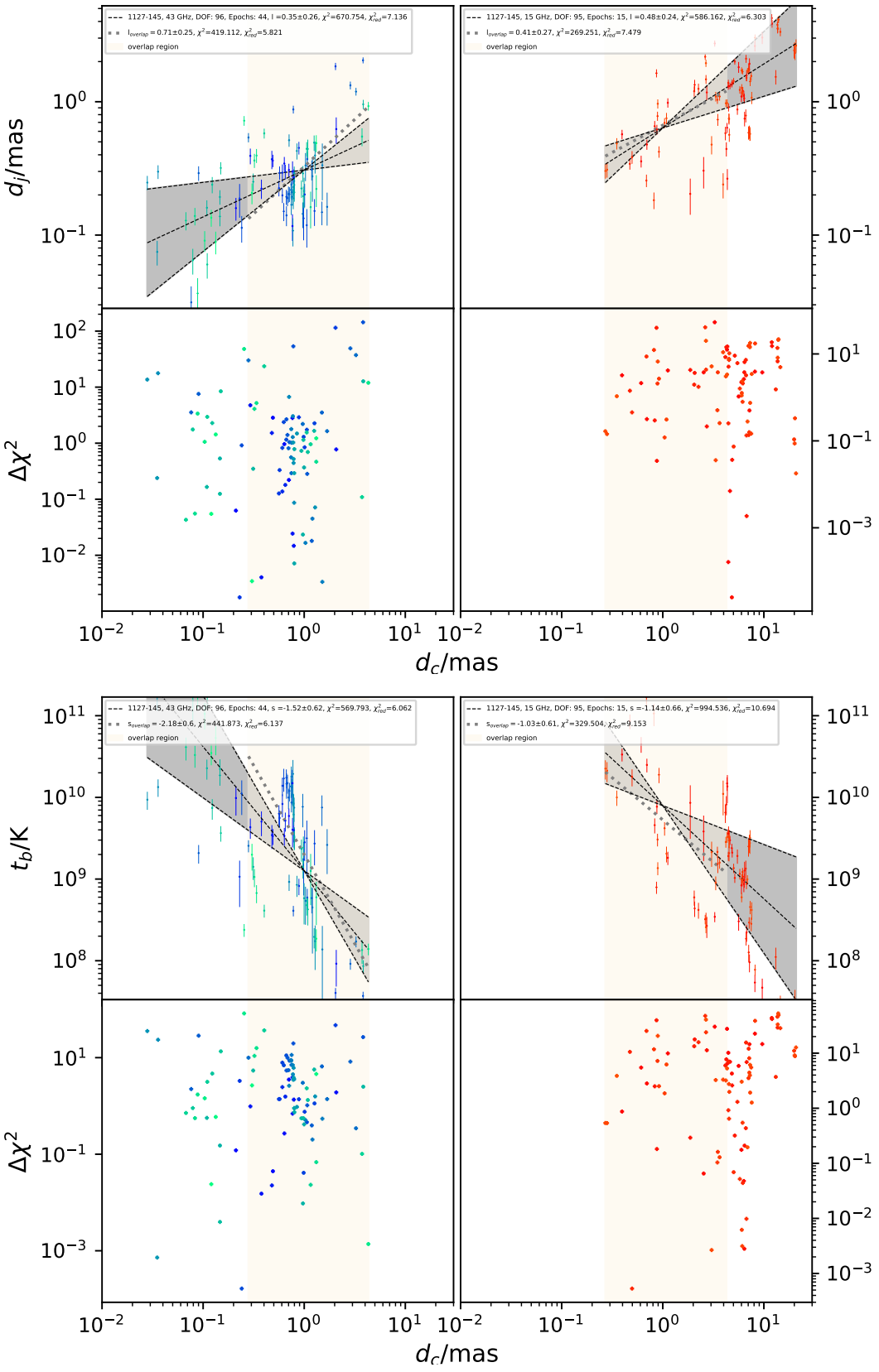

FIGURE 4.25: 1127-145; *Left columns:* 43 GHz data; *Right columns:* 15 GHz data; *Top* diameter gradient fit; *bottom* brightness temperature gradient fit

1156+295 (Q) features collimated jets in both frequencies and consistent brightness temperature gradients, see Fig. 4.26. In the 15 GHz jet a transition in the geometry is indicated because the overlap region shows a flatter diameter gradient than the entire jet length. A break point of the geometry can be constrained at $x_b \sim 2.5$ mas, where the jet switches from parabolic ($l_{\rm in} \sim 0.7$) to hyperbolic ($l_{\rm out} \sim 1.2$) (Fig. 4.27, top).

1219+285 (B) features l-values which are consistent, within the errors, with a conical and a parabolic jet shape for both frequencies. They are also indistinguishable between the frequencies. The s-values at 43 GHz are flatter than expected for a conical jet which may hint to a jet that is more consistently described with a rather confined geometry. At 15 GHz the brightness temperature is consistent with a freely expanding jet.

1222+216 (Q) shows a parabolic jet shape at 43 GHz and a conical jet shape at 15 GHz. A transition however cannot be consistently constrained. Due to the scattering of the data and the large error bars, both frequencies taken together are also best described by a single power law. The s-values are consistent with a confined jet at 43 GHz, however the values are more in line with a magnetic field in the jet of helical structure rather than the torodial or polodial component dominating. The fits are shown in Fig. 4.29.

1253-055 (Q) is a complex source which shows a parabolic jet shape at 43 GHz and a conical shape at 15 GHz. The s-values at 43 GHz are consistent with a freely expanding jet, however the errors are quite large for this fit, due to the large scatter within the data. At least this is a hint for a helical magnetic field within the jet in this source. The s-values at 15 GHz are in line with the conical jet, see Fig. 4.30 Akiyama et al. (2018) finds a geometry transition in this source at ~ 1 mas using VLBA data at 1.4 GHz and MERLIN data at 1.6 GHz. MERLIN is a compact array and resolves the source on kpc scales. Considering the 43 GHz and 15 GHz data a break point of the geometry is found at $x_b \sim 0.6$ mas. The inner jet geometry scaling is parabolic ($l_{\rm in} \sim 0.5$). After the transition the jet is still confined ($l_{\rm out} \sim 0.8$), see Fig. 4.27(top). It is remarkable to note that Akiyama et al. (2018) find the geometry break in the region where the jet structure at 43 GHz is very complex, featuring a strong bright component and a dip in the d_j gradients. I want to emphasize that these different break points not necessarily contradict each other. Taking different data into account may vary the break points that can be found within the structure of this source. It is remarkable that compared across these large distance, the results are that consistent.

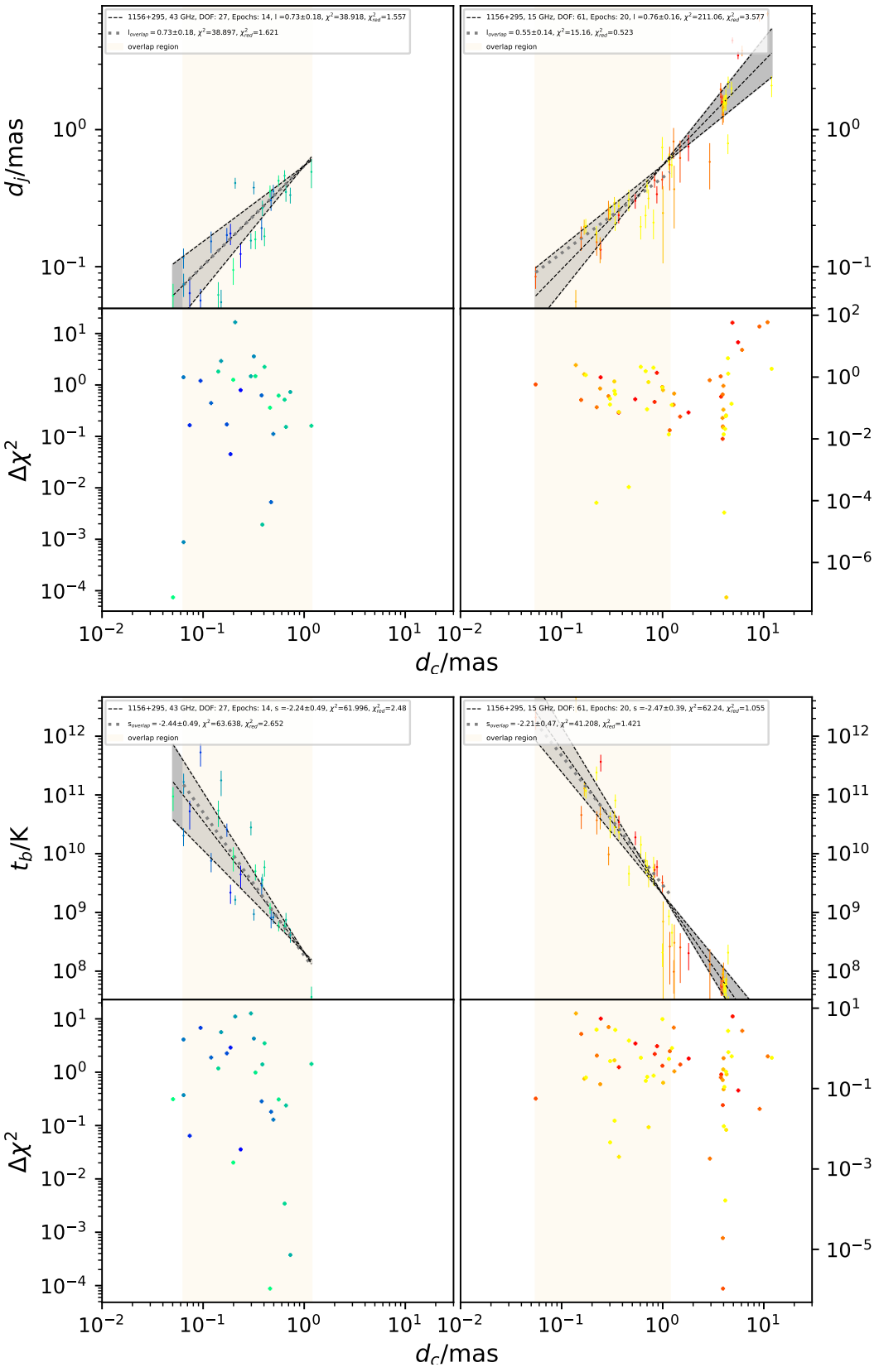

FIGURE 4.26: 1156+295; *Left columns:* 43 GHz data; *Right columns:* 15 GHz data; *Top* diameter gradient fit; *bottom* brightness temperature gradient fit

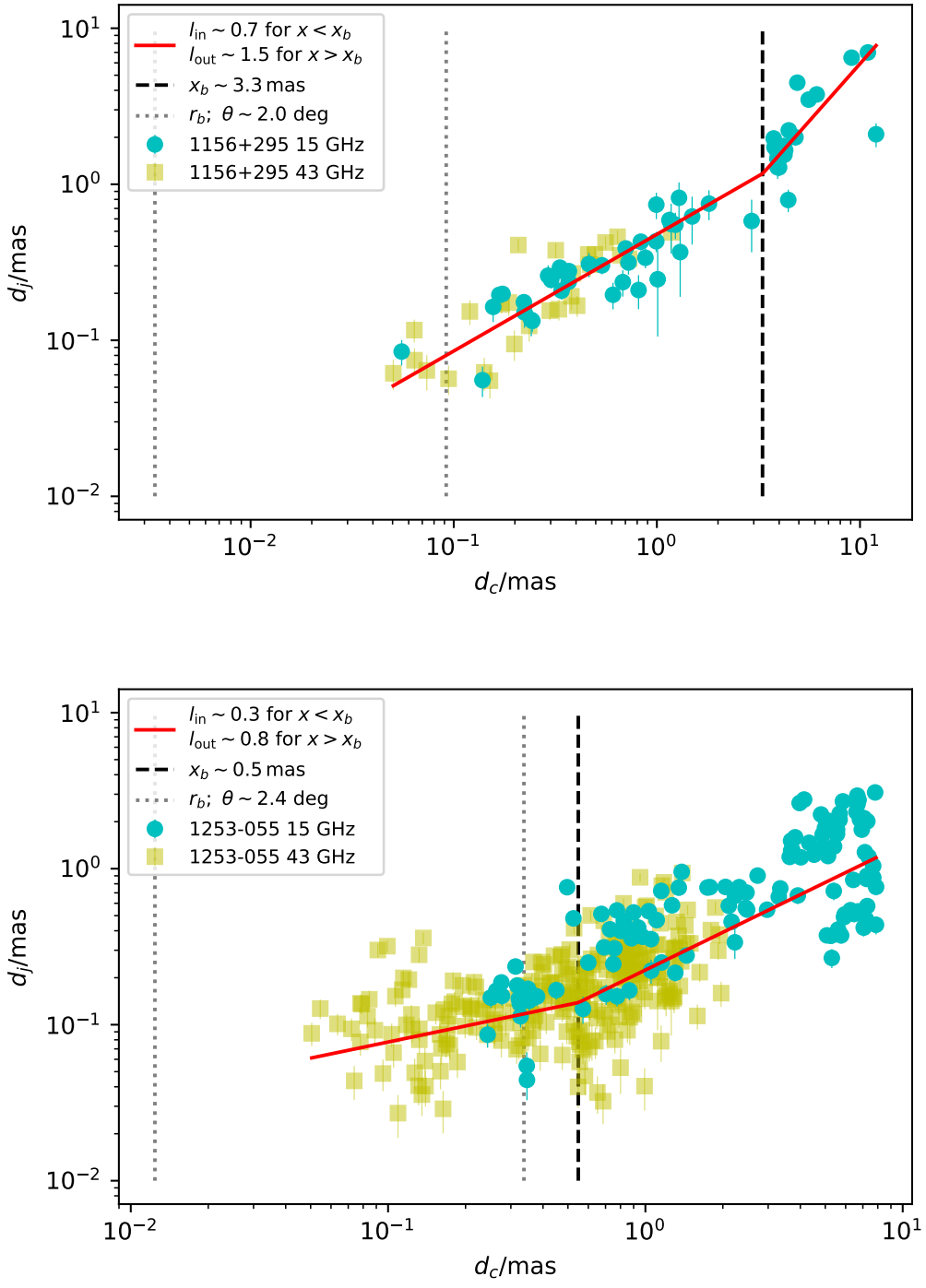

FIGURE 4.27: *Top:* 1156+295; *Bottom:* 1253-055; Both frequencies are fit together in order to constrain a break point as well as an outer and inner l-value.

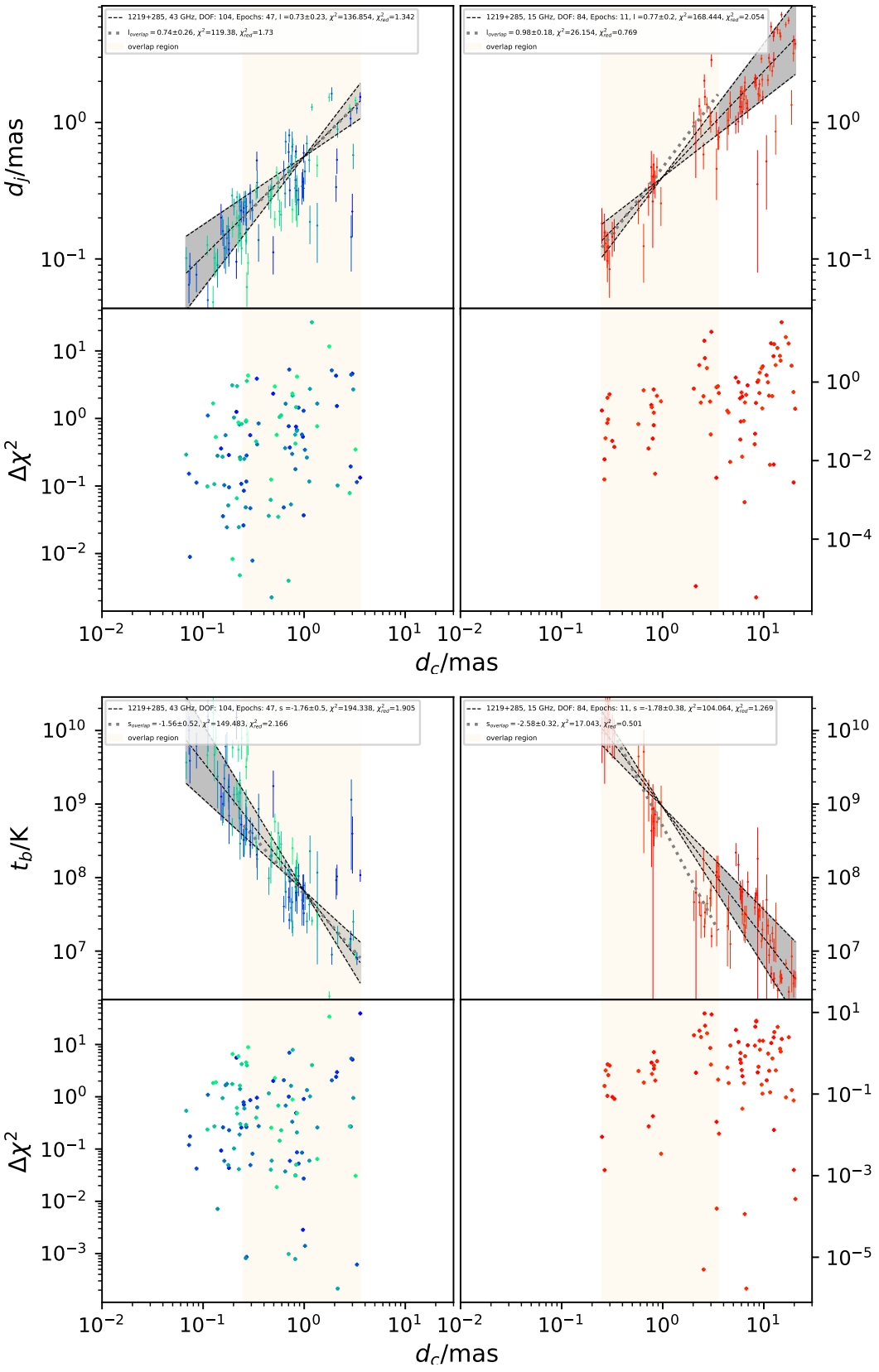

FIGURE 4.28: 1219+285; *Left columns:* 43 GHz data; *Right columns:* 15 GHz data; *Top* diameter gradient fit; *bottom* brightness temperature gradient fit.

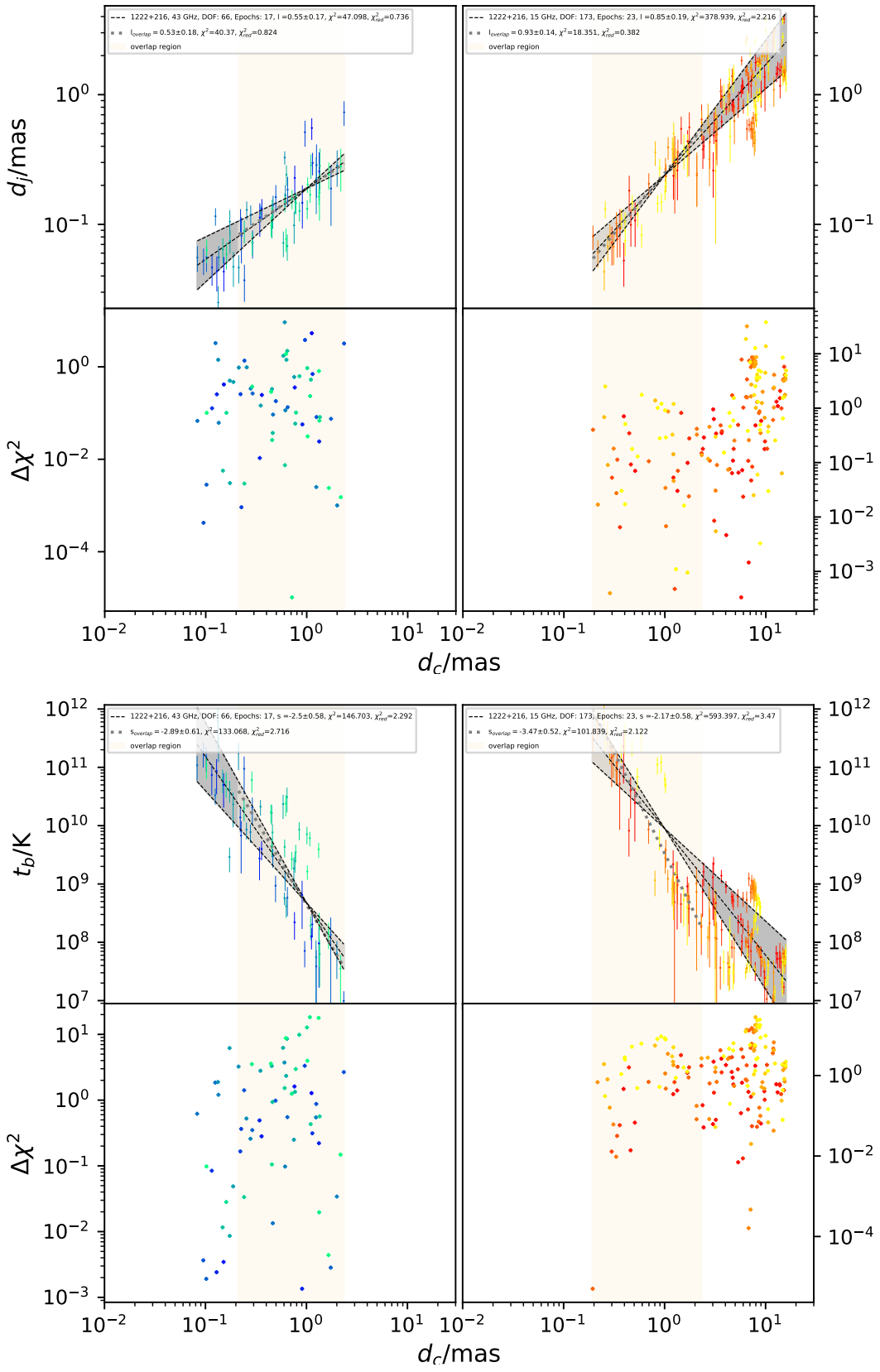

FIGURE 4.29: 1222+216; *Left columns:* 43 GHz data; *Right columns:* 15 GHz data; *Top* diameter gradient fit; *bottom* brightness temperature gradient fit.

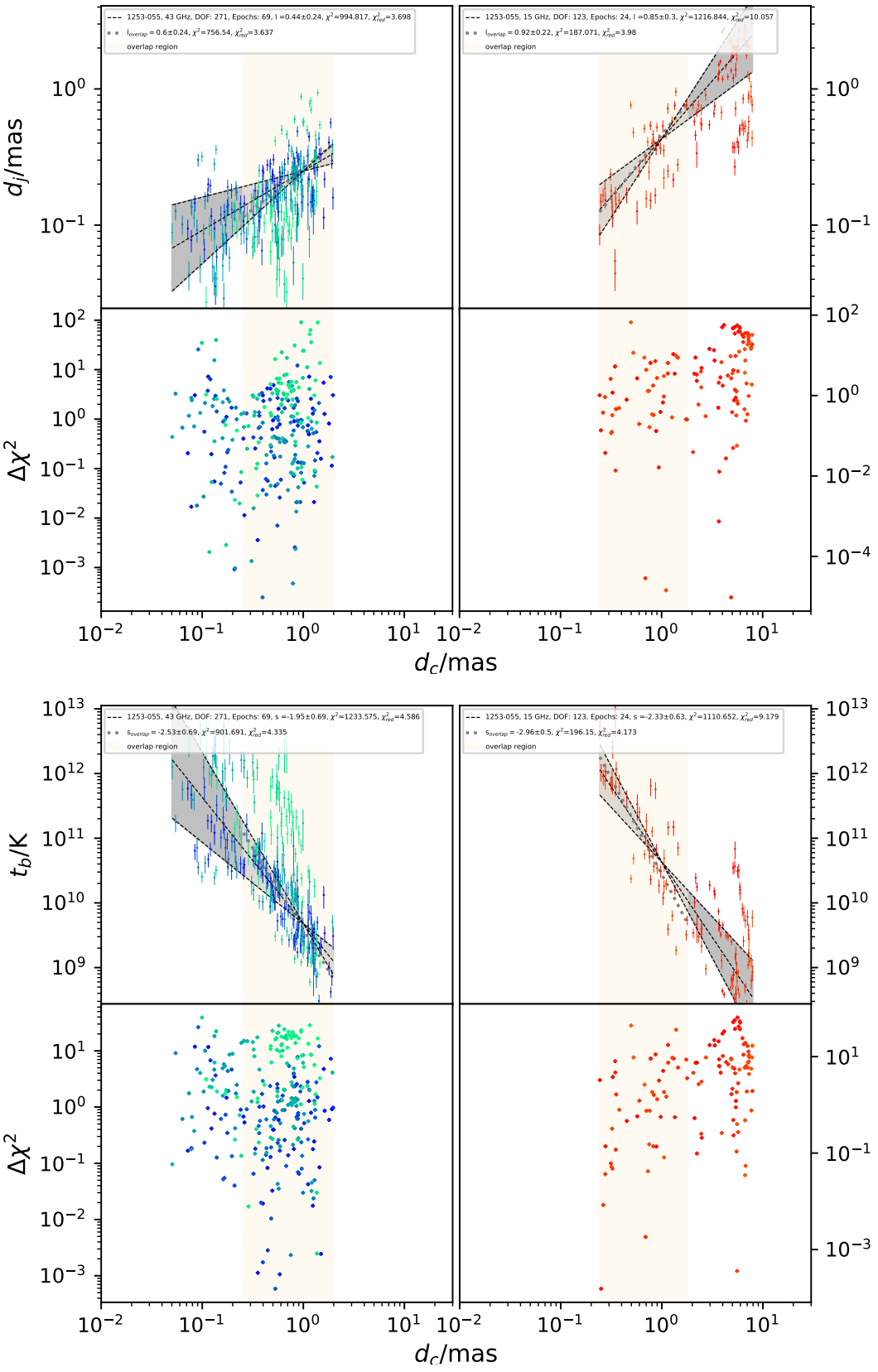

FIGURE 4.30: 1253-055; *Left columns:* 43 GHz data; *Right columns:* 15 GHz data; *Top* diameter gradient fit; *bottom* brightness temperature gradient fit.

1308+326 (Q) is consistent with a classical Blandford & Königl (1979) jet with respect to the jet geometry and the brightness temperature gradients (Fig. 4.31).

1633+382 (Q) is a slightly confined jet at both frequencies, which is also reflected in slightly flatter brightness temperature gradients. The jet at the different frequencies is not distinguishable. Both frequencies show a dip in the d_j-gradient and an excess in the T_b gradient between $1 \lesssim d_c/\mathrm{mas} \lesssim 4$. At 43 GHz there is another region that features excesses in T_b and dips in d_j between $0.2 \lesssim d_c/\mathrm{mas} \lesssim 0.6$. These regions may be a hint to several recollimation shocks within the jet. The fits are shown in Fig. 4.32

1652+398 (B) shows a parabolic jet at both frequencies and consistently flat brightness temperature gradients, see Fig. 4.33.

1730-130 (Q) features a classical Blandford & Königl (1979) jet at 43 GHz with a conical jet and s-values consistent with the canonical value. This is also true in the overlap region at 15 GHz. However along the entire 15 GHz jet, the fit is heavily influenced by a consistently appearing component between $20 \lesssim d_c/\mathrm{mas} \lesssim 30$, which is relatively small and bright. This has the consequence, that the 15 GHz jet appears parabolic with a consistent flat T_b gradient, which could hint to a recollimation zone in this region. The fits are shown in Fig. 4.34.

1749+096 (B) features l-values which are consistent with a conical jet at both frequencies. The s-values, also at both frequencies, are steeper than the canonical value, which hints to the presence of a helical magnetic field structure (fig. 4.35).

2200+420 (B) is an extensively observed jet (most observed epochs in the sample) with a very complex structure. At 43 GHz the jet shape is consistent with a cone in the overlap region and along the entire jet length. This also holds for the 15 GHz jet in the overlap region, see Fig. 4.36. Along the entire jet length, the geometry of this source is consistent with a hyperbola, indicating an abrupt opening of the jet. Casadio et al. (2021) confirmed this conical behavior closer to the physical jet basis by also taking GMVA data at 86 GHz into account. At ~ 1.5 mas Casadio et al. (2019) find a recollimation shock which they trace back to accelerating model components. This region is remarkable within the d_j gradients because at this point the jet shows a dip in the d_j-gradient and an excess in the T_b-gradient, consistently at both frequencies. At ~ 2.0 mas from the radio core a geometry break can be constrained in this source, where the jet transitions from parabolic to hyperbolic, see Fig. 4.37.

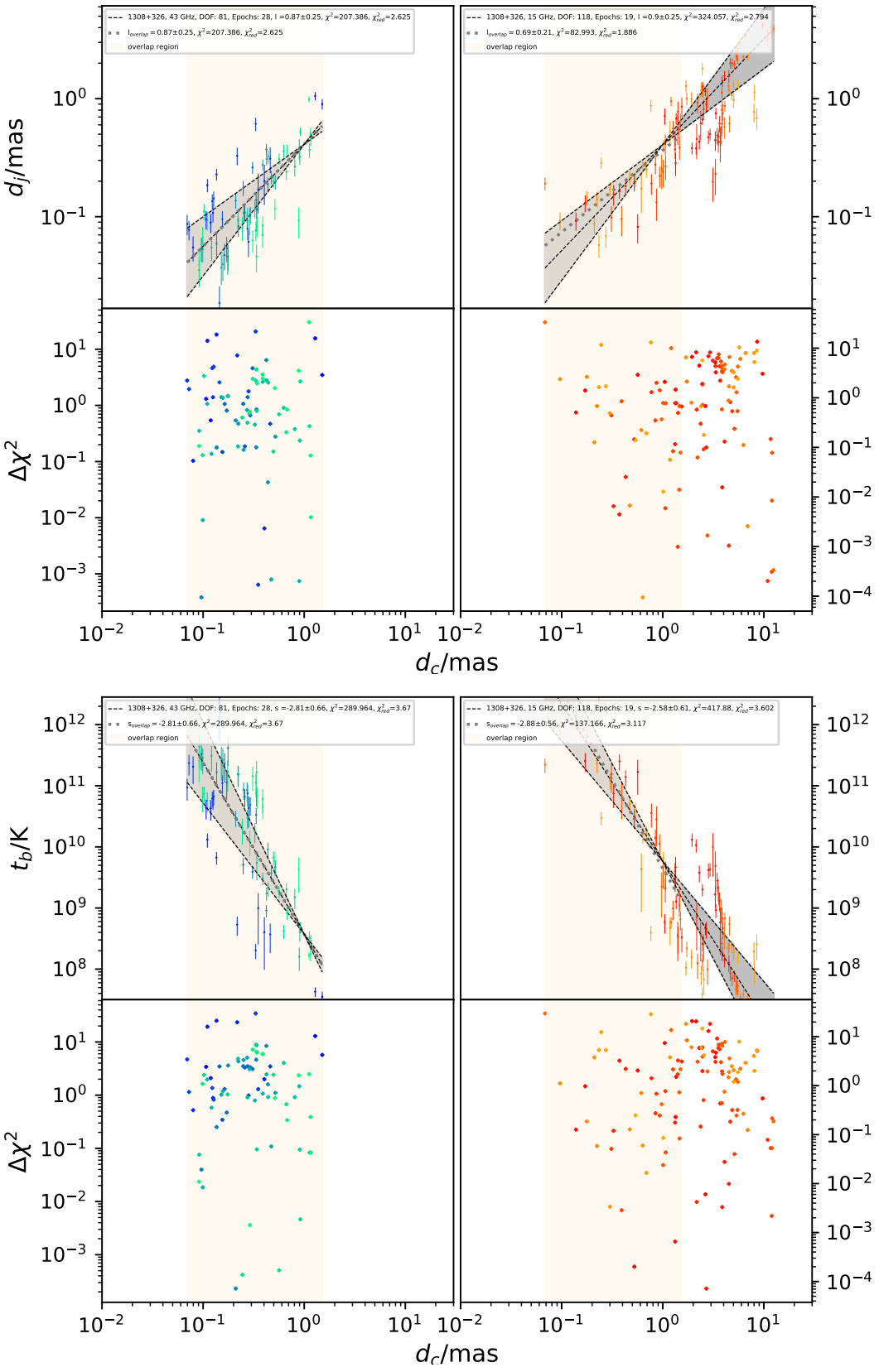

FIGURE 4.31: 1308+326; *Left columns:* 43 GHz data; *Right columns:* 15 GHz data; *Top* diameter gradient fit; *bottom* brightness temperature gradient fit.

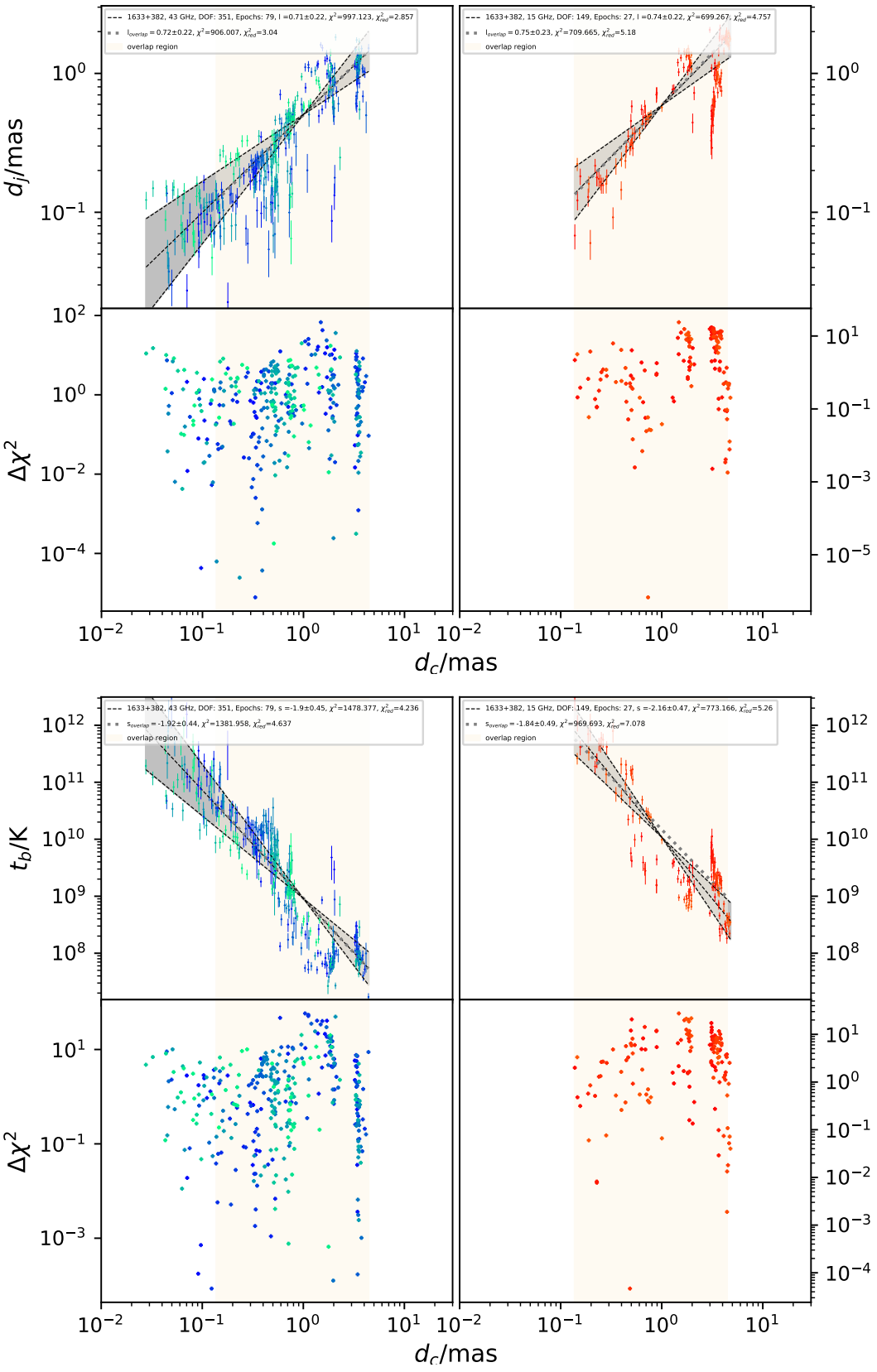

FIGURE 4.32: 1633+382; *Left columns:* 43 GHz data; *Right columns:* 15 GHz data; *Top* diameter gradient fit; *bottom* brightness temperature gradient fit.

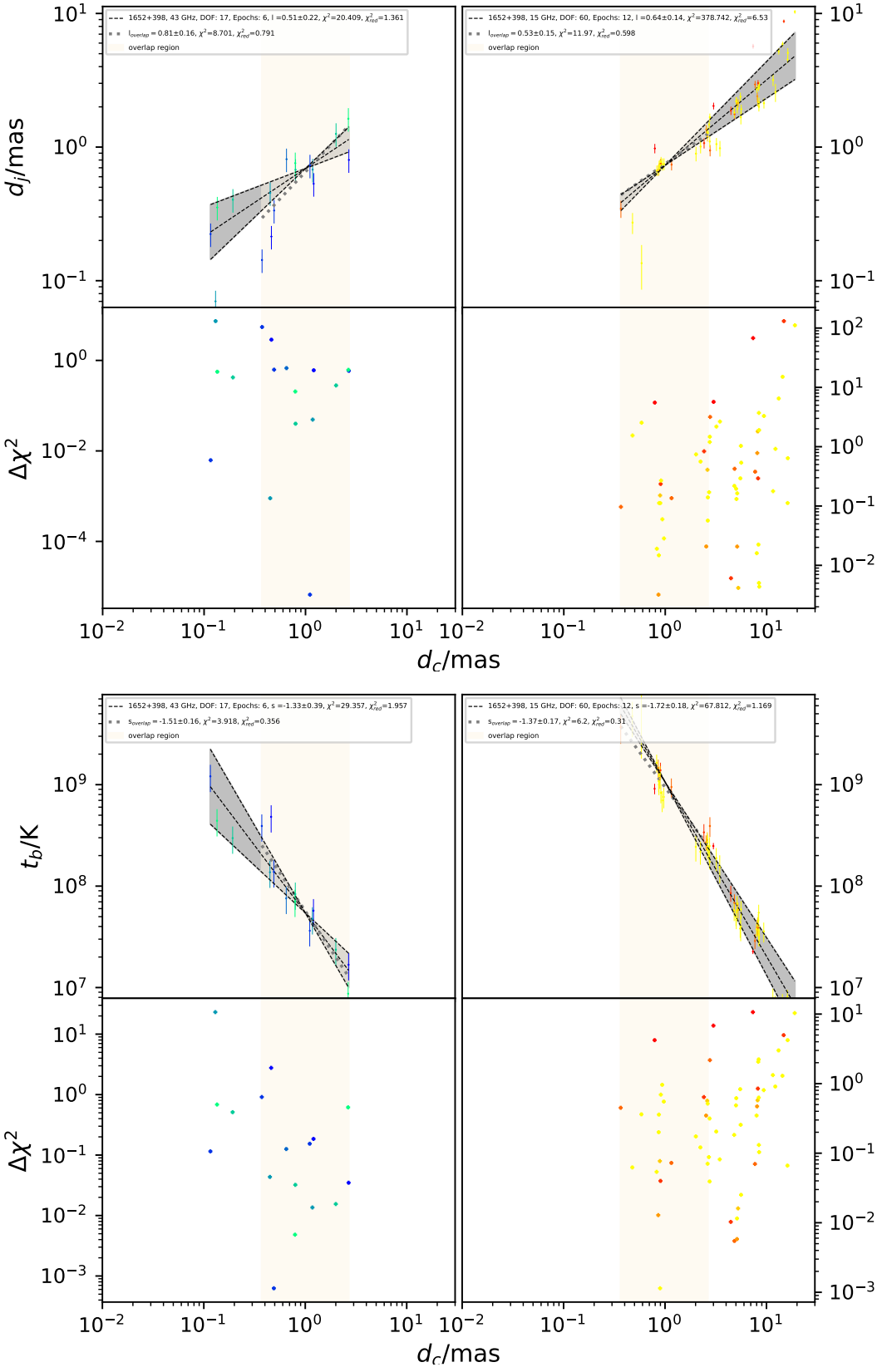

FIGURE 4.33: 1652+398; *Left columns:* 43 GHz data; *Right columns:* 15 GHz data; *Top* diameter gradient fit; *bottom* brightness temperature gradient fit.

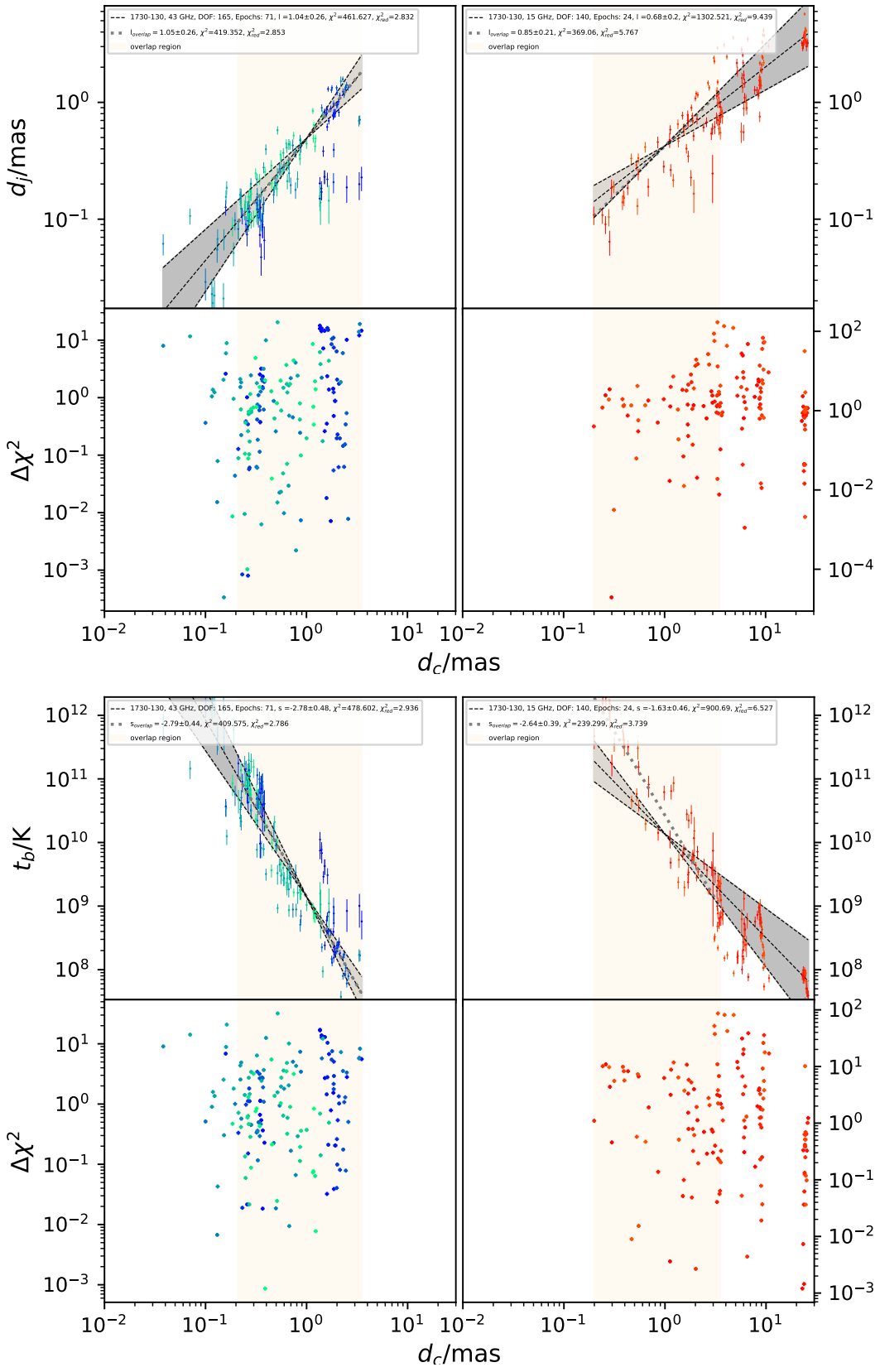

FIGURE 4.34: 1730-130; *Left columns:* 43 GHz data; *Right columns:* 15 GHz data; *Top* diameter gradient fit; *bottom* brightness temperature gradient fit.

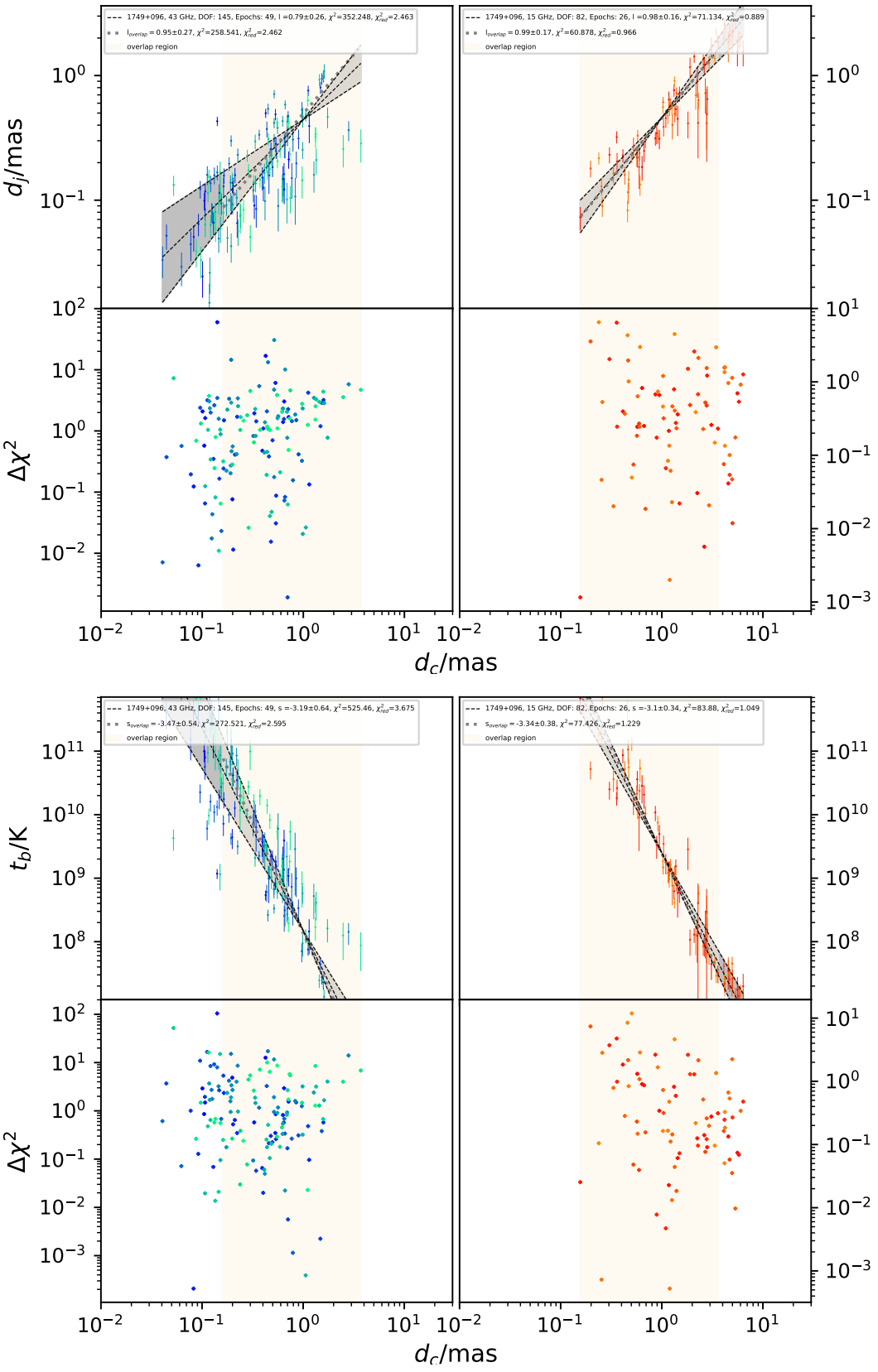

FIGURE 4.35: 1749+096; *Left columns:* 43 GHz data; *Right columns:* 15 GHz data; *Top* diameter gradient fit; *bottom* brightness temperature gradient fit.

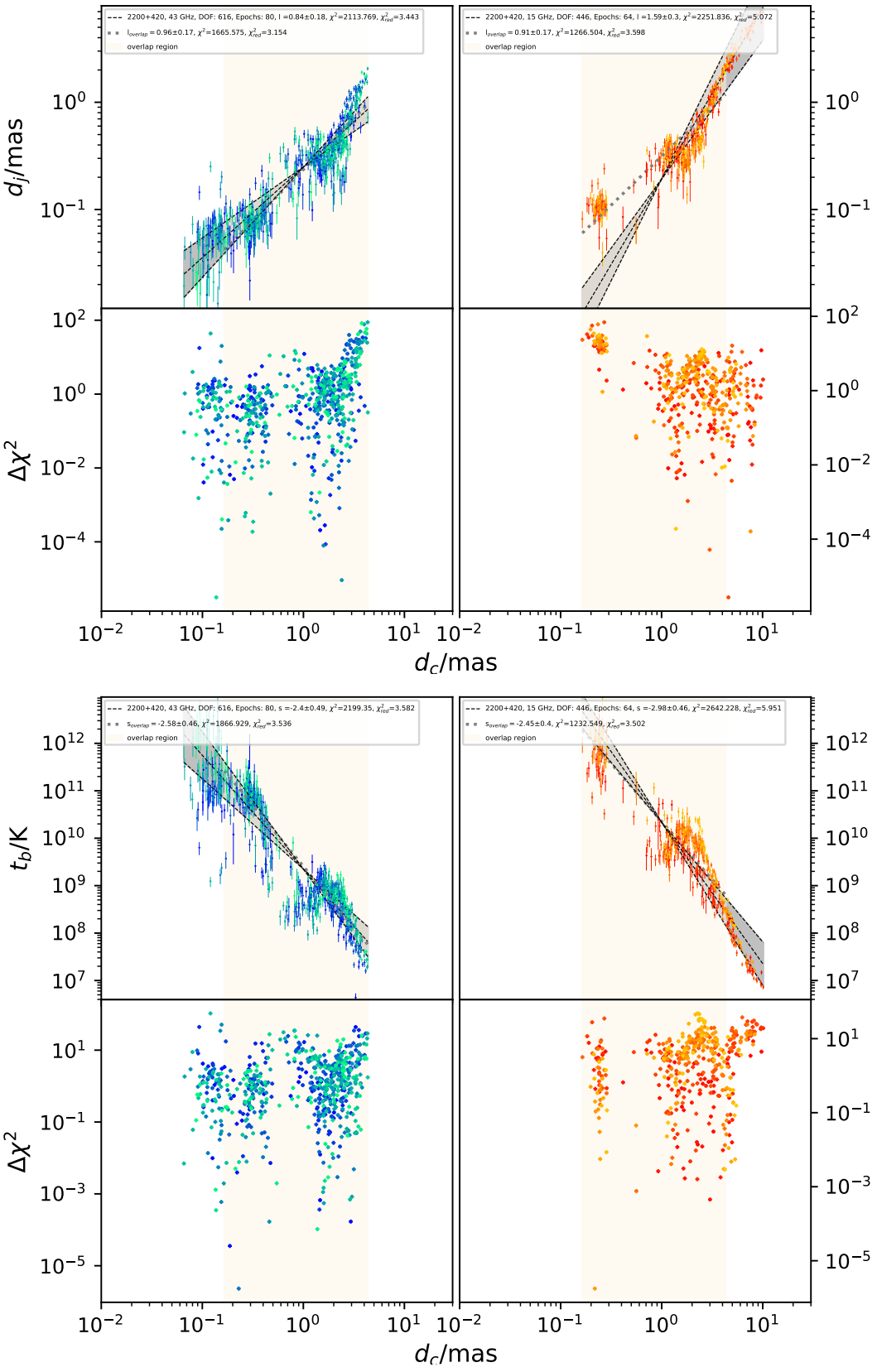

FIGURE 4.36: 2200+420; *Left columns:* 43 GHz data; *Right columns:* 15 GHz data; *Top* diameter gradient fit; *bottom* brightness temperature gradient fit.

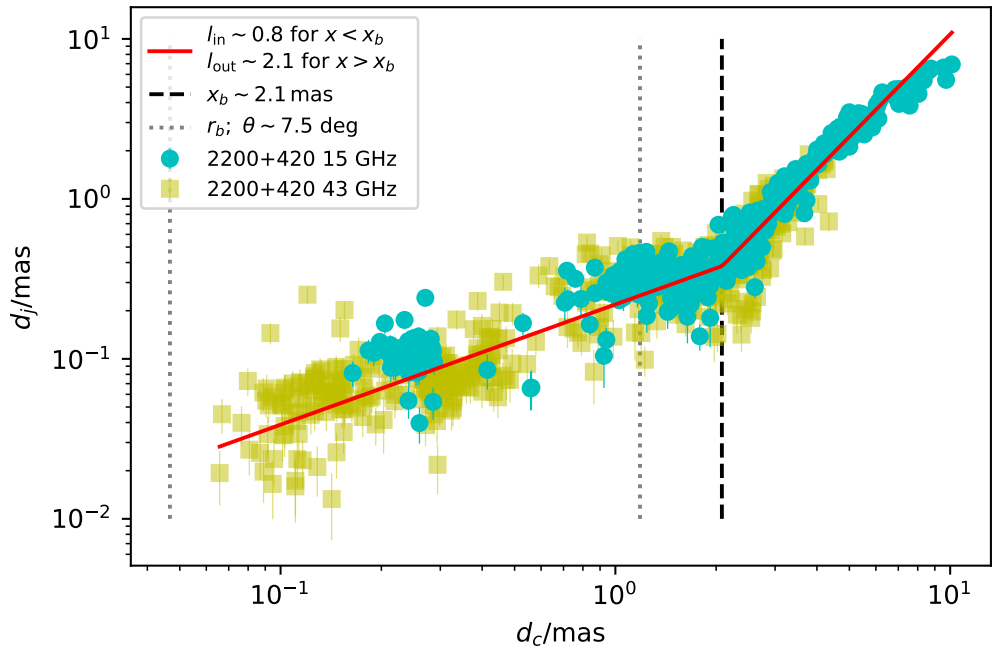

FIGURE 4.37: 2200+420; Both frequencies are fit together in order to constrain a break point as well as an outer and inner l-value.

2223-052 (B) feature diameter gradients at 43 GHz are consistent with a conical jet however the 15 GHz data is consistent with a parabolic jet. In this case this is probably caused by data points close to the radio core with small error bars in a single epoch (color code). An indication that the measured diameter gradient at 15 GHz are probably unnaturally influenced by data points from single epochs is the brightness temperature gradient, which for both frequencies is consistent with the canonical value for a freely expanding jet. Another hint that there is no true geometry transition in this source is that it is nor possible to constrain a proper break point in the geometry of this source.

2230+114 (B) shows a parabolic jet at 43 GHz and a less confined (not yet conical) jet at 15 GHz. The brightness temperature gradient at 43 GHz is consistent with a confined jet and consistent with the canonical value at 15 GHz, see Fig. 4.39.

2251+158 (B) also shows a parabolic jet at 43 GHz and a less confined (not yet conical) jet at 15 GHz. The brightness temperature gradient at 43 GHz is consistent with a confined jet and consistent with the canonical value at 15 GHz, see Fig. 4.40.

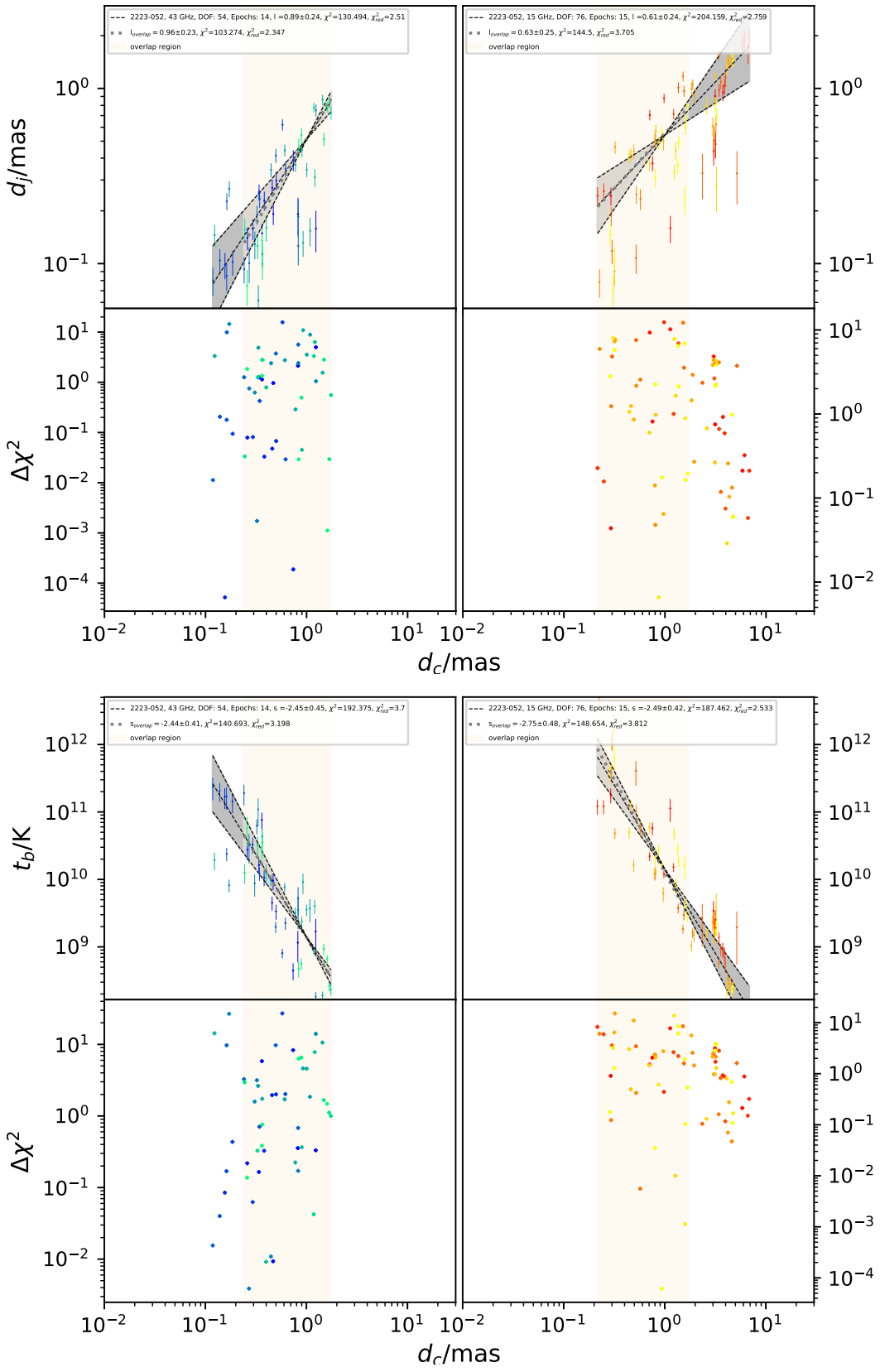

FIGURE 4.38: 2223-052; *Left columns:* 43 GHz data; *Right columns:* 15 GHz data; *Top* diameter gradient fit; *bottom* brightness temperature gradient fit.

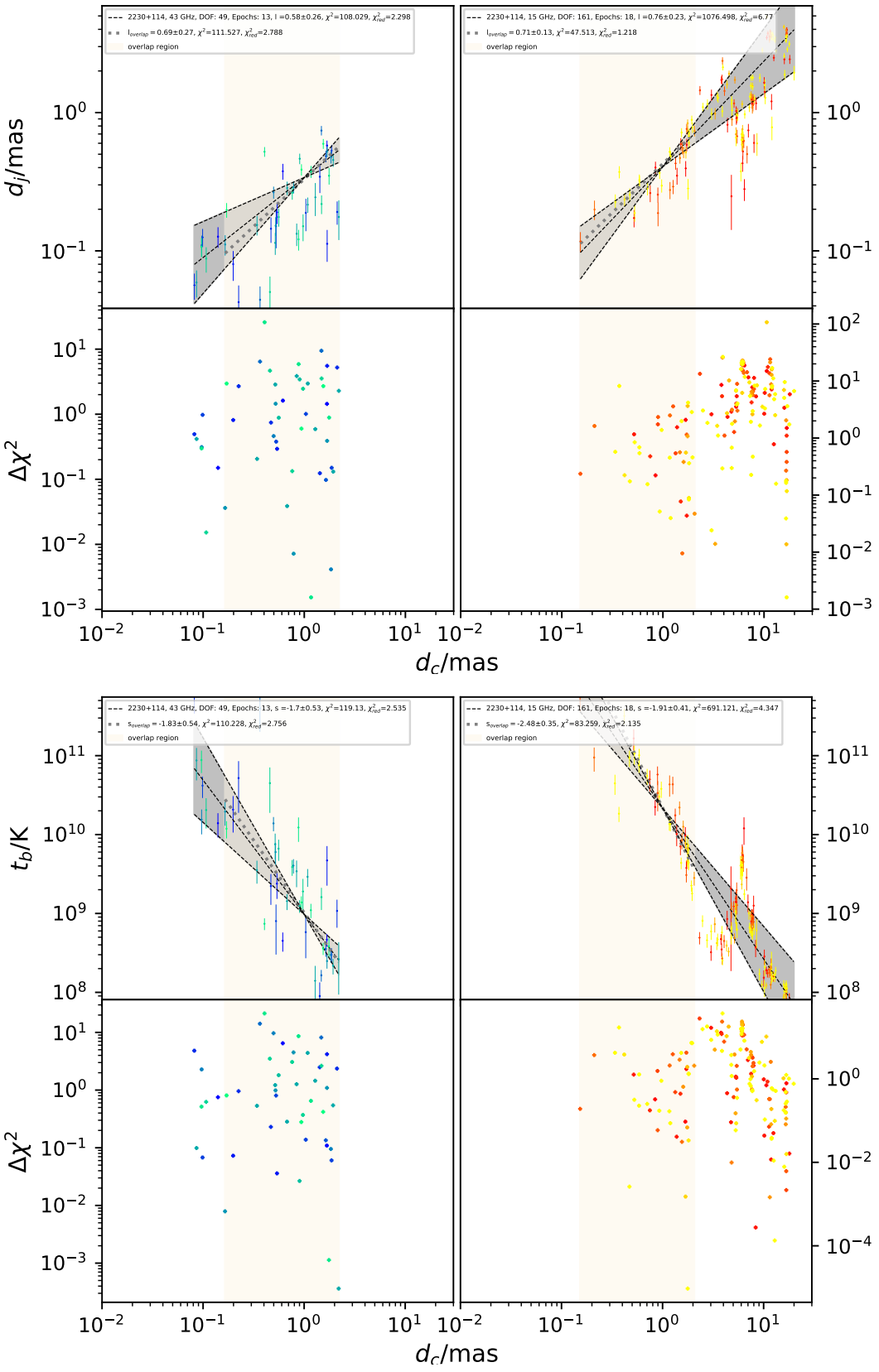

FIGURE 4.39: 2230+114; *Left columns:* 43 GHz data; *Right columns:* 15 GHz data; *Top* diameter gradient fit; *bottom* brightness temperature gradient fit.

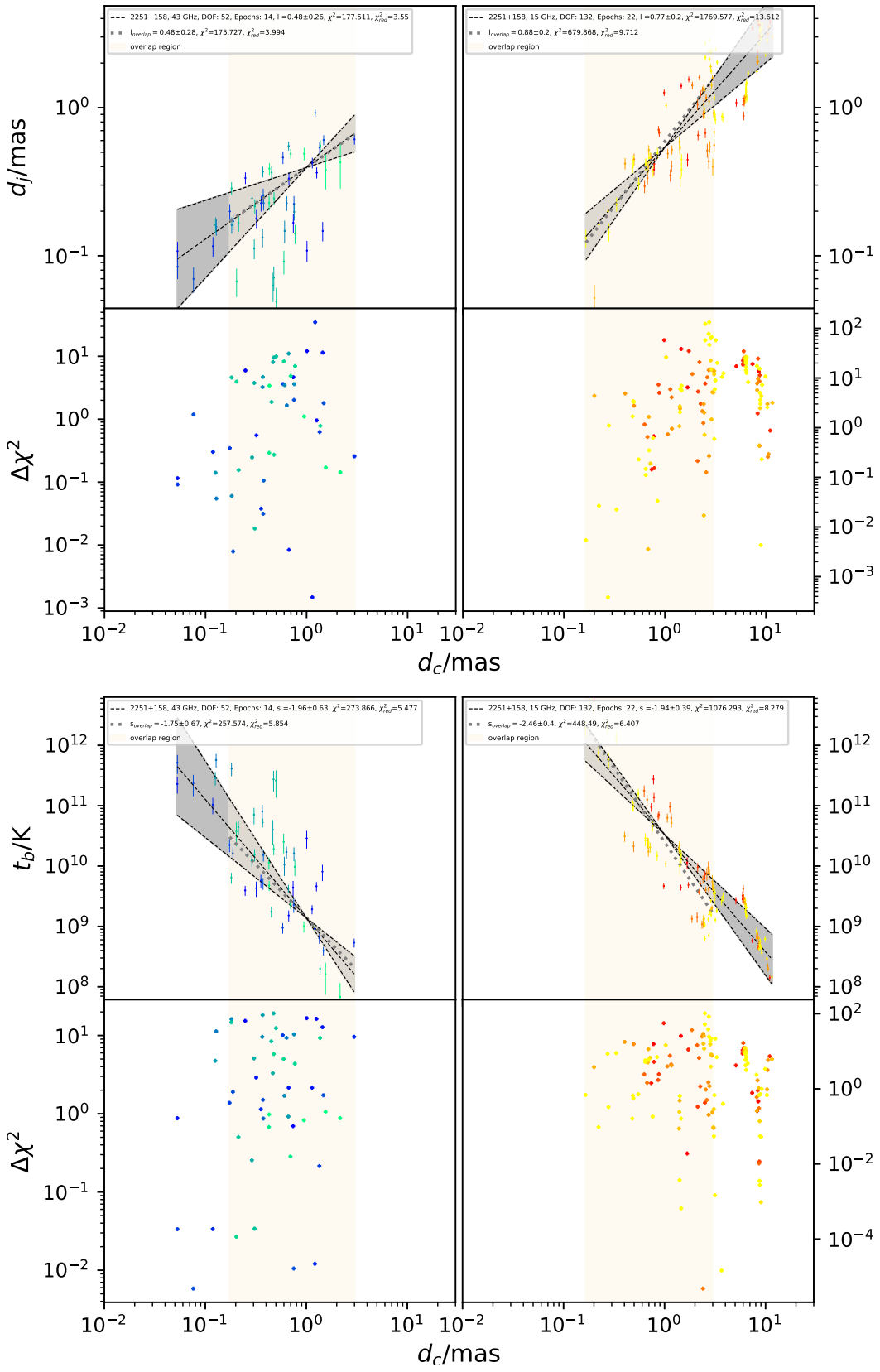

FIGURE 4.40: 2251+158; *Left columns:* 43 GHz data; *Right columns:* 15 GHz data; *Top* diameter gradient fit; *bottom* brightness temperature gradient fit.

Chapter 5

Results from the γ-ray light curve analysis

Starrheit treibt die Seele ungetrübt in
Mauern endloser Leere

Des Wesens Reiz, P. R. Burd, A. Kieckhöfel

In this chapter I will show and discuss the OU, PSD slope and flare shape asymmetry analysis for a large sample of monthly-binned blazars as well as for the 28 sources from the radio sample, analyzed in chapter 4. Two larger samples of monthly-binned blazars will be analyzed. For the sample used in Peñil et al. (2020) and Burd et al. (2021), the '1 GeV' sample[1], the results from Burd et al. (2021) are briefly reported and also extended to study possible differences between BL Lacs and FSRQs. This sample contained 2278 sources and a observation time span of 119 months ($\sim$ 10 years). For the purpose of this thesis, Prof. Sara Buson kindly provided me with an extension of the sample described in Sec. 3.2.1, which contains 3308 monthly binned sources in total, spanning a observation time period of 161 months ($\sim$ 13.5 years) in the energy band $E > 100$ MeV. Additionally to these larger samples, Andrea Gokus provided me with weekly-binned light curves from the 28 blazar jet sources from the diameter and brightness temperature gradient analysis which is the sample that will be analyzed in this chapter. All histograms shown are binned with the Bayesian block algorithm. The extracted OU $\mu, \sigma\sqrt{\Delta t}, \theta\Delta t$ parameters will be referred to as μ, σ, θ for convenience in the following analysis (see '6.Conclusion and outlook' in B21).

[1]The sample is actually computed for energies $E > 1$ GeV

5.1 1 GeV sample

First, I will briefly summarize the main results from Burd et al. (2021) and show how these results can be expanded.

- It is possible to create blazar light curves based on extracted OU parameters μ, σ, θ.
- The flares from the monthly binned blazar light curves show no preference for longer/shorter rise and decay times. If acceleration governs the rise time and cooling governs the decay time of flares this is unexpected.
- The OU process can reproduce blazar light curves with different colored noise, ranging from white to red noise. Also light curves, where a source only shows one major outbreak in an observation time of 10 years can be reproduced.
- The OU process is a description for the fluctuations of a logarithmic energy flux. The physical process amplifies these random fluctuations exponentially. Such processes could be realized by following scenarios:
  - Non-linear evolution of fluid-dynamical instabilities that lead to reconnection events, resulting in particle acceleration (Yuan et al. 2016; Blandford et al. 2017; Christie et al. 2019).
  - Acceleration of particles confined by random sequences of shock waves due to fluctuation in the jet velocity (Böttcher & Baring 2019).

The study in B21 aimed at showing that the OU process can describe a whole variety of different light curves. Systematics regarding differences in source classes have not been investigated in this paper. With the same data set and the same TS9 filter as used in B21, I analyze the OU parameters and the PSD slopes with respect to differences between FSRQs and BL Lacs. Figure 5.1 shows the distributions of the OU parameters and the PSD slopes for FSRQs and BL Lacs. The μ-distribution (top left) for BL Lacs shows systematically lower values than for FSRQs (KS: $p \sim 1.6 \times 10^{-7}\%$). The σ distributions (top right) also show smaller values for BL Lacs than for FSRQs (KS: $p \sim 9 \times 10^{-10}\%$), whereas FSRQs show systematically lower values in the θ-distribution (bottom left, KS: $p \sim 0.023\%$). At a lower significance, also in the PSD slopes (bottom right) a difference between the two classes can be seen (KS: $p \sim 1.6\%$). FSRQs tend to show smaller ξ-values that correspond to steeper PSD slopes.

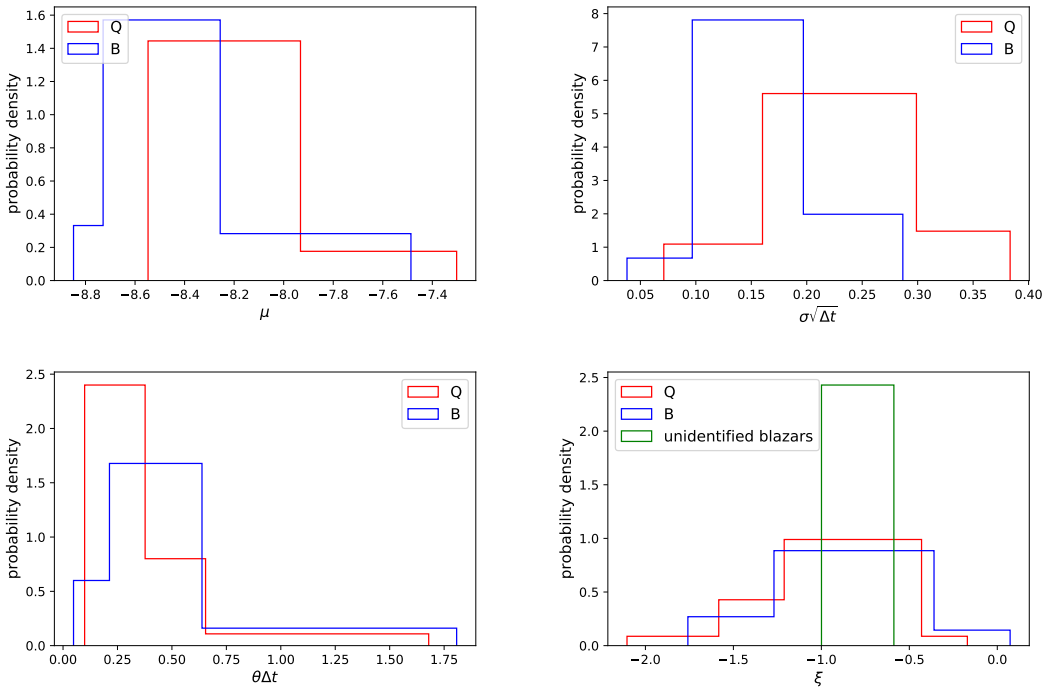

FIGURE 5.1: Comparison of the FSRQs (red) and the BL Lacs (blue) with respect to the OU parameters μ (top left), σ (top right), θ (bottom left) and the PSD slope (bottom right)

5.2 100 MeV sample

In order to systematically analyze these light curves, I applied different test statistics (TS) filter. In each case I require at least 38% of data points in a light curve to remain in order for it to be considered. This threshold has proven to be a good balance between keeping enough data to apply the OU-extraction in a single light curve while not excluding too many light curves completely. For the respective remaining light curves I analyze the Ornstein-Uhlenbeck parameter, the power spectral density slope ξ and the rise and decay time asymmetry. In each case a KS test is performed in order to find out whether there is a systematic difference between FSRQs and BL Lacs.

5.2.1 OU parameters and PSD slopes

The TS1 filter applied leaves 2178 blazars, composed of 832 BL Lacs, 604 FSRQs and 724 unidentified (unclassified) blazars. Figure 5.2 (top left) shows the extracted μ distribution. BL Lacs show systematically smaller μ-values than FSRQs (KS: $p \sim 0$). Figure 5.3 (top row) shows the extracted σ (left) and θ (right) distribution. The distribution of FSRQs suggests, that FSRQs have a systematically higher probability

to show smaller σ-values than BL Lac objects (KS: $p \sim 9 \times 10^{-5}$). Also regarding the θ distribtuion, FSRQs are more likely to feature smaller θ-values than BL Lacs (KS: $p \sim 4 \times 10^{-14}$). The θ-distribution features two prominent peaks around $\theta \sim 0.4$ and $\theta \sim 1.5$. Figure 5.4 (top row) shows the PSD slope ξ distribution. FSRQs have a higher probability to feature smaller ξ-values and therefore steeper PSD slopes than BL Lacs. (KS: $p \sim 0$). The scatter plot Fig. 5.4 (top right) shows the OU parameters versus the PSD slope. Light curves showing $\theta > 1$ typically feature PSD slopes around zero.

The TS4 filter applied leaves 780 blazars, composed of 396 BL Lacs, 311 FSRQs and 73 unidentified (unclassified) blazars. Figure 5.2 (top right) shows the extracted μ distribution. BL Lacs show systematically smaller μ-values than FSRQs (KS: $p \sim 0$). Figure 5.3 (mid row) shows the extracted σ (left) and θ (right) distribution. The distribution of FSRQs suggests, that FSRQs have a systematically higher probability to show smaller σ-values than BL Lac objects (KS: $p \sim 0$). Also regarding the θ distribtuion, FSRQs are more likely to feature smaller θ-values than BL Lacs (KS: $p \sim 0$). The θ-distribution features two prominent peaks around ~ 0.4 and ~ 1.5 for the BL Lacs. In case of the FSRQs, the second peak vanishes. Figure 5.4 (mid row) shows the PSD slope ξ distribution. FSRQs have a higher probability to feature smaller ξ-values and therefore steeper PSD slopes than BL Lacs. (KS: $p \sim 0$). The scatter plot Fig. 5.4 (top right) shows the impact of the OU parameters on the PSD slope. Light curves, where $\theta > 1$ typically feature PSD slopes around zero. All in all there are less of these sources than with the TS1 filter which is also reflected in the vanishing of the peak at $\theta \sim 1.5$ of the FSRQs θ distribution.

The TS9 filter applied leaves 375 blazars, composed of 202 BL Lacs, 162 FSRQs and 11 unidentified (unclassified) blazars. Figure 5.2 (bottom) shows the extracted μ distribution. BL Lacs show systematically smaller μ-values than FSRQs (KS: $p \sim 3 \times 10^{-16}$). Figure 5.3 (bottom row) shows the extracted σ (left) and θ (right) distribution. The distribution of FSRQs suggests, that FSRQs have a systematically higher probability to show smaller σ-values than BL Lac objects (KS: $p \sim 9 \times 10^{-5}$). Also regarding the θ distribution, FSRQs are more likely to feature smaller θ-values than BL Lacs (KS: $p \sim 1 \times 10^{-9}$). In both source classes, the second prominent peak in the θ-distribution at ~ 1.5 vanishes. Figure 5.4 (mid row) shows the ξ distribution. FSRQs have a higher probability to feature smaller ξ-values and therefore steeper PSD slopes than BL Lacs (KS: $p \sim 0$). The scatter plot Fig. 5.4 (top right) shows the impact of the OU parameters on the PSD slope. Light curves, where $\theta > 1$ typically feature PSD slopes around zero. There are even fewer sources with flat PSD slopes left according to the vanishing peak in the θ-distribution at $\theta \sim 1.5$.

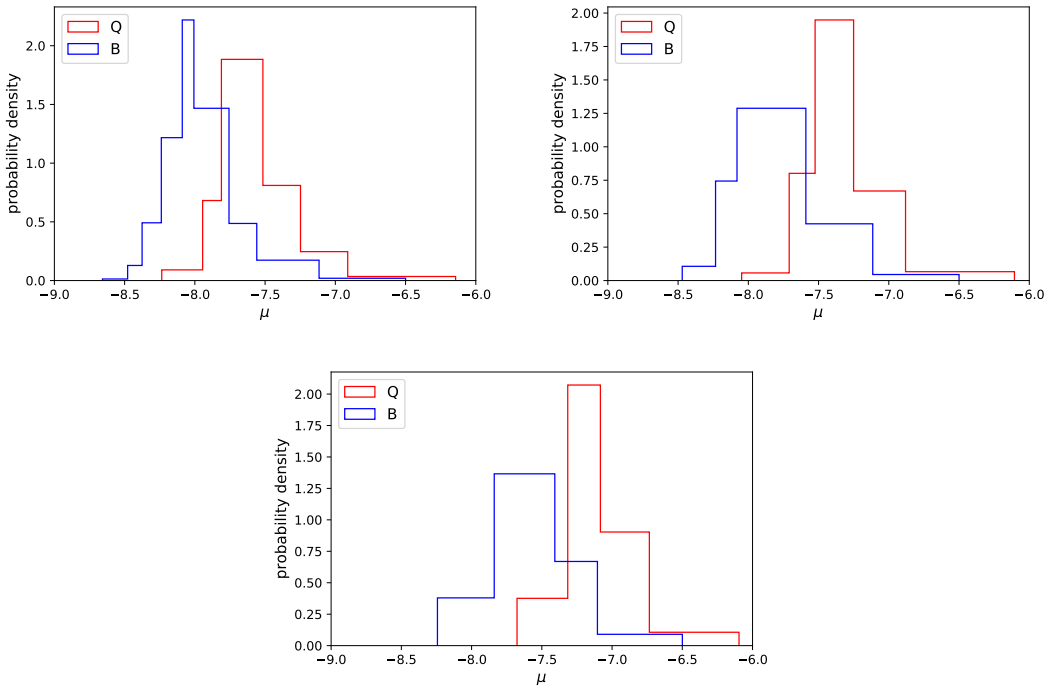

FIGURE 5.2: Distributions of the μ-values for FSRQs (red) and BL Lacs (blue) given different TS filter. *Top left:* μ-value distribution for a TS1 filter. *Top right:* μ-value distribution for a TS4 filter. *Bottom:* μ-value distribution for a TS9 filter.

5.2.2 Asymmetry of flare shapes

With the Bayesian block parametrization of the light curves and deploying the HOP algorithm, I have extracted the flare shapes for each TS filter, see Fig. 5.5. The histograms suggest that there is no trend in the asymmetry measures for all TS filters, meaning that every flare shape is present in the 100 MeV sample, which is consistent with the findings of Burd et al. (2021) and the 1 GeV sample.

5.3 Results from the jet gradient sample

I analyzed the 20 weekly binned sources from the jet gradient sample with a TS4 filter, which left 17 sources to be considered, in order to discard the white noise sources. The same analysis as for the 100 MeV, monthly binned sample was performed. The results are shown in Fig. 5.6. Overall the differences between the source classes can still be measured, however the significance is far lower. BL Lacs show, smaller μ values than FSRQs (KS: $p \sim 4.7\%$). FSRQs on the other hand show smaller σ (KS: $p \sim 7.6\%$) and θ (KS: $p \sim 4.7\%$) values. FSRQs have a higher probability to feature steeper PSD

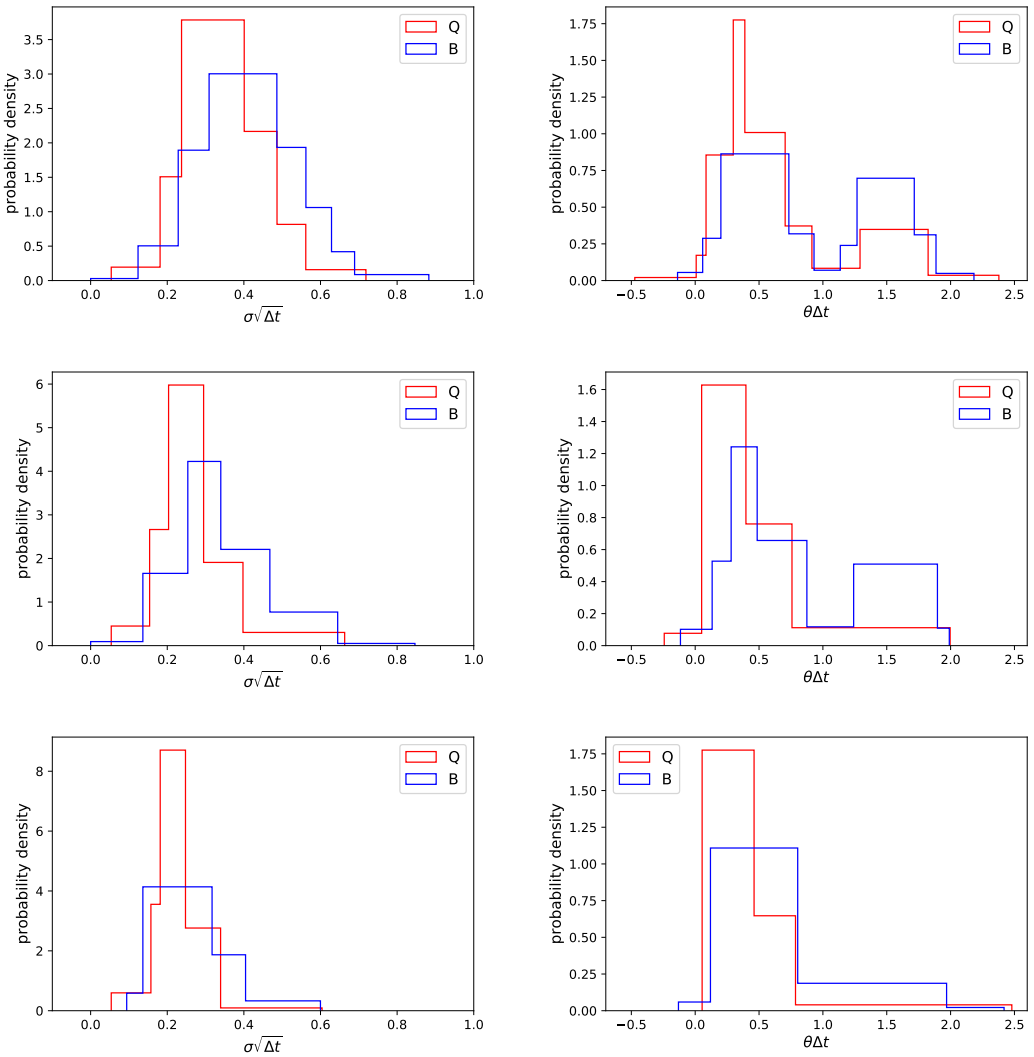

FIGURE 5.3: Distributions of the σ (left column) and θ-values (right coliumn) for FSRQs (red) and BL Lacs (blue), given different TS filters. *Top row:* TS1 filter. *Mid row:* TS4 filter. *Bottom row:* TS9 filter.

slopes (KS: $p \sim 2.0\%$). Regarding the flare shapes, asymmetry of every kind occurs, no tendency for rise times being systematically larger or shorter than decay times.

5.4 Discussion

5.4.1 General comments

For all discussed samples (1 GeV, 100 MeV, jet-gradient sample) BL Lac objects show smaller μ values than FSRQs which means that these sources are generally dimmer for *Fermi*-LAT than FSRQs. This can be understood since BL Lacs, observed with the

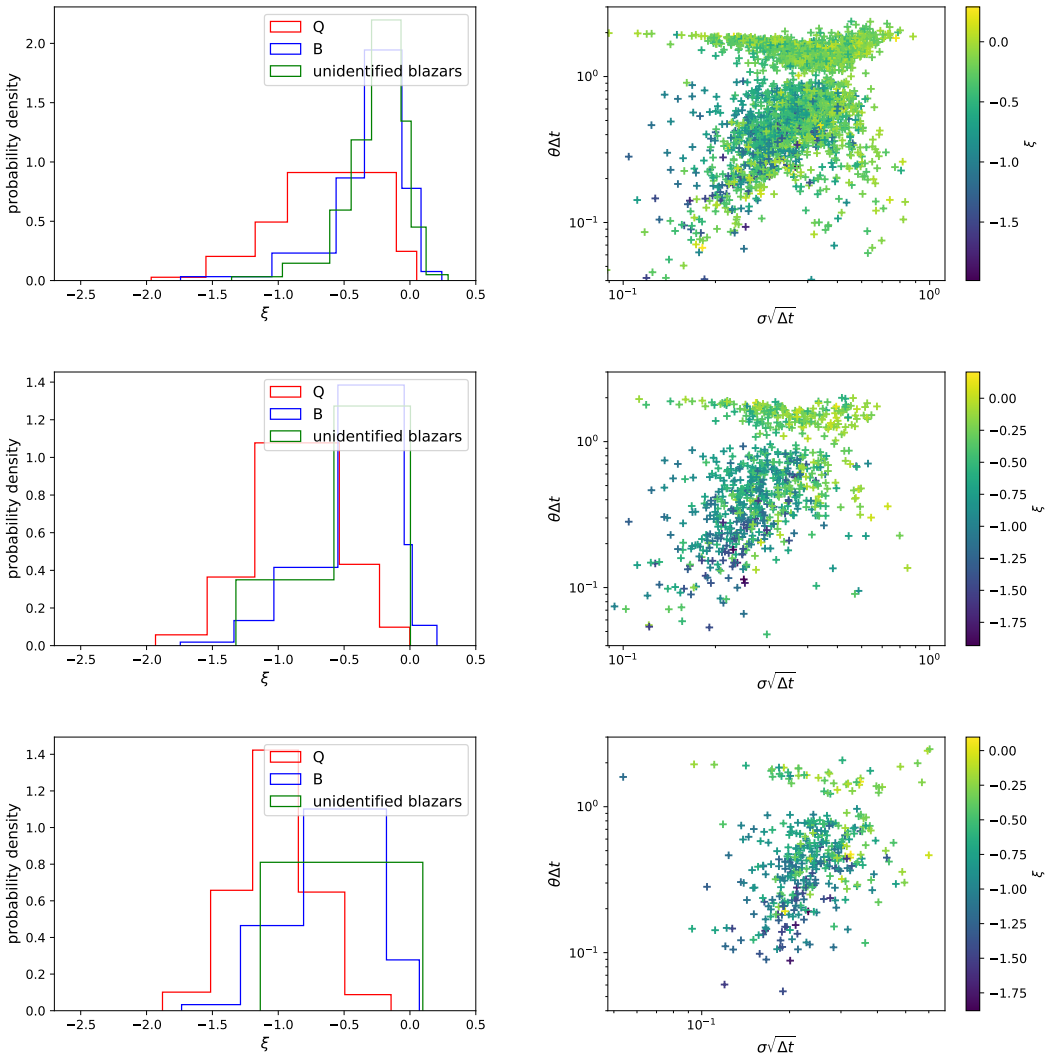

FIGURE 5.4: Distributions of the ξ-values (left column) for FSRQs (red), BL Lacs (blue) and unclassified blazars (green) and scatter plot showing σ and θ versus ξ (right column), given different TS filters. *Top row:* TS1 filter. *Mid row:* TS4 filter. *Bottom row:* TS9 filter.

Fermi-LAT typically show their synchrotron and high energy peak in the SED at larger energies than FSRQs (Abdo et al. 2010a; Ghisellini et al. 2017). For all samples, FSRQs show a tendency for smaller θ values, indicating that FSRQs show variability on larger time scales with respect to the time binning in the light curve than BL Lac objects which is consistent with the findings of Abdo et al. (2010b). In all samples, FSRQs show systematically smaller ξ-values which means that the PSD slope for FSRQs is systematically steeper than for BL Lac objects. The PSD slope is also an indication for the variability time scale. The steeper the slope, the larger the time scales on which the variability takes place with respect to the time binning of the light curve. Steeper PSD slopes in FSRQs are consistent with smaller θ-values. For all samples, no trend for the

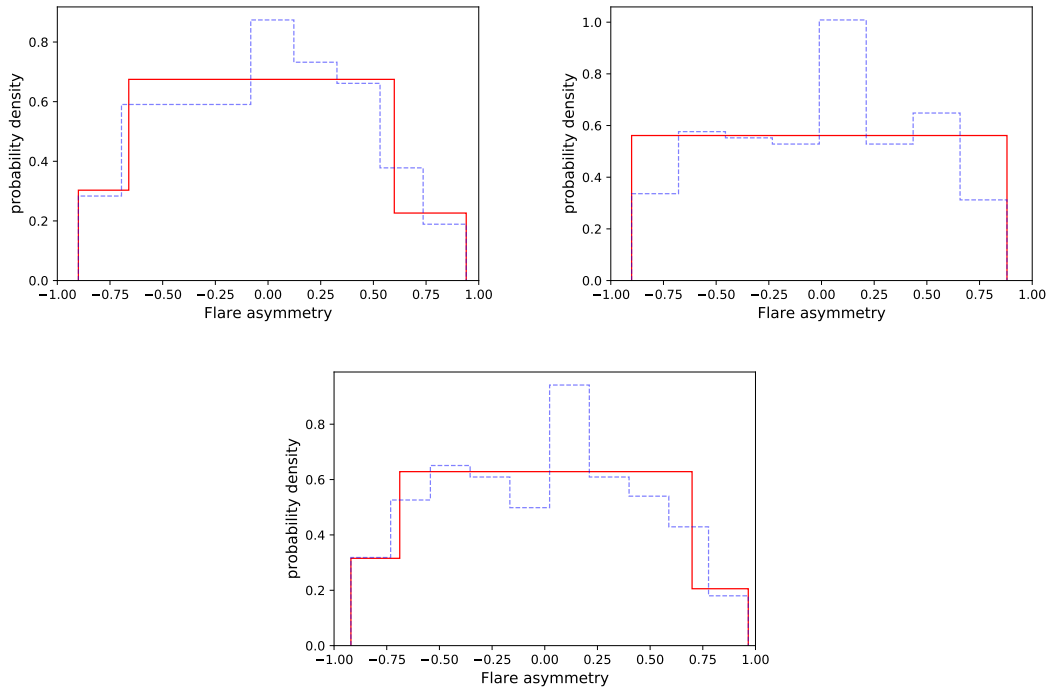

FIGURE 5.5: Flare asymmetry measure for TS1 (top left), TS4 (top right) and TS9 (bottom).

extracted flare shapes can be found. No flare shape can be ruled out or is favored. This is consistent with previous findings (e.g., Roy et al. 2019; Meyer et al. 2019; Burd et al. 2021; Wagner et al. 2021).

5.4.2 The effect of the TS filter in the 100 MeV sample

How to properly chose TS filter is a matter of debate in every single project, dealing with *Fermi*-LAT light curves. Conservatively, each data point is a detection as soon as TS ≥ 25 which would equate to a $\sim 5\sigma$ detection. However this would cut any sample dramatically. For example the 100 MeV sample, a TS25 filter with the requirement of at least 38 % data points left in a light curve, would cut the sample down to 163 sources that can be studied. The argument can be made that as soon as it is known that a source is located at the observed region, be it by former observation, cross-checking with different wavelengths or any other way, the TS cut may be set as low as TS $= 1$. This is due to the fact that the LAT likelihood method has been proved to provide reliable estimates for values as low as 1 (S. Buson, priv. comm.). In any case this is a matter of debate. The effect of the TS filter, however, can be studied in this context and is best seen in Fig. 5.4. As the TS filter is set from 1 to 4 to 9 from top to bottom, more and more white noise sources ($\xi \sim 0$) and sources where $\theta > 1$ fall out of the sample. An

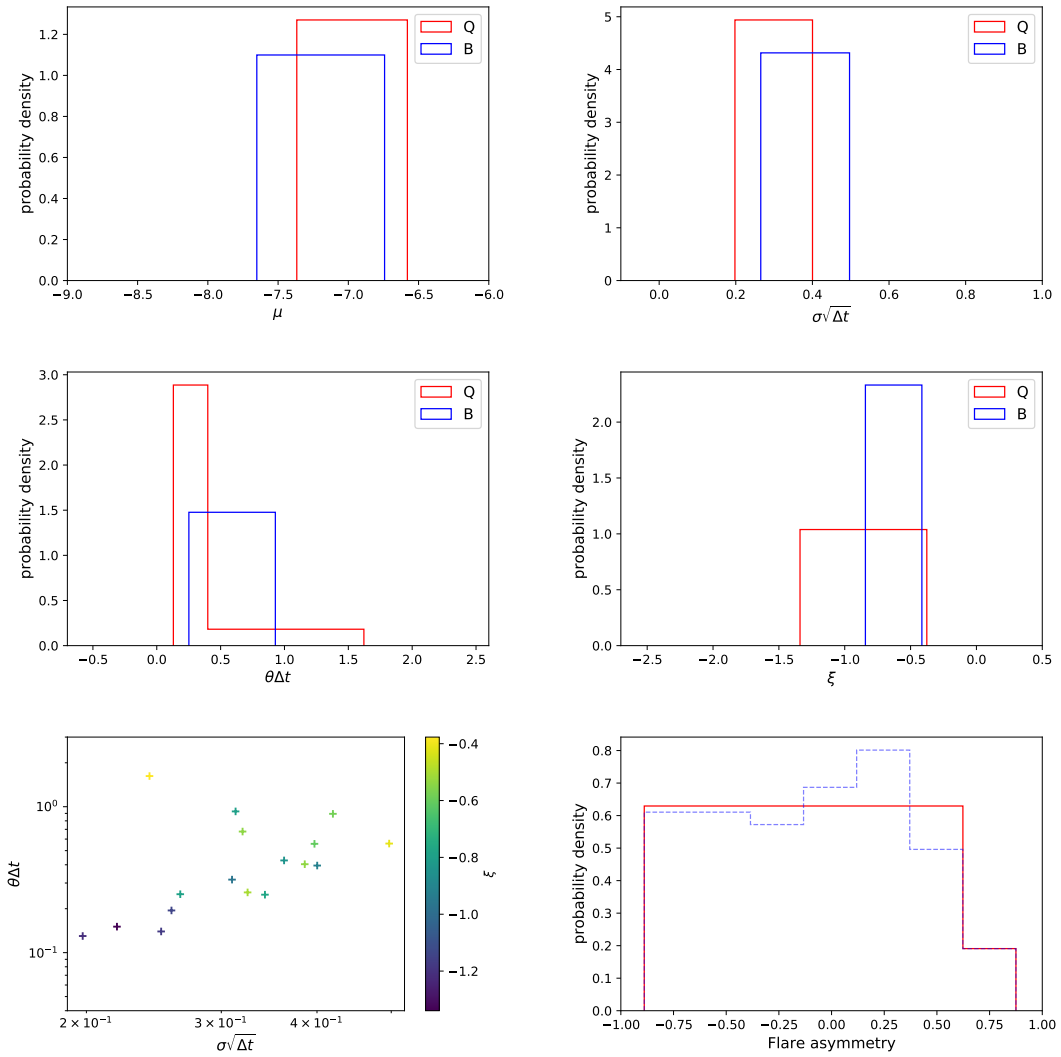

FIGURE 5.6: Analysis of the 20 sources from the jet-gradient sample. *Top left:* μ-distribution, *Top right:* σ-distribution, *Mid left:* θ-distribution, *Mid right:* ξ-distribution, *Bottom left:* impact of the OU parameters on ξ, *Bottom right:* flare asymmetry measure.

extracted $\theta > 1$ is typically a good indication for sources, where little to no variability can be observed, where the flux variations are purely dominated by white noise.

5.4.3 The σ distributions

In the 1 GeV sample, the σ distribution suggests, that BL Lac objects show systematically smaller values than FSRQs. This is reversed in both, the monthly binned 100 MeV sample as well as the weekly binned jet-gradient sample (also at $E > 100$ MeV). This means that the maximum random amplitude for FSRQs is larger at higher energies but smaller at lower energies than for BL Lac objects. This does not contradict the idea

that FSRQs show a larger degree of variability in *Fermi*-LAT light curves. If the σ-value is relatively large while also the θ-value is relatively large, the resulting light curve is basically still white noise with a larger variance. Such light curves are typically not identified as sources with large variability since the largest amplitudes are comparable to the variance in such sources. This effect of large σ-values sill resulting in white noise, can nicely be seen in the scatter plots in Fig. 5.7. The impact of σ and θ on ξ can be seen in the case of FSRQs (left) and BL Lacs (right). I used a TS9 filter which makes it possible to see the difference by eye due to not too many data points overlaying each other. BL Lac objects show larger σ-values but also flatter PSD slopes, often comparable to white noise. This is also prominent in the cases where $\theta > 0$, while FSRQs typically show steeper PSD slopes between pink and red noise. This shows that FSRQs typically still show more variability than BL Lac objects, even with a tendency for smaller σ-values.

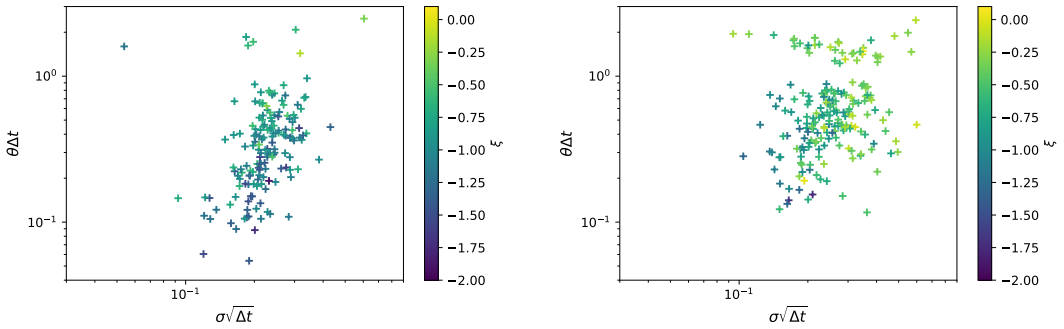

FIGURE 5.7: Impact of the TS9 filtered OU parameters on ξ for FSRQs (left) and BL Lacs (right)

Chapter 6

Summary and future perspectives

Brich dein Ich

Des Wesens Reiz, P. R. Burd, A. Kieckhöfel

In this chapter I will discuss the results from the jet gradient study and the blazar light curve study in context. I will furthermore go through the seven questions asked in Sect. 1.8 and discuss the answers obtained in this thesis. In the end a final section on suggestions for future work will be given.

6.1 Radio and gamma results in context

In order to assess whether the behavior of *Fermi*-LAT light curves are systematically related jet parameters obtained from VLBA observations, first the question has to be answered, whether it is possible to separate the source classes with the OU parameters in the light curve analysis and the jet parameters in the VLBI analysis. In chapter 4 I showed that systematical differences between FSRQs and BL Lacs can be found with respect to the jet collimation, measured with the diameter gradients of several epochs for each source and the jet complexity, measured with the $\chi^2_{\rm red}$ obtained from a single power law fit. Overall FSRQs are more complex and more collimated than BL Lac objects. Also the *Fermi*-LAT light curves showed systematic differences in the source classes. An analysis of the OU parameters revealed that FSRQs show more variability at > 1 GeV and > 100 MeV. This is based on the systematically steeper PSD slopes and the systematically smaller θ-values. The rank correlation tests $\tau_{\rm Kendall}$ and $R_{\rm Spearman}$ (see tables 6.1-6.2) suggest possible anti-correlation of the OU parameters, the PSD slope and the $\chi^2_{\rm red}$ of the single power law jet parameter fit at 15 GHz, as signature for

TABLE 6.1: τ_{Kendall} for the tested parameters pairs, comparing the jet complexity and the OU parameters.

tested Parameter	σ	θ	ξ
$\chi^2_{\mathrm{red,s15}}$	-0.46	-0.34	-0.44
$\chi^2_{\mathrm{red,l15}}$	-0.4	-0.49	-0.38
$\chi^2_{\mathrm{red,s15,ol}}$	-0.46	-0.34	-0.35
$\chi^2_{\mathrm{red,l15,ol}}$	-0.38	-0.24	-0.19
$\chi^2_{\mathrm{red,s43}}$	-0.22	-0.31	-0.26
$\chi^2_{\mathrm{red,l43}}$	-0.29	-0.18	-0.25
$\chi^2_{\mathrm{red,s43,ol}}$	-0.35	-0.35	-0.37
$\chi^2_{\mathrm{red,l43,ol}}$	-0.29	-0.18	-0.22

TABLE 6.2: R_{Spearman} for the tested parameters pairs, comparing the jet complexity and the OU parameters.

tested Parameter	σ	θ	ξ
$\chi^2_{\mathrm{red,s15}}$	-0.63	-0.51	-0.65
$\chi^2_{\mathrm{red,l15}}$	-0.58	-0.61	-0.54
$\chi^2_{\mathrm{red,s15,ol}}$	-0.59	-0.51	-0.52
$\chi^2_{\mathrm{red,l15,ol}}$	-0.41	-0.35	-0.29
$\chi^2_{\mathrm{red,s43}}$	-0.33	-0.43	-0.4
$\chi^2_{\mathrm{red,l43}}$	-0.38	-0.27	-0.41
$\chi^2_{\mathrm{red,s43,ol}}$	-0.5	-0.5	-0.53
$\chi^2_{\mathrm{red,l43,ol}}$	-0.37	-0.24	-0.36

the complexity of a jet. The R_{Pearson} (table 6.3) suggests that it is unlikely that this anti-correlation is based on a simple linear connection. If the anti-correlation is true it would mean, that more complex jets, that show more bright knots than a continuous flow and also possible different jet geometry zones (e.g. recollimation zones, geometry transition zones, etc.) are more likely be connected to *Fermi*-LAT light curves with OU parameters that favor stronger variability. From this it is not possible to test or infer causality. It is not clear whether a complex jet is a condition for more variability or the other way around. It is also not possible to constrain the location of the γ-ray emitting region other than that is linked in some way to the jet complexity. The fact that a possible connection between the jet complexity and the γ-ray variability is most likely not linear suggests that these effects might even interact in some way.

TABLE 6.3: R_{Pearson} for the tested parameters pairs, comparing the jet complexity and the OU parameters.

tested Parameter	σ	θ	ξ
$\chi^2_{\mathrm{red,s15}}$	-0.43	-0.41	-0.61
$\chi^2_{\mathrm{red,l15}}$	-0.37	-0.45	-0.6
$\chi^2_{\mathrm{red,s15,ol}}$	-0.3	-0.35	-0.49
$\chi^2_{\mathrm{red,l15,ol}}$	-0.22	-0.43	-0.49
$\chi^2_{\mathrm{red,s43}}$	-0.19	-0.17	-0.28
$\chi^2_{\mathrm{red,l43}}$	-0.3	-0.27	-0.34
$\chi^2_{\mathrm{red,s43,ol}}$	-0.22	-0.19	-0.31
$\chi^2_{\mathrm{red,l43,ol}}$	-0.32	-0.24	-0.35

6.2 What about my plan?

Here I will summarize this thesis in the light of the questions asked in Sect. 1.8.

1. *Considering the jet model discussed in this chapter, what is the behavior of blazars regarding the parameters s, l, n, b?* All 28 sources in the VLBI sample, discussed in this thesis are well understood within the framework of a Blandford & Königl (1979)-jet with the extensions discussed in Sect.1.6 and the parameter space assessed in Fig.4.5. FSRQs typically show a more complex structure than BL Lac objects and are able to hold the collimation further down the jet. The scaling of the magnetic field depends on how the electron energy density is de-coupled from b, see Eq. 1.7e. In the case of equipartition between the electron energy density and the magnetic field strength density, most sources show a helical field with a stronger tendency for stronger torodial components, while when determining b through particle conservation this tendency is not present.

2. *Is it possible to find geometry breaks within* pc*-scale jets in a high frequency sample (*15GHz, 43GHz*)?* In 9 of the 28 sources I constrained a geometry transition zone, $0219+421$, $0336-019$, $0415+379$, $0528+134$, $0836+710$, $1101+384$, $1156+295$, $1253-055$ and $2200+420$. These were found by analyzing both frequencies at once. FSRQs showing these breaks have a tendency to show larger jet radii at the break point than BL Lac objects.

3. *If found, do these breaks occur due to external (of the jet) influences like altering pressure profile due to Bondi accretion, or is it plausible that these breaks happen due to inner mechanism in the jet?* Since all break points are located outside

the respective Bondi sphere along the jet axis, it is unlikely that external pressure gradients are the sole cause for these geometry transitions to occur.

4. *Can the magnetic field in the radio jet be scaled to the region of the central engine, the SMBH? If so, how strong is the magnetic field in these regions?* I showed a method, inspired by Baczko et al. (2016) which allows to calculate magnetic field strengths in the radio core of blazars that yields comparable results to core shift studies from Pushkarev et al. (2012). I scaled the obtained core magnetic field strengths to the ergosphere of the SMBH in a Blandford & Znajek (1977) and Eddington scenario in order to obtain the distance between radio core and SMBH. Both showed differences in the absolute values of the core position with respect to the SMBH. However the trends are seen consistently. FSRQs show larger distances between the radio cores and the SMBHs.

5. *Knowing the stochastic nature of γ-ray light curves, is it possible to quantify details regarding the flux density variations in such light curves, in particular with regard to the Ornstein-Uhlenbeck parameters μ, σ, θ and the power spectral density?* In Burd et al. (2021) I showed that *Fermi*-LAT light curves can be described by an OU process. I used the algorithms, developed for this paper, to obtain the OU parameters for the three samples in chapter 6. FSRQs show systematically smaller θ-values, larger μ-values and steeper PSD slopes which are an indication for stronger variability on larger time scales. BL Lacs with larger σ-values than FSRQs are typically white noise sources. This means that these sources show white noise with a large variance, where the maximum flux are comparable to the variance of the light curve. Consistently with Roy et al. (2019), Meyer et al. (2019), Burd et al. (2021) and Wagner et al. (2021) I did not find a preferred asymmetry in the extracted flare shapes.

6. *Do the jet parameters s, l, n, b play a role in the nature of the γ-ray variability?* In Subsect. 6.1 I showed that the jet parameters are not correlated in any way with the OU parameters. However on a more abstract level, there is possible anti-correlation between the jet complexity and the likeliness for more variability (smaller θ- values, larger σ- values and smaller ξ-values) in the *Fermi*-LAT light curve. FSRQs show systematically larger complexity, but smaller θ-values and steeper PSD slopes.

7. *Is there a systematic difference of any kind regarding the source classes of BL Lacs and FSRQs?* FSRQs and BL Lacs differ in a number of ways:

   (a) FSRQs are more collimated than BL Lac obejcts, further down the jet.

   (b) FSRQs are more complex than BL Lacs and the jet parameters n and b are dependent on l.

(c) BL Lacs show stronger magnetic fields in the radio cores than FSRQs.

(d) The radio core of BL Lacs is closer to the SMBH than the radio core of FSRQs.

(e) FSRQs show steeper PSD slopes than BL Lac objects and smaller θ-values.

(f) FSRQs show variability on larger time scales with respect to the time binning.

(g) The jet complexity is anti-correlated with the PSD slope as well as the OU parameters σ and θ

6.3 Work that needs to be done

The systematics in the VLBI jet need to be tested on a larger sample. A first step would be the study of the jet parameters on the entire MOJAVE1 sample, for example. A study at even higher frequencies would allow to study the jet parameters even closer to the physical jet base. This limits the number of sources that can be studied dramatically due to frequency dependent antenna sensitivities. Regarding the overlap sample of 15 GHz and 43 GHz observed sources, the sample studied in this thesis is nearly complete. A caveat is of course the limited observation time window between 2003 and 2013. Studies at even higher frequencies and better resolution for example with the Event Horizon Telescope (EHT) will most probably be limited to a few sources for the coming decades. The analysis done in this thesis regarding the VLBI data is not time sensitive. Regarding a time series analysis this can be extended, however when extracting jet parameters, information from a single epoch does not give reliable information on (for example) the jet geometry (Kovalev et al. 2020). This means that a study of possible time-sensitive changes in jet geometry (or brightness temperature) has to be handled with caution but can be done in principle. Regarding the γ-ray light curves, different time binnings and time samplings can be studied. On the very high energy end, this is heavily limited by the number of sources that are monitored in the TeV regime. The possibility to bin the time on smaller scales (weeks, days, hours, minutes) is also limited by the received flux density. The finest time binnings can reliably only be acquired for the brightest sources which also limits a systematic analysis to a small sample. The main question that remains from this work is the following. If the anti-correlation between the jet complexity and the tendency to show more and stronger variability is true, what is the cause? Does the γ-ray emitting region influence the jet structure, does the jet structure influence the γ-ray emitting region or do these concepts interact in a highly non-trivial way? A way to assess this would be to properly constrain mechanisms for particle acceleration that allow for the different flare shapes found in this and several other works. Instruments that allow a fine time binning at different energies will help to

put constrains on these. From a theoretical point of view, the OU parameters, explicitly their physical connection to the jet, need to be explained. Phenomenologically they can be used to characterize a light curve. However the physical meaning of these parameters is not clear. The mean reversion rate μ for instance is related to quiescent states in a light curve. Is such a state just a superposition of unresolved flares or the result of a more or less constant energy flux at a certain level? Regarding the σ and θ parameters the question arises, what physics regulate the amplitude and the time scale variability occurs on. If the OU is used to assess real physical meaning in light curves beyond a phenomenological assessment these questions need to be answered. Also models beyond the OU could be studied, where the memory in a light curve goes beyond a single step into the past.

6.4 Used software

Throughout this work I made use of the following software[1]:

1. python 3.8
2. astropy (Astropy Collaboration et al. 2013; Price-Whelan et al. 2018)
3. scipy (Virtanen et al. 2019; Virtanen et al. 2020)
4. numpy (Harris et al. 2020)
5. matplotlib (Hunter 2007)
6. DIFMAP (Shepherd 1997)
7. OU code available at `https://github.com/PRBurd/astro-wue`
8. Bayesian block + HOP analysis tools available at `https://github.com/swagner-astro/lightcurves`
9. jet gradient analysis tools available at `https://github.com/PRBurd/tb`
10. cosmological distance calculator available at `https://github.com/PRBurd/useful_stuff`

[1] the exact version may vary since I worked on different machines

List of Figures

1.1 The radius of the ISCO is plotted versus a_*. In the case of a Schwarzschild black hole, where $a_* = 0$, $r_{\mathrm{ISCO}} = 6r_g$. The more energy of the black hole is stored within the rotation of the black hole ($a_* \to 1$), the smaller r_{ISCO} can be with respect to the gravitational radius. 9

1.2 The spectral energy distribution of Mrk 421, measured across the EM spectrum. The low energy peak is typically explained by synchrotron radiation, while the high energy peak in this particular case is well described by two-zone leptonic model (model not shown in plot). Plot taken from: Abdo et al. (2011). 12

1.3 Images from GMRT observations at 610 MHz from the BL Lac object $1807 + 698$ (left) and the FSRQ $1222 + 216$ (right). The BL Lac object resembles the morphology of a rotated FR1 radio galaxy and the FSRQ resembles the morphology of a rotated FR2 radio galaxy. 13

1.4 *Top:* Sine waves (left) of frequencies $(1, 2, 4)$ Hz (red, green, blue) yield PSDs, showing prominent peaks at given frequencies (right). *Mid:* A function (red line), composed of sine-waves can be analyzed with the PSD to find the composing frequencies, with prominent peaks at 2 Hz and 4 Hz. *Bottom, left:* Random time series showing variations on long time scales with respect to the time sampling (blue line) around $x(t) = 6$ and a random time series showing variations on small time scales with respect to the time sampling (red line), around $x(t) = 0$. The shift is used for clear illustration. Random time series show PSDs of different power law behavior (PSD $\propto f^{\xi}$). For time series, where the variation occurs on large time scales with respect to the time sampling, the PSD-slope becomes steep (blue), whereas for time series where the variation occurs on shorter time scales, the PSD-slope flattens (here: $\xi \sim 0$). 16

1.5 The different cases of OU time series (red,green,blue) are shown shifted from each other for clearness $(\mu_r.\mu_g, \mu_b) = (0, 3, 6)$. *Left:* The different OU time series (red,green,blue) are generated using $\sigma_r, \sigma_g, \sigma b = (0.1, 0.5, 1)$ and a fixed $\theta_{r,g,b} = 0.5$. The σ parameter impacts the maximum random amplitude of a given time series, where larger σ-values indicate larger random amplitudes. *Right*: The different OU time series are generated using $(\theta_r, \theta_g, \theta_b) = (1.5, 0.7, 0.1)$, while $\sigma_{r,g,b} = 0.5$ is fixed in this case. The larger θ, the more a time series is drawn back to the mean reversion level μ. 19

1.6 Synchrotron spectrum of a single emitting region. In the optically thick region ($\tau > 1$), the power of the synchrotron emission of one electron bulk (blob) depends on the frequency as $\propto \nu^{5/2}$. At $\tau = 1$ the spectrum has a maximum. In sources where only one synchrotron emission region was found, an anti-correlation between the peak position of the synchrotron spectrum and the size of the emission region was found (O'Dea 1998). In the optically thin region, the spectrum falls with ν^{α}. If the emitting region is boosted towards an observer, the frequency is blue shifted (blue line shifted to the right with respect to the red line) and the emitted power is augmented. Adapted from Burd (2017) 23
1.7 In sources that are dominated by beamed emission, where not only one synchrotron emission region is observed, typically in blazar jets, the power spectrum smears out to a flat spectrum, as higher energetic powers get enhanced by a power law, cancelling out the falling of the spectrum as a power law in the optically thin region of a single emission region. At higher observing frequencies, the part of the source, where the emission becomes optically thin, comes closer and closer to the physical jet base which is known as core shift (Sokolovsky et al. 2011; Kudryavtseva et al. 2011) which depends on the geometry of the jet (a conical jet is illustrated here). Illustration taken from Burd (2017). 24
1.8 If a fast moving emitting region ($\beta \to 1$) travels towards an observer with a small inclination angle ϑ, the apparent motion becomes super luminal. Adapted from Burd (2017) 25
1.9 The apparent speed is plotted vs. the observation angle ϑ, according to Eq. 1.6d. Dependent on the internal velocity (color coded). The dashed line marks the region where $\beta_{\mathrm{app}} = 1$. Generally it can be seen, that for small inclination angles and large β_{int} values, an apparent super-luminal motion can be observed. 26
1.10 The different types of jet geometries are shown for comparison. The scales of the jet axis r and the diameter d_j are shown in arbitrary units. For $l > 0$ the apex of the jet lies at $r = 0$. For the cylindrical case $l = 0$ not artificial apex is shown. In reality of course also a cylindrical jet would start somewhere and probably open up at some point. 28
1.11 Schematic illustration of a jet, showing a parabolic shape (blue lines) where the flow is magnetically dominated and accelerated. The jet shows a geometry transition from parabolic to conical 30

2.1 Locations of the VLBA antennas across the USA; credit: Image courtesy of NRAO/AUI and Earth image courtesy of the SeaWiFS Project NASA/GSFC and ORBIMAGE 34
2.2 The intensity distribution of a source (grey area) is described in the (l, m, n)-system (red). The antennas, connected by a basesline $\vec{b}_{\lambda}$ are described in the (v, w, w)-system (blue). A coherent wave arrives at a reference (left) antenna and also at the right antenna with a geometric delay τ_g. From: Burd (2017) 36
2.3 Radio image of $0219 + 428$ observed at 15 GHz with the VLBA in 2008. The data for this image is taken from the MOJAVE website. The jet of this source extends up to ~ 15 mas from the radio core. The jet is model fit with circular Gaussian components, see parameters in Tab. 2.1. 40

2.4 The location difference between the 15 GHz jet (red) and the 43 GHz jet (blue) cannot be resolved with the VLBA. The overlap region is defined as the distance between the smallest resolved core distance at 15 GHz and the largest core distance at 43 GHz. 44

3.1 Schematic illustration of the *Fermi* LAT. An incident photon, passing through the converter tracker and the calorimeter, producing an electron/positron pair. From: Atwood et al. (2009). 53
3.2 OU time series with 500 simulated time steps and $(\mu, \sigma, \theta) = (0, 0.5, 0.5)$. *Left:* the red colored data points are used to extract the σ parameter in a region $[\pm(0.343 \pm 0.004)$ std] around the mean. With this procedure, the bins fluctuating very close to the mean - representing stochastic fluctuations (σ) - are factored in. *Right:* the red colored data points are used to extract the θ parameter in a region $[\pm(1.48 \pm 0.34)$ std] around the mean. The bins determined with this procedure represent fluctuations that deviate largely form the mean which are assumed to be due to the deterministic drift of the stochastic process (θ). 58
3.3 Bayesian block representation of the monthly binned light curve of Mrk 421. The x-axes represent the time in MJD and the y-axes represent the flux in erg $\mathrm{cm}^{-2}\,\mathrm{s}^{-1}$. *Top*: Definition of a flare as given in Meyer et al. (2019), where all Bayesian blocks above a certain base line are defined as a flare. All subsequent blocks belong to the flare, until a block again is below the baseline. *Second from top:* The 'half'-method abandons the necessity of a baseline (of any kind). The valley between two subsequent groups is split in half in order to define the start end the end of one HOP group. *Third from top:* The 'flip' method also is independent of a baseline. The slope of a HOP group is extrapolated by flipping the length of the adjacent block onto the valley block. The start then sits at the left side of the bordering edge of the valley block minus the length of the adjacent block. *Bottom:* The 'sharp'-method , cuts the HOP group right at the edges. 61

4.1 Values at 15 GHz are shown in blue and 43 GHz in red. Distribution of l-values along the entire jet (left panel) and along the overlap-region (right). 66
4.2 Colors indicate source classes (red: FSRQs, blue: BL Lacs, green: RGs). *Top two lines*: Distributions along the entire jet for both frequencies; *Bottom two lines*: Distributions constrained to the overlap-region of both frequencies. *Left column:* Distribution of l-values. *Right column* χ^2_{red} value distribution for the l-fits. 67
4.3 Distribution of s-values along the entire jet (top panel) and along the overlap-region (bottom). Values at 15 GHz are shown in blue and 43 GHz in red. 70
4.4 For all cases, the Bayesian histogram binning (solid lines) and the classical uniform binning (dashed lines) is shown. The colors indicate the source classes (red: FSRQs, blue: BL Lacs, green: RGs). *Top two lines*: Distributions along the entire jet for both frequencies; *Bottom two lines*: Distributions along the overlap-region of both frequencies. *Left column:* Distribution of s-values. 71

4.5 The colores (red,blue,green) indicate the source classes (Q,B,G) at 15 GHz, the colors (orange,cyan,yellowgreen), indicate the source classes (Q,B,G) at 43 GHz. The parameter space spanned by the direct measurement of the s and l values can be constrained with the additional information of the b-value distributions (see sections below) in order to constrain the parameter range of n and α. *Left:* respective entire jet length. *Right:* respective overlap region 72
4.6 *Top two rows:* Distribution of the b-values at both frequencies (top 15GHz, bottom 43GHz) for the case equipartition (left) and particle conservation (right). *Third row:* $b - l$ scatter plots help to find out whether torodial, polodial or helical magnetic fields are preferred in the case of equipartition (left) and particle conservation (right). *Bottom row:* Distribution of the magnetic field strength in the radio core at 15 GHz (left) and 43 GHz (right). 74
4.7 Distance between the radio core and the SMBH's ergosphere in the case of a Blandford & Znajek (1977) magnetic field (top) and an Eddinggton magnetic field (bottom). 79
4.8 FSRQs are shown in red, BL Lacs in blue. *Top:* Distribution of the break points. *Bottom:* The distribution of the jet radii at the respective geometry break point. 82
4.9 0219+428; *Left columns:* 43 GHz data; *Right columns:* 15 GHz data; *Top* diameter gradient fit; *bottom* brightness temperature gradient fit. 84
4.10 *Top:* 0219+428; *Bottom:* 0336-019 ; Both frequencies are fit together in order to constrain a break point as well as an outer and inner l-value. . . 85
4.11 0336-019; *Left columns:* 43 GHz data; *Right columns:* 15 GHz data; *Top* diameter gradient fit; *bottom* brightness temperature gradient fit. 87
4.12 0415+379; *Left columns:* 43 GHz data; *Right columns:* 15 GHz data; *Top* diameter gradient fit; *bottom* brightness temperature gradient fit. 88
4.13 *Top:* 0415+379; *Bottom:* 0528+134; Both frequencies are fit together in order to constrain a break point as well as an outer and inner l-value. . . 89
4.14 0430+052; *Left columns:* 43 GHz data; *Right columns:* 15 GHz data; *Top* diameter gradient fit; *bottom* brightness temperature gradient fit. 90
4.15 0528+134; *Left columns:* 43 GHz data; *Right columns:* 15 GHz data; *Top* diameter gradient fit; *bottom* brightness temperature gradient fit 92
4.16 0716+714; *Left columns:* 43 GHz data; *Right columns:* 15 GHz data; *Top* diameter gradient fit; *bottom* brightness temperature gradient fit 93
4.17 0735+178; *Left columns:* 43 GHz data; *Right columns:* 15 GHz data; *Top* diameter gradient fit; *bottom* brightness temperature gradient fit 94
4.18 0827+243; *Left columns:* 43 GHz data; *Right columns:* 15 GHz data; *Top* diameter gradient fit; *bottom* brightness temperature gradient fit 96
4.19 0829+046; *Left columns:* 43 GHz data; *Right columns:* 15 GHz data; *Top* diameter gradient fit; *bottom* brightness temperature gradient fit 97
4.20 0836+710; *Left columns:* 43 GHz data; *Right columns:* 15 GHz data; *Top* diameter gradient fit; *bottom* brightness temperature gradient fit 98
4.21 *Top:* 0836+710; *Bottom:* 1101+384; Both frequencies are fit together in order to constrain a break point as well as an outer and inner l-value. . . 99
4.22 0851+202; *Left columns:* 43 GHz data; *Right columns:* 15 GHz data; *Top* diameter gradient fit; *bottom* brightness temperature gradient fit 101

4.23 0954+658; *Left columns:* 43 GHz data; *Right columns:* 15 GHz data; *Top* diameter gradient fit; *bottom* brightness temperature gradient fit 102
4.24 1101+384; *Left columns:* 43 GHz data; *Right columns:* 15 GHz data; *Top* diameter gradient fit; *bottom* brightness temperature gradient fit 103
4.25 1127-145; *Left columns:* 43 GHz data; *Right columns:* 15 GHz data; *Top* diameter gradient fit; *bottom* brightness temperature gradient fit 104
4.26 1156+295; *Left columns:* 43 GHz data; *Right columns:* 15 GHz data; *Top* diameter gradient fit; *bottom* brightness temperature gradient fit 106
4.27 *Top:* 1156+295; *Bottom:* 1253-055; Both frequencies are fit together in order to constrain a break point as well as an outer and inner l-value. . . 107
4.28 1219+285; *Left columns:* 43 GHz data; *Right columns:* 15 GHz data; *Top* diameter gradient fit; *bottom* brightness temperature gradient fit. 108
4.29 1222+216; *Left columns:* 43 GHz data; *Right columns:* 15 GHz data; *Top* diameter gradient fit; *bottom* brightness temperature gradient fit. 109
4.30 1253-055; *Left columns:* 43 GHz data; *Right columns:* 15 GHz data; *Top* diameter gradient fit; *bottom* brightness temperature gradient fit. 110
4.31 1308+326; *Left columns:* 43 GHz data; *Right columns:* 15 GHz data; *Top* diameter gradient fit; *bottom* brightness temperature gradient fit. 112
4.32 1633+382; *Left columns:* 43 GHz data; *Right columns:* 15 GHz data; *Top* diameter gradient fit; *bottom* brightness temperature gradient fit. 113
4.33 1652+398; *Left columns:* 43 GHz data; *Right columns:* 15 GHz data; *Top* diameter gradient fit; *bottom* brightness temperature gradient fit. 114
4.34 1730-130; *Left columns:* 43 GHz data; *Right columns:* 15 GHz data; *Top* diameter gradient fit; *bottom* brightness temperature gradient fit. 115
4.35 1749+096; *Left columns:* 43 GHz data; *Right columns:* 15 GHz data; *Top* diameter gradient fit; *bottom* brightness temperature gradient fit. 116
4.36 2200+420; *Left columns:* 43 GHz data; *Right columns:* 15 GHz data; *Top* diameter gradient fit; *bottom* brightness temperature gradient fit. 117
4.37 2200+420; Both frequencies are fit together in order to constrain a break point as well as an outer and inner l-value. 118
4.38 2223-052; *Left columns:* 43 GHz data; *Right columns:* 15 GHz data; *Top* diameter gradient fit; *bottom* brightness temperature gradient fit. 119
4.39 2230+114; *Left columns:* 43 GHz data; *Right columns:* 15 GHz data; *Top* diameter gradient fit; *bottom* brightness temperature gradient fit. 120
4.40 2251+158; *Left columns:* 43 GHz data; *Right columns:* 15 GHz data; *Top* diameter gradient fit; *bottom* brightness temperature gradient fit. 121

5.1 Comparison of the FSRQs (red) and the BL Lacs (blue) with respect to the OU parameters μ (top left), σ (top right), θ (bottom left) and the PSD slope (bottom right) 125
5.2 Distributions of the μ-values for FSRQs (red) and BL Lacs (blue) given different TS filter. *Top left:* μ-value distribution for a TS1 filter. *Top right:* μ-value distribution for a TS4 filter. *Bottom:* μ-value distribution for a TS9 filter. 127
5.3 Distributions of the σ (left column) and θ-values (right coliumn) for FSRQs (red) and BL Lacs (blue), given different TS filters. *Top row:* TS1 filter. *Mid row:* TS4 filter. *Bottom row:* TS9 filter. 128

5.4 Distributions of the ξ-values (left column) for FSRQs (red), BL Lacs (blue) and unclassified blazars (green) and scatter plot showing σ and θ versus ξ (right column), given different TS filters. *Top row:* TS1 filter. *Mid row:* TS4 filter. *Bottom row:* TS9 filter. 129
5.5 Flare asymmetry measure for TS1 (top left), TS4 (top right) and TS9 (bottom). 130
5.6 Analysis of the 20 sources from the jet-gradient sample. *Top left:* μ-distribution, *Top right:* σ-distribution, *Mid left:* θ-distribution, *Mid right:* ξ-distribution, *Bottom left:* impact of the OU parameters on ξ, *Bottom right:* flare asymmetry measure. 131
5.7 Impact of the TS9 filtered OU parameters on ξ for FSRQs (left) and BL Lacs (right) 132

List of Tables

1.1 Summary of the unification model; Credit: Matthias Kadler, edited by Paul Ray Burd 11

2.1 MODELFIT parameters from the example, shown in Fig. 2.3, exported from DIFMAP; Col. 1: flux density in Jy, col. 2: x-position from the map center in deg, col. 3: y-position from the map center in deg, col. 4: major axis in deg, col. 5: minor axis in deg, col. 6: position angle in deg 40

2.2 Source properties of the pc-scale radio jet study 42

4.1 Fitting results of jet geometry and brightness-temperature gradients. For each source, the top row refers to the full jet length probed and the bottom row refers to the overlap region probed at both frequencies; Columns: (1) IAU B 1950 name, (2) Fit parameter of jet-geometry at 15 GHz l (reduced χ^2), (3) Fit parameter of jet-geometry at 43 GHz l (reduced χ^2), (4) Fit parameter of brightness-temperature gradient at 15 GHz l (reduced χ^2), (3) Fit parameter of brightness-temperature gradient at 43 GHz l (reduced χ^2). From: Burd et al. (2022) 65

4.2 Different correlation tests are performed on obtained parameters; col. 1: tested pair, col.2: test, col. 3: p-value, Values From: Burd et al. (2022) . 68

4.3 Different correlation tests are performed on obtained parameters; col. 1: tested pair, col.2: test, col. 3: p-value, Values From: Burd et al. (2022) . 69

4.4 Col.1: Source (class); Col.2: $b_{\rm eq}$; Col.3: $b_{\rm pc}$; Col.4: magnetic field strength in the radio core; Col.5: jet power; Col.6: magnetic field in the ergosphere (Blandford & Znajek (1977)); Col.7: magnetic field in the ergosphere (Eddington); Col.8: distance of the radio core from the SMBH in the Blandford & Znajek (1977) case; Col.9: distance of the radio core from the SMBH in the Eddington case. 75

4.5 Geometry transition properties of individual sources. From: Burd et al. (2022) 81

6.1 $\tau_{\rm Kendall}$ for the tested parameters pairs, comparing the jet complexity and the OU parameters. 134

6.2 $R_{\rm Spearman}$ for the tested parameters pairs, comparing the jet complexity and the OU parameters. 134

6.3 $R_{\rm Pearson}$ for the tested parameters pairs, comparing the jet complexity and the OU parameters. 135

Bibliography

Aalto S., Costagliola F., Muller S., et al., 2016, A&A 590, A73

Aalto S., Falstad N., Muller S., et al., 2020, A&A 640, A104

Abdo A.A., Ackermann M., Agudo I., et al., 2010a, ApJ 716, 30

Abdo A.A., Ackermann M., Ajello M., et al., 2010b, ApJ 722, 520

Abdo A.A., Ackermann M., Ajello M., et al., 2011, ApJ 736, 131

Abdollahi S., Acero F., Ackermann M., et al., 2020, ApJS 247, 33

Abramowicz M.A., Fragile P.C., 2013, Living Reviews in Relativity 16, 1

Ajello M., Angioni R., Axelsson M., et al., 2020, ApJ 892, 105

Akiyama K., Asada K., Fish V., et al., 2018, Galaxies 6, 15

Albert J., Aliu E., Anderhub H., et al., 2007a, ApJ 663, 125

Albert J., Aliu E., Anderhub H., et al., 2007b, ApJ 669, 862

Aleksić J., Ansoldi S., Antonelli L.A., et al., 2014, Science 346, 1080

Aleksić J., Antonelli L.A., Antoranz P., et al., 2011, A&A 530, A4

Alfvén H., 1942, Nature 150, 405

Angioni R., Ros E., Kadler M., et al., 2019, A&A 627, A148

Ansoldi S., Antonelli L.A., Arcaro C., et al., 2018, ApJL 863, L10

Antonucci R., 1993, ARA&A 31, 473

Antonucci R., 2013, Nature 495, 165

Antonucci R., 2015, arXiv e-prints arXiv:1501.02001

Arbet-Engels A., Baack D., Balbo M., et al., 2021, A&A 647, A88

Arras P., Frank P., Haim P., et al., 2022, Nature Astronomy 6, 259

Arras P., Knollmüller J., Junklewitz H., Enßlin T.A., 2018, arXiv e-prints arXiv:1803.02174

Asada K., Nakamura M., 2012, ApJL 745, L28

Astropy Collaboration Robitaille T.P., Tollerud E.J., et al., 2013, A&A 558, A33

Atwood W.B., Abdo A.A., Ackermann M., et al., 2009, ApJ 697, 1071

Baczko A.K., Ros E., Kadler M., et al., 2022, A&A 658, A119

Baczko A.K., Schulz R., Kadler M., et al., 2016, A&A 593, A47

Balmaverde B., Baldi R.D., Capetti A., 2008, A&A 486, 119

Bennert N., Jungwiert B., Komossa S., et al., 2006, A&A 456, 953

Bignami G.F., Boella G., Burger J.J., et al., 1975, Space Science Instrumentation 1, 245

Bignami G.F., Hermsen W., 1983, ARA&A 21, 67

Blandford R., Yuan Y., Hoshino M., Sironi L., 2017, Space Sci. Rev. 207, 291

Blandford R.D., Königl A., 1979, ApJ 232, 34

Blandford R.D., Znajek R.L., 1977, MNRAS 179, 433

Boccardi B., Perucho M., Casadio C., et al., 2021, A&A 647, A67

Bondi H., 1952, MNRAS 112, 195

Böttcher M., Baring M.G., 2019, ApJ 887, 133

Bridle A.H., Schwab F.R., 1999, In: Taylor G.B., Carilli C.L., Perley R.A. (eds.) Synthesis Imaging in Radio Astronomy II, Vol. 180. Astronomical Society of the Pacific Conference Series, Astronomical Society of the pacific, San Francisco, p. 371

Burd P.R., 2017, *Master's thesis*, JMU Würzburg, Emil-Fischer-Straße 31, 97070 Würzburg

Burd P.R., Kadler M., Mannheim K., et al., 2022, A&A 660, A1

Burd P.R., Kohlhepp L., Wagner S.M., et al., 2021, A&A 645, A62

Burke B.F., Graham-Smith F., 2009, An Introduction to Radio Astronomy, Cambridge University Press, Cambridge

Casadio C., MacDonald N.R., Boccardi B., et al., 2021, A&A 649, A153

Casadio C., Marscher A.P., Jorstad S.G., et al., 2019, A&A 622, A158

Cawthorne T.V., 2006, MNRAS 367, 851

Cawthorne T.V., Cobb W.K., 1990, ApJ 350, 536

Cawthorne T.V., Jorstad S.G., Marscher A.P., 2013, ApJ 772, 14

Chakraborty N., Cologna G., 2015, In: 34th International Cosmic Ray Conference (ICRC2015), Vol. 34. International Cosmic Ray Conference, p. 872

Chatterjee R., Marscher A.P., Jorstad S.G., et al., 2011, ApJ 734, 43

Christie I.M., Petropoulou M., Sironi L., Giannios D., 2019, MNRAS 482, 65

Clark B.G., 1980, A&A 89, 377

Clark B.G., 1999, In: Taylor G.B., Carilli C.L., Perley R.A. (eds.) Synthesis Imaging in Radio Astronomy II, Vol. 180. Astronomical Society of the Pacific Conference Series, p. 1

Cohen M.H., Lister M.L., Homan D.C., et al., 2007, ApJ 658, 232

Condon J.J., Ransom S.M., 2016, Essential Radio Astronomy, Princeton Series in Modern Observational Astronomy, Princeton University Press, Princeton

Cooper N.J., Lister M.L., Kochanczyk M.D., 2007, ApJS 171, 376

Cornwell T., Braun R., 1989, In: Perley R.A., Schwab F.R., Bridle A.H. (eds.) Synthesis Imaging in Radio Astronomy, Vol. 6. Astronomical Society of the Pacific Conference Series, p. 167

Cornwell T., Fomalont E.B., 1989, In: Perley R.A., Schwab F.R., Bridle A.H. (eds.) Synthesis Imaging in Radio Astronomy, Vol. 6. Astronomical Society of the Pacific Conference Series, p. 185

Cornwell T.J., 1989, Science 245, 263

Daly R.A., 2009, ApJ 696, L32

Daly R.A., 2011, MNRAS 414, 1253

Daly R.A., Marscher A.P., 1988, ApJ 334, 539

Daly R.A., Sprinkle T.B., 2014, MNRAS 438, 3233

Deka K., Shah Z., Misra R., Ahmed G.A., 2021, Journal of High Energy Astrophysics 31, 23

Eichler D., 1993, ApJ 419, 111

Einstein A., 1905, Annalen der Physik 322, 891

Eisenstein D.J., Hut P., 1998, ApJ 498, 137

Eracleous M., Halpern J.P., 2004, ApJS 150, 181

Esparza-Arredondo D., Gonzalez-Martín O., Dultzin D., et al., 2021, A&A 651, A91

Event Horizon Telescope Collaboration Akiyama K., Alberdi A., et al., 2019, ApJL 875, L6

Falomo R., Carangelo N., Treves A., 2003, MNRAS 343, 505

Falomo R., Scarpa R., Bersanelli M., 1994, ApJS 93, 125

Fan J.H., Yuan Y.H., Huang Y., et al., 2008, In: Bureau M., Athanassoula E., Barbuy B. (eds.) Formation and Evolution of Galaxy Bulges, Vol. 245., p.243

Fanaroff B.L., Riley J.M., 1974, MNRAS 167, 31P

Fichtel C.E., Hartman R.C., Kniffen D.A., et al., 1975, ApJ 198, 163

Finke J.D., 2016, ApJ 830, 94

Fomalont E.B., 1999, In: Taylor G.B., Carilli C.L., Perley R.A. (eds.) Synthesis Imaging in Radio Astronomy II, Vol. 180. Astronomical Society of the Pacific Conference Series, Astronomical Society of the pacific, San Francisco, p. 301

Fossati G., Maraschi L., Celotti A., et al., 1998, MNRAS 299, 433

Fromm C.M., Perucho M., Ros E., et al., 2015, A&A 576, A43

Gaspari M., Ruszkowski M., Oh S.P., 2013, MNRAS 432, 3401

Gebhardt K., Adams J., Richstone D., et al., 2011, ApJ 729, 119

Ghisellini G., Celotti A., Fossati G., et al., 1998, MNRAS 301, 451

Ghisellini G., Foschini L., Tavecchio F., Pian E., 2007, MNRAS 382, L82

Ghisellini G., Righi C., Costamante L., Tavecchio F., 2017, MNRAS 469, 255

Ghisellini G., Tavecchio F., 2008, MNRAS 387, 1669

Giannios D., Uzdensky D.A., Begelman M.C., 2009, MNRAS 395, L29

Gillespie D.T., 1996, Physical Review E 54, 2084

Giroletti M., Giovannini G., Taylor G.B., Falomo R., 2006, ApJ 646, 801

Godfrey L.E.H., Shabala S.S., 2013, ApJ 767, 12

Gokus A., Paliya V.S., Wagner S.M., et al., 2021, A&A 649, A77

Gupta S., Pandey U., Singh K., et al., 2012, New Astronomy 17, 8

Hada K., Doi A., Wajima K., et al., 2018, ApJ 860, 141

Harris C.R., Millman K.J., van der Walt S.J., et al., 2020, Nature 585, 357–362

Hodge M.A., Lister M.L., Aller M.F., et al., 2018, ApJ 862, 151

Hogg D.W., 1999, arXiv e-prints astro–ph/9905116

Holt S.S., Neff S.G., Urry C.M., (eds.) 1992, Testing the AGN paradigm; Proceedings of the 2nd Annual Topical Astrophysics Conference, Univ. of Maryland, College Park, Oct. 14-16, 1991, Vol. 254 of *American Institute of Physics Conference Series*, American Institute of Physics Conference Series

Homan D.C., Lister M.L., Kovalev Y.Y., et al., 2015, ApJ 798, 134

Hönig S.F., Kishimoto M., 2010, A&A 523, A27

Hönig S.F., Kishimoto M., Gandhi P., et al., 2010, A&A 515, A23

Hovatta T., Aller M.F., Aller H.D., et al., 2014, AJ 147, 143

Hovatta T., Petropoulou M., Richards J.L., et al., 2015, MNRAS 448, 3121

Hovatta T., Valtaoja E., Tornikoski M., Lähteenmäki A., 2009, A&A 498, 723

Hunter J.D., 2007, Computing in Science & Engineering 9, 90

Hunter S.D., Bertsch D.L., Dingus B.L., et al., 1993, ApJ 409, 134

Högbom J.A., 1974, A&AS 15, 417

IceCube CollaborationAartsen M.G., Ackermann M., et al., 2018a, Science 361, eaat1378

IceCube CollaborationAartsen M.G., Ackermann M., et al., 2018b, Science 361, 147

Jackson N., Browne I.W.A., 1991, MNRAS 250, 414

Jennison R.C., 1958, MNRAS 118, 276

Jorstad S., Marscher A., 2016, Galaxies 4

Jorstad S.G., Marscher A.P., Mattox J.R., et al., 2001, ApJ 134, 181

Jorstad S.G., Marscher A.P., Morozova D.A., et al., 2017, ApJ 846, 98

Junkkarinen V., 1984, PASP 96, 539

Kadler M., Krauß F., Mannheim K., et al., 2016, Nature Physics 12, 807

Kadler M., Ros E., Lobanov A.P., et al., 2004, A&A 426, 481

Kadler M., Ros E., Perucho M., et al., 2008, ApJ 680, 867

Kappes A., Perucho M., Kadler M., et al., 2019, A&A 631, A49

Kaspi S., Smith P.S., Netzer H., et al., 2000, ApJ 533, 631

Keenan M., Meyer E.T., Georganopoulos M., et al., 2021, MNRAS

Keivani A., Murase K., Petropoulou M., et al., 2018, ApJ 864, 84

Kellermann K.I., Kovalev Y.Y., Lister M.L., et al., 2007, Ap&SS 311, 231

Kellermann K.I., Lister M.L., Homan D.C., et al., 2004, ApJ 609, 539

Kellermann K.I., Pauliny-Toth I.I.K., Williams P.J.S., 1969, ApJ 157, 1

Kelly B.C., Bechtold J., Siemiginowska A., 2009, ApJ 698, 895

Kelly B.C., Becker A.C., Sobolewska M., et al., 2014, The Astrophysical Journal 788, 33

Kelly B.C., Sobolewska M., Siemiginowska A., 2011, ApJ 730, 52

Kerr R.P., 1963, Phys. Rev. Lett. 11, 237

Kharb P., Lister M.L., Cooper N.J., 2010, ApJ 710, 764

Kino M., Takahara F., Hada K., Doi A., 2014, ApJ 786, 5

Knopf M., 2020, *Bachelor's thesis*, JMU Würzburg, Emil-Fischer-Straße 31, 97070 Würzburg

Kohlhepp L., 2020, *Bachelor's thesis*, JMU Würzburg, Emil-Fischer-Straße 31, 97070 Würzburg

Kopp R.A., Pneuman G.W., 1976, Solar Physics 50, 85

Kovalev Y.Y., Kellermann K.I., Lister M.L., et al., 2005, AJ 130, 2473

Kovalev Y.Y., Pushkarev A.B., Nokhrina E.E., et al., 2020, MNRAS 495, 3576

Krauß F., Wilms J., Kadler M., et al., 2016, A&A 591, A130

Krolik J.H., 1999, Active galactic nuclei : from the central black hole to the galactic environment, Princeton University Press, Princeton

Krolik J.H., Begelman M.C., 1988, ApJ 329, 702

Kudryavtseva N.A., Gabuzda D.C., Aller M.F., Aller H.D., 2011, MNRAS 415, 1631

Königl A., 1981, ApJ 243, 700

Lico R., Giroletti M., Orienti M., et al., 2012, A&A 545, A117

Lind K.R., Blandford R.D., 1985, ApJ 295, 358

Lister M.L., Aller H.D., Aller M.F., et al., 2009, AJ 137, 3718

Lister M.L., Aller M.F., Aller H.D., et al., 2018, ApJS 234, 12

Lister M.L., Aller M.F., Aller H.D., et al., 2016, AJ 152, 12

Lister M.L., Homan D.C., Hovatta T., et al., 2019, ApJ 874, 43

Lister M.L., Homan D.C., Hovatta T., et al., 2019, ApJ 874, 43

Lister M.L., Homan D.C., Kellermann K.I., et al., 2021, ApJ 923, 30

Lomb N.R., 1976, Ap&SS 39, 447

Lyubarskii Y.E., 1997, MNRAS 292, 679

MAGIC CollaborationAcciari V.A., Ansoldi S., et al., 2020, A&A 640, A132

MAGIC Collaboration Acciari V.A., Ansoldi S., et al., 2020, MNRAS 496, 3912

MAGIC CollaborationAhnen M.L., Ansoldi S., et al., 2018, A&A 619, A45

Mannheim K., 1993, A&A 269, 67

Mannheim K., Protheroe R.J., Rachen J.P., 2000, Phys. Rev. D 63, 023003

Marscher A., 2016, Galaxies 4, 37

Marscher A.P., Jorstad S.G., D'Arcangelo F.D., et al., 2008, Nature 452, 966

Marscher A.P., Jorstad S.G., Larionov V.M., et al., 2010, ApJL 710, L126

Marziani P., Sulentic J.W., Dultzin-Hacyan D., et al., 1996, ApJS 104, 37

Mattox J.R., Bertsch D.L., Chiang J., et al., 1996, ApJ 461, 396

Mertens F., Lobanov A.P., Walker R.C., Hardee P.E., 2016, A&A 595, A54

Meyer E.T., Fossati G., Georganopoulos M., Lister M.L., 2011, ApJ 740, 98

Meyer M., Scargle J.D., Blandford R.D., 2019, ApJ 877, 39

Michel A., Huchra J., 1988, PASP 100, 1423

Misner C.W., Thorne K.S., Wheeler J.A., 1973, Gravitation, W. H. Freeman and Company, San Francisco

Mücke A., Protheroe R.J., 2001, Astroparticle Physics 15, 121

Mücke A., Protheroe R.J., Engel R., et al., 2003, Astroparticle Physics 18, 593

Müller C., Burd P.R., Schulz R., et al., 2016, A&A 593, L19

Müller C., Kadler M., Ojha R., et al., 2018, A&A 610, A1

Nakahara S., Doi A., Murata Y., et al., 2018, ApJ 854, 148

Nakahara S., Doi A., Murata Y., et al., 2020, AJ 159, 14

Nilsson K., Pursimo T., Villforth C., et al., 2012, A&A 547, A1

Nishikawa K., Mizuno Y., Gómez J.L., et al., 2020, MNRAS 493, 2652

O'Dea C.P., 1998, PASP 110, 493

Orienti M., D'Ammando F., Giroletti M., et al., 2020, MNRAS 491, 858

O'Sullivan S.P., Gabuzda D.C., 2009, MNRAS 400, 26

Paiano S., Landoni M., Falomo R., et al., 2017, ApJ 837, 144

Pâris I., Petitjean P., Ross N.P., et al., 2017, A&A 597, A79

Park J., Hada K., Kino M., et al., 2019, ApJ 887, 147

Park J., Hada K., Nakamura M., et al., 2021, ApJ 909, 76

Peñil P., Domínguez A., Buson S., et al., 2020, ApJ 896, 134

Perucho M., Kovalev Y.Y., Lobanov A.P., et al., 2012, ApJ 749, 55

Peterson B.M., Ferrarese L., Gilbert K.M., et al., 2004a, ApJ 613, 682

Peterson B.M., Ferrarese L., Gilbert K.M., et al., 2004b, ApJ 613, 682

Petropoulou M., Sironi L., Spitkovsky A., Giannios D., 2019, ApJ 880, 37

Pier E.A., Krolik J.H., 1992, ApJ 401, 99

Pier E.A., Krolik J.H., 1993, ApJ 418, 673

Piner B.G., Pant N., Edwards P.G., 2010, ApJ 723, 1150

Potter W.J., Cotter G., 2012, MNRAS 423, 756

Potter W.J., Cotter G., 2013a, MNRAS 429, 1189

Potter W.J., Cotter G., 2013b, MNRAS 431, 1840

Potter W.J., Cotter G., 2013c, MNRAS 436, 304

Potter W.J., Cotter G., 2015, MNRAS 453, 4070

Price-Whelan A.M., Sipőcz B.M., Günther H.M., et al., 2018, AJ 156, 123

Pushkarev A., Kovalev Y., Lister M., et al., 2017a, Galaxies 5, 93

Pushkarev A.B., Hovatta T., Kovalev Y.Y., et al., 2012, A&A 545, A113

Pushkarev A.B., Kovalev Y.Y., 2012, A&A 544, A34

Pushkarev A.B., Kovalev Y.Y., Lister M.L., Savolainen T., 2009, A&A 507, L33

Pushkarev A.B., Kovalev Y.Y., Lister M.L., Savolainen T., 2017b, MNRAS 468, 4992

Rayleigh L., 1879, The London, Edinburgh, and Dublin Philosophical Magazine and Journal of Science 8, 261

Richter N., 2019, *Bachelor's thesis*, JMU Würzburg, Emil-Fischer-Straße 31, 97070 Würzburg

Romney J.D., 1999, In: Taylor G.B., Carilli C.L., Perley R.A. (eds.) Synthesis Imaging in Radio Astronomy II, Vol. 180. Astronomical Society of the Pacific Conference Series, Astronomical Society of the pacific, San Francisco, p. 57

Roy N., Chatterjee R., Joshi M., Ghosh A., 2019, MNRAS 482, 743

Russell H.R., Fabian A.C., McNamara B.R., Broderick A.E., 2015, MNRAS 451, 588

Rybicki G.B., Lightman A.P., 1979, Radiative processes in astrophysics, New York, Wiley-Interscience, 1979. 393 p.

Scargle J.D., 1981, ApJS 45, 1

Scargle J.D., 1982, ApJ 263, 835

Scargle J.D., 2020, ApJ 895, 90

Scargle J.D., Norris J.P., Jackson B., Chiang J., 2013a, ApJ 764, 167

Scargle J.D., Norris J.P., Jackson B., Chiang J., 2013b, arXiv e-prints arXiv:1304.2818

Schneider D.P., Richards G.T., Hall P.B., et al., 2010, AJ 139, 2360

Schwarzschild K., 1916, Abh. Konigl. Preuss. Akad. Wissenschaften Jahre 1906,92, Berlin,1907 1916, 189

Seeg M., 2017, *Bachelor's thesis*, JMU Würzburg, Emil-Fischer-Straße 31, 97070 Würzburg

Shakura N.I., Sunyaev R.A., 1973, A&A 24, 337

Shepherd M.C., 1997, In: Hunt G., Payne H. (eds.) Astronomical Data Analysis Software and Systems VI, Vol. 125. Astronomical Society of the Pacific Conference Series, Astronomical Society of the pacific, San Francisco, p. 77

Shukla A., Mannheim K., 2020, Nature Communications 11, 4176

Shukla A., Mannheim K., Patel S.R., et al., 2018, ApJL 854, L26

Sobolewska M.A., Siemiginowska A., Kelly B.C., Nalewajko K., 2014, ApJ 786, 143

Sokolovsky K.V., Kovalev Y.Y., Pushkarev A.B., Lobanov A.P., 2011, A&A 532, A38

Stadnik M., Romani R.W., 2014, ApJ 784, 151

Stickel M., Fried J.W., Kuehr H., 1988, A&A 191, L16

Stickel M., Fried J.W., Kuehr H., 1989, Astron. Astrophys. Suppl. 80, 103

Stickel M., Fried J.W., Kuehr H., 1993, Astron. Astrophys. Suppl. 98, 393

Stickel M., Kuehr H., 1993, Astron. Astrophys. Suppl. 100, 395

Strauss M.A., Huchra J.P., Davis M., et al., 1992, ApJS 83, 29

Takata T., Mukuta Y., Mizumoto Y., 2018, ApJ 869, 178

Tavecchio F., Ghisellini G., 2008, MNRAS 385, L98

Taylor G.B., Carilli C.L., Perley R.A., (eds.) 1999, Synthesis Imaging in Radio Astronomy II, Vol. 180 of *Astronomical Society of the Pacific Conference Series*, Astronomical Society of the Pacific Conference Series, Astronomical Society of the pacific, San Francisco

Thompson A.R., Moran J.M., Swenson G.W., 1986, Interferometry and synthesis in radio astronomy, New York, Wiley-Interscience, 1986, 554 p.

Thompson D.J., Bertsch D.L., Dingus B.L., et al., 1995, ApJS 101, 259

Thompson D.J., Bertsch D.L., Dingus B.L., et al., 1993a, ApJL 415, L13

Thompson D.J., Bertsch D.L., Fichtel C.E., et al., 1993b, ApJS 86, 629

Timmer J., König M., 1995, A&A 300, 707

Torres-Zafra J., Cellone S.A., Buzzoni A., et al., 2018, MNRAS 474, 3162

Townsend R.H.D., 2010, ApJS 191, 247

Tseng C.Y., Asada K., Nakamura M., et al., 2016, ApJ 833, 288

Uhlenbeck G.E., Ornstein L.S., 1930, Physical Review 36, 823

Ulrich M.H., Kinman T.D., Lynds C.R., et al., 1975, ApJ 198, 261

Ulrich M.H., Maraschi L., Urry C.M., 1997, ARA&A 35, 445

Urry C.M., Padovani P., 1995, PASP 107, 803

Uttley P., McHardy I.M., Vaughan S., 2005, MNRAS 359, 345

Vega-García L., Lobanov A.P., Perucho M., et al., 2020, A&A 641, A40

Vega-García L., Perucho M., Lobanov A.P., 2019, A&A 627, A79

Vermeulen R.C., Ogle P.M., Tran H.D., et al., 1995, ApJL 452, L5

Vestergaard M., Peterson B.M., 2006, ApJ 641, 689

Virtanen P., Gommers R., Oliphant T.E., et al., 2019, arXiv e-prints arXiv:1907.10121

Virtanen P., Gommers R., Oliphant T.E., et al., 2020, Nature Methods 17, 261

Wagner S., 2020, *Master's thesis*, JMU Würzburg, Emil-Fischer-Straße 31, 97070 Würzburg

Wagner S.M., Burd P., Dorner D., et al., 2021, PoS ICRC2021, 868

Wandel A., Peterson B.M., Malkan M.A., 1999, ApJ 526, 579

Wilkes B.J., 1986, MNRAS 218, 331

Wilks S.S., 1938, The Annals of Mathematical Statistics 9, 60

Wills B.J., Wills D., Breger M., et al., 1992, ApJ 398, 454

Wills D., Lynds R., 1978, ApJS 36, 317

Wold 1939, Journal of the Royal Statistical Society 102, 295

Wood M., Caputo R., Charles E., et al., 2018, PoS ICRC2017, 824 [35,824(2017)]

Wright A.E., Ables J.G., Allen D.A., 1983, MNRAS 205, 793

Yaji Y., Tashiro M.S., Isobe N., et al., 2010, ApJ 714, 37

Yuan Y., Nalewajko K., Zrake J., et al., 2016, ApJ 828, 92

Acknowledgements

This research has made use of data from the MOJAVE database that is maintained by the MOJAVE team (Lister et al. 2018).
This study makes use of VLBA data from the VLBA-BU Blazar Monitoring Program (BEAM-ME and VLBA-BU-BLAZAR; http://www.bu.edu/blazars/BEAM-ME.html, funded by NASA through the Fermi Guest Investigator Program. The VLBA is an instrument of the National Radio Astronomy Observatory. The National Radio Astronomy Observatory is a facility of the National Science Foundation operated by Associated Universities, Inc.
The *DATEV Stiftung Zukunft* is acknowledged for funding the interdisciplinary data lab *DataSphere@JMUW*.
This research made use of Astropy,[2] a community-developed core Python package for Astronomy (Astropy Collaboration et al. 2013; Price-Whelan et al. 2018)
First of all I want to thank Prof. Kadler for supervising this thesis. He also supervised my BSc and MSc thesis. In numerous discussion rounds, he helped me to make my work better and provided me with valuable insight. For this I am grateful. I thank Prof. Kovalev, Prof. Lister and Prof. Homan from the MOJAVE team for critical and insightful comments on the jet-gradients work.
I want to thank Sarah Wagner, Luca Kohlhepp and Dr. Scargle who intensively worked with me on the OU project and equally are responsible for the success of this part of the work. I also thank Prof. Buson and Andrea Gokus for providing me with the light curves analyzed in the OU paper and throughout this thesis. I also want to thank Prof. Buson for numerous discussions on blazar light curves.
I thank Prof. Mannheim, not only for funding me over the last 4.5 years but also for the numerous and in times long discussions and insights on not only science relevant topics, which also helped me to become a better person. Your consistent support made it possible for me to invest time in many different aspects of science, supervise or co-supervise a number of students, and gave me the opportunity to build up the data lab. For all these opportunities and all the advise, I am grateful.
I want to thank my dear band colleagues Andy, Jonas, Phil and Amrkus for, also in hard times, holding on to music.
I especially thank Andy for editing my German abstract.
I thank my mother Evelyn and my sisters Natalie and Thea for enduring me over the decades.
I thank my wonderful sons Edgar and Ragnar for showing me a kind of love I could have never imagined exists without them. I am endlessly proud of you and I am grateful from

[2] http://www.astropy.org

all of my heart to be able to see you grow up and learn about the world. Thank you for your love. In the end I want to thank my wonderful wife Svenja. Without you I would be lost in this world. You and our kids fill my heart with love. I thank you from all of my heart for being a wonderful, supportive and loving mother and wife. I also thank you for your love.

Appendix A

Significant contributions to Co-Authored papers

Wagner et al. (2021): Statistical properties of flux variations in blazar light curves at GeV and TeV energies This paper is a continuation of the efforts surrounding the understanding of blazar light curves. We analyzed a two samples of γ-ray detected blazars with the Bayesian block+HOP algorithm procedure and the Ornstein-Uhlenbeck parameter extraction. We compared TeV-blazar light curves, observed with FACT and GeV-blazar light curves, observed with *Fermi*, both daily binned. Also in this sample, there is no evidence for systematic higher rise and decay times for the identified flares. The OU parameters depend on the energy of the light curve. *Fermi*-detected light curves (GeV) show OU-parameters that favor a stronger variability and therefore more complex light curves. Overall the analysis points to the fact that the variation in flux in both samples is a superposition of fluctuation on smaller time scales which is expected for magnetic reconnection events. I provided the OU analysis for the GeV and TeV light curves.

Baczko et al. 2021 submitted and revised: Ambilateral collimation study of the twin-jets in NGC 1052 In this paper the jet geometry of NGC 1052 was studied thoroughly. We combines RadioAstron data with 15, 22 and 43 GHz data and geometry transition for both the jet and counter-jet. For both, the receding and the approaching jet, the geometry beyond the break point at ($\sim 10^4 R_s$) is conical. However, the receding jet is nearly cylindrical upstream the break points ($l \sim 0.16$) while the approaching jet is closer to parabolic in this region ($l \sim 0.36$). This shows that there are systematic differences between both jets of the AGN. In this work I provided a consistency check

on the geometry break point and the diameter scaling of the jet based on the method discussed in this work.

Kappes 2021 submitted and revised : The sub-arcsecond view on the high-redshift blazar GB 1508+5714 by the International LOFAR Telescope In this paper possible CMB quenching was assessed in a high redshift blazar (z=4.30) was assessed. Using LOFAR observations we are able to constrain the morphology, spatially resolved spectral indices and hot spot advance speed on this source. With the flux density measurements in the different region in the source, we could fit the broad band SED with different models. The results show that a model where the cooling electrons from the source, interact via inverse Compton scattering with the cosmic microwave backgorund is favored (CMB quenching). For this work I provided the imaging consistentcy check, the constrain on the inclination angle and the hot spot advance speed.

Kappes et al. (2019): LOFAR measures the hotspot advance speed of the high-redshift blazar S5 0836+710 In this paper we constrained the advance speed of the hot spot of S5 0836+710, which was made possible by LOFAR observations. For this paper I calibrated and imaged the different sub-bands from the LOFAR observation and made the hot-spot interpretation of the extended emission of this source with a simple 'stick in the sky' model plausible, which was later backed by intra-LOFAR spectral index.

Müller et al. (2016): The MHz-peaked radio spectrum of the unusual γ-ray source PMN J1603-4904 In this paper we constrained the synchrotron peak of the radio spectrum of PMN J1603-4904 and classified this sources as MHz-peak source with a maximum linear size of $\sim$ 1.4 kpc. In this paper I calibrated, imaged and analyzed GMRT data at 600 MHz and 300 MHz which was crucial in order to constrain the peak of the radio spectrum.